Proceedings of the

13th Patras Workshop On Axions, WIMPs and WISPs

May 15 – 19, 2017
Thessaloniki
Greece

Editor:
Marios Maroudas

VERLAG DEUTSCHES ELEKTRONEN-SYNCHROTRON

Proceedings of the

13th Patras Workshop on Axions, WIMPs and WISPs

PATRAS 2017

May 15 – 19, 2017

Thessaloniki, Greece

Editor: Marios Maroudas

Verlag Deutsches Elektronen-Synchrotron

Impressum

Proceedings of the 13th Patras Workshop on Axions, WIMPs and WISPs (PATRAS 2017)

May 15 – 19, 2017, Thessaloniki, Greece

Conference homepage
`https://axion-wimp2017.desy.de`

Slides at
`https://axion-wimp2017.desy.de/e28905/`

Online proceedings at
`http://www-library.desy.de/confprocs.html`

Editor:
Marios Maroudas
December 2017
DESY-PROC-2017-02
ISBN 978-3-945931-17-2
ISSN 1435-8077

Published by
Verlag Deutsches Elektronen-Synchrotron
Notkestraße 85
22607 Hamburg
Germany

Printed by
Kopierstelle Deutsches Elektronen-Synchrotron

Organizing Committee

Konstantin Zioutas (Chairman) and Vassilis Anastassopoulos
Department of Physics
University of Patras
26504 Patra
Greece

Laura Baudis
Physik Institut
University of Zurich
Winterthurerstr. 190
8057 Zurich
Switzerland

Joerg Jaeckel
Institut für theoretische Physik
Universität Heidelberg
Philosophenweg 16
69120 Heidelberg
Germany

Axel Lindner and Andreas Ringwald
Deutsches Elektronen Synchrotron (DESY)
Notkestraße 85
D-22607 Hamburg
Germany

Marc Schumann
Physikalisches Institut
University of Freiburg
Hermann-Herder-Str. 3
D-79104 Freiburg
Germany

Yannis K. Semertzidis
Department of Physics
KAIST & Center for Axion and Precision Physics Research, IBS
291 Daehak-ro, Yuseong-gu
34141 Daejeon
Republic of Korea

Conference Secretary and Local Organization

Barbara Wittmann
Deutsches Elektronen Synchrotron (DESY)
Notkestraße 85
D-22607 Hamburg
Germany

Konstantin Zioutas and Vassilis Anastassopoulos
Department of Physics
University of Patras
26504 Patra
Greece

Antonios Gardikiotis
Mesologgiou 37 A
26222 Patra
Greece

Marios Maroudas
Panachaikou 23
26224 Patra
Greece

Hero Ziouta
I. Passalidi 146
55133 Kalamaria
Greece


13th Patras Workshop
on Axions, WIMPs and WISPs
15 - 19 May 2017, Thessaloniki / Greece
Scientific programme:
Direct / indirect searches for Dark Matter
Direct / indirect searches for Axions & WISPs
Searches for Hidden Sector Photons
Astrophysical signatures for dark matter
Review of collider experiments
New developments: theory / experiment
Scalar Dark Energy: theory / experiment
http://axion-wimp.desy.de
Organizing committee:
Konstantin Zioutas (Chair, University of Patras)
Vassilis Anastassopoulos (University of Patras)
Laura Baudis (University of Zurich)
Joerg Jaeckel (University of Heidelberg)
Axel Lindner (DESY)
Andreas Ringwald (DESY)
Marc Schumann (University of Freiburg)
Yannis Semertzidis (CAPP/IBS & KAIST)
SPONSORS: CERN, DESY, UNIVERSITY FREIBURG, UNIVERSITY HEIDELBERG, UNIVERSITY PATRAS, UNIVERSITÄT ZÜRICH, CAST

Preface

Laboratory experiments along with astrophysical observations, as well as new developments in theory, are pushing to unravel new physics beyond the Standard Model. The intense search for the elusive particles of the dark sector continues. Axions and WIMPs remain the two leading candidates for dark matter. Also the dark energy remains among the biggest mysteries in all physics even though much effort and many ideas are put forward to decipher its nature. Worldwide efforts continue with new clever ideas coming-up in order to spot these or eventually other (un)predicted particles. The challenge is big as well as the physics motivation. No doubt, we are living through an exciting time and breakthroughs can happen any time soon. The last 5 years we had already two historic events: the discovery of the HIGGS particle at CERN and the observation of the gravitational waves by LIGO in USA. Both have shaken the field of astro-particle physics. After all, astro-particle physics is aiming to find out the workings of the Universe from its beginning until the present time.

Various such hot topics and many more important aspects of particle and astroparticle physics were openly discussed between experimentalists and theorists at the 13th Patras Workshop on Axions, WIMPs, and WISPs. The event took place from May 15 - May 19, 2017 in Thessaloniki/Greece. As in the past, it was a very fruitful and lively meeting in an inspiring and cooperative atmosphere, which allowed for many open and constructive discussions, which initiated new collaboration work.

Many participants have noticed the spirit of the PATRAS workshop and its atmosphere, which cannot be brought to paper, but many of its scientific highlights are collected in these proceedings. We are looking forward to the 14th Patras Workshop, which will be held in DESY, from June 18 - June 22, 2018.

Konstantin Zioutas (Chairman)

Acknowledgements

The organizers would like to thank the University of Patras, CAST, CAPP/IBS & KAIST / Daejeon, CERN, DESY, the University of Freiburg, the University of Heidelberg and the University of Zurich for support. Special thanks also to Antonios Gardikiotis and Marios Maroudas for their real help. The help and patience of Zoe Kolokytha from ELKE/University of Patras is also acknowledged. All participants recognized once more the perfect organization of the workshop in every detail thanks to the full engagement before and during the workshop of Hero Ziouta, the assistant to the chair.

The organizing committee

Contents

Chapter 1

Axion Dark Matter and Searches for Axions and WISPs

Testing a new WISP Model with Laboratory Experiments

Pedro Alvarez[1], *Paola Arias*[2], *Carlos Maldonado*[2]

[1]Departamento de Fisica, Universidad de Antofagasta, Aptdo 02800, Chile.
[2]Departamento de Física, Universidad de Santiago de Chile, Santiago, Chile.

DOI: http://dx.doi.org/10.3204/DESY-PROC-2017-02/arias_paola

We explore the phenomenological consequences of a model with axion-like particles and hidden photons mixing with photons. In this model, the hidden photon is directly coupled to the photon, while the axion coupling is induced by an external electromagnetic field. We consider vacuum effects on a polarised photon beam, like changes in the ellipticity and rotation angles.

1 Introduction

In this work we would like to go beyond the straightforward extension of the Standard Model, namely the one-missing-particle paradigm. On the one hand, seems timely, due to the extraordinary refinement in sensitivity of latest years of experiments looking for WISPs (Weakly Interactive Slim Particles). On the other hand, there are some proposals of more complex models with rich phenomenology, such as [1], where they consider a model with a hidden photon (HP) coupled to an axion-like field (ALP), and the kinetic mixing term. Also in [2] a model with axion-like particle + hidden photon was invoked to explain the 3.55 keV line in the spectra of galaxy clusters. More recently a similar model was considered [3], where the pseudo-scalar boson is the QCD axion, which is coupled to the hidden photon. We have chosen to follow the construct in [2], therefore the hidden photon is the mediator between visible and hidden sector. In this work we are interested in observables effects of this model, focusing on vacuum effects, like dichroism and birefringence.

2 The model and equations of motion

We consider the following effective Lagrangian:

$$\mathcal{L} = -\frac{1}{4} f_{\mu\nu} f^{\mu\nu} - \frac{1}{4} x_{\mu\nu} x^{\mu\nu} + \frac{1}{2} \partial_\mu \phi \partial^\mu \phi + \frac{1}{2} \sin\chi f_{\mu\nu} x^{\mu\nu} + \frac{1}{4} g \phi x_{\mu\nu} \tilde{x}^{\mu\nu} - \frac{m_\phi^2}{2} \phi^2 + \frac{m_{\gamma'}^2 \cos^2\chi}{2} x_\mu x^\mu.$$

Here a_μ is the photon field, $(x_{\mu\nu})$ the HP field and ϕ is the ALP. The HP is directly coupled to photons via the kinetic mixing term, parametrised by $\sin\chi$. As it is well known, defining $X_\mu = x_\mu - a_\mu \sin\chi$ and $A_\mu = a_\mu \cos\chi$, removes the kinetic mixing, but at the price to inherit a coupling in the mass sector between photons and HPs, and also a term of the form $g \tan^2\chi \phi F_{\mu\nu} \tilde{F}^{\mu\nu}$, meaning an explicit coupling between photons and ALPs.

We start assuming a photon beam source of frequency ω, propagating in z direction, and the plane wave approximation, i.e, $\vec{A}(z,t) = e^{i\omega t}\vec{A}(z)$, $\phi(z,t) = e^{i\omega t}\phi(z)$ and $\vec{X}(z,t) = e^{i\omega t}\vec{X}(z)$. We also include an homogeneous magnetic field $\vec{B}$, oriented in the $\hat{x}$ direction. Additionally, we assume no external hidden fields are present. Secondly, we linearise the equations of motion assuming the external electromagnetic field is much stronger than the photon source $|\vec{A}_{\rm ext}| \gg |\vec{A}|$, and terms of the form $\phi|\vec{A}|$, $|\vec{A}||\vec{X}|$, $\phi|\vec{X}|$ can be neglected. Finally, considering a relativistic approximation, i.e, $(\omega^2 + {\partial_z}^2) \approx 2\omega(\omega - i\partial_z)$, we find the following equations[1]:

$$\left(\omega - i\partial_z - \tfrac{m_{\gamma'}^2}{2\omega}\begin{pmatrix}\sin^2\chi & \sin\chi\cos\chi\\ \sin\chi\cos\chi & \cos^2\chi\end{pmatrix}\right)\begin{pmatrix}A_\perp\\ X_\perp\end{pmatrix} = 0, \tag{1}$$

$$\left(\omega - i\partial_z - \tfrac{1}{2\omega}\begin{pmatrix}m_{\gamma'}^2\sin^2\chi & m_{\gamma'}^2\sin\chi\cos\chi & gB\omega\,\tan^2\chi\\ m_{\gamma'}^2\sin\chi\cos\chi & m_{\gamma'}^2\cos^2\chi & gB\omega\,\tan\chi\\ gB\omega\,\tan^2\chi & gB\omega\,\tan\chi & m_\phi^2\end{pmatrix}\right)\begin{pmatrix}A_\parallel\\ X_\parallel\\ \phi\end{pmatrix} = 0. \tag{2}$$

Where $\parallel$ and $\perp$ are the parallel and perpendicular components of the photon field to the external magnetic field, respectively. Equations (1) and (2) are of the Schroedinger-type, $i\partial_z\Psi(z) = H\Psi(z)$, where Eq. (1) is the usual one for a model of HP-photon oscillation. To solve Eq. (2) we introduce a rotation matrix that diagonalises the Hamiltonian, i.e, $R^T H R = {\rm d}iag\,(\omega_1,\omega_2,\omega_3)$, where the eigenvalues are given by: $\omega_1 = \omega = k$, $\omega_2 = \omega - \Omega - \Delta$ and $\omega_3 = \omega - \Omega + \Delta$, with:

$$\Omega \equiv \frac{m_{\gamma'}^2 + m_\phi^2}{4\omega}, \qquad \Delta \equiv \frac{gB}{2\cos^2\chi}\sqrt{\sin^2\chi + x^2\cos^4\chi}, \qquad x \equiv \frac{m_{\gamma'}^2 - m_\phi^2}{2gB\omega}. \tag{3}$$

The rotation matrix can be conveniently written in terms of two angles, θ and χ:

$$R = \begin{pmatrix}\cos\chi & \cos\theta\sin\chi & -\sin\theta\sin\chi\\ -\sin\chi & \cos\theta\cos\chi & -\cos\chi\sin\theta\\ 0 & \sin\theta & \cos\theta\end{pmatrix},\ \sin\theta = \frac{\sin\chi}{\sqrt{\mathcal{F}^2 + \sin^2\chi}}, \quad \mathcal{F} = \left(x + \frac{2\Delta}{Bg}\right).$$

The states $X_\parallel$ and ϕ are sterile to matter currents. Note that the limit $B \to 0$ can be obtained by taking $\theta = \{0, n\pi\}$ when $m_{\gamma'} > m_\phi$ and $\theta = (2n+1)\pi/2$ when $m_\phi > m_{\gamma'}$.

The evolution of the interaction states can be obtained from the evolution of mass eigenstates, related by $\Psi(z) = R\Psi'(z)$, prime fields being mass eigenstates. Solving for both amplitudes of the photon after transversing a region of length L we find:

$$A_\parallel(L) = e^{-i\omega L}\left(\cos^2\chi + \sin^2\chi\left(e^{i(\Omega+\Delta)L}\cos^2\theta + e^{i(\Omega-\Delta)L}\sin^2\theta\right)\right), \tag{4}$$

$$A_\perp(L) = e^{-2iL\omega}\cos^2\chi\sin^2\chi\left(1 - e^{iLm_{\gamma'}^2/(2\omega)}\right)^2. \tag{5}$$

3 Ellipticity and rotation effects

After transversing the magnetic region L, the beam has changed its amplitude and phase as we see in Eqs. (4)-(5), meaning that the beam develops a small ellipticity component and a rotation of the polarisation plane. Thus, the amplitudes evolve according to $A_{\parallel,\perp}(z) \propto (1 - \epsilon_{\parallel,\perp}(z))e^{-i\omega z + i\varphi_{\parallel,\perp}(z)}$, the constant of proportionality being the initial polarisation angle, α_0,

[1] We work in the gauge $\partial_i A_i = 0$ and $A_0 = X_0 = 0$.

with respect to the direction of the magnetic field $\vec{B}$. The change in the ellipticity and rotation angles it is given, respectively, by $\psi = \sin(2\alpha_0)\left(\varphi_\parallel - \varphi_\perp\right)/2$ and $\delta\alpha = \sin(2\alpha_0)\left(\epsilon_\parallel - \epsilon_\perp\right)/2$. After some manipulation of $A_\parallel(z)$ we find:

$$\varphi_\parallel = \sin^2\chi\left[\sin(\Omega z)\cos(\Delta z) + \cos(2\theta)\sin(\Delta z)\cos(\Omega z)\right], \quad (6)$$

$$\epsilon_\parallel = \sin^2\chi\left[1 - \cos(\Omega z)\cos(\Delta z) + \cos(2\theta)\sin(\Omega z)\sin(\Delta z)\right]. \quad (7)$$

A similar analysis for $A_\perp$ gives $\varphi_\perp = \sin^2\chi\sin\left(m_{\gamma'}^2 z/2\omega\right)$ and $\epsilon_\perp = 2\sin^2\chi\sin^2\left(m_{\gamma'}^2 z/4\omega\right)$.

Let us point out that the dimensionless parameter x, defined in Eq. (3), can be used to define two different regimes: $|x| \ll \chi$, which translates into $\theta \to \pi/4$ and $|x| \gg \chi$, which translates into $\theta \to 0$, if $m_{\gamma'} > m_\phi$, or $\theta \to \pi/2$, if $m_{\gamma'} < m_\phi$. In Fig. (1) we present exclusion plots to the ALP parameters using both ellipticity and rotation measurements.

Ellipticity effects: Let us first focus on the small mass region, where $|x| \ll 1$ and thus, $\theta \sim \pi/4$: this parameter space can remain uncovered if: *i)* there is a cancellation between the parallel and perpendicular contributions $\varphi_\parallel - \varphi_\perp \sim 0$, which happens if both ΔL and $\Omega L \ll 1$. *ii)* $\Delta L \gg 1$ and $\Omega L \ll 1$ and $\psi = 3\chi^2 m_{\gamma'}^2 L/(8\omega) < |\psi_{exp}|$, where we take $|\psi_{exp}| \sim 9 \times 10^{-11}$ as benchmark measured value of the ellipticity angle, as suggested by [4]. For instance, for $\chi = 10^{-1}$, the opposite holds, meaning $3\chi^2 m_{\gamma'}^2 L/(8\omega) > |\psi_{exp}|$, and therefore the small mass region can be constrained up to $g \approx 10^{-9}$ eV^{-1}, see Fig. (1). Going below those values of g it is not possible due to the cancellation explained in *i)*. On the other hand, for $\chi = 10^{-2}$ the opposite aforementioned condition also holds, but we see some stripes or gaps in sensitivity in the low mass region. They appear because when the condition $g = 4\pi n/(B\chi L)$, where $n \in Z$ is fulfilled, the ellipticity angle drops below $|\psi_{exp}|$. These gaps in sensitivity can be covered either by changing slightly any of the parameters: B, L, ω. Finally, for masses $m_{\gamma'} \gtrsim 10^{-5}$ eV, the condition $|x| \ll \chi$ is no longer fulfilled and the angle θ starts slowly to approach to $\pi/2$ as m_ϕ grows over $m_{\gamma'}$. When $\chi \ll |x|$, the expression for the ellipticity angle is well approximated by

$$\psi \propto \chi^2 \frac{g^2 B^2 \omega^2}{m_\phi^4}\left(-\frac{m_\phi^2 L}{2\omega} + \sin(\frac{m_\phi^2 L}{2\omega})\right), \quad (8)$$

This is almost the same expression of the ellipticity angle for the photon-ALP model (see e.g. [5]), but with the replacement of $g\chi^2$ by the ALP to photon coupling $g_{\phi\gamma\gamma}$. If $m_{\gamma'} > m_\phi$, then the above equation changes, replacing $m_\phi \to m_{\gamma'}$ and an overall minus sign. Eq. (8) explains the already familiar V shape in the mass region $m_\phi \gtrsim 10^{-4}$ eV.

Rotation effects: In the low mass region $m_\phi, m_{\gamma'} \lesssim 10^{-6}$ eV, the conditions $|x| \ll \chi$ and $\Omega L \ll 1$ hold, thus we can approximate $\epsilon_\parallel \approx 2\chi^2 \sin^2(gB\chi L/4)$ and $\epsilon_\perp \sim \chi^2 m_{\gamma'}^4 L^2/(8\omega) \sim 0$. Therefore, in the low mass region the rotation angle $\delta\alpha$ is mass independent. This gives us the smallest g to be constrained as

$$g \leq \frac{2\sqrt{2|\delta\alpha_{\rm exp}|}}{BL\chi^2} = 2.5 \times 10^{-12}\,{\rm GeV}^{-1}\left[\frac{2.5\,{\rm T}}{B}\frac{1\,{\rm m}}{L}\left(\frac{|\delta\alpha_{\rm exp}|}{5.2\times10^{-10}}\right)^{1/2}\left(\frac{10^{-1}}{\chi}\right)^2\right]. \quad (9)$$

As the mass grows, we move to the weak mixing regime $\chi \lesssim |x|$, where the ALP starts to decouple from the photon and HP. The change in the polarisation plane can be well approximated as (for $m_{\gamma'} < m_\phi$)

$$\delta\alpha \propto 2\chi^2\left(\sin^2\left(\frac{\Omega L - \Delta L}{2}\right) - \sin^2\left(\frac{m_{\gamma'}^2 L}{2\omega}\right)\right). \quad (10)$$

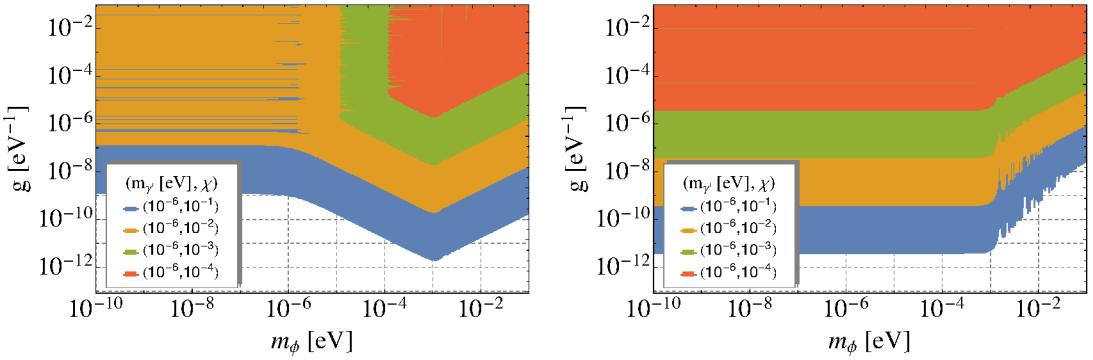

Figure 1: l.h.s. ellipticity constraints on the ALP and r.h.s. using rotation measurements, for different HP parameters. We have considered $|\delta\alpha_{exp}| = 5.2 \times 10^{-10}$ and $|\psi_{\rm exp}| = 9 \times 10^{-11}$. Both figures assume benchmark values $B = 2.5$ T, $L = 1$ m, $\omega = 1$ eV and $\alpha_0 = 45^\circ$.

When $|x| \gg 1$ the difference $\Omega L - \Delta L$ goes to $m_{\gamma'}^2 L/(2\omega)$ and the right hand side of the above equation cancels. This is the limit where the ALP decouples, and therefore the rotation effect is only due to the HP.

4 Conclusions

In this work we have considered a model that mixes photons, ALPs and HPs, we have shown interesting features on observable effects, in this case rotation of the polarisation plane and ellipticity of the beam. The parameters of the model can still be reasonably constrained using existing results from laboratory experiments. The next step is to consider more stringent scenarios, such as stellar production and early universe.

Acknowledgments: This work has been supported by FONDECYT project 1161150.

References

[1] E. Masso and J. Redondo, JCAP **0509** (2005) 015

[2] J. Jaeckel, J. Redondo and A. Ringwald, Phys. Rev. D **89** (2014) 103511 doi:10.1103/PhysRevD.89.103511

[3] K. Kaneta, H. S. Lee and S. Yun, Phys. Rev. Lett. **118** (2017) no.10, 101802 doi:10.1103/PhysRevLett.118.101802

[4] F. Della Valle, A. Ejlli, U. Gastaldi, G. Messineo, E. Milotti, R. Pengo, G. Ruoso and G. Zavattini, Eur. Phys. J. C **76** (2016) no.1, 24.

[5] G. Raffelt and L. Stodolsky, Phys. Rev. D **37** (1988) 1237.

Proposed Bragg-Coherent Axion Search with CUORE

Frank T. Avignone III, Richard J. Creswick

Department of Physics and Astronomy, University of South Carolina
Columbia, South Carolina 29208, USA

DOI: http://dx.doi.org/10.3204/DESY-PROC-2017-02/avignone_frank

We propose a technique for searching for axions with data from the CUORE detector using the Bragg-Coherent axion-photon conversion in the 988 single TeO_2 crystal bolometers of the 740 kg CUORE array. The search would be for the 14.4-keV axions from axion branch of the M1 ground-state transition from the ^{57}Fe in the solar core.

The Strong-CP problem is very familiar to all who attended this conference. The Peccei–Quinn suggested solution to the problem is also well known; however, the Goldstone boson that results from the breaking of PQ symmetry has thus far escaped detection. At this conference there were many suggested, as well as attempted, experimental efforts of detection. For completeness, we give a brief review of the formal aspects of the problem. We revisit a technique that we introduced in 1998 [1, 2], but in this case the proposed detector is the 740-kg array of 988 TeO_2 bolometers of the CUORE detector. Here, we very briefly review the theoretical motivation of the problem. To quote Roberto Peccei, "Introducing a global chiral U(1) symmetry – which has become known as a $U(1)_{PQ}$ symmetry – provides perhaps the most cogent solution to the strong CP problem. To make the SM Lagrangian $U(1)_{PQ}$ invariant, it must be augmented by axion interactions [3, 4]."

$$\mathcal{L}_{\rm total} = \mathcal{L}_{\rm SM} + \bar{\theta}\frac{g_s^2}{32\pi^2}G_b^{\mu\nu}\widetilde{G}_{b\mu\nu} - \frac{1}{2}\partial_\mu a\partial^\mu a + \mathcal{L}_{\rm int}[\partial^\mu a/f_a, \Psi] + \zeta\frac{a}{f_a}\frac{g_s^2}{32\pi^2}G_b^{\mu\nu}\widetilde{G}_{b\mu\nu}.$$

The last term is needed to ensure that the $U(1)_{PQ}$ has a chiral anomaly. This last term represents an effective potential for the axion field, and its minimum occurs at $\langle a\rangle = -\bar{\theta}f_a/\zeta$. One notes that the last term cancels the first (CP-offending) term, and good CP symmetry is restored. However, the broken U(1)-symmetry results in a Goldstone boson, the axion, which is the main motivation for this conference, and many of the talks presented.

The axion obeys the general property of the two-photon interaction as they are cousins to the neutral Pi-zero. Axion coupling to photons is governed by the Primakoff diagram, and the Lagrangian governing this interaction is written:

$$\mathcal{L}_{a\gamma} = \frac{1}{4}g_{a\gamma}F_{\nu\mu}\widetilde{F}^{\nu\mu}a = -g_{a\gamma}a\vec{E}\cdot\vec{B},$$

where F is the electromagnetic field strength tensor, $\widetilde{F}$ is its dual while "a" is the axion field. In both the hadronic and GUT models, the coupling constant is given by:

$$g_{a\gamma} = \frac{\alpha}{2\pi f_a}\left(\frac{A^{\rm EM}}{A^{\rm C}} - \frac{2}{3}\frac{4+z}{1+z}\right) = \frac{\alpha}{2\pi f_a}\left(\frac{A^{\rm EM}}{A^{\rm C}} - 1.95 \pm 0.08\right),$$

where $A^{\rm EM}$ is the electromagnetic anomaly, and $A^{\rm C}$ is the color anomaly. In the DFSZ (GUT) model $A^{\rm EM}/A^{\rm C} = 8/3$, and in the KSVZ (hadronic) model, this ratio is zero in most versions, because there is no electromagnetic anomaly. Accordingly, $g_{a\gamma}^{\rm KSVZ}/g_{a\gamma}^{\rm DFSZ} = 2.72$. In both models, the value of $g_{aN}^{\rm eff}$ depends sensitively on nuclear parameters.

The source of axions of interest here are from the 14.4-keV M1 ground-state transition in ^{57}Fe in the solar core. The axion branching ratio in nuclear decay was presented by Haxton in Avignone et al., [5], and by Haxton and Lee [6].

$$\Gamma_a/\Gamma_\gamma = (k_a/k_\gamma)^3 \frac{1}{2\pi\alpha}\frac{1}{(1+\delta^2)}\left[\frac{g_{aN}^0\beta + g_{aN}^3}{(\mu_0 - 1/2)\beta + \mu_3 - \eta}\right]^2$$

This ratio enters into the calculation of the axion flux from nuclear transitions, hence it will depend on the model where, g_{aN}^0 and g_{aN}^3, are the isoscalar and isovector coupling constants, respectively. We use the values of the relevant nuclear parameters given by Haxton and Lee [6]:

$$\mu_0 = 0.88 : \beta = -1.19 : \delta = 0.002 : \mu_3 = 4.71 : \eta = 0.80, \text{ and}$$
$$\Gamma_a/\Gamma_\gamma = (k_a/k_\gamma)^3 1.82(-1.19 g_{aN}^0 + g_{aN}^3)^2; \text{ where we define } g_{aN}^{\rm eff} \equiv (-1.19 g_{aN}^0 + g_{aN}^3).$$

Recall that the sign on -1.19 is negative when the unpaired nucleon is a neutron. In the case that the unpaired nucleon is a proton, the sign is positive. The flux can be written:

$$\Phi_a(14.4\,{\rm keV}) = \frac{n(^{57}{\rm Fe})}{4\pi d^2 \tau_\gamma} 2\frac{\Gamma_a}{\Gamma_\gamma}\int_0^R e^{-E/kT(r)}\rho(r) 4\pi r^2\, dr.$$

In the above equation, $n(^{57}{\rm Fe}) = (3\times 10^{17})\,^{57}$Fe/g is the number of ^{57}Fe nuclei per gram of solar material, τ_γ is the mean-life of the M1 ground state transition, d is the earth sun distance, $\rho(r)$, and is the radial dependent solar mass density. The solar temperature profile was taken from the standard solar model of Bahcall and Pinsonneault [7]. Integrating, and substituting values for the all the parameters, we obtain:

$$\Phi_a^{\rm KSVZ}(^{57}{\rm Fe}) = 4.56\times 10^{23}(g_{aN}^{\rm eff})^2_{\rm KSVZ}\,{\rm cm}^{-2}{\rm s}^{-1}.$$

This is the same value determined by the CAST Collaboration [8], and depends on the particular solar thermal profile used. The effective axion-nucleon coupling is very model dependent.

Coherent Bragg conversion in single crystals

The derivation of the axion-to-photon conversion rate was given earlier [9]. The formalism follows from the vector diagram shown in Fig. 1.

The coherent cross section was given in ref. [9], and is written as follows:

$$\sigma(\vec{\rho}) = g_{a\gamma\gamma}^2 \frac{4\pi^2\alpha N_c \hbar^3 c^3}{v_c}\sum_{\vec{G}}\left|\frac{\widetilde{\rho}(\vec{G})}{G^2}\right|^2 \frac{|\vec{\rho}\times\vec{G}|^2}{G^2}\delta(E_a - E_\gamma)$$
$$\widetilde{\rho}(\vec{p} - \vec{k}) = 0, \text{ unless } \vec{p} - \vec{k} = \vec{G}.$$

Accordingly, only when the line from the solar core to the crystal satisfies this condition (a Bragg condition) will the cross section not vanish. To achieve our goal, the uncertainties in

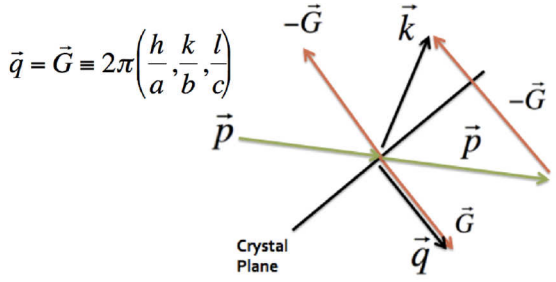

Figure 1: A vector diagram showing the initial axion momentum, $\vec{p}$, the reflected momentum, $\vec{k}$, the momentum transfer, $\vec{q}$, and the reciprocal lattice vector, $\vec{G}$.

the orientation angles of each of the crystals in the array must be determined. The required data are the energy, $14.4\,\mathrm{keV} \pm \delta E$, where δE reflects the energy resolution, and the time of the event, $t \pm \delta t$, where δt is determined from the uncertainty in the absolute orientations of the individual crystal bolometers. A typical plot of the detection rates, with an unrealistic coupling is shown in Fig. 2.

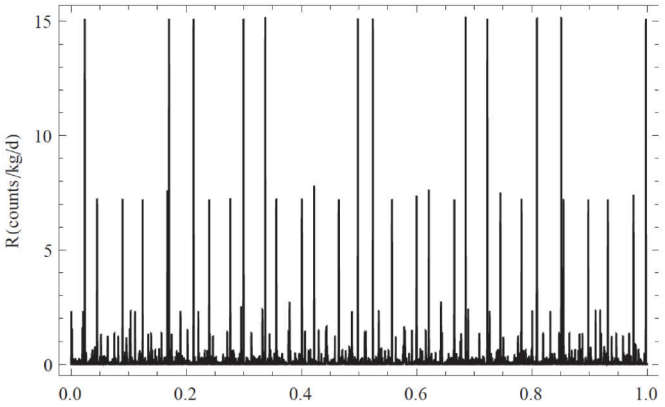

Figure 2: The theoretical pattern of predicted count rates at the predicted times when the Bragg condidtions are satisfied. The horizontal axis represents 24 hours of a particular day. These rates were calculated with a unrealisticly large value of the axion-photon coupling constant, $10^{-8}\,\mathrm{GeV}^{-1}$.

The CUORE detector

The Cryogenic Underground Observatory for Rare Events (CUORE) is a multipurpose array of 988, 750 gram TeO_2 bolometers in the LNGS in Assergi, Italy [10]. Its main mission is to search for the neutrino-less double-beta decay ($0\nu\beta\beta$-decay) of ^{130}Te; however, it also has the capability to search for Cold Dark Matter (CDM) as well as axions.

For such a large detector mass one would expect a very sensitive search; however, the sensitivity depends on the product, $(g_{aN}^{\mathrm{eff}} \times g_{a\gamma\gamma})$. Our analyses lead us to conclude that our sensi-

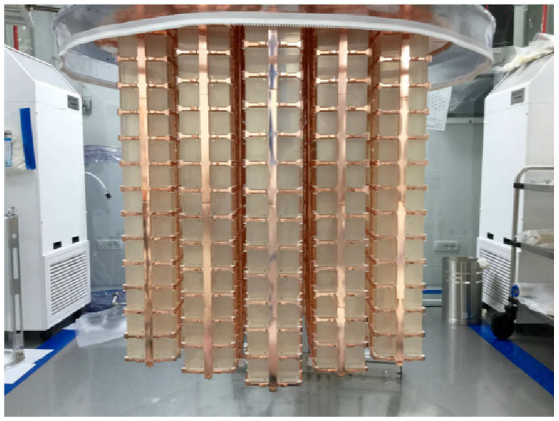

Figure 3: The CUORE array of 988 TeO_2 Bolometers in 19 towers prior to installation in the cryostat. All crystal axes are nomonaly equally oriented with small uncertainties.

tivity would be about the same as that publisted by the CAST Collaboration below 0.07 eV [8]; however, CAST looses coherence for axion masses above ∼0.07 eV. CUORE does not have a coherence issue at these energies, and therefore could explore a significant portion of the $(g_{a\gamma\gamma} - m_{\rm axion})$-space not reachable by CAST. CUORE started collecting physics data in early 2017. At this point, the axion search group is in the process of determining the uncertainties in the absolute orientation of the crystals.

References

[1] R. J. Creswick *et al.*, Phys. Lett. B **247**, 235 (1998).

[2] F. T. Avignone III *et al.*, Phys. Rev. Lett. **81**, 5068 (1998).

[3] R. D. Peccei and H. R. Quinn, Phys. Rev. D **16**, 791 (1977).

[4] R. D. Peccei, Lect. Notes Phys. **741**, 3 (2008).

[5] F. T. Avignone III *et al.*, Phys. Rev. D **37**, 618 (1988).

[6] W. C. Haxton and K. Y. Lee, Phys. Rev. Lett. **66**, 2557 (1991).

[7] J. N. Bahcall and M. H. Pinsonneault, Rev. Mod. Phys. **67**, 78 (1995).

[8] S. Andriamonje *et al.* (The CAST Collaboration), JCAP **0912**, 002 (2009).

[9] D. Li, R. J. Creswick, F. T. Avignone III and Y. Wang, JCAP **1602**, 031 (2016).

[10] A. D'Abbaddo *et al.* (The CUORE Collaboration), arXiv: 1612.04276 [physics.ins-det] (2016).

Sensitivity of Oriented Single Crystal Germanium Bolometers to 14.4 keV solar axions emitted by the M1 nuclear transition of ^{57}Fe

Richard Creswick[1], *Dawei Li*[1], *Frank. T. Avignone III*[1], *and Yuanxu Wang*[2]
[1]Department of Physics and Astronomy, University of South Carolina, Columbia, SC, USA
[2]School of Physics and Electronics, Henan University, Jinming Street, Kaifeng, Henan, China

DOI: http://dx.doi.org/10.3204/DESY-PROC-2017-02/creswick_richard

We present a calculation of the sensitivity of single crystal germanium bolometers to monoenergetic 14.4 keV axions emitted by the M1 nuclear transition of ^{57}Fe in the Sun. The narrow 14.4 keV Fe-57 line leads to very sharp temporal features in the counting rate, effectively reducing the background by several orders of magnitude. For a detector of mass 100 kg. operating for five years, we find an expected model-independent limit on the product of the axion-photon and axion-nucleon coupling $g_{a\gamma\gamma}g_{aN}^{\rm eff} < 5.5\times10^{-16}$ GeV^{-1} for axion masses less than 100 eV with 95% confidence level.

1 Introduction

Since axions, or more generally axion-like particles (ALPs), can couple with electromagnetic fields or directly with leptons or quarks, the Sun could be an excellent axion emitter. Solar axions could be generated by Primakoff conversion of photons, Bremsstrahlung, Compton scattering, electron atomic recombination, atomic deexcitation, and by nuclear M1 transitions.

Searches for solar axions have been carried out with magnetic helioscopes [1, 2], low temperature bolometers [3] and thin foil nuclear targets [4]. There are several existing and proposed low-background, low-temperature germanium bolometers including the Majorana demonstrator, Gerda, CDMS, SuperCDMS and LEGEND. The low-threshold and very low background possible in germanium detectors make them ideal to search for axions with a few keV energy.

In this paper we calculate the expected conversion rate of 14.4 keV solar axions produced in the M1 nuclear transition of ^{57}Fe and detected via the coherent inverse Primakoff process in Ge single crystals. We use the dramatic time dependence of this counting rate to place a bound on the product $g_{aN}^{\rm eff}g_{a\gamma\gamma}$ for a 100 kg detector operating for five years.

2 Flux of 14.4 keV Solar Axions

The stable isotope ^{57}Fe has a natural abundance of 2.2% in the solar core, and mass fraction of 2.8×10^{-5}. The first excited state of ^{57}Fe can be thermally excited in the interior of the Sun ($kT \approx 1.3$ keV) and relax to the ground state by emitting a photon with energy 14.4 keV in an M1 transition. Since the axion is a pseudoscalar, it is also possible for the nucleus to decay to the ground state by emitting a 14.4 keV axion. The branching ratio has been calculated by

Haxton and Lee [5], and based on the standard model of the Sun [6], Moriyama[7] has calculated the total flux of 14.4 keV axions from the Sun to be

$$\Phi_0 = 4.56 \times 10^{23} (g_{aN}^{\rm eff})^2 {\rm cm}^{-2}{\rm s}^{-1}$$

where $g_{aN}^{\rm eff} \equiv -1.19 g_{aN}^0 + g_{aN}^3$ is the effective axion-nucleon coupling constant [1, 3].

The production of 14.4 keV axions is confined to the solar core. Using the standard model of the Sun[6], 90% of the 14.4 keV solar axions come from a region that is about 0.10 $R_\odot$ in radius, which subtends an angle of about 8.7×10^{-4}rad (0.05 degrees) at the Earth. As we will show in the next section, this is comparable to the angular width of "Bragg rings" within which coherent Bragg conversion of axions to photons can take place, and so the Sun cannot be treated as a point source. We take the finite size of the axion-producing part of the Sun into account by defining a Gaussian brightness function

$$f(\hat{\boldsymbol{p}} - \hat{\boldsymbol{p}}_0) = \frac{1}{2\pi\Omega^2} \exp\Big(-\frac{|\hat{\boldsymbol{p}} - \hat{\boldsymbol{p}}_0|^2}{2\Omega^2}\Big)$$

which describes the angular distribution of the axion flux over the celestial sphere. Here $\hat{\boldsymbol{p}}_0$ is a unit vector that points to the center of the Sun, $\hat{\boldsymbol{p}}$ points to an arbitrary point in the sky and $\Omega = 0.87$ mrad is the angular size of the region producing axions.

The natural linewidth of the 14.4 keV transition is extremely small, 4.7×10^{-9} eV, but thermal Doppler broadening in the solar core results in a Gaussian lineshape of width $\Delta = 2.17$ eV (FWHM=5.11 eV). Taking into account both the finite size of the solar core and Doppler broadening of the line, the differential axion flux is

$$\frac{d^2\Phi}{dE d\hat{\boldsymbol{p}}} = \Phi_0 \times \frac{1}{\sqrt{2\pi\Delta^2}} \exp\Big[-\frac{(E-E_0)^2}{2\Delta^2}\Big] f(\hat{\boldsymbol{p}} - \hat{\boldsymbol{p}}_0) {\rm cm}^{-2}{\rm keV}^{-1}{\rm s}^{-1}{\rm sr}^{-1}$$

3 Coherent Bragg-Primakoff Conversion of Axions to Photons

The cross section as a function of the energy and direction of the axion for the conversion to a photon by the inverse Primakoff effect was given earlier[8]:

$$\sigma_{a\gamma}(E, \hat{\boldsymbol{p}}) = m\hbar c \frac{4\pi^2 \alpha N_a}{\mu_c v_c} g_{a\gamma}^2 E^2 \sum_{\boldsymbol{G}} \Big| \frac{\tilde{\rho}_c(\boldsymbol{G})}{G^2} \Big|^2 |\hat{\boldsymbol{p}} \times \hat{\boldsymbol{G}}|^2 \delta\Big[E - \frac{\hbar c G}{2\hat{\boldsymbol{p}} \cdot \hat{\boldsymbol{G}}}\Big]$$

where m is the mass of the detector, N_a Avogadro's constant, μ_c is the molar mass of the unit cell, v_c is the volume of the conventional unit cell, α is the fine structure constant, $\boldsymbol{G}$ is a reciprocal lattice vector, $g_{a\gamma}$ is the coupling of the axion to the electromagnetic field and $\hat{\boldsymbol{p}}$ is a unit vector parallel to the incoming axion.

The Fourier transform of the charge density distribution, $\tilde{\rho}_c$ (in units of the electron charge) was calculated within density functional theory [9, 10] using WIEN2k [11]. The delta function ensures that coherent conversion can only take place when the Bragg condition

$$E_a = \frac{\hbar c G}{2\hat{\boldsymbol{p}} \cdot \hat{\boldsymbol{G}}}$$

is satisfied. For an axion with energy E_a and a reciprocal vector $\boldsymbol{G}$ the locus of points that satisfy the Bragg condition form a circle of radius $\cos\theta = \hat{\boldsymbol{p}} \cdot \hat{\boldsymbol{G}} = \hbar c G/2E_a$. The Doppler broadening of the axion spectrum expands the Bragg circle to an annulus, or Bragg ring, of width

$$\Delta\theta = \frac{\Delta}{E_0}\cot\theta \sim 1.46 \times 10^{-4}\text{rad}$$

or about 0.01 degrees. This is comparable to the angular size of the core. The angular velocity of the Sun is $7.27 \times 10^{-5}\text{s}^{-1}$, so it takes the Sun just a matter of seconds to pass through one of these Bragg rings. Conversion of axions to photons can only take place during these very brief time intervals.

The time dependent counting rate is

$$\frac{\dot{N}}{m} = 4\pi^2\alpha N_a \Phi_0 \frac{\hbar c E_0^2 g_{a\gamma}^2}{\mu_c v_c} \sum_{\boldsymbol{G}} \Big|\frac{\tilde{\rho}_c(\boldsymbol{G})}{G^2}\Big|^2 \frac{|\hat{\boldsymbol{p}}_0 \times \hat{\boldsymbol{G}}|^2}{\sqrt{2\pi\sigma_E^2}} \exp\Big[-\frac{(E_a(\hat{\boldsymbol{p}}_0, \boldsymbol{G}) - E_0)^2}{2\sigma_E^2}\Big]\text{s}^{-1}\text{kg}^{-1}$$

where $\hat{\boldsymbol{p}}_0$ is a unit vector pointing to the center of the Sun, $E_0 = 14.4$ keV is the center of the axion line, and

$$\sigma_E^2 = \frac{2E_0^2\Omega^2}{\hbar c G} + \Delta^2$$

is the effective width of the Bragg ring taking into account Doppler broadening, the size of the solar core and the angle at which the Sun crosses the ring.

4 Statistical Bounds on $g_{a\gamma}g_{aN}^{eff}$

The theoretical counting rate depends both on the coupling of axions to the nucleus through the flux and the coupling of axions to the electromagnetic field in the detector. The CAST collaboration [2] has placed a bound on the product of

$$g_{a\gamma}g_{aN}^{\text{eff}} < 1.36 \times 10^{-16}\text{GeV}^{-1}\ 95\%\ \text{CL}$$

for axion masses $m_a < .03$ eV. One of the advantages of detection by the coherent inverse Primakoff effect in crystals is that the rate is very insensitive to axion masses less than about 100 eV.

The total instantaneous counting rate can be written as

$$\dot{N}(t) = \dot{N}_a(t) + B$$

where B is the background rate (assumed constant) and $\dot{N}_a(t)$ is the axion counting rate.

We construct a random function [8] χ using the theoretical counting rate over the time of the experiment, T, and the times of individual events. By the central limit theorem the probability distribution for χ is Gaussian with mean

$$\langle\chi\rangle = \sqrt{\int_0^T dt\big(\dot{N}_a(t) - \langle\dot{N}_a\rangle\big)^2}$$

and, in the limit $B \gg |\dot{N}_a|$ the variance is

$$\Delta\chi^2 = B$$

Low-energy backgrounds as small as $0.02\text{keV}^{-1}\text{kg}^{-1}\text{d}^{-1}$ have been reported [12] for current generation germanium bolometers, and energy resolutions on the order of 200 eV are possible. If we set energy cuts at 14.4 ± 0.25keV, the background rate is approximately $0.01\text{kg}^{-1}\text{d}^{-1}$. We then find a bound on the product of the couplings

$$g_{aN}^{\text{eff}} g_{a\gamma} < 5.5 \times 10^{-16}\text{GeV}^{-1} \ 95\% \text{ C.L.}$$

which is is about a factor of three larger than the bound set by CAST [1], but is better than the CAST bound for axion masses greater then 0.1 eV.

5 Acknowledgments

This work was supported by the US National Science Foundation Grant PHY-1307204.

References

[1] S. Andriamonje *et al* (CAST Collaboration), *J. Cosmol. Astropart. Phys* **12** (2009) 002.

[2] M. Arik *et al* (CAST Collaboration), *Phys. Rev. Lett.* **112** (2014) 091302.

[3] F. Alessandria *et al.*, *J. Cosmol. Astropart. Phys* **05** (2013) 007.

[4] T. Namba, *Phys. Lett. B* **645** (2007) 398.

[5] W. C. Haxton and K. Y. Lee, *Phys. Rev. Lett.* **66** (1991) 2557 .

[6] John N. Bahcall and M.H. Pinsonneault, *Rev.Mod.Phys.* **64** (1992) 885.

[7] S. Moriyama, *Phys. Rev. Lett.* **75** (1995) 3222.

[8] R. J. Creswick *et al Phys. Lett. B* **427** (1998) 235. and D. Li, R.J. Creswick, F.T. Avignone, and Y. Wang, J. Cosm. and Astrpart. Phys. **10** (2015) 065

[9] P. Hohenberg and W. Kohn, *Phys. Rev.* **136** (1964) B864.

[10] W. Kohn and L. J. Sham, *Self-Consistent Equations Including Exchange and Correlation Effects*, *Phys. Rev.* **140** (1965) A1133.

[11] P. Blaha and K. Schwarz and G.K.H. Madsen and D. Kvasnicka and J. Luitz, Vienna University of Technology, Vienna, Austria (2001)

[12] S.R. Elliot *et al* J. Phys Conf. Series **888** (2017) 012035

Inferences on the Higgs Boson and Axion Masses through a Maximum Entropy Principle

Alexandre Alves[1], *Alex G. Dias*[2], *Roberto da Silva*[3]

[1]Federal University of São Paulo, Physics Department, Diadema, Brazil
[2]Federal University of ABC, Center of Natural and Human Sciences, Santo André, Brazil
[3]Federal University of Rio Grande do Sul, Physics Institute, Porto Alegre, Brazil

DOI: http://dx.doi.org/10.3204/DESY-PROC-2017-02/dias_alex

The Maximum Entropy Principle (MEP) is a method that can be used to infer the value of an unknown quantity in a set of probability functions. In this work we review two applications of MEP: one giving a precise inference of the Higgs boson mass value; and the other one allowing to infer the mass of the axion. In particular, for the axion we assume that it has a decay channel into pairs of neutrinos, in addition to the decay into two photons. The Shannon entropy associated to an initial ensemble of axions decaying into photons and neutrinos is then built for maximization.

The Method of Maximum Entropy Principle

Among the biggest challenges of physics is to find an explanation for the values of the masses of the elementary particles. With the discovery of the Higgs boson at the LHC, and the measurements of its properties, we have now the experimental evidence that the mechanism of spontaneous symmetry breaking is effectively behind the mass generation for the elementary particles, as implemented in the Standard Model (SM). Although this represented an invaluable advance for understanding of subatomic physics, the spontaneous symmetry breaking mechanism in the SM does not determine the value of the masses of the elementary particles, except for the photon which is correctly left massless and all the neutrinos which are incorrectly left massless. It means that some still missing mechanism must supplement, or totally replace, the spontaneous symmetry breaking in order to allow a full determination of the masses of the elementary particles.

In particular, for the Higgs boson some ideas have arised relating its mass to the maximum of a probability distribution built from the branching ratios [1], [2]. As observed in Ref. [1] a probability distribution function constructed multiplying the main branching ratios for the SM Higgs boson decay has a peak very close to the measured value $M_H \approx 125$ GeV. This could be connected to some sort of entropy so that such a mass value maximizes, simultaneously, the decay probabilities into all SM particles. In the work of Ref. [2] we presented a development based on the Shannon entropy built with the Higgs boson branching ratios, showing that the value of the Higgs boson mass follows from a Maximum Entropy Principle (MEP).

In the following we present a short review of our MEP method to infer the mass of the SM Higgs boson. After that we also review an application of MEP for inferring the mass of the axion assuming a specific low energy effective Lagrangian [3].

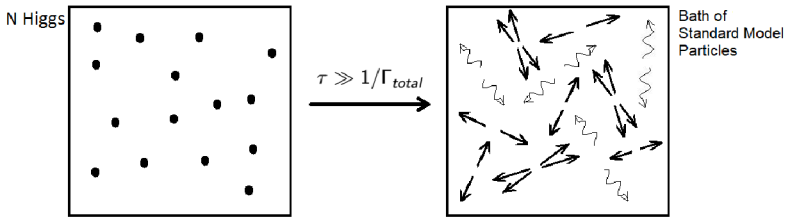

Figure 1: System of N Higgs boson decaying into a bath of Standard Model particles.

Inferring the Higgs boson mass

Consider an initial state of N Higgs bosons that evolves, through decay, to a final state composed by many different particles as represented in Fig. 1. After a time $\tau \gg 1/\Gamma_{total}$ the system transforms into a thermal bath of particles from the Higgs boson decays, according to its branching ratios $BR_k(M_H|\boldsymbol{\theta}) = \Gamma_k(M_H|\boldsymbol{\theta})/\Gamma_{total}(M_H|\boldsymbol{\theta})$, where $k = \gamma\gamma,\ gg,\ Z\gamma,\ q\bar{q},\ \ell^+\ell^-,\ WW^*,\ ZZ^*$, are the 14 main SM decay modes; and $\boldsymbol{\theta}$ represents all the other predetermined parameters entering into the formula; $\Gamma_k(M_H|\boldsymbol{\theta})$ and $\Gamma_{total}(M_H|\boldsymbol{\theta})$ are the partial and the total Higgs boson widths, respectively. The probability that the N Higgs bosons system evolve to a given final state of a bath of Standard Model particles, defined by a partition of n_1 particles decaying into the mode 1, n_2 particles decaying into the mode 2, and so on until n_m particles decaying into the mode m, is given by

$$P(\{n_k\}_{k=1}^m) \equiv \frac{N!}{n_1! \cdots n_m!} \prod_{k=1}^{m} \left[BR_k(M_H|\boldsymbol{\theta})\right]^{n_k}, \tag{1}$$

in which $\sum_i n_i = N$. We define the Shannon entropy [4] associated to the decay of the system of N Higgs bosons summing over each possible partition as

$$S_N = -\sum_{\{n\}}^{N} P(\{n_k\}_{k=1}^m)\ \ln\left[P(\{n_k\}_{k=1}^m)\right] = -\langle \ln(P) \rangle. \tag{2}$$

It can be shown, taking the asymptotic limit $N \to \infty$ formula for S_N [5], that maximization of S_N is equivalent to the maximization of

$$S_\infty(M_H|\boldsymbol{\theta}) = \ln\left(\prod_{k=1}^{m} BR_k(M_H|\boldsymbol{\theta})\right) \tag{3}$$

The expression in Eq. (3) is in fact the log-likelihood from the product of the branching ratios. Thus, we see as an outcome of MEP that the simultaneous maximization of the Higgs boson decays into Standard Model particles is equivalent to the maximization of the log-likelihood.

Taking into account several sets of values within the experimental errors in the Standard Model electroweak parameters $\boldsymbol{\theta}$ [6], a gaussian probability distribution function, $P_H(\hat{M}_H)$, is then fitted with the maximum solutions, $\hat{M}_H$, of $S_\infty(M_H|\boldsymbol{\theta})$. The result is shown in Fig. 2. The peak of $P_H(\hat{M}_H)$ is interpreted as the most probable value for the mass of the SM Higgs boson derived from MEP. Such a peak occurs for $M_H^{th} = 125.04 \pm 0.25$ GeV, and reflects the combined uncertainties over the SM parameters. It must be pointed out that this mass value

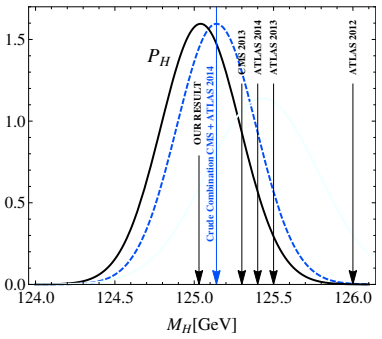

Figure 2: Probability distribution function $P(M_H)$ obtained in [2] from the maximum solution of S_∞ is shown in the black curve.

determined from MEP is almost identical to the latest experimental value $M_H^{exp} = 125.09 \pm 0.21\,(stat.) \pm 0.11\,(syst.)\,\text{GeV}$ [7].

Inferring the axion mass

We now review an application of MEP for inferring the mass of the hypothetical axion under two general assumptions. First, the axion can decay into pairs of neutrinos, in addition to the typical two photons decay channel. Second, the effective Lagrangian describing the axion field, $A(x)$, interactions with the electromagnetic strength tensor, $F^{\mu\nu}$, and neutrinos fields, ν_i, is

$$\mathscr{L}_{eff} = \frac{1}{2}\partial_\mu A\,\partial^\mu A - \frac{1}{2}m_A^2\,A^2 - \frac{g_{A\gamma}}{4}\,A\,F^{\mu\nu}\widetilde{F}_{\mu\nu} - \frac{g_{A\nu}}{2}\,\overline{\nu}_i\gamma^\mu\gamma_5\nu_i\,\partial_\mu A\,, \tag{4}$$

where $i = 1, 2, 3$, and $\widetilde{F}_{\mu\nu} = \frac{1}{2}\epsilon_{\mu\nu\sigma\rho}F^{\sigma\rho}$. The axion-photon and the axion-neutrinos couplings are defined in terms of the axion decay constant, f_A, the fine structure constant, α, and the order 1 model dependent anomaly coefficients, $C_{A\nu}$, $\widetilde{C}_{A\gamma}$, as $g_{A\gamma} = \alpha\widetilde{C}_{A\gamma}/2\pi f_A$ and $g_{A\nu} = C_{A\nu}/f_A$. The effective Lagrangian in Eq. (4) can be derived from a kind of DFSZ axion model with the addition of right-handed neutrinos [3]. It can be seen that the axion branching ratios $BR_{A\to\gamma\gamma}$ and $BR_{A\to\nu_i\nu_i}$ computed with Eq. (4) depend only on the ratio $C_{A\nu}/\widetilde{C}_{A\gamma}$, the mass of the axion, m_A, and the lightest neutrino mass, m_1.

The neutrinos squared mass differences, $\Delta m_{12}^2 = m_2^2 - m_1^2 = (7.45 \pm 0.25) \times 10^{-5}\,\text{eV}^2$ and $\Delta m_{31}^2 = m_3^2 - m_1^2 = (2.55 \pm 0.05) \times 10^{-3}\,\text{eV}^2$ [8], assuming the normal hierarchy, enter as a prior information for the maximization of $S(m_A|m_1, r_\nu) = \ln(BR_0 BR_1 BR_2 BR_3)$. Still, there is the bound on the sum of neutrinos masses $0.059\ \text{eV} < \sum_i m_i < 0.23\ \text{eV}$, from the measurements of cosmic microwave background anisotropies [9], implying that $0 \leq m_1 < 0.0712$ eV.

It is shown in green on Fig. 3 the maximum points of the entropy $S(m_A|m_1, r_\nu)$. The boundaries given by the gray curves are defined by the largest (upper) and lowest (lower) allowed value of m_1. For the DFSZ model with right-handed neutrinos the anomaly coefficients are such that $r_\nu < 0.46$ and the region beyond the red dashed line in Fig. 3 is excluded. Taking into account the astrophysical bounds from red giants [10] we obtain $r_\nu < 0.034$, excluding the region beyond the green dashed line in Fig. 3, and this implies that $0.1\ \text{eV} < m_A < 6.3\ \text{eV}$.

A more strong inference can be made maximizing the entropy as being a function of three unknowns, i. e., $S \equiv S(m_A, m_1, r_\nu)$. In this case we have a more sharp prediction of $0.1\ \text{eV} <$

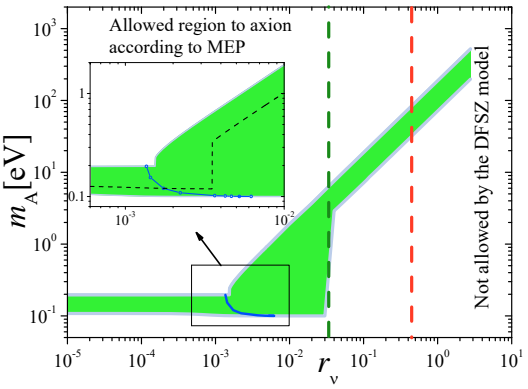

Figure 3: Green region represents the maximum points of $S(m_A|m_1, r_\nu)$ as obtained in Ref. [3].

$m_A < 0.2$ eV, which is represented with the blue line in Fig. 3.

Finally, supposing that the axion can decay only into a pair of the lightest neutrino the inference made with MEP is a linear relation between m_A and m_1, with the proportionality coefficient depending on r_ν.

Acknowledgments: The authors thank CNPq and Fapesp. A. G. D. also thanks the organizers of Patras 2017 workshop, in special Hero and Konstantin Zioutas for their hospitality.

References

[1] D. d'Enterria, "On the Gaussian peak of the product of decay probabilities of the standard model Higgs boson at a mass $m_H \sim 125$ GeV," arXiv:1208.1993 [hep-ph].

[2] A. Alves, A. G. Dias and R. da Silva, "Maximum Entropy Principle and the Higgs Boson Mass," Physica A **420**, 1 (2015) [arXiv:1408.0827 [hep-ph]].

[3] A. Alves, A. G. Dias and R. Silva, "Maximum Entropy Inferences on the Axion Mass in Models with Axion-Neutrino Interaction," Braz. J. Phys. **47**, no. 4, 426 (2017) [arXiv:1703.02061 [hep-ph]].

[4] C. E. Shannon, "A mathematical theory of communication," Bell Syst. Tech. J. **27**, 379 (1948) [Bell Syst. Tech. J. **27**, 623 (1948)].

[5] J. Cichon and Z. Golebiewski, *23rd International Meeting on Probabilistic, Combinatorial and Asymptotic Methods for the Analysis of Algorithms*, http://luc.devroye.org/AofA2012-CfP.html.

[6] S. Dawson *et al.*, "Working Group Report: Higgs Boson," arXiv:1310.8361 [hep-ex].

[7] G. Aad *et al.* [ATLAS and CMS Collaborations], "Combined Measurement of the Higgs Boson Mass in pp Collisions at $\sqrt{s} = 7$ and 8 TeV with the ATLAS and CMS Experiments," Phys. Rev. Lett. **114**, 191803 (2015) [arXiv:1503.07589 [hep-ex]].

[8] S. F. King, "Unified Models of Neutrinos, Flavour and CP Violation," Prog. Part. Nucl. Phys. **94**, 217 (2017) [arXiv:1701.04413 [hep-ph]].

[9] P. A. R. Ade *et al.* [Planck Collaboration], "Planck 2015 results. XIII. Cosmological parameters," Astron. Astrophys. **594**, A13 (2016) [arXiv:1502.01589 [astro-ph.CO]].

[10] N. Viaux, M. Catelan, P. B. Stetson, G. Raffelt, J. Redondo, A. A. R. Valcarce and A. Weiss, "Neutrino and axion bounds from the globular cluster M5 (NGC 5904)," Phys. Rev. Lett. **111**, 231301 (2013) [arXiv:1311.1669 [astro-ph.SR]].

Search for streaming dark matter axions or other exotica

A. Gardikiotis[1], *V. Anastassopoulos*[1], *S. Bertolucci*[2], *G. Cantatore*[3], *S. Cetin*[4], *H. Fischer*[5], *W. Funk*[6], *D.H.H. Hoffmann*[7,8], *S. Hofmann*[9], *M. Karuza*[10], *M. Maroudas*[1], *Y. Semertzidis*[11], *I. Tkachev*[12], *K. Zioutas*[1,6]

[1]University of Patras, Patras, Greece
[2]INFN, LNF, Bologna, Italy
[3]University and INFN Trieste, Italy
[4]Istanbul Bilgi University, Faculty of Engineering and Natural Sciences, Eyup, Istanbul, Turkeyi
[5]University of Freiburg, Germany
[6]CERN, Geneva, Switzerland
[7]Xi'An Jiaoton University, School of Science, Xi'An, China
[8]National Research Nuclear University MEPhI, Moscow, Russian Federation
[9]Munich, Germany
[10]Department of Physics, Center for micro, nano sciences and technologies, University of Rijeka, Croatia, and, INFN Trieste, Italy
[11]Department of physics, KAIST, and Center for Axion and Precision Physics Research, IBS, Daejeon, Republic of Korea
[12]INR, Moscow, Russia

DOI: http://dx.doi.org/10.3204/DESY-PROC-2017-02/gardikiotis_antonios

We suggest a new approach to search for galactic axions or other similar exotica. Streaming dark matter (DM) could have a better discovery potential because of flux enhancement, due to gravitational lensing when the Sun and/or a planet are aligned with a DM stream [1]. Of interest are also axion miniclusters, in particular, if the solar system has trapped one during its formation. Wide-band axion antennae fit this concept, but also the proposed fast narrow band scanning. A network of detectors can provide full time coverage and a large axion mass acceptance. Other DM searches may profit from this proposal.

1 Introduction

Axions appear in the solution of Peccei and Quinn, to explain the absence of the CP-violation in quantum chromodynamics. Axions are excellent cold dark matter (CDM) candidates in the mass range around (1-100) μeV. Beyond that range there are also good dark matter candidates, the so-called axions like particles (ALPs). The axion haloscope technique suggested by P. Sikivie [2] is still a widely used method searching for DM axions. Experimental tests for axions predominantly rely on their electromagnetic coupling resulting in their inverse Primakoff resonant conversion into microwave photons inside a strong magnetic field. This technique, along with more recent ideas, allows to search for this elusive particle by slowly scanning the potential axion rest mass range around $\sim 10^{-5}$ eV/c^2 by tuning the resonance frequency of the

cavity. The quality factor of the cavity Q defines the width of the resonance (1/Q). It is this very narrow resonance response function of the magnetic axion haloscope, which on the one hand optimizes its sensitivity and on the other hand increases the scanning time accordingly. The expected power generated by axion-photon conversions is proportional to the local axion dark matter density ρ_α. For example, the time required, for a cavity inside the CAST magnet, to reach a sensitivity of $g_{\alpha\gamma\gamma} = 10^{-14}$ GeV^{-1} is ∼10 days.

We present here a new approach for terrestrial axion detection that is based on streaming DM axions. A temporal DM flux enhancement can occur due to gravitational lensing effects by the solar system bodies. This novel detection concept (for axions or other similar exotica) requires a "wide band" antenna and/or a fast narrow band scanning scheme [1, 3].

2 The new concept for relic axions detection

The search for DM, and in particular for relic axions, has been based on the assumed isotropic halo distribution in our galaxy, with a broad velocity distribution around 240 km/s and an average density of ∼0.3 GeV/cm^3. This target choice might have been one of the reasons behind the non-observation of the axion so far.

Instead, the proposed new detection concept is based on streaming DM axions which propagate near the ecliptic or streams which are temporally aligned with the Sun→Earth direction or any axion cluster reaching the Earth. The Sun can focus low speed (0.001c-0.3c) incident particles downstream at the position of the Earth [4]. In the ideal case of perfect alignment stream→Sun→Earth, the axion flux enhancement of the stream can be very large (∼10^6) or even more. Planets are also capable of gravitational lensing for slow moving particles. For example, Jupiter can focus particles with speeds around 10^{-3}c, which fits the widely assumed detectable dark matter distribution on Earth [5]. It is this temporally axion signal amplification, which (axion) DM searches might utilize. In fact, streaming DM might have a density, which is ∼0.3 to 30% of the local mean DM density (∼0.3 GeV/cm^3)[6].

A DM stream propagating along the Sun-Earth direction could surpass the local DM density, and this will give rise to an unexpectedly large DM flux exposure to an axion haloscope. High precision planet orbital data, spacecraft explorations and laser ranging techniques put an upper limit for the dark matter density at Earth's location of the order 10^5 GeV/cm^3 [7]. Also more recent studies on local dark matter density set similar limits [8].

Assuming an alignment of a DM stream towards the Earth via the Sun or a planet, lasts only few minutes, this period is equivalent to few years for a conventional detection scheme. In order to utilize sudden axion burst like phenomena the relic axion antenna should be able
1) to extend the frequency band range to the maximum and
2) to decrease the scanning time for each frequency to the minimum.

Even for a tiny DM stream, the large flux enhancement (in particles due to the Sun's gravitational focusing) can result to a much better detection sensitivity. A network of "wide band" antennae with fast narrow axion mass scanning mode could be ideal for this novel detection scheme.

3 Streaming dark matter axions

In a wide variety of axion Dark Matter models, a sizable (or even dominant) fraction of axions is confined in a very dense axionic clumps, or miniclusters, with masses M∼10^{-12}M$_\odot$. The

axion miniclusters originate from specific density perturbations which are a consequence of non-linear axion dynamics around the QCD epoch [9]. There may be $\sim 10^{24}$ dense axionic clumps (miniclusters) in the galaxy and their concentration on the solar neighbour being $\sim 10^{10}$ pc^{-3}. Typical miniclusters have radius of $\sim 10^7$ km and their axion density is $\sim 10^8$ GeV/cm^3. In fact, in the course of time a fraction of them has been tidally disrupted and forms streams, with an axion density being "only" an order of magnitude larger than the average DM distribution. This clumpy structure can lead to observable signal in femto or micro-lensing missions like LSST project or Gaia, but it is also probable to reveal a potential signal in axion haloscopes [10, 11].

In case, an axion minicluster is captured by the solar system a direct encounter of the detector with the axion minicluster will enhance the axion density by about 10^5x the DM average; The Earth's crossing time of such dense axionic clumps is a few days per year [1,3]. The effect of axion miniclusters may be important for direct DM axion searches and deserves a more thorough study.

In addition, streaming DM can also be present due to other tidal streams like the Sagittarius stream [3]. It is widely accepted that, in cosmic time scale, the Milky Way disrupts the near Sagittarius (Sgr) Dwarf elliptical galaxy during its multiple passages through the galactic disk [12]. The Sgr DM debris could represent a significant halo sub-structure in the galaxy today, thus affecting also the interpretation of DM direct searches [13]. The Sagittarius dark matter debris in some models induces an energy-dependent enhancement of direct search event rates of as much as $\sim$20 - 45% and is likely to have a non-negligible influence on dark matter detection experiments [14]. Finally, other (un)predictable streams of DM, including caustics [15], may propagate along a gravitationally favourable direction like one from the Sun or Planet-X towards the Earth, which may temporally enhance the local axion flux. An example of potential interest is the alignment (within 5.5°) Galactic Center→Sun→Earth, which repeats once annually (18^{th}December).

4 Conclusions

Compared to the widely assumed isotropic DM distribution, streaming DM axions or other particles with similar properties, may be finally the better source for their discovery. The assumed isotropic halo of our galaxy, does not take into account substructures of DM in the form of streams or clumps whose particle density can be as much as 10^5 GeV/cm^3. Such a density, is not excluded by local bounds based on planetary precision measurements. Therefore, the possibility of large density fluctuations is likely in our solar system. These fluctuations can boost the local axion density up to several orders of magnitude, and so the axion detectability, provided an axion antenna is sensitive to such axion burst like events. Relic axion or other exotic particles streams and/or tidally disrupted axion miniclusters can be gravitationally focused at the position of the Earth by the Sun and/or a solar planet. Even a tiny flux might get temporally strongly enhanced due to gravitational lensing effects, surpassing thus on the long term the isotropic local DM detection sensitivity [3]. It is worth noticing the observed correlation between solar activity and planetary positions, while similar planetary correlation is also observed, for the Earth's atmospheric electron density (TEC) [16]. Such observations support the assumption that DM axions (or other similar exotica) may well constitute a component of slow speed invisible streams, which in general cannot be predicted except the 18^{th} December alignment (Earth→Sun→Galactic Center). And this, because around this period of the year, the Earth's

Ionosphere shows an anomalous high electron density [15].

In order to utilize any Earth DM encounter, the haloscope antenna should cover ideally the whole calendar year with a quasi-wideband performance, with the fastest possible scanning mode. The reduced sensitivity should be compensated by the burst like impulse of DM flux. CAST-CAPP is preparing a port for such a possibility by using wide band electronics to be sensitive to a wide axion mass range. Since one single axion haloscope cannot fulfil all these requirements, it is obvious that this proposal can be fully realized by a network of haloscopes or other type of detectors, preferentially distributed around the Globe, in order to secure a possible discovery. Therefore, trapped axion miniclusters and streaming DM axions being gravitationally focused by the Sun and/or a Planet, can become instrumental in axion research.

References

[1] K. Zioutas, V. Anastassopoulos, S. Bertolucci, G. Cantatore, S.A. Cetin, H. Fischer, W. Funk, A. Gardikiotis, D.H.H. Hoffmann, S. Hofmann, M. Karuza, M. Maroudas, Y.K. Semertzidis, I. Tkachev [arXiv:1703.01436v1 [astro-ph.IM]] (2017)

[2] P. Sikivie , Phys. Rev. Lett. **51**, 1415 (1983); Erratum Phys. Rev. Lett. **52**, 695 (1984). DOI:https://doi.org/10.1103/PhysRevLett.51.1415

[3] H. Fischer, Y. Semertzidis, K. Zioutas, Newsletter of the EP department, CERN (2017) https://ep-news.web.cern.ch/content/search-axions-streaming-dark-matter

[4] B.R. Patla, R.J. Nemiroff, D.H.H. Hoffmann, K. Zioutas, ApJ. **780**, 158 (2014) DOI: http://iopscience.iop.org/article/10.1088/0004-637X/780/2/158/meta

[5] P. Sikivie, I. I. Tkachev, Yun Wang, Phys. Rev. Lett. **75**, 2911 (1995) DOI: 10.1103/PhysRevLett.75.2911

[6] K. Freese, P. Gondolo, H. Jo Newberg, Phys. Rev. D **71**, 043516 (2005) DOI: 10.1103/PhysRevD.71.043516

[7] J.M. Frère, F.S. Ling, G. Vertongen, Phys. Rev. D **77**, 083005 (2008) DOI: https://journals.aps.org/prd/abstract/10.1103/PhysRevD.77.083005

[8] N. P. Pitjev, E. V. Pitjeva, Astronomy Letters **39**, 141 (2013) DOI: 10.1134/S1063773713020060

[9] P. Tinyakov, I. Tkachev, K. Zioutas, JCAP01 **1601**, 035 (2016) DOI: http://dx.doi.org/10.1088/1475-7516/2016/01/035

[10] J. Enander, A. Pargner, T. Schwetz, [arXiv:1708.04466v1 [astro-ph.CO]] (2017)

[11] V.I. Dokuchaev, Yu. N. Eroshenko, I.I. Tkachev, JETP **125**, 434 (2017) DOI: 10.1134/S1063776117080039

[12] C. Ruhland, E. F. Bell, H.W. Rix, X.X. Xue, ApJ. **731**, 119 (2011) DOI: 10.1088/0004-637X/731/2/119

[13] S.L.J. Gibbons, V. Belokurov, N.W. Evans, MNRAS **464**, 794 (2017) DOI: https://doi.org/10.1093/mnras/stw2328

[14] C. W. Purcell, A. R. Zentner, M.-Y. Wang, JCAP08 , 027 (2012) DOI: 10.1088/1475-7516/2012/08/027

[15] P. Sikivie, J.R. Ipser, Phys. Lett. B **291**, 288 (1992) DOI:https://doi.org/10.1016/0370-2693(92)91047-D

[16] S. Bertolucci, K. Zioutas, S. Hofmann, M. Maroudas, Phys. Dark Univ. **17**, 13 (2017) DOI: https://doi.org/10.1016/j.dark.2017.06.001

Fermi-LAT and NuSTAR as Stellar Axionscopes

Maurizio Giannotti

Barry University, Miami Shores, US

DOI: http://dx.doi.org/10.3204/DESY-PROC-2017-02/giannotti_maurizio

We overview the potential of airborne X-ray and gamma-ray telescopes to probe the axion-like particles parameter space.

1 Introduction

Besides contributing to stellar cooling, axion-like particles (ALPs) produced in stars could decay or, in the presence of an external magnetic field, oscillate into photons, providing a way for direct detection. This strategy is currently adopted by experiments such as CAST [1] and NuSTAR [2] to look for solar axions.

Other stars could contribute as well to a potentially observable photon flux detectable on Earth with current space born X-ray and gamma-ray instruments. Interestingly, in certain regions of the ALP parameter space such instruments, developed with the purpose of studying high energy photons, not ALPs, could exceed the probing potential of dedicated experiments such as ALPS II [3] and IAXO [4, 5].

2 Light ALPs form Supernovae

Of particular interests for the study of ALPs are supernova (SN) events. In the extreme conditions of the SN core, ALPs can be efficiently produced and, given the small couplings we are interested in, stream freely out of it. The total production rate of light ALPs ($m_a < T$) per unit energy (integrated over the explosion time) can be approximated as[1]

$$\frac{dN_a}{dE} \simeq C\, g_{12}^2\, (E/E_0)^\beta\, e^{-(\beta+1)E/E_0}\,, \tag{1}$$

with $g_{12} = g_{a\gamma}/(10^{-12}\mathrm{GeV}^{-1})$. The other parameters depend on the progenitor mass. For a progenitor of 10-18$M_\odot$, one finds $C \simeq (5-9)\times 10^{48}$ MeV^{-1} $E_0 \simeq 100$ MeV, and $\beta \simeq 2$ [6, 7]. Notice that the average ALP energy is approximately $3E_0(1+\beta)^{-1} \simeq 100$ MeV and the spectrum is maximal for $E \simeq 2E_0(1+\beta)^{-1} \simeq 60$ MeV. Integrating over the energy, we find a production of a few $10^{49} g_{12}^2$ ALPs over the time of the SN explosion.

[1]Here we are assuming that ALPs interact only with photons. In this case, they can be produced in the SN core through the Primakoff process [6], in which the ALP converts into a photon in the proton electrostatic field. It is, however, also possible that ALPs interact with nuclei. In particular, standard QCD axions do. In this case, the nuclear Bremsstrahlung may be more efficient. In general, the two spectra produced by these processes are similar in shape, with the Nuclear Bremsstrahlung peaked at a slightly lower energy.

If light enough, some of these ALPs oscillate into photons in the external magnetic field, producing a flux F_γ on earth

$$\frac{dF_\gamma}{dE} = \frac{1}{4\pi d^2}\frac{dN_a}{dE} \times P_{a\gamma}\,, \tag{2}$$

where $P_{a\gamma}$ is the oscillation probability and d the SN distance.

Since (for sufficiently light ALPs) the energy dependence in $P_{a\gamma}$ drops for photons of energy above 10 MeV or so [6], the photon spectrum resembles the ALP spectrum. Thus, one expects a photon flux on earth with average energy $\sim$ 100 MeV, peacked at about 60 MeV. The ideal instruments to study the (ALP-induced) SN photon flux are, therefore, detectors sensitive to gamma rays in the energy band between a few MeV and a few 100 MeV.

Unfortunately, SN events close enough to be analyzed are fairly rare and presently, the only SN event we can consider to efficiently constrain the ALP-photon coupling is SN1987A. In this case we have to rely on the old and poorly known Gamma-Ray Spectrometer (GRS) on the Solar Maximum Mission (SMM). The effective area of the GRS, about 100 cm^2 in the energy range 10-100 MeV,[2] is quite small, compared to the newer instruments. Nevertheless, the absence of any photon excess observed by this instrument at the time of the neutrino burst from SN1987A allows to set a stringent bound (comparable to the IAXO potential in that region) on the axion-photon coupling, $g_{a\gamma} \lesssim 5\times10^{-12}$ GeV^{-1}, for masses $m_a \lesssim 4.4\times10^{-10}$ eV [6] (see green shaded area in the left panel of Fig. 1).

The Fermi Large Area Telescope (Fermi LAT) is currently the ideal candidate to probe axions in the event of a next galactic SN explosion, though it performs considerably better at higher energies $E \gtrsim 1$ GeV. Its effective area at energies above 1 GeV is about 1 m^2 but the effective area averaged over the ALP spectrum is only 5500 cm^2.

For a galactic SN, one finds $d \lesssim 10\,$kpc and $B \simeq$ a few μG. With these conditions, assuming massless ALPs with energies higher than a few 10 MeV and an axion-photon coupling $g_{a\gamma} \sim 10^{-13} - 10^{-10}$ GeV^{-1}, one finds $P_{a\gamma} \simeq (g_{a\gamma}B_T d)^2/4$, where d is the SN distance and B_T the component of the magnetic field orthogonal to the photon beam [6]. Interestingly, in these conditions the distance dependence in Eq. (2) drops. This approximation is valid when the SN distance is much smaller than the coherence length of the galactic magnetic field, $l \sim 10$ kpc. In the case of more distant sources, the flux is reduced because of the average over several magnetic domains. As a rough estimate, we should expect $F_\gamma \simeq g_{12}^4 \mathrm{cm}^{-2}$ for $d \ll l$, where we have integrated Eq. (2) over all the frequencies. Using this rough estimate and the average effective area, one should therefore expect about $5\times10^3\, g_{12}^2$ events in the Fermi LAT, in case of a galactic SN explosion. Assuming 5 to 7 events for a 2 σ signal, (the exact number depends on the background and is not necessarily the same for all SNe [7]), one finds that Fermi LAT has the potential to probe the axion coupling down to $g_{a\gamma} \sim$ a few 10^{-13} GeV^{-1} for a galactic SN. The accurate result [7] is shown in Fig. 1 and is quite impressive. In the hypothesis of a future galactic SN during the time of the Fermi mission, we would be able to explore a region of the ALP parameter space with a very rich phenomenology, including the region of the transparency hints [8] and part of the region invoked for the stellar cooling anomalies [9, 10].

Next generation instruments, such as e-Astrogram [11] and ComPair [12], are especially efficient at lower energies and, more importantly, have a much smaller point spread function with respect to Fermi LAT at the energies expected from SN events. However, their effective areas averaged over the expected photon spectrum is about a factor of 4-5 smaller than the

[2]Note, however, that there is little information about the response of this instrument in the literature. Moreover, the instrument was looking at the sun at the time of the explosion and so could have detected only off-axis SN photons.

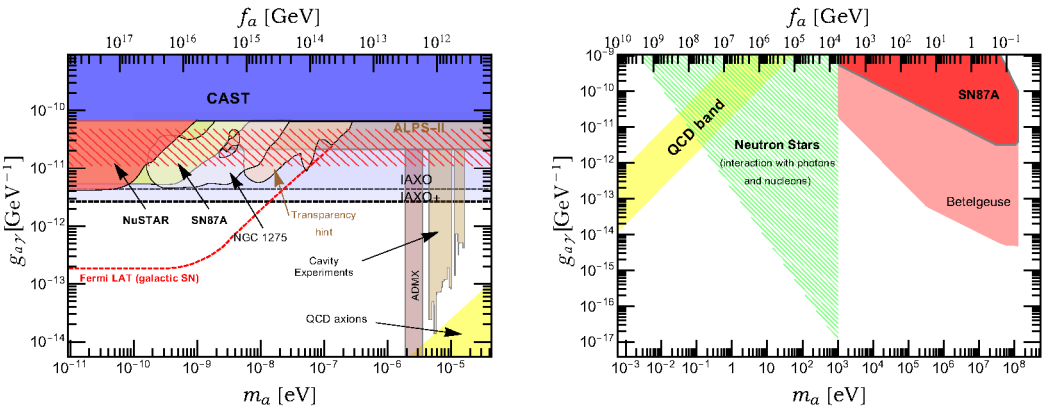

Figure 1: *Left panel:* Low mass ALPs parameter space. The hash-dashed region indicates the range of parameters expected to explain the stellar cooling anomalies [13, 9], which superimpose partially over the transparency hint region, invoked to explain the transparency of the universe to very high energy gamma rays [8]. This region is partially excluded by the search for spectral irregularities in the gamma ray spectrum of NGC 1275 [14]. The dashed red line is the expected Fermi potential for a next galactic SN [7] discussed in the text. *Right panel:* Bounds on heavy ALPs from NS and SN. Notice that the bound from the NS assumes interaction with both neutrons and photons. The region assumes $m_a < 2m_e$, so that the decay channel into $e^+ e^-$ is forbidden. The regions labeled SN1987A and Betelgeuse are extracted from ref. [21]. The mass region between 1 and 10 keV is not shown in the original literature and has been extrapolated in this plot.

Fermi LAT one. Although we have not performed a detailed analysis of the response function of these new instruments, it is unlikely that they would improve substantially (if at all) on the Fermi potential. A full analysis of the potential of the next generation of gamma ray observatories for galactic SN is in preparation.

3 Massive ALPs from Supernovae and Neutron Stars

The interest in massive ALPs has increased in last few years thanks to improvements in the experimental potential to probe them [15, 16] (see also B. Dobrich contribution to these proceedings). Non-minimal QCD axion models, such as those discussed in [17, 18, 19], predict massive ALPs, which interact with photons and standard model fermions. If massive enough, ALPs could *decay* rather than oscillate into photons, and produce a sufficient photon flux on earth, regardless of the magnetic field.

The phenomenology of photons from massive ALPs from astrophysical sources is quite interesting. In particular, the arrival time of these photons could, in general, be much longer than the typical explosion time [20, 21]. In studying the experimental potential it is therefore necessary to account for longer detection times.

A thorough analysis of the constraints on ALPs from SN1987A was presented in [21], where the authors also estimated the Fermi LAT potential in case the close red supergiant Betelgeuse were to go SN. The result is shown in the right panel of Fig. 1. The analysis assumes ALPs

interacting with photons only. The figure shows also the Fermi exclusion plot derived from the analysis of 5 years of gamma-ray data for a sample of 4 nearby neutron stars (NS) [22]. Notice, however, that the region shown is model dependent and assumes axions interacting not only with photons but also with neutrons, with $g_{a\gamma} \simeq 10^{-2} g_{an}$ GeV^{-1}. In fact, in the proton-poor NS environment the Primakoff production process is very modest and the only efficient axion production mechanism is the neutron bremsstrahlung.

4 Betelgeuse

One of the most interesting stars to study ALPs, besides our sun, is Betelgeuse [23], a supergiant in the constellation of Orion, about 200 pc from the sun. Though not the closest star to our sun, Betelgeuse has a much higher core temperature than nearer stars and would therefore be a better source of ALPs.

Light ALPs can be efficiently produced in the star through the Primakoff process, which requires interaction with photons only, and then converted into photons in the galactic magnetic field. Using $B_T = 2.9$ μG, $d = 197$ pc, and $m_a = 0$, we find that the expected photon spectrum on earth is well approximated by

$$\frac{dN_\gamma}{dE\,dt} \simeq C\, g_{10}^2\, (E/E_0)^\beta\, e^{-(\beta+1)E/E_0}\,, \tag{3}$$

with $C \simeq (0.4 - 1)$ keV^{-2} cm^{-2} s^{-1}, $\beta \simeq 2$, $E_0 \simeq 60 - 100$ keV. The coefficients depend on the stellar model, which is the greatest source of uncertainty.

This mechanism would produce a photon flux peaked in the hard X-ray region, at about 50-60 keV. Most X-ray detectors are not very efficient in this region. Currently, the most efficient is NuSTAR [2], though its effective area is steeply reduced at energies above a few 10 keV. Integrating over the effective area in [2], one can expect $\sim 300\, g_{10}^2$ photons from ALP conversion per second in NuSTAR, a value considerably larger than $\sim 3\, g_{10}^2\, \mathrm{s}^{-1}$ photons in Chandra or $\sim 2\, g_{10}^2\, \mathrm{s}^{-1}$ photons in XMM-Newton. Assuming a background $\simeq 10^{-3}\, \gamma\, \mathrm{s}^{-1}$ [2], one should expect NuSTAR to be able to probe values of the axion-photon coupling down to a few 10^{-12} GeV^{-1}, the same level of sensitivity expected by IAXO. An estimate of the NuSTAR sensitivity is shown in the left panel in Fig. 1. A more comprehensive and detailed analysis is in preparation.

Regardless of the precise level of sensitivity, it is in general obvious that NuSTAR observations of Betelgeuse would allow to probe couplings at least as low as those reached by the SN1987A analysis, for masses below $m_a \sim$ a few 10^{-11} eV, without being subject to the same level of uncertainties.

Acknowledgments

I would like to thank B. Döbrich, B. Grefenstette, M. Meyer, A. Mirizzi, K. Perez, J. Ruz Armendariz, O. Straniero and J. K. Vogel for useful discussions and suggestions. A special thank to the organizers of this very interesting workshop.

References

[1] V. Anastassopoulos *et al.* [CAST Collaboration], Nature Phys. **13** (2017) 584 doi:10.1038/nphys4109 [arXiv:1705.02290 [hep-ex]].

[2] F. A. Harrison *et al.*, Astrophys. J. **770** (2013) 103 doi:10.1088/0004-637X/770/2/103 [arXiv:1301.7307 [astro-ph.IM]].

[3] R. Bhre *et al.*, JINST **8** (2013) T09001 doi:10.1088/1748-0221/8/09/T09001 [arXiv:1302.5647 [physics.ins-det]].

[4] E. Armengaud *et al.*, JINST **9** (2014) T05002 doi:10.1088/1748-0221/9/05/T05002 [arXiv:1401.3233 [physics.ins-det]].

[5] M. Giannotti, J. Ruz and J. K. Vogel, PoS ICHEP **2016** (2016) 195 [arXiv:1611.04652 [physics.ins-det]].

[6] A. Payez, C. Evoli, T. Fischer, M. Giannotti, A. Mirizzi and A. Ringwald, JCAP **1502** (2015) no.02, 006 doi:10.1088/1475-7516/2015/02/006 [arXiv:1410.3747 [astro-ph.HE]].

[7] M. Meyer, M. Giannotti, A. Mirizzi, J. Conrad and M. A. Snchez-Conde, Phys. Rev. Lett. **118** (2017) no.1, 011103 doi:10.1103/PhysRevLett.118.011103 [arXiv:1609.02350 [astro-ph.HE]].

[8] M. Meyer, D. Horns and M. Raue, "First lower limits on the photon–axion-like particle coupling from very-high-energy gamma-ray observation," Phys. Rev. D **87**, 035027 (2013) [arXiv:1302.1208 [astro-ph.HE]].

[9] M. Giannotti, I. Irastorza, J. Redondo and A. Ringwald, JCAP **1605** (2016) no.05, 057 doi:10.1088/1475-7516/2016/05/057 [arXiv:1512.08108 [astro-ph.HE]].

[10] M. Giannotti, I. G. Irastorza, J. Redondo, A. Ringwald and K. Saikawa, JCAP **1710** (2017) no.10, 010 doi:10.1088/1475-7516/2017/10/010 [arXiv:1708.02111 [hep-ph]].

[11] A. De Angelis *et al.* [e-ASTROGAM Collaboration], Exper. Astron. **44** (2017) no.1, 25 doi:10.1007/s10686-017-9533-6 [arXiv:1611.02232 [astro-ph.HE]].

[12] A. A. Moiseev *et al.*, arXiv:1508.07349 [astro-ph.IM].

[13] A. Ayala, I. Domnguez, M. Giannotti, A. Mirizzi and O. Straniero, Phys. Rev. Lett. **113** (2014) no.19, 191302 doi:10.1103/PhysRevLett.113.191302 [arXiv:1406.6053 [astro-ph.SR]].

[14] M. Ajello *et al.* [Fermi-LAT Collaboration], Phys. Rev. Lett. **116** (2016) no.16, 161101 doi:10.1103/PhysRevLett.116.161101 [arXiv:1603.06978 [astro-ph.HE]].

[15] B. Döbrich, arXiv:1708.05776 [hep-ph].

[16] M. J. Dolan, T. Ferber, C. Hearty, F. Kahlhoefer and K. Schmidt-Hoberg, arXiv:1709.00009 [hep-ph].

[17] Z. Berezhiani, L. Gianfagna and M. Giannotti, Phys. Lett. B **500** (2001) 286 doi:10.1016/S0370-2693(00)01392-7 [hep-ph/0009290].

[18] L. Gianfagna, M. Giannotti and F. Nesti, JHEP **0410** (2004) 044 doi:10.1088/1126-6708/2004/10/044 [hep-ph/0409185].

[19] K. R. Dienes, E. Dudas and T. Gherghetta, Phys. Rev. D **62** (2000) 105023 doi:10.1103/PhysRevD.62.105023 [hep-ph/9912455].

[20] M. Giannotti, L. D. Duffy and R. Nita, JCAP **1101**, 015 (2011) doi:10.1088/1475-7516/2011/01/015 [arXiv:1009.5714 [astro-ph.HE]].

[21] J. Jaeckel, P. C. Malta and J. Redondo, arXiv:1702.02964 [hep-ph].

[22] B. Berenji, J. Gaskins and M. Meyer, Phys. Rev. D **93** (2016) no.4, 045019 doi:10.1103/PhysRevD.93.045019 [arXiv:1602.00091 [astro-ph.HE]].

[23] E. D. Carlson, Phys. Lett. B **344**, 245 (1995). doi:10.1016/0370-2693(94)01529-L

ABRACADABRA, A Search for Low-Mass Axion Dark Matter

Reyco Henning[1,2] *on behalf of the ABRACADABRA collaboration: Janet Conrad*[3]*, Joe Formaggio*[3]*, Sarah Heine*[3]*, Yoni Kahn*[4]*, Joe Minervini*[3]*, Jonathan Ouellet*[3]*, Kerstin Perez*[3]*, Alexey Radovinsky*[3]*, Ben Safdi*[3]*, Chiara Salemi*[1]*, Jesse Thaler*[3]*, Daniel Winklehner*[3]*, Lindley Winslow*[3]*,*

[1]University of North Carolina at Chapel Hill, Chapel Hill, NC, USA
[2]Triangle Universities Nuclear Laboratory, Durham, NC, USA
[3]Massachusetts Institute of Technology, Cambridge, MA, USA
[4]Princeton University, Princeton, NJ, USA

DOI: http://dx.doi.org/10.3204/DESY-PROC-2017-02/henning_reyco

ABRACADABRA is a proposed experiment to search for ultralight ($10^{-14} - 10^{-6}$eV) axion dark matter. When ultralight axion dark matter encounters a static magnetic field, it sources an effective electric current that follows the magnetic field lines and oscillates at the axion Compton frequency. In the presence of axion dark matter, a large toroidal magnet will act like an oscillating current ring, whose induced magnetic flux can be measured by an external pickup loop inductively coupled to a SQUID magnetometer. Both broadband and resonant readout circuits are considered. ABRACADABRA is fielding a 10-cm prototype in 2017 with the intention of scaling to a 1 m^3 experiment. The long term goal is to probe QCD axions at the GUT-scale.

1 Motivation

The Peccei-Quinn (PQ) mechanism was proposed to solve the strong-CP problem. It requires a massless pseudo-scalar, known as the axion, which couples to QCD in such a way that the lowest-energy field configuration is one where the neutron electric dipole moment vanishes. In the process of solving the strong-CP problem, the axion acquires a small mass, which is inversely proportional to its decay constant, f_a. For decay constants at the grand unified (GUT) scale, $f_a \simeq 10^{16}$ GeV, the axion mass is $m_a \simeq 10^{-9}$ eV. Beyond the QCD axion, there may also be axion-like particles, which are light pseudo-scalars that do not couple to QCD. Indeed, in certain string-theory constructions that admit a QCD axion-like state, a spectrum of additional axion-like particles may be expected [1, 2].

ABRACADABRA ("A Broadband or Resonant Approach to Cosmic Axion Detection with an Amplifying B-field Ring Apparatus") specifically targets $f_a > 10^{12}$ GeV, and thus axion masses $m_a < 10^{-6}$ eV [3]. In UV-complete models, such as string constructions, it has been difficult to obtain f_a as low as 10^{12} GeV; $f_a \simeq 10^{15} - 10^{16}$ GeV is seen to be much more generic [1]. For example, the so-called "model-independent axion" in heterotic string theory has $f_a \simeq 1.1 \times 10^{16}$ GeV, and similar findings are also seen in type IIB and M-theory constructions [4]. The string-axion models, along with the generic expectation that new physics should appear around the GUT scale and the existence of a viable axion DM cosmology at these

scales, motivates the broadband search for axion DM at scales $f_a > 10^{12}$ GeV.

2 Principle

The axion DM field a should be treated locally as a classical, time-dependent background field

$$a(t) = a_0 \sin(m_a t) = \frac{\sqrt{2\rho_{\rm DM}}}{m_a} \sin(m_a t)\,, \tag{1}$$

where the normalization of the field is found by requiring the energy-density of the field to equal the local DM density $\rho_{\rm DM} \approx 0.3$ GeV/cm^3 [5]. Treating the axion field a as a background field, Ampère's circuit law becomes [6]:

$$\nabla \times \mathbf{B} = \frac{\partial \mathbf{E}}{\partial t} - g_{a\gamma\gamma} \left(\mathbf{E} \times \nabla a - \mathbf{B} \frac{\partial a}{\partial t} \right) . \tag{2}$$

For the QCD axion, $g_{a\gamma\gamma} = g\alpha_{\rm EM}/(2\pi f_a)$, where $\alpha_{\rm EM}$ is the electromagnetic fine-structure constant and g is an $\mathcal{O}(1)$ number equal to ~ 0.75 (-1.92) for the DFSZ model [7, 8] (KSVZ model [9, 10]). Thus, in the presence of a static magnetic field $\mathbf{B}_0$, there is an axion-sourced effective current. We can treat the axion-DM-induced modification to Maxwell's equations as an effective electric current:

$$\mathbf{J}_{\rm eff} = g_{a\gamma\gamma} \sqrt{2\rho_{\rm DM}} \cos(m_a t) \mathbf{B}_0 \tag{3}$$

This effective current then sources a real magnetic field perpendicular to $\mathbf{B}_0$, oscillating at frequency m_a. ABRACADABRA uses a toroidal $\mathbf{B}_0$ to create such an axion-induced, oscillating magnetic field that is measured in the toroidal bore.

3 Proposed Design

The proposed design is shown schematically in Fig. 1a. The static magnetic field $\mathbf{B}_0$ is generated by a constant, persistent current in a superconducting wire wrapping a toroid, and the axion effective current is detected with a superconducting pickup loop in the toroid bore. In the absence of axion DM (or noise), there is no magnetic flux through the pickup loop. With axion DM, there will be an oscillating magnetic flux through the pickup loop proportional to $g_{a\gamma\gamma}\sqrt{\rho_{\rm DM}}$. An alternative design is to wrap the torus in a gapped superconducting sheath that serves as RF shield and pick-up loop.

We consider two distinct circuits for reading out the signal, both based on a superconducting quantum interference device (SQUID). The broadband circuit uses a untuned magnetometer in an ideally zero-resistance setup, while the resonant circuit uses a tuned magnetometer with irreducible resistance. Both readout circuits can probe multiple orders of magnitude in the axion DM parameter space, though the broadband approach has increased sensitivity at low axion masses. The resonant circuit is technically more challenging because it requires a high-Q ($\sim 10^6$), tunable, cryogenic LC resonator. An optimal scan strategy using both circuits is being developed by the collaboration.

At cryogenic temperatures ($T \lesssim 60\,$mK), thermal current and voltage noise are subdominant to the current shot noise $S_{J,0}$ in the SQUID tunnel junctions, which sets an absolute

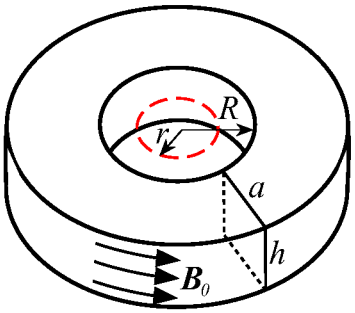

(a) A toroidal geometry to generate a static magnetic field $\mathbf{B}_0$. The dashed red circle shows the location of the superconducting pickup loop of radius $r \leq R$.

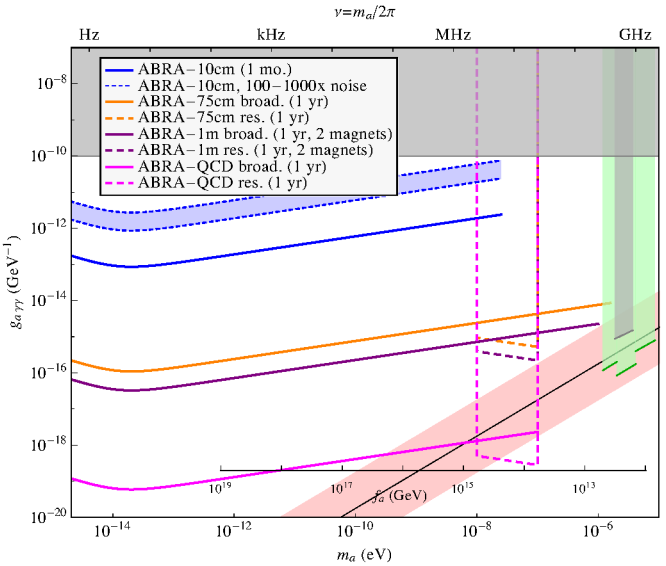

(b) The projected reach of the ABRA for different configurations described in the text. The grey regions show current constraints from ADMX and IAXO, while the red band shows the theoretical prediction for the QCD axion. Green bands show projected exclusion ranges.

(temperature-independent) floor for the magnetometer noise. In the resonant circuit, the dominant source of noise is thermal noise, even below 60 mK. At very low frequencies ($\lesssim 50\,\mathrm{Hz}$) the SQUID $1/f$ noise dominates.

4 Status and plans

The ultimate goal of the collaboration is to build ABRA-QCD to probe the theoretically well-motivated GUT-scale QCD axion. ABRA-QCD will require a 5 T magnet with a $\sim 100\,\mathrm{m}^3$ volume. To get there, we propose a series of at least three experiments, ABRA-10cm, ABRA-1m, and ABRA-QCD, that step through the parameter space m_a vs. $g_{a\gamma\gamma}$ in steps of 2-3 orders of magnitude in $g_{a\gamma\gamma}$, as shown in fig. 1b. The first prototype, ABRA-10cm, is being assembled at MIT with a magnet constructed by Superconducting Systems Inc.[1] A superconducting shield surrounds the magnet and magnetometer and the target toroidal magnetic field is 1 T. An initial run of the SQUID current sensor with no shielding, magnet, and no tuning shows noise levels that are, not surprisingly, a factor of $10^2 - 10^3$ higher than expected. The noise will be reduced significantly in the future; however even at these noise levels we can still achieve a world-leading axion limit.

For ABRA-1m we are considering two independent detectors that would provide independent verification of a possible positive signal and perform coincidence studies. The results from these will guide the design of the optimal configuration for ABRA-QCD, ie. multiple magnets vs. a

[1] http://www.superconductingsystems.com

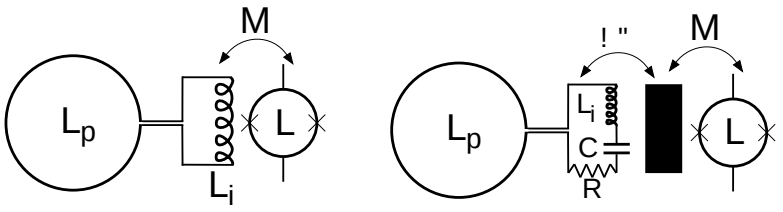

Figure 2: Schematics of proposed readout circuits. **Left:** broadband (untuned magnetometer). The sheath with inductance L_p is connected in series with an input coil L_i, which has mutual inductance M with the SQUID of self-inductance L. For inductance matching, $L_i \approx L_p$. **Right:** resonant (tuned magnetometer). L_p is now in series with both L_i and a tunable capacitor C.

single magnet design. ABRA-75cm is another possible intermediate step that has lower cost but does not retire as many risk as ABRA-1m.

5 Acknowledgments

This material is based upon work supported by the National Science Foundation under Grant No. NSF-PHY-1658693. The author would like to acknowledge the support of the US Department of Energy Office of Nuclear Physics under grants DE-FG02-97ER4104 and DE-FG02-97ER41033.

References

[1] P. Svrcek and E. Witten, "Axions In String Theory," *JHEP*, vol. 06, p. 051, 2006.

[2] A. Arvanitaki, S. Dimopoulos, S. Dubovsky, N. Kaloper, and J. March-Russell, "String axiverse," *Phys. Rev. D*, vol. 81, p. 123530, Jun 2010.

[3] Y. Kahn, B. R. Safdi, and J. Thaler *Phys. Rev. Lett.*, vol. 117, no. 14, p. 141801, 2016.

[4] J. Jaeckel and A. Ringwald *Ann. Rev. Nucl. Part. Sci.*, vol. 60, p. 405, 2010.

[5] J. I. Read, "The Local Dark Matter Density," *J. Phys.*, vol. G41, p. 063101, 2014.

[6] P. Sikivie, "Experimental Tests of the Invisible Axion," *Phys. Rev. Lett.*, vol. 51, pp. 1415–1417, 1983. [Erratum: Phys. Rev. Lett.52,695(1984)].

[7] M. Dine, W. Fischler, and M. Srednicki, "A Simple Solution to the Strong CP Problem with a Harmless Axion," *Phys. Lett.*, vol. B104, p. 199, 1981.

[8] A. R. Zhitnitsky, "On Possible Suppression of the Axion Hadron Interactions. (In Russian)," *Sov. J. Nucl. Phys.*, vol. 31, p. 260, 1980. [Yad. Fiz.31,497(1980)].

[9] J. E. Kim, "Weak Interaction Singlet and Strong CP Invariance," *Phys. Rev. Lett.*, vol. 43, p. 103, 1979.

[10] M. A. Shifman, A. I. Vainshtein, and V. I. Zakharov, "Can Confinement Ensure Natural CP Invariance of Strong Interactions?," *Nucl. Phys.*, vol. B166, p. 493, 1980.

A Preview of Global Fits of Axion Models in GAMBIT

Sebastian Hoof (for the GAMBIT Collaboration)

Department of Physics, Imperial College London, London, United Kingdom

DOI: http://dx.doi.org/10.3204/DESY-PROC-2017-02/hoof_sebastian

There are currently many experimental searches underway that try to detect QCD axions and axion-like particles. These, in addition to other constraints from astrophysics and cosmology, require a consistent and statistically rigorous analysis of the large landscape of axion models. Here, we present the rationale, methodology and preliminary results for global fits of axion models using the recently developed software framework GAMBIT.

1 Introduction

The QCD axion first appeared in the context of the Peccei-Quinn (PQ) mechanism, which was introduced to solve the Strong CP problem [1, 2]. Both Weinberg [3] and Wilczek [4] realised that the PQ mechanism gives rise to a pseudo-scalar particle. The QCD axion also turned out to be an excellent dark matter (DM) candidate [5–8]. There also exists a much broader class of axion models, dubbed axion-like particles (ALPs), which are also well-motivated due to being DM candidates or appear in other contexts [9, 10].

It is important to note that there are multiple possibilities of how to extend the Standard Model to include QCD axions or ALPs. In fact, the initial models of KSVZ type [11, 12] or DFSZ type [13, 14] define a "band" of models in parameter space [15, 16]. Recently, several authors categorised the original axion band in terms of phenomenologically interesting models as well as extended it [17–20]. Hence, many possible axion models have to be compared to the available data.

Furthermore, there is already a wide range of experiments, observations, and theoretical arguments to constrain axion models. These efforts will grow in the coming years due to a continuing stream of new ideas and collaborations – as, e.g., seen in various talks throughout this conference. We therefore expect that the existing, early proposals [21–25] will be complemented by future detectors and observations.

While the QCD axion has been studied extensively in the literature, theory uncertainties in its properties remain and ought to be taken into account. This also applies to the recent advances in lattice simulations of the temperature dependence of the axion mass [26, 27].

Finally, any analysis of data is based on assumptions and, when combining different results, it is important to ensure their consistency. One example is the dependency of the signal predictions on the local DM abundance in axions for haloscope searches. The signal needs to be rescaled according to this quantity while, at the same time, one needs to consider the range of possible values for the local DM abundance.

We argue that, in light of the points raised above, it is important to consistently combine all available results in a statistically rigorous way. In the following, we introduce *global fits* as a method to, in principle, address and incorporate all of the issues mentioned in the introduction.

2 Global fits of axion models in GAMBIT

The underlying idea of global fits is to test one or multiple models against all available data and prior information. The goals of such studies are, e.g., parameter extraction, model comparison and discovery assessment. In order to achieve these goals, one has to make use of powerful algorithms to explore the parameter space. Ultimately, identifying the models that "best" describe the data is also the goal of the recently published software framework GAMBIT [28–33].

2.1 General overview

GAMBIT, the **G**lobal **A**nd **M**odular **B**eyond-the-Standard-Model **I**nference **T**ool, is a software framework for global fits. As the name suggests, one of GAMBIT's main features is modularity. This allows for easily integrating new components such as additional models, likelihoods and sampling algorithms. The user has the freedom to only include the likelihoods deemed relevant for a problem and perform a Bayesian *or* frequentist analysis. To this end, GAMBIT provides internal sampling routines and can also use a number of popular, external samplers [32].

Using this framework, the Collaboration published a number of physics studies regarding the MSSM [34], scalar singlet dark matter model [35], and GUT scale SUSY models [36]. These will be complemented by, amongst other studies, a global fit of axion models. For more information on GAMBIT, we encourage the reader to consider the sections of Ref. [28] relevant to their interests.

2.2 Results for axion global fits

In our first study of axions in GAMBIT, we consider the case where the PQ symmetry is broken *before* the end of inflation (and not restored afterwards). As a consequence, the entire Universe is contained within one causally-connected bubble with homogeneous initial conditions for the axion field [5]. However, the initial field value need not be of order one, such that constraints from overproduction of dark matter can be avoided [37]. Since the initial field value θ_i is uniformly chosen from the interval of $-\pi$ to π [38–40], this possibility comes at the price of a certain degree of fine-tuning. One also has to consider potentially problematic isocurvature perturbations [38–40] but, in exchange, an axion population from topological defects is diluted away by inflation.

We want to include all of the most relevant constraints and experiments for this case, such as results from ALPS [41], CAST [42, 43], various haloscope searches [44–50], Supernova 1987A [51], H.E.S.S. [52], various telescope searches [53–56], HB stars/R-parameter [57] and the somewhat controversial WD cooling hints [57–62]. Most of these constraints have already been successfully implemented in GAMBIT.

The structure of GAMBIT allows us to set up a family of axion models, including generalised QCD axion and ALP models as well as more specific models such as DFSZ or KSVZ. We consider an axion mass range from about 10^{-10} eV to 10 eV. We will provide more details about the implementation of the various models in our upcoming publication. For this summary, it suffices

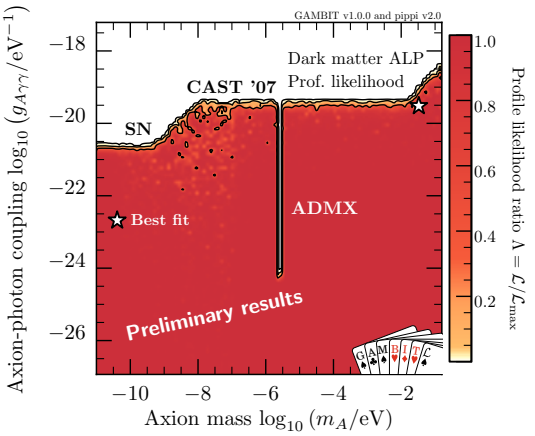

Figure 1: Exclusion limits for the axion-photon coupling (using Diver [32]). We used our generic ALP model and assumed axions to be all of the DM. The exclusion regions are mostly due to Supernova 1987A (SN) [51], ADMX [47–50] and CAST 2007 results [42].

to say that the QCD axion mass is given by

$$m_A(T) = \frac{\Lambda^2}{f_A} \begin{cases} 1 & \text{if } T \leq T_{\text{crit}} \\ \left(\frac{T_{\text{crit}}}{T}\right)^{\beta/2} & \text{otherwise} \end{cases} , \tag{1}$$

where the energy scale Λ, the exponent β and the critical temperature T_{crit} are variable nuisance parameters, which are scanned over the range allowed by recent lattice results [27]. For ALPs, one simply sets $\beta = 0$. The axion-photon coupling $g_{A\gamma\gamma}$ is given by,

$$g_{A\gamma\gamma} = \frac{\alpha_{\text{EM}}}{2\pi f_A} \left(\frac{E}{N} - \widetilde{C}_{A\gamma\gamma} \right) , \tag{2}$$

with the anomaly factor E/N and the model-independent contribution $\tilde{C}_{A\gamma\gamma}$ (we use the value obtained from di Cortana *et al.* [64]). For ALPs, on the other hand, we replace the term in brackets by a single, arbitrary coupling constant.

Using the already included likelihood functions, we can show that we are able to reproduce existing exclusion limits. An example for this is the m_A-$g_{A\gamma\gamma}$-plane as shown in Fig. 1 for DM made out of ALPs. For the latter, we sampled the likelihood for a general ALP model (fixing $\Lambda = 10^{16}$ GeV, imposing relic density within uncertainties and sampling over the local halo density). The profile likelihood therefore follows closely the naïvely expected exclusion results from, e.g., overplotting various exclusion curves (such as in Ref. [16]).

As pointed out earlier, we rescale the signal expectation for, e.g., the ADMX experiment and are therefore sensitive to potential preferences regarding values of parameters such as θ_{i}. Even though there is no *a priori* argument for why certain values of θ_{i} should be preferred over others, this prior information will still influence a Bayesian analysis. In fact, in the pre-inflationary PQ symmetry breaking scenario, θ_{i} is uniformly distributed in the interval from $-\pi$ to π. We therefore have a physically-motivated prior with "natural" values of $\mathcal{O}(1)$. The Bayesian analysis automatically captures this well-known fine-tuning argument, and the limits

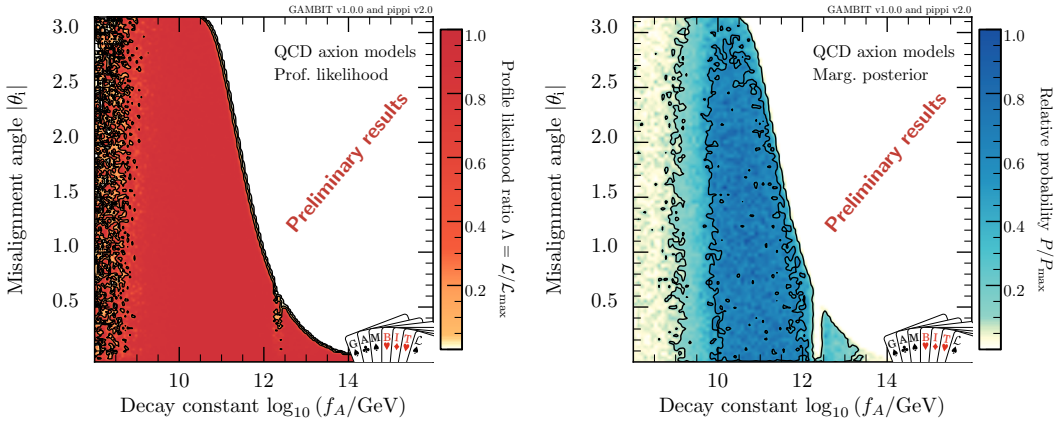

Figure 2: Frequentist (*left*, using Diver [32]) vs Bayesian (*right*, using MultiNest [65–67]) inference. We sample θ_i uniformly in the interval of -3.14 to 3.14 and only impose an upper limit on axions being the DM using Planck results [68].

from ADMX persist in the right panel of Fig. 2, while the profile likelihood should be ignorant of that fact. However, the completeness of our sampling depends on the choice of priors. Better sampling can be achieved by combining the results of various scans (at least for the frequentist approach) or optimising our sampler settings.

Improving the sampling, including the remaining likelihood functions and using the advantages of both frequentist and Bayesian methods are the remaining steps for concluding this first study. In our final analysis we will also compare with so-called "cooling hints" for the existence of axions [57–62].

3 Outlook

In order to consistently combine the increasing amount of information on axions, we propose to use the global fitting framework GAMBIT. This will allow us to compare different axion models in our upcoming study on the pre-inflationary PQ breaking case. The other case, where the PQ symmetry breaks after inflation, is left for future work. Furthermore, GAMBIT offers the opportunity to combine axions with other beyond-the-Standard-Model physics, such as in the recently proposed SMASH model [63].

Acknowledgments

SH would like to thank all the contact persons from the experimental collaborations and individual authors of Refs [41–62] for helpful discussions and their data as well as the members of the GAMBIT collaboration for helpful discussions and support. SH is funded by the Imperial College President's PhD Scholarship scheme.

References

[1] R. D. Peccei and H. R. Quinn, Phys. Rev. Lett. **38** (1977) 1440. doi:10.1103/PhysRevLett.38.1440

[2] R. D. Peccei and H. R. Quinn, Phys. Rev. D **16** (1977) 1791. doi:10.1103/PhysRevD.16.1791

[3] S. Weinberg, Phys. Rev. Lett. **40** (1978) 223. doi:10.1103/PhysRevLett.40.223

[4] F. Wilczek, Phys. Rev. Lett. **40** (1978) 279. doi:10.1103/PhysRevLett.40.279

[5] J. Preskill, M. B. Wise and F. Wilczek, Phys. Lett. **120B** (1983) 127. doi:10.1016/0370-2693(83)90637-8

[6] L. F. Abbott and P. Sikivie, Phys. Lett. **120B** (1983) 133. doi:10.1016/0370-2693(83)90638-X

[7] M. Dine and W. Fischler, Phys. Lett. **120B** (1983) 137. doi:10.1016/0370-2693(83)90639-1

[8] M. S. Turner, Phys. Rev. D **33** (1986) 889. doi:10.1103/PhysRevD.33.889

[9] J. E. Kim, Phys. Rept. **150** (1987) 1. doi:10.1016/0370-1573(87)90017-2

[10] J. Jaeckel and A. Ringwald, Ann. Rev. Nucl. Part. Sci. **60** (2010) 405 doi:10.1146/annurev.nucl.012809.104433 [arXiv:1002.0329 [hep-ph]].

[11] J. E. Kim, Phys. Rev. Lett. **43** (1979) 103. doi:10.1103/PhysRevLett.43.103

[12] M. A. Shifman, A. I. Vainshtein and V. I. Zakharov, Nucl. Phys. B **166** (1980) 493. doi:10.1016/0550-3213(80)90209-6

[13] A. R. Zhitnitsky, Sov. J. Nucl. Phys. **31** (1980) 260 [Yad. Fiz. **31** (1980) 497].

[14] M. Dine, W. Fischler and M. Srednicki, Phys. Lett. **104B** (1981) 199. doi:10.1016/0370-2693(81)90590-6

[15] J. E. Kim, Phys. Rev. D **58** (1998) 055006 doi:10.1103/PhysRevD.58.055006 [hep-ph/9802220].

[16] C. Patrignani *et al.* [Particle Data Group], Chin. Phys. C **40** (2016) no.10, 100001. doi:10.1088/1674-1137/40/10/100001

[17] L. Di Luzio, F. Mescia and E. Nardi, Phys. Rev. Lett. **118** (2017) no.3, 031801 doi:10.1103/PhysRevLett.118.031801 [arXiv:1610.07593 [hep-ph]].

[18] M. Farina, D. Pappadopulo, F. Rompineve and A. Tesi, JHEP **1701** (2017) 095 doi:10.1007/JHEP01(2017)095 [arXiv:1611.09855 [hep-ph]].

[19] L. Di Luzio, F. Mescia and E. Nardi, Phys. Rev. D **96** (2017) no.7, 075003 doi:10.1103/PhysRevD.96.075003 [arXiv:1705.05370 [hep-ph]].

[20] P. Agrawal, J. Fan, M. Reece and L. T. Wang, arXiv:1709.06085 [hep-ph].

[21] P. Sikivie, Phys. Rev. Lett. **51** (1983) 1415 Erratum: [Phys. Rev. Lett. **52** (1984) 695]. doi:10.1103/PhysRevLett.51.1415, 10.1103/PhysRevLett.52.695.2

[22] P. Sikivie, Phys. Rev. D **32** (1985) 2988 Erratum: [Phys. Rev. D **36** (1987) 974]. doi:10.1103/PhysRevD.36.974, 10.1103/PhysRevD.32.2988

[23] K. Van Bibber, N. R. Dagdeviren, S. E. Koonin, A. Kerman and H. N. Nelson, Phys. Rev. Lett. **59** (1987) 759. doi:10.1103/PhysRevLett.59.759

[24] A. A. Anselm, Yad. Fiz. **42** (1985) 1480.

[25] A. A. Anselm, Phys. Rev. D **37** (1988) 2001. doi:10.1103/PhysRevD.37.2001

[26] P. Petreczky, H. P. Schadler and S. Sharma, Phys. Lett. B **762** (2016) 498 doi:10.1016/j.physletb.2016.09.063 [arXiv:1606.03145 [hep-lat]].

[27] S. Borsanyi *et al.*, Nature **539** (2016) no.7627, 69 doi:10.1038/nature20115 [arXiv:1606.07494 [hep-lat]].

[28] P. Athron *et al.* [GAMBIT Collaboration], arXiv:1705.07908 [hep-ph].

[29] C. Balzs *et al.* [GAMBIT Collaboration], arXiv:1705.07919 [hep-ph].

[30] T. Bringmann *et al.* [GAMBIT Dark Matter Workgroup], arXiv:1705.07920 [hep-ph].

[31] F. U. Bernlochner *et al.* [GAMBIT Collaboration], arXiv:1705.07933 [hep-ph].

[32] G. D. Martinez *et al.* [GAMBIT Collaboration], arXiv:1705.07959 [hep-ph].

[33] P. Athron *et al.* [GAMBIT Collaboration], arXiv:1705.07936 [hep-ph].

[34] P. Athron *et al.* [GAMBIT Collaboration], arXiv:1705.07917 [hep-ph].

[35] P. Athron *et al.* [GAMBIT Collaboration], Eur. Phys. J. C **77** (2017) no.8, 568 doi:10.1140/epjc/s10052-017-5113-1 [arXiv:1705.07931 [hep-ph]].

[36] P. Athron *et al.* [GAMBIT Collaboration], arXiv:1705.07935 [hep-ph].

[37] S. Y. Pi, Phys. Rev. Lett. **52** (1984) 1725. doi:10.1103/PhysRevLett.52.1725

[38] M. Axenides, R. H. Brandenberger and M. S. Turner, Phys. Lett. **126B** (1983) 178. doi:10.1016/0370-2693(83)90586-5

[39] A. D. Linde, JETP Lett. **40** (1984) 1333 [Pisma Zh. Eksp. Teor. Fiz. **40** (1984) 496].

[40] A. D. Linde, Phys. Lett. **158B** (1985) 375. doi:10.1016/0370-2693(85)90436-8

[41] K. Ehret *et al.*, Phys. Lett. B **689** (2010) 149 doi:10.1016/j.physletb.2010.04.066 [arXiv:1004.1313 [hep-ex]].

[42] S. Andriamonje *et al.* [CAST Collaboration], JCAP **0704** (2007) 010 doi:10.1088/1475-7516/2007/04/010 [hep-ex/0702006].

[43] V. Anastassopoulos *et al.* [CAST Collaboration], Nature Phys. **13** (2017) 584 doi:10.1038/nphys4109 [arXiv:1705.02290 [hep-ex]].

[44] S. De Panfilis *et al.*, Phys. Rev. Lett. **59** (1987) 839. doi:10.1103/PhysRevLett.59.839

[45] W. Wuensch *et al.*, Phys. Rev. D **40** (1989) 3153. doi:10.1103/PhysRevD.40.3153

[46] C. Hagmann, P. Sikivie, N. S. Sullivan and D. B. Tanner, Phys. Rev. D **42** (1990) 1297. doi:10.1103/PhysRevD.42.1297

[47] C. Hagmann *et al.* [ADMX Collaboration], Phys. Rev. Lett. **80** (1998) 2043 doi:10.1103/PhysRevLett.80.2043 [astro-ph/9801286].

[48] S. J. Asztalos *et al.* [ADMX Collaboration], Phys. Rev. D **64** (2001) 092003. doi:10.1103/PhysRevD.64.092003

[49] S. J. Asztalos *et al.* [ADMX Collaboration], Phys. Rev. D **69** (2004) 011101 doi:10.1103/PhysRevD.69.011101 [astro-ph/0310042].

[50] S. J. Asztalos *et al.* [ADMX Collaboration], Phys. Rev. Lett. **104** (2010) 041301 doi:10.1103/PhysRevLett.104.041301 [arXiv:0910.5914 [astro-ph.CO]].

[51] A. Payez, C. Evoli, T. Fischer, M. Giannotti, A. Mirizzi and A. Ringwald, JCAP **1502** (2015) no.02, 006 doi:10.1088/1475-7516/2015/02/006 [arXiv:1410.3747 [astro-ph.HE]].

[52] A. Abramowski *et al.* [H.E.S.S. Collaboration], Phys. Rev. D **88** (2013) no.10, 102003 doi:10.1103/PhysRevD.88.102003 [arXiv:1311.3148 [astro-ph.HE]].

[53] M. A. Bershady, M. T. Ressell and M. S. Turner, Phys. Rev. Lett. **66** (1991) 1398. doi:10.1103/PhysRevLett.66.1398

[54] M. T. Ressell, Phys. Rev. D **44** (1991) 3001. doi:10.1103/PhysRevD.44.3001

[55] J. M. Overduin and P. S. Wesson, Phys. Rept. **402** (2004) 267 doi:10.1016/j.physrep.2004.07.006 [astro-ph/0407207].

[56] D. Grin, G. Covone, J. P. Kneib, M. Kamionkowski, A. Blain and E. Jullo, Phys. Rev. D **75** (2007) 105018 doi:10.1103/PhysRevD.75.105018 [astro-ph/0611502].

[57] M. Giannotti, I. Irastorza, J. Redondo and A. Ringwald, JCAP **1605** (2016) no.05, 057 doi:10.1088/1475-7516/2016/05/057 [arXiv:1512.08108 [astro-ph.HE]].

[58] A. H. Corsico, L. G. Althaus, M. M. M. Bertolami, A. D. Romero, E. Garcia-Berro, J. Isern and S. O. Kepler, Mon. Not. Roy. Astron. Soc. **424** (2012) 2792 doi:10.1111/j.1365-2966.2012.21401.x [arXiv:1205.6180 [astro-ph.SR]].

[59] A. H. Crsico *et al.*, JCAP **1607** (2016) no.07, 036 doi:10.1088/1475-7516/2016/07/036 [arXiv:1605.06458 [astro-ph.SR]].

[60] T. Battich, A. H. Crsico, L. G. Althaus, M. M. Miller Bertolami and M. M. M. Bertolami, JCAP **1608** (2016) no.08, 062 doi:10.1088/1475-7516/2016/08/062 [arXiv:1605.07668 [astro-ph.SR]].

[61] A. H. Corsico, L. G. Althaus, A. D. Romero, A. S. Mukadam, E. Garcia-Berro, J. Isern, S. O. Kepler and M. A. Corti, JCAP **1212** (2012) 010 doi:10.1088/1475-7516/2012/12/010 [arXiv:1211.3389 [astro-ph.SR]].

[62] M. Giannotti, I. G. Irastorza, J. Redondo, A. Ringwald and K. Saikawa, JCAP **1710** (2017) no.10, 010 doi:10.1088/1475-7516/2017/10/010 [arXiv:1708.02111 [hep-ph]].

[63] G. Ballesteros, J. Redondo, A. Ringwald and C. Tamarit, JCAP **1708** (2017) no.08, 001 doi:10.1088/1475-7516/2017/08/001 [arXiv:1610.01639 [hep-ph]].

[64] G. Grilli di Cortona, E. Hardy, J. Pardo Vega and G. Villadoro, JHEP **1601** (2016) 034 doi:10.1007/JHEP01(2016)034 [arXiv:1511.02867 [hep-ph]].

[65] F. Feroz and M. P. Hobson, Mon. Not. Roy. Astron. Soc. **384** (2008) 449 doi:10.1111/j.1365-2966.2007.12353.x [arXiv:0704.3704 [astro-ph]].

[66] F. Feroz, M. P. Hobson and M. Bridges, Mon. Not. Roy. Astron. Soc. **398** (2009) 1601 doi:10.1111/j.1365-2966.2009.14548.x [arXiv:0809.3437 [astro-ph]].

[67] F. Feroz, M. P. Hobson, E. Cameron and A. N. Pettitt, arXiv:1306.2144 [astro-ph.IM].

[68] P. A. R. Ade *et al.* [Planck Collaboration], Astron. Astrophys. **594** (2016) A13 doi:10.1051/0004-6361/201525830 [arXiv:1502.01589 [astro-ph.CO]].

The CAST Experiment: Status Report

Marin Karuza[1] [2] *for the CAST Collaboration.*

[1] *University of Rijeka, Rijeka, Croatia*
[2] *INFN Sezione di Trieste, Trieste, Italy*

DOI: http://dx.doi.org/10.3204/DESY-PROC-2017-02/karuza_marin

The CAST (Cern Axion Solar Telescope) experiment has been looking at the Sun for more than a decade now in its quest of observing a signal coming from the conversion of the axions in the telescope's magnetic field. Such a signal has not been observed thus allowing the collaboration to set only an upper limit to the axion - photon coupling constant in the parameter space. The final results will be presented as well as a new set of detectors that are looking into the dark sector. The new detectors, currently in operation, are KWISP which is directly sensitive to the chameleon coupling to matter, INGRID which is probing the chameleon coupling to photons and CAST - CAPP that is looking for dark matter axions. Also an additional dark matter axion detector, the RADES system, will be installed this year. While the search of axions is now limited to ones that are constituents of the galactic halo, the experiment continues to look at the Sun in an effort to see a signal of solar chameleons which are created in the Sun's tachocline via Primakoff effect and are particle candidate constituents of the dark energy in the Universe.

1 Axion limits and searches

The CAST (Cern Axion Solar Telescope) experiment is using a LHC prototype dipole magnet in its effort to answer some of of still open questions in the modern physics. The unanswered questions are about the composition of the Universe and non observation of CP violation in interactions including strong force. One of the answers to both questions contemporarily is the presence of a scalar field via Peccei-Quinn [1] symmetry which is spontaneously broken. The breaking of the symmetry results in a new particle, Nambu-Goldstone boson, called the axion. One of the best places to look for them is the Sun since they can be produced there by Primakoff effect. It has been shown [2] that axions can be detected on Earth by converting them to photons in a magnetic field which is in the case of CAST provided by LHC dipole magnet capable of achieving fields of 9 T over approximately 9 m length. The magnet is mounted on a movable platform that follows the Sun for 90 minutes in the morning and in the evening. The movement is constrained by minimum/maximum angle allowed by the cryogenic operation of the magnet. The tracking accuracy is monitored by geometric surveys and twice per year by following the Sun with an optical telescope and camera which are mounted on the magnet. The optical axis of the Sun filming system is parallel to the axis of the V1 bore. It must be noted that the Sun is observed by different set of detectors in the morning and evening data taking which are placed on opposite ends of the magnet. The expected signal from an axion to photon conversion in the magnetic field is in X-rays and is peaked at about 4 keV. The latest results on axion limits were obtained with measurements taken in the period 2013-2015. The results were

taken with vacuum inside the magnet bores with a new Micromegas [3] detector sitting behind a X-ray telescope built for axion searches. The result has been published in Nature Physics [4]

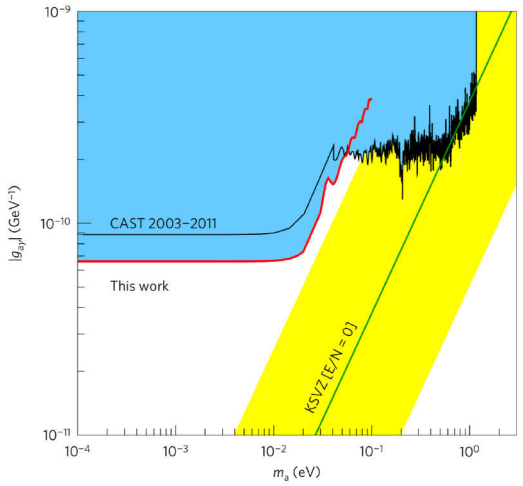

Figure 1: CAST excluded region at 95% confidence level in axion photon coupling vs axion mass plane. Plot taken from Nature Physics [4].

With this measurements the search for solar axions has been concluded since it is improbable that the limits with a current setup can be significantly improved. However a dedicated detector together with a X-ray telescope will remain on beam as a test facility for future experiments. In the meantime CAST magnet will be used also for relic axion searches. Obviously in this case the tracking capability is not needed anymore and data can be acquired continuously. Two such setups are being developed for CAST magnet, the CAST/CAPP and RADES experiment. Both experiments are based on RF cavities designed at built for the CAST magnet. The features include phase matching between cavities, tunability and fast scanning.

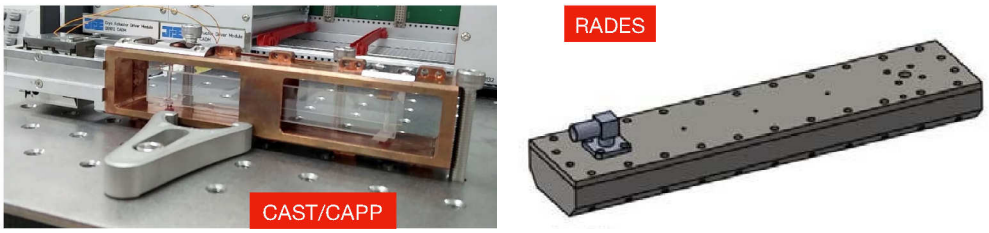

Figure 2: CAST/CAPP cavity tuning mechanism in its assembly frame on the left and RADES design on the right.

The last feature becomes important if the axion dark matter density is not uniform as is suggested by some distribution models. In particular, axion streaming and or clustering is of high probability [8] because of solar or planetary gravitational focusing of relic axions. Those fluctuations can boost the axion density up to several orders of magnitude raising the axion detectability provided the axion antenna is sensitive to axion bursts.

2 Dark energy searches

Beyond for the searches for solar and relic axions as candidate particles for dark matter, the CAST collaboration has started also a search for dark energy candidate. Notably, the so called chameleons. To be able to account for the accelerated expansion of the Universe, and at the same time not contradicting the observation a screening mechanism is added to the chameleon potential. With this mechanism the mass of the chameleons depends on the surrounding matter density. The assumed chameleon potential depends on the coupling of the field both to matter and photons. CAST is a unique experiment which can independently measure both coupling constants. First measurements of the coupling to photons was done with an SDD detector [5], and currently the measurements with an InGrid detector [6] are in progress. The other coupling constant can be measured by measuring the recoil of a thin membrane due to chameleon flux which has not enough energy to penetrate it. This normally happens at a grazing incidence to a material surface which also enables focussing of this hypothetical flux by an X-ray telescope. Furthermore the chameleon flux can be periodically interrupted by an surface that is oscillating in and out of the flux thus making it time dependent. It is obvious that the readout of the membrane position which is proportional to the pressure applied has to be extremely sensitive in order to fill still available gaps in the chameleon properties' parameter space. Two readout schemes have been proposed. One is so called KWISP 1.5 a Michelson interferometer with homodyne readout, an intermediate version on the way to Fabry - Perot based enhanced sensitivity detector [7]. The sensing element and the interferometer are placed in a vacuum chamber in order to minimise the the background noise in a part of the setup where beams propagate on different paths. Outside the vacuum chamber are only the light source and the readout electronics. The membrane and the chopper wheel have similar densities thus reflecting chameleons in the same energy range at the same angle with respect to the chameleon beam. KWISP 1.5 has performed a first measurement in December 2016. The occasion was related to

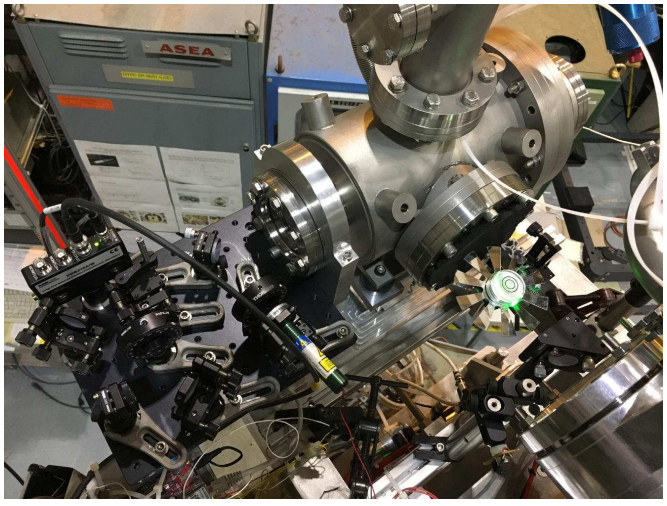

Figure 3: Photo of the KWISP 1.5 setup on beam. A breadboard with optical elements attached to the vacuum chamber can be seen on the left, while a chopper is in the middle between X-ray telescope and the vaccum chamber hosting the sensing element.

the alignment of Sun with the galactic center when an enhanced flux of chameleons due to the gravitational lensing could be expected. Data taking campaigns during which the setup was tested and improved followed during February and April.

3 Conclusion

Although the solar axion measurements are basically concluded, the CAST experiment has evolved and is becoming a Dark detector. It will search for Dark Matter with CAST/CAPP and RADES detectors, while also searching for signs of Dark Energy in form of chameleons through their coupling to matter and photons which makes it unique among Dark Energy detectors.

4 Acknowledgments

This work has been supported by MSE (Croatia) and Croatian Science Foundation under the project IP-2014-09-3720 and University of Rijeka grant 13.12.2.2.09.

5 Bibliography

References

[1] R.D. Peccei and H.R.Quinn, Phys. Rev. Lett. **38**, 1440 (1877). doi:10.1103/PhysRevLett.38.1440

[2] P. Sikivie, Phys. Rev. Lett. **51**, 1415 (1983). doi:10.1103/PhysRevLett.51.1415

[3] P. Abbon *et al.*, New. J. Phys. **9**, 170 (2007). doi:10.1088/1367-2630/9/6/170

[4] V. Anastassopoulos *et al.*, Nat. Phys. **13**, 584 (2017). doi:10.1038/NPHYS4109

[5] V. Anastassopoulos *et al.*, Phys. Lett. B **749**, 172 (2015). doi:10.1016/j.physletb.2015.07.049

[6] C. Krieger *et al.*, Nucl. Instrum. Meth. A **867**, 101 (2017). doi:0.1016/j.nima.2017.04.007

[7] M. Karuza *et al.*, "KWISP: an ultra-sensitive force sensor for the Dark Energy sector," Phys. Dark Univ. **12**, 100 (2016). doi:10.1016/j.dark.2016.02.004

[8] K. Zioutas *et al.*, "Search for Axions in streaming Dark Matter," [arXiv:1703.01436 [physics.ins-det]].

Searching for Axion Dark Matter using Radio Telescopes

Katharine Kelley[1], *P. J. Quinn*[1]

[1]International Centre for Radio Astronomy Research (ICRAR), University of Western Australia, Ken and Julie Michael Building, 7 Fairway, Crawley, WA 6009, Australia

DOI: http://dx.doi.org/10.3204/DESY-PROC-2017-02/kelley_katharine

We investigate the use of next generation radio telescopes such as the Square Kilometre Array (SKA) to detect axion two-photon coupling in the astrophysical environment. The uncertainty surrounding astrophysical magnetic fields presents new challenges, but with a frequency range corresponding to axions of mass $1.7-57\mu$eV and a spectral profile with a number of distinguishing features, SKA-mid offers a tantalising opportunity to constrain axion dark matter properties. To determine the sensitivity of SKA-mid to an axion signal, we consider observations of the Galactic centre and interstellar medium, and find that this new telescope could allow us to probe axion couplings $\gtrsim 10^{-16}\mathrm{GeV}^{-1}$.

1 Introduction

In this paper we motivate the use of radio telescopes in the search for cold dark matter (CDM) axions. We focus on the axion predicted by Weinberg [1] and Wilczek [2] following the introduction of a new $U(1)$ symmetry by Peccei & Quinn [3], and assume that it comprises all dark matter in the halo of our Galaxy. This axion has a mass constrained to be in the range $1-1,000\mu\mathrm{eVc}^{-2}$ [4, 5, 6, 7, 8, 9], for which conversion in a static magnetic field would produce a spectral line in the frequency range $0.2-200$GHz. It is this property that leads us to consider whether next generation radio telescopes such as the Square Kilometre Array (SKA) may contribute to detection efforts.

The SKA is a radio telescope planned for construction in Australia and Southern Africa. When built, it will be the largest radio telescope in the world and will provide sensitivity and spatial resolution at least an order of magnitude better than current technologies. The array comprises two key components, SKA-low with frequency range $100-350$MHz, and SKA-mid with frequency range $0.4-13.8$GHz. For axion conversion in the dark halo of our Galaxy, SKA-mid's construction as an array of parabolic dishes offers the best opportunity for detection, its frequency range corresponding to an axion mass of $1.7-57\mu$eV (see Figure 1). The timeline for construction is approximately $10-15$ years, however there exist today two precursor telescopes, the Australian SKA Pathfinder (ASKAP) and the Karoo Array Telescope (MeerKAT), which are already providing new and valuable data. To investigate whether these radio telescopes could indeed contribute to the global search for axion dark matter, we set out below in Section 2 our key considerations for axion conversion in an astrophysical magnetic field, and assess in Section 3 the coupling strength that may be probed by observing the Galactic centre and interstellar medium.

2 Axion two-photon coupling in astrophysical magnetic fields

The photon production rate associated with axion conversion in a magnetic field is well documented in the literature (most notably [10]). We revisit this calculation with the astrophysical environment in mind and find a few key areas for consideration: (1) The spatial profile of the magnetic field plays an important role in determining both the photon production rate and the properties of the real photon produced; (2) The astrophysical environment will contain non-static as well as static fields, and the production of higher energy photons in a strong non-static field is worthy of consideration; and (3) The frame of axion conversion relative to the observer's frame must be taken into consideration when establishing the width of the spectral profile.

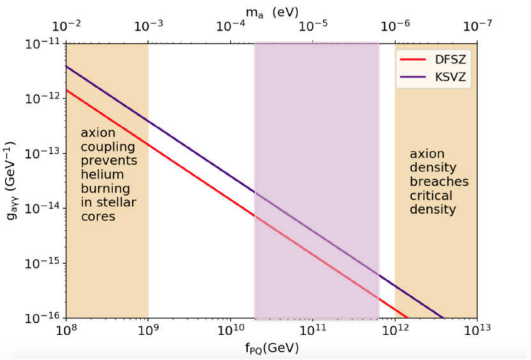

Figure 1: The mass, m_a, and coupling strength, $g_{a\gamma\gamma}$, of the axion are determined by the P-Q symmetry breaking scale, f_{pq}, and constrained by astrophysical observations. The reference to KSVZ and DFSZ relates to the two generally accepted axion models from which its properties are derived, and the pink shaded area shows the breadth of parameter space that could be probed based on the frequency range of SKA-mid.

We find that in considering the non-relativistic cold dark matter axion, the magnetic field is required to provide momentum to the interaction, and as a result only certain modes of the magnetic field contribute to the photon production rate. This is required by energy/momentum conservation and is one of the principal differences with laboratory based experiments seeking to detect the same phenomenon. With the momentum of the axion, $\mathbf{k}_a$, assumed to be negligible, only those modes which satisfy $\Delta E = m_a c^2$ will contribute to the interaction, where $\Delta E = \hbar k_{\gamma'} c - \hbar\omega_{\gamma'}$, $\hbar\omega_{\gamma'}$ is the energy of the virtual photon and $\hbar k_a$ its momentum. In the case of a static field for which $\hbar\omega_{\gamma'} = 0$, this reduces to those modes with $k_{\gamma'} = m_a c/\hbar$. The photon production rate, $\Gamma(N_a)$, for axion conversion in a non-static inhomogeneous field can then be written as,

$$\Gamma(N_a) \approx 2.2 \times 10^{25} \mathrm{Tesla}^{-2}\mathrm{kg}^{-1}\mathrm{ms}^{-2} \left(\frac{\rho_{DM}}{T}\right) \int d^3\mathbf{k}_\gamma \; k_\gamma \left|B(\mathbf{k}_\gamma, \omega_\gamma - \omega_a)\right|^2$$

where T is the time over which the temporal fluctuation of the magnetic field repeats, ρ_{DM} is the dark matter density, and $B(\mathbf{k}_\gamma, \omega_\gamma - \omega_a)$ is the Fourier transform of the classical magnetic field at a given energy and momentum. For a static-field this photon production rate can then be simplified to,

$$\Gamma(N_a) \approx 1.3 \times 10^{20} \mathrm{Tesla}^{-2}\mathrm{kg}^{-1}\mathrm{s}^{-1} \left(\frac{\rho_{DM}}{V}\right) \left|B\left(\frac{m_a c}{\hbar}\right)\right|^2 \quad (1)$$

where V is the volume observed. Important assumptions must be made about the astrophysical environment in order to apply these equations. The magnetic field must be inhomogeneous on scales that can be seen by the axion, and the plasma density must be less than that required for resonance conversion. While there are great uncertainties in the small scale structure of the Galaxy, the average electron density of order 1cm^{-3} and the extremely high plasma density required for resonance conversion of a non-relativistic axion, leads us to believe that there is merit in investigating the use of radio telescopes further.

3 Observing axion conversion in the interstellar medium with the SKA

In order to determine the energy produced in a given region in the Milky Way, we must make an assumption about both the density of dark matter at a given point and the strength and profile of the magnetic field. We use Equation 1 to determine the photon production rate at the Galactic centre and throughout the interstellar medium, making the assumption that the related magnetic field does not change on timescales visible to the axion.

We calculate the density of dark matter using an adjusted NFW profile with a central core density of 10GeVcm^{-3} and a density at Earth of 0.4GeVcm^{-3}. The strength of the magnetic field is assumed to have a strength of 50μG within a radius of 1kpc of the Galactic centre and a profile that reduces radially along the Galactic disk as $r(kpc)^{-1}$. Within each region we then assume that the profile of the magnetic field is turbulent on small scales and can be described by a Kolmogorov spectrum.

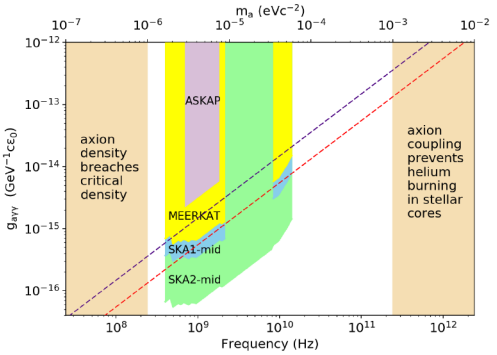

Figure 2: The sensitivity of SKA-mid shows considerable improvement on the pre-cursor telescopes, the Australian SKA Pathfinder (ASKAP) and the Karoo Array Telescope (MeerKAT). In this Figure we show the coupling strength that could be probed by observing the interstellar medium across the frequency range accessible to ASKAP, MeerKAT and SKA-mid. The system temperature of the SKA is minimised between $\sim 2-7$GHz, corresponding to an axion mass of $\sim 8.26-28.91\mu\text{eVc}^{-2}$ and providing a good opportunity for detection of both the KSVZ and DFSZ axion. Figure taken from [11].

To calculate the flux at Earth that results from photons being produced via axion conversion across the interstellar medium, we assume that the energy propagates in all directions and is shared across the surface of a sphere, with radius given by the distance between the region of conversion and the Earth. We also assume that the dark halo of the Milky Way displays no net rotation, and that the Galactic disk is moving through this halo with a rotational velocity at Earth of 220kms^{-1}. Using these assumptions for an axion of mass 2.05μeV the flux at Earth is calculated to be 3.7μJy. The axion signature will be observed as a spectral line with a central frequency of

$\sim$ 500MHz and a width given by the axion velocity and relative frames of the conversion and the observer, in this case $\sim$ 200kHz. The polarisation of the signal should also trace the polarisation of the magnetic field when observing a coherent single source. Such distinguishing features should allow an axion line to be identified from astrophysical foregrounds and other spectral lines. In particular, synchrotron radiation which makes up a large portion of foregrounds at this frequency should have a polarisation perpendicular to the axion signal.

Using this flux, we are able to compare the strength of the axion signal with the limiting sensitivity of SKA-mid. Using only a 24 hour integration time we find that the limiting sensitivity of SKA-mid is 0.04mK, compared to a signal temperature of 1.17mK when utilising the full $(1\text{km})^2$ collecting area of SKA-mid Phase 2 to observe axion conversion in the Galactic centre and interstellar medium. Figure 2 shows the coupling strength that could be probed by such observations, and it is clear that this technology has the potential to open up a new window for the detection of axion dark matter.

4 Acknowledgments

We would like to thank the conference organisers for providing a forum for fruitful discussion. We also thank Prof. Ian McArthur at the University of Western Australia for his invaluable guidance in preparing this work.

5 Bibliography

References

[1] S. Weinberg, Phys. Rev. Lett. **40**, 223 (1978). doi:10.1103/PhysRevLett.40.223

[2] F. Wilczek, Phys. Rev. Lett. **40**, 279 (1978). doi:10.1103/PhysRevLett.40.279

[3] R. D. Peccei and H. R. Quinn, Phys. Rev. Lett. **38**, 1440 (1977). doi:10.1103/PhysRevLett.38.1440

[4] D. A. Dicus, E. W. Kolb, V. L. Teplitz and R. V. Wagoner, Phys. Rev. D. **18**, 1829 (1978). doi:10.1103/PhysRevD.18.1829

[5] D. A. Dicus, E. W. Kolb, V. L. Teplitz and R. V. Wagoner, Phys. Rev. D. **22**, 839 (1980). doi:10.1103/PhysRevD.22.839

[6] G. G. Raffelt and D. S. P. Dearborn, Phys. Rev. D. **36**, 2211 (1987). doi:10.1103/PhysRevD.36.2211

[7] A. Burrows, M. S. Turner and R. P. Brinkmann, Phys. Rev. D. **39**, 1020 (1989). doi:10.1103/PhysRevD.39.1020

[8] J. Preskill, M. B. Wise and F. Wilczek, Phys. Lett. B **120**, 127 (1983). doi:10.1016/0370-2693(83)90637-8

[9] M. Dine and W. Fischler, Phys. Lett. B **120**, 137 (1983). doi:10.1016/0370-2693(83)90639-1

[10] P. Sikivie, Phys. Rev. Lett. **51**, 1415 (1983). doi:10.1103/PhysRevLett.51.1415

[11] K. Kelley and P. J. Quinn, ApJ Lett. **845**, L4 (2017). doi:10.3847/2041-8213/aa808d

First Axion Dark Matter Search with Toroidal Geometry

Byeong Rok Ko

Center for Axion and Precision Physics Research (CAPP), Institute for Basic Science (IBS), Daejeon 34141, Republic of Korea

DOI: http://dx.doi.org/10.3204/DESY-PROC-2017-02/ko_byeong_rok

We report the first axion dark matter search with toroidal geometry. Exclusion limits of the axion-photon coupling $g_{a\gamma\gamma}$ over the axion mass range from 24.7 to 29.1 μeV at the 95% confidence level are set through this pioneering search. Prospects for axion dark matter searches with larger scale toroidal geometry are also given.

1 Introduction

In the last Patras workshop at Jeju Island in Republic of Korea, we, IBS/CAPP, introduced axion haloscopes with toroidal geometry we will pursue [1]. At the end of our presentation, we promised that we will show up at this Patras workshop with "CAPPuccino submarine". The CAPPuccino submarine is a copper (cappuccino color) toroidal cavity system whose lateral shape is similar to a submarine as shown in Fig. 1.

We are now referring to the axion dark matter searches with toroidal geometry at our center as ACTION for "**A**xion haloscopes at **C**APP with **T**oro**I**dal res**ON**ators" and the ACTION in this proceedings is the "simplified ACTION". In this proceedings, we mainly show the first axion haloscope search from the simplified ACTION experiment and also discuss the prospects for larger scale ACTION experiments [2].

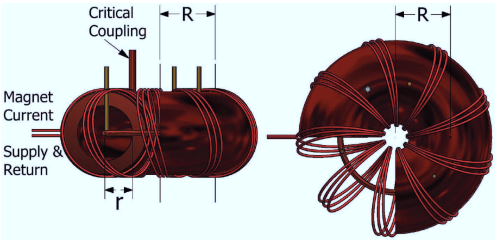

Figure 1: Lateral (left) and top (right) views of the CAPPuccino submarine. Note that it is a cut-away view to show details of the system.

2 Simplified ACTION

The simplified ACTION experiment constitutes a tunable copper toroidal cavity, toroidal coils which provide a static magnetic field, and a typical heterodyne receiver chain. The experiment was conducted at room temperature. A torus is defined by $x = (R + r\cos\theta)\cos\phi$, $y = (R + r\cos\theta)\sin\phi$, and $z = r\sin\theta$, where ϕ and θ are angles that make a full circle of radius R and r, respectively. As shown in Fig. 1, R is the distance from the center of the torus to the center of the tube and r is the radius of the tube.

Our cavity tube's R and r are 4 and 2 cm, respectively, and the cavity thickness is 1 cm.

The frequency tuning system constitutes a copper tuning hoop whose R and r are 4 and 0.2 cm, respectively, and three brass posts for linking between the hoop and a piezo linear actuator that controls the movement of our frequency tuning system. The quasi-TM_{010} (QTM_1) modes of the cavity are tuned by moving up and down our frequency tuning system along the axis parallel to the brass posts. Two magnetic loop couplings were employed, one for weakly coupled magnetic loop coupling and the other for critically coupled magnetic loop coupling, i.e. $\beta \simeq 1$ to maximize the axion signal power in axion haloscope searches [3].

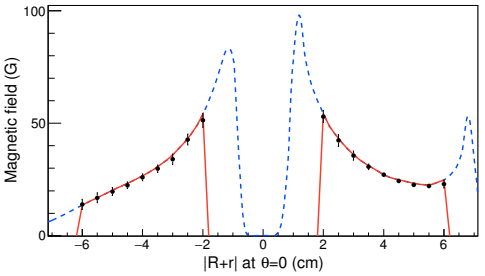

Figure 2: Magnetic field as a function of radial position $|R+r|$ at $\theta = 0$. Dashed (blue) lines are obtained from the finite element method and correspond to the toroidal cavity system, and solid lines (red) correspond to the cavity tube. Dots with error bars are measurement values. The results at positive $R + r$ are along a coil, while those at negative $R+r$ are between two neighboring coils.

A static magnetic field was provided by a 1.6 mm diameter copper wire ramped up to 20 A with three winding turns, as shown in Fig. 1. Figure 2 shows good agreement between measurement with a Hall probe and a simulation [4] of the magnetic field induced by the coils. The B_{avg} from the magnetic field map provided by the simulation turns out to be 32 G.

With the magnetic field map and the electric field map of the QTM_1 mode in the toroidal cavity, we numerically evaluated the form factor of the QTM_1 mode as a function of the QTM_1 frequency, as shown in Fig. 3, where the highest frequency appears when the frequency tuning system is located at the center of the cavity tube, such as in Fig. 1. As shown in Fig. 3, we found no significant drop-off in the form factors of the QTM_1 modes, which is attributed to the absence of the cavity endcaps in toroidal geometry.

Our receiver chain consists of a single data acquisition channel that is analogous to that adopted in ADMX [5] except for the cryogenic parts. Power from the cavity goes through a directional coupler, an isolator, an amplifier, a band-pass filter, and a mixer, and is then measured by a spectrum analyzer at the end. Cavity associates, ν (resonant frequency), and Q_L (quality factor with $\beta \simeq 1$) are measured with a network analyzer by toggling microwave switches. The gain and noise temperature of the chain were measured to be about 35 dB and 400 K, respectively, taking into account all the attenuation in the chain, for the frequency range from 6 to 7 GHz.

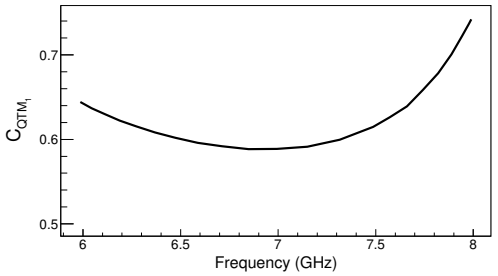

Figure 3: Form factors of the QTM_1 mode of the toroidal cavity as a function of the QTM_1 frequency.

The signal-to-noise ratio (SNR) in the simpli-

fied ACTION experiment is

$$\mathrm{SNR} = \frac{P_{a,g_{a\gamma\gamma}\sim 6.5\times10^{-8}\ \mathrm{GeV}^{-1}}}{P_n}\sqrt{N}, \tag{1}$$

where $P_{a,g_{a\gamma\gamma}\sim 6.5\times10^{-8}\ \mathrm{GeV}^{-1}}$ is the signal power when $g_{a\gamma\gamma} \sim 6.5 \times 10^{-8}$ GeV^{-1}, which is approximately the limit achieved by the ALPS collaboration [6]. P_n is the noise power equating to $k_B T_n b_a$, and N is the number of power spectra, where k_B is the Boltzmann constant, T_n is the system noise temperature which is a sum of the noise temperature from the cavity ($T_{n,\mathrm{cavity}}$) and the receiver chain ($T_{n,\mathrm{chain}}$), and b_a is the signal bandwidth. We iterated data taking as long as $\beta \simeq 1$, or equivalently, a critical coupling was made, which resulted in about 3,500 measurements. In every measurement, we collected 3,100 power spectra and averaged them to reach at least an SNR in Eq. (1) of about 8, which resulted in an SNR of 10 or higher after overlapping the power spectra at the end.

Our overall analysis basically follows the pioneer study described in Ref. [7]. With an intermediate frequency of 38 MHz, we take power spectra over a bandwidth of 3 MHz, which allows 10 power spectra to overlap in most of the cavity resonant frequencies with a discrete frequency step of 300 kHz. Power spectra are divided by the noise power estimated from the measured and calibrated system noise temperatures. The five-parameter fit also developed in Ref. [7] is then employed to eliminate the residual structure of the power spectrum. The background-subtracted power spectra are combined in order to further reduce the power fluctuation. We found no significant excess from the combined power spectrum and thus set exclusion limits of $g_{a\gamma\gamma}$ for $24.7 < m_a < 29.1$ μeV. No frequency bins in the combined power spectrum exceeded a threshold of $5.5\sigma_{P_n}$, where σ_{P_n} is the rms of the noise power P_n. We found σ_{P_n} was underestimated due to the five-parameter fit as reported in Ref. [8] and thus corrected for it accordingly before applying the threshold of $5.5\sigma_{P_n}$.

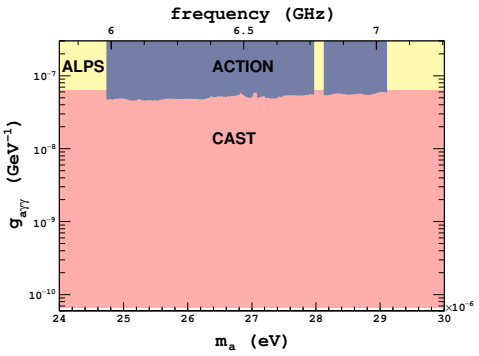

Figure 4: Excluded parameter space at the 95% C.L. by this experiment together with previous results from ALPS [6] and CAST [9]. No limits are set from 6.77 to 6.80 GHz due to with a quasi-TE mode in that frequency region and the TE mode is also confirmed by a simulation [4].

Our SNR in each frequency bin in the combined power spectrum was also combined with weighting according to the Lorentzian lineshape, depending on the Q_L at each resonant frequency of the cavity. With the tail of the assumed Maxwellian axion signal shape, the best SNR is achieved by taking about 80% of the signal and associate noise power; however, doing so inevitably degrades SNR in Eq. (1) by about 20%. Because the axion mass is unknown, we are also unable to locate the axion signal in the right frequency bin, or equivalently, the axion signal can be split into two adjacent frequency bins. On average, the signal power reduction due to the frequency binning is about 20%. The five-parameter fit also degrades the signal power by about 20%, as reported in Refs. [7, 8]. Taking into account the signal power reductions described above, our SNR for $g_{a\gamma\gamma} \sim 6.5 \times 10^{-8}$ GeV^{-1} is greater or equal to 10, as mentioned earlier. The 95% upper limits of the power excess in the combined power spectrum are calculated in units of σ_{P_n}; then, the 95% exclusion limits of $g_{a\gamma\gamma}$ are extracted using $g_{a\gamma\gamma} \sim 6.5 \times 10^{-8}$

GeV^{-1} and the associated SNRs we achieved in this work. Figure 4 shows the excluded parameter space at a 95% confidence level (C.L.) by the simplified ACTION experiment.

3 Prospects for axion dark matter searches with larger scale toroidal geometry

The prospects for axion dark matter searches with two larger-scale toroidal geometries that could be sensitive to the KSVZ [13, 14] and DFSZ [15, 16] models are now discussed. A similar discussion can be found elsewhere [17]. One is called the "large ACTION", and the other is the "small ACTION", where the cavity volume of the former is about 9,870 L and that of the latter is about 80 L. The B_{avg} targets for the large and small ACTION experiments are 5 and 12 T, respectively, where the peak fields of the former and latter would be about 9 and 17 T. Hence, the large and small toroidal magnets can be realized by employing NbTi and Nb_3Sn superconducting wires, respectively. The details of the expected experimental parameters for the ACTION experiments can be found in [2] and Fig. 5 shows the exclusion limits expected from the large and small ACTION experiments.

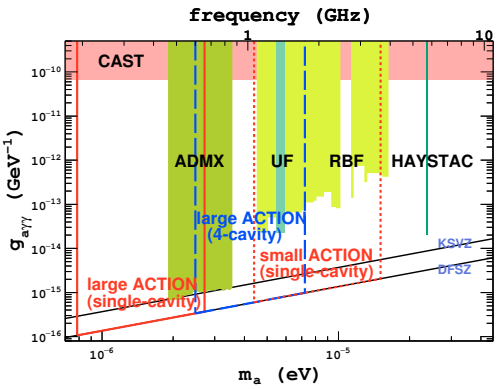

Figure 5: Expected exclusion limits by the large (solid lines with a single-cavity and dashed lines with a 4-cavity) and small (dotted lines with a single-cavity) ACTION experiments. Present exclusion limits [7, 8, 9, 10, 11, 12] are also shown.

4 Summary

In summary, we, IBS/CAPP, have reported
an axion haloscope search employing toroidal geometry using the simplified ACTION experiment. The simplified ACTION experiment excludes the axion-photon coupling $g_{a\gamma\gamma}$ down to about 5×10^{-8} GeV^{-1} over the axion mass range from 24.7 to 29.1 μeV at the 95% C.L. This is the first axion haloscope search utilizing toroidal geometry since the advent of the axion haloscope search by Sikivie [3]. We have also discussed the prospects for axion dark matter searches with larger scale toroidal geometry that could be sensitive to cosmologically relevant couplings over the axion mass range from 0.79 to 15.05 μeV with several configurations of tuning hoops, search modes, and multiple-cavity system.

Acknowledgments

This work was supported by IBS-R017-D1-2017-a00.

References

[1] B. R. Ko, "Contributed to the 12th Patras workshop on Axions, WIMPs and WISPs, Jeju Island, South Korea, June 20 to 26, 2016"; arXiv:1609.03752.

[2] J. Choi, H. Themann, M. J. Lee, B. R. Ko, and Y. K. Semertzidis, Phys. Rev. D **96**, 061102(R) (2017).

[3] P. Sikivie, Phys. Rev. Lett. **51**, 1415 (1983).

[4] http://www.cst.com.

[5] H. Peng *et al.*, Nucl. Instrum. Methods Phys. Res., Sect. A **444**, 569 (2000).

[6] K. Ehret *et al.*, Phys. Lett. B **689**, 149 (2010).

[7] C. Hagmann *et al.*, Phys. Rev. Lett. **80**, 2043 (1998); S. J. Asztalos *et al.*, Phys. Rev. D **64**, 092003 (2001).

[8] B. M. Brubaker *et al.*, Phys. Rev. Lett. **118**, 061302 (2017).

[9] V. Anastassopoulos *et al.* (CAST Collaboration), Nature Physics **13**, 584-590 (2017).

[10] S. DePanfilis *et al.*, Phys. Rev. Lett. **59**, 839 (1987); W. U. Wuensch *et al.*, Phys. Rev. D **40**, 3153 (1989).

[11] C. Hagmann, P. Sikivie, N. S. Sullivan, and D. B. Tanner, Phys. Rev. D **42**, 1297 (1990).

[12] S. J. Asztalos *et al.*, Astrophys. J. Lett. **571**, L27 (2002); Phys. Rev. D **69**, 011101(R) (2004); Phys. Rev. Lett. **104**, 041301 (2010).

[13] J. E. Kim, Phys. Rev. Lett. **43**, 103 (1979).

[14] M. A. Shifman, A. I. Vainshtein, and V. I. Zakharov, Nucl. Phys. B **166**, 493 (1980).

[15] A. R. Zhitnitskii, Sov. J. Nucl. Phys. **31**, 260 (1980).

[16] M. Dine, W. Fischler, and M. Srednicki, Phys. Lett. B **140**, 199 (1981).

[17] Oliver K. Baker *et al.*, Phys. Rev. D **85**, 035018 (2012).

An Improved Signal Model for Axion Dark Matter Searches

Erik W. Lentz[1]

[1] Physics Department, University of Washington, Seattle, WA 98195-1580

DOI: http://dx.doi.org/10.3204/DESY-PROC-2017-02/lentz_erik

To date, most direct detection searches for axion dark matter, such as those by the Axion Dark Matter Experiment (ADMX) microwave cavity search, have assumed a signal shape based on an isothermal spherical model of the Milky Way halo. Such a model is not capable of capturing contributions from realistic infall, nor from a baryonic disk. Modern N-Body simulations of structure formation can produce realistic Milky Way-like halos which include the influences of baryons, infall, and environmental influences. An analysis of the Romulus25 N-Body simulation shows that the axion signals from MW-like halos are narrower than the SHM by nearly a factor of two, which has important implications for cavity searches. An improved signal shape and an account of the relevant halo dynamics are also given. This proceedings largely follows the recent publication by Lentz et al.[14] (L2017).

1 Introduction

The QCD axion is a compelling candidate for the dark matter (DM), with well-bounded parameter space of mass and coupling, Fig.1. Starting at milli-eV masses, there is a bound above which the axion would have been seen in various astrophysical processes [19, 9, 6, 27, 16, 15]. Approaching micro-eV masses, there is a bound below which the (misalignment) creation mechanism would produce more axions than there is dark matter [1, 8, 18, 16]. This lower bound is somewhat soft as axion creation mechanisms can be suppressed in the details of some axion theories [15]. The two diagonal lines represent benchmark axion models. KSVZ represents a theory where the axion couples to hadrons only [12, 22], and DFSZ couples to both hadrons and leptons [7, 28] as consistent with grand unified theories. The search window is then given by the region between KSVZ and DFSZ and the lower and upper mass bounds.

The axion's low mass and feeble couplings lead to unconventional search techniques. An attractive method used to search for axion DM threads a magnetic field through a resonant cavity, stimulating the decay of DM axions into microwaves via an inverse Primakov process parameterized by the Lagrangian

$$\mathcal{L}_{int} = \frac{g_{a\gamma\gamma}}{4\pi} a F \tilde{F} \tag{1}$$

where a is the axion field, F and $\tilde{F}$ are the electromagnetic field strength and its dual, and $g_{a\gamma\gamma}$ is the coupling strength [23]. Nearly all the power from axion decays is transfered into microwaves of frequency set by the decayed axion energy

$$E_\gamma = \hbar\nu = m_a c^2 + m_a v^2/2 \tag{2}$$

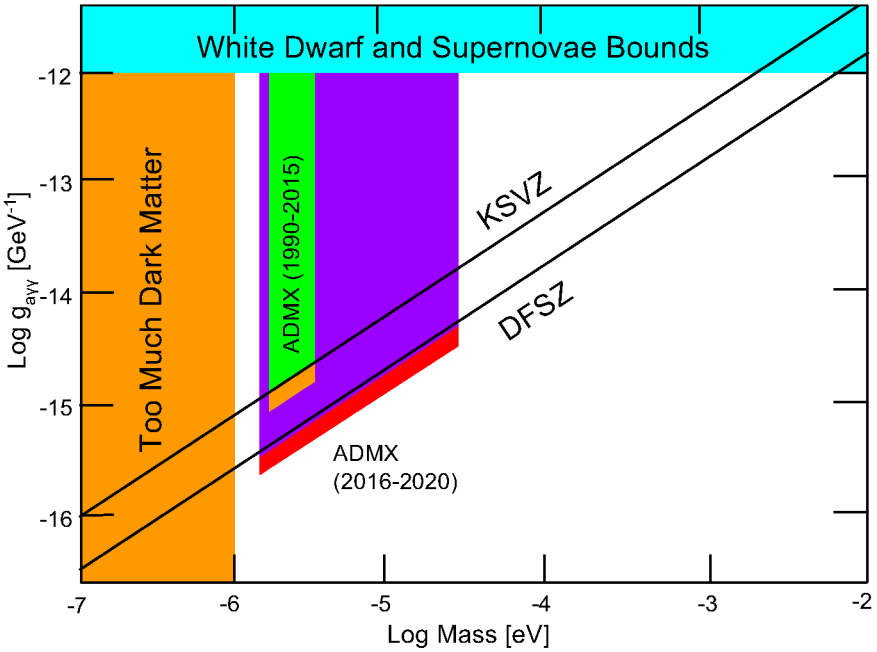

Figure 1: Illustration of the QCD axion parameter space over the plausible DM region, with current astronomical and cosmological constraints, benchmark theories, plus the ADMX limits in green and Generation 2 projections shown in purple Under the new signal model, an increase of the SNR of 1.8 would translate to an improvement in the coupling limit of $\sqrt{1.8}$, illustrated in orange and red respectively.

where m_a is the axion mass, v is the axion speed in the lab frame, and ν is the microwave frequency. The energy distribution of axions is sampled by tuning the cavity over large ranges in frequency, making the microwave power spectrum the figure of interest. The resonant microwaves are detected by a receiver sensitive to sub-yocto-watt power. These experiments can have frequency resolution to a part in 10^9 or better [2], well within the range of resolving fine structure in the axion distribution.

Some axion searches use a filter shape derived from the Standard Halo Model (SHM) despite their good energy resolution [2], which comes from the assumption that the MW halo is given by a thermalized pressure-less self-gravitating sphere of particles. The velocity distribution of the SHM near the Earth is given by a Maxwellian distribution below the escape velocity

$$f_{\vec{v}} \propto e^{-\vec{v}\cdot\vec{v}/2\sigma_v^2} \tag{3}$$

where $\sigma_v = v_c/\sqrt{2}$ [3] and the v_c is the circular speed. The SHM is broadly predictive, but incapable of describing fine structure due to cosmological infall history, interactions with baryonic matter, or axion-specific physics.

Infall history and baryonic interactions in galaxies like the MW can instead be simulated using modern structure-formation techniques. One powerful simulation tool is the N-Body+Smoothed-Particle Hydrodynamics (N-Body+SPH) method. Capable of accurately re-

solving the inner structures of galaxies and their halos using cold dark matter and well-calibrated baryonic models, N-Body+SPH simulations are poised to give accurate models of DM structure for direct searches. This has already been done for WIMPs, which have not yielded significant differences from the SHM [24, 11, 5]. As the energy spectra for cavity axion searches is different from the speed spectra relevant to WIMP nuclear recoil searches, an axion-specific analysis of structure-formation simulations is worthwhile.

2 Approach and Results

This study utilizes the results of the Romulus 25 (R25) N-Body+SPH simulation produced by the UW N-Body Shop [26], based on the ChaNGa N-Body+SPH code. R25 was created on the Blue Waters petascale computing facility. To analyze specific galaxies and halos in R25, the Amiga Halo Finder (AHF) [13] is used to create the catalogue on R25, also at Blue Waters. Finally, the analysis was greatly assisted by the Pynbody N-body analysis software package [17].

R25 describes a 25 Mpc periodic cosmological box filled with DM particles, evolving gas and star particles, and super-massive black holes (SMBHs). The box is placed in a ΛCDM cosmological setting and resolved to $10^5 M_\odot$ particle resolution and 250 pc plummer-equivalent force resolution; these are more than sufficient to resolve the local axion distribution on the kpc scale. R25 is large enough that it has O(30) MW-mass halos at z=0. Such a large set allows for a sampling of galaxies where reduction down to a MW-like sample is quantifiable via the use of filters on a halos catalogue.

The galaxy halos analyzed here are selected using filters in line with the current understanding of MW halo mass, rotational velocity structure, and relatively quiet recent formation history [4, 10, 21] without being so constraining as to limit halo statistics.

$$0.5 \times 10^{12} M_\odot \leq M_{vir} \leq 1.6 \times 10^{12} M_\odot \tag{4}$$

$$R_{vir} \leq 250 \text{ kpc} \tag{5}$$

$$z_{major} \geq 0.75 \tag{6}$$

$$175 \text{ km/s} \leq v_{circ} \leq 275 \text{ km/s} \tag{7}$$

where M_{vir} is the virialized mass, R_{vir} is the enclosing virial radius, and z_{major} is the redshift of last major merger, which is set by the progenitor ratio of 4:1. Several halos experienced no major mergers during the simulation. v_{circ} is the circular velocity in the plane of the galaxy at 8 kpc, which did eliminate several halos from the set satisfying Eqs.4 -6. R25 contains 16 halos which satisfy the filters at $z = 0$, which still cover a wide morphological range.

Terrestrial DM search experiments are moving with respect to the galactic center. The lab is held to be in the galaxy's local standard of rest, approximated as a circular orbit about the center of the galaxy of $r_l = 8$ kpc, coincident with the Sun-MW orbital shape and radius. The solar sample of particles is given by a 2 kpc by 4 kpc toroid about the solar orbit, which is taken to be in the baryonic disk,

$$-2 \text{ kpc} \leq z \leq 2 \text{ kpc} \ , \ r_l - 1 \text{ kpc} \leq r \leq r_l + 1 \text{ kpc} \tag{8}$$

where r_l is chosen to match the MW solar radius of 8 kpc, though the spectral shapes are reasonably robust to the choice of radius. Halo sample energy spectra are formed by calculating the energy for each particle and compiling a normalized histogram over all sample particles.

The orbit speed of the lab is given by setting the acceleration of disk particles at the orbit radius to orbital motion

$$\bar{a}(r_l) = \frac{v_l^2}{r_l} \tag{9}$$

where the RHS is the centripetal acceleration of the lab frame and $\bar{a}$ is the average acceleration at the lab radius. In order to approximate the velocity distribution in a point-like lab, this sample region assumes a cylindrically symmetric, homogeneous, equi-potential, steady-state system within. To evaluate the particles in the lab frame, a Galilean boost is performed on each sample particle using the solar orbital velocity

$$(v_r, v_t, v_z) \rightarrow (v_r, v_t - v_l, v_z) \tag{10}$$

where v_l is taken to be the circular velocity in the presence of DM+baryons at the orbit radius and v_r, v_t, v_z are a particle's radial, tangential, and z-component velocities respectively. The laboratory speed, energy, and other spectra can now be calculated by forming distribution functions over the desired observable.

The lab frame microwave spectra show a marked difference from the SHM, Fig.2. This apparent narrowing and enhancement of the signal is present over all but one of the 16 halos. Also, recall that filters in Eqs.4 -7 allow galaxies which deviate from the MW. Specifically, the galaxies inside halos h32, h34, h36, h44, and h48 have older stars and larger bulges than is expected for the MW. These galaxies lower the mean deviation as they produce spectra preferentially closer to the SHM than the rest of the halos; such halos are still included, as filters based on morphology are not considered here.

The characteristic spectral shape over a wide range of galaxies communicates a level of robustness in the line shape and gives confidence in a signal model based on these spectra. The solid black line of Fig.2 represents the fitted model signal shape. The proposed signal shape keeps a Maxwellian-like form

$$f_\nu \propto \left(\frac{(\nu - \nu_o)h}{m_a T}\right)^\alpha e^{-\left(\frac{(\nu-\nu_o)h}{m_a T}\right)^\beta} \tag{11}$$

where the parameters are constrained to be positive. The best-fit parameters are found using a log-normal local M-estimate using parameter data from individually least-squares-fit halos and are calculated to be $\alpha = 0.36 \pm 0.13$, $\beta = 1.39 \pm 0.28$, and $T = (4.7 \pm 1.9) \times 10^{-7}$, with the errors given by the roots of covariance matrix diagonals.

The narrowing of the observed shapes has implications for axion search experiments. The modeled signal shape has a 90% width—the minimum span which contains 90% of the distribution—that is 1.8 times narrower than the SHM. Such a narrowing of the signal shape would improve a search's SNR by the same factor. For an axion cavity search like ADMX, the increase in sensitivity translates to an improvement in the coupling limit of $\sqrt{1.8}$, suggesting past data runs [2, 25] have near-DFSZ sensitivity, Fig.1.

Observations of local velocity distributions show two main causes of the narrow spectra: bulk rotation and velocity anisotropy. These halo features are very similar to what is expected in a dark disk, where the baryonic disk pulls DM into co-rotating orbits. A DM-only version of R25 (R25D), created before the full SPH run, produces many of the same halos as the full run including our MWs. Analogue halos are pulled to provide insight as to how the baryons contribute to the signal narrowing.

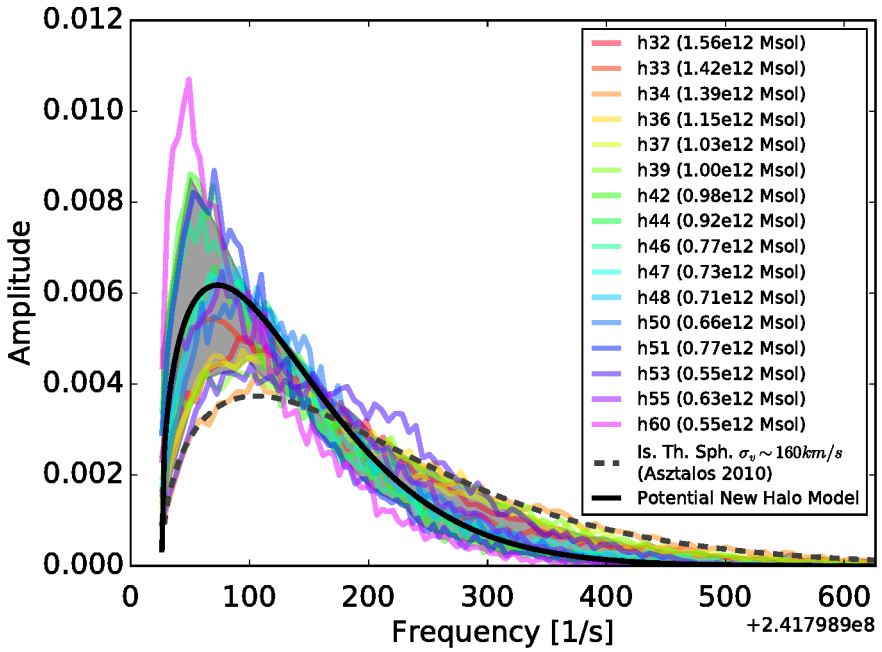

Figure 2: Frequency spectra of MW-like halos from Romulus25 at $z = 0$ and the SHM composed of 10^{-6} eV c^{-2} axions, given by Figure 3 of L2017. The solid black line represents the new shape of the form Eq.11 fitted to to the halos, with the gray representing the data-based error estimate using the two-thirds rule.

The local axion spectra for the R25D halos are not wider but narrower! Fig.3. Bulk motions appear to remain stationary in the median but with decreased dispersion, in contradiction with the existence of a dark disk. Another important kinematical difference becomes apparent when comparing the two halo types: temperature. The effective speed dispersion increases significantly when baryons are included. An increase in circular velocity is also observed. Both the heating and velocity increase are caused by an amplification of the total core mass due to the presence of the galaxy. The sum of these impacts are sufficient to account for the widening factors observed. Baryons don't cause a narrower signal, the signal appears to be narrower in spite of the baryons!

3 Summary

Halos from the Romulus25 simulation show major differences from the SHM in spectra relevant to axion DM searches. The class of galaxies satisfying the above constraints, which include the MW, are observed to produce significantly narrower DM energy spectra than the SHM. A conservative estimate of the new shape is constructed and serves to improve the signal-to-noise of axion cavity searches by 1.8, increasing the sensitivity of previous analyses and improving

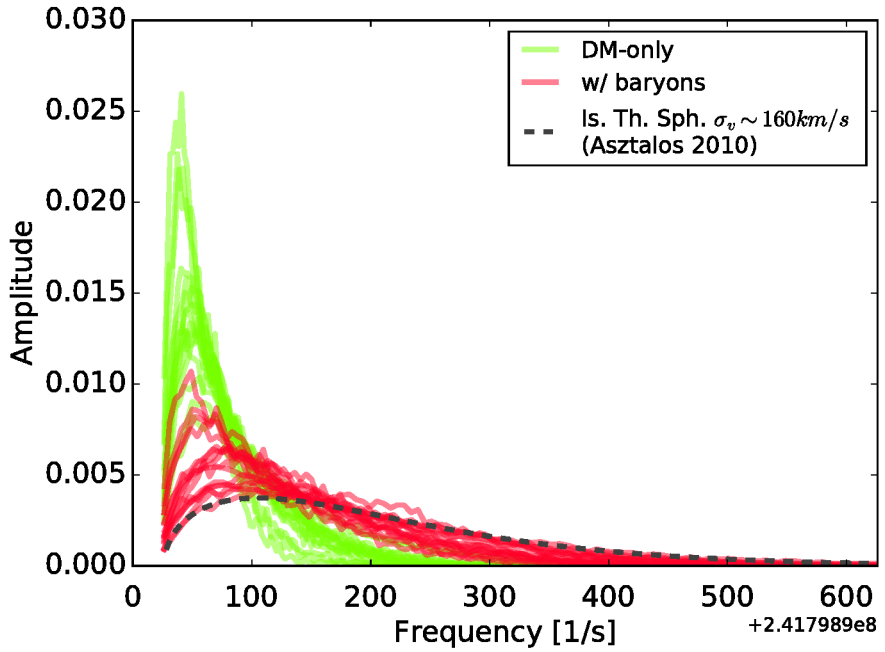

Figure 3: Frequency spectra of MW-like halos from Romulus25 at $z = 0$ and the SHM composed of 10^{-6} eV c^{-2} axions. The solid black line represents the new shape fitted to to the halos, with the gray representing the data-based error estimate using the two-thirds rule.

future observations through the option of scanning at a higher sensitivity or a higher search rate. The kinematical causes for narrowing appears to be bulk rotational motions, velocity anisotropy, and heating. Baryon potentials do not cause this narrowing but serve more to disrupt it. Preliminary studies of the dynamics point to the resonant nature of collision-less gravitational virialization. Research is underway to further classify these dynamical causes.

4 Acknowledgements

I gratefully acknowledge the support of the U.S. Department of Energy office of High Energy Physics, supported by the DOE grant DE-SC0011665. This research is part of the Blue Waters sustained-petascale computing project, which is supported by the National Science Foundation (awards OCI-0725070 and ACI-1238993) and the state of Illinois. Blue Waters is a joint effort of the University of Illinois at Urbana-Champaign and its National Center for Supercomputing Applications. This work is also part of a PRAC allocation support by the National Science Foundation (award number OCI-1144357).

References

[1] Abbott, L. F., Sikivie, P., 1983, PhLB 120, 133

[2] Asztalos, S., Carosi, G., Hagmann, C., et al., 2010, PhRvL, 104d1301A

[3] Binney, J., Tremaine, S., 2008, Princeton Univ. Press, ISBN-13: 978-0-691-13026-2

[4] Bovy, J., Allende Prieto, C., Beers, T., et al., 2012, ApJ, 759, 131

[5] Bozorgnia, N., Calore, F., Schaller, M., et al., 2016, JCAP, 05, 024B

[6] Corsico, A., Althaus, L., L., Romero, A., et al., 2012, JCAP 1212, 010

[7] Dine, M., Fischler, W., Srednicki, M., 1981, PhLB, 104, 199D

[8] Dine, M., Fischler, W., 1983, PhLB 120, 137

[9] Isern, J., Garcia-Berro, E., Althaus, L., et al., 2010, A&A, 512A, 86I

[10] Kafle, P., Sharma, S., Lewis, G., Bland-Hawthorn, J., 2012, ApJ, 761, 98

[11] Kelso, C., Savage, C., Valluri, M., et al., 2016, JCAP, 08, 071K

[12] Kim, J., 1979, PhRvL, 43, 103K

[13] Knollmann, S., Knebe, A., 2009, ApJS, 182, 608K

[14] Lentz, E., Quinn, T., Rosenberg, L., Tremmel, M., 2017, ApJ, 845, 121L

[15] Marsh, D., 2016, PhR, 643, 1M

[16] C. Patrignani et al. (Particle Data Group), 2016, Chin. Phys. C, 40, 100001

[17] Pontzen, A., Roškar, R., Stinson, G., Woods, R., 2013, pynbody:N-Body/SPH analysis for python, Astrophysics Source Code Library

[18] Preskill, J., Wise, M. B., Wilczek, F., 1983, PhLB 120, 127

[19] Raffelt, G. G., 2008, LNP, 741, 51R

[20] Reid, M. J., Menten, K. M., Brunthaler, A., et al., 2014, ApJ, 783, 130R

[21] Ruchti, G., Read, J., Feltzing, S., et al., 2015, MNRAS, 450, 2874

[22] Shifman, M., Vainshtein, A., Zakharov, V., 1980, NuPhB, 166, 493S

[23] Sikivie, P., 1983, PhRvL, 51, 1415

[24] Sloane, J., Buckley, M., Brooks, A., et al., 2016, ApJ, 831, 93S

[25] Stern, I., ADMX, ADMX-HF Collaborations, 2014, AIPC, 1604, 456S

[26] Tremmel, M., Karcher, M., Governato, F., et al., 2017, MNRAS, 470, 1121T

[27] Viaux, N., Catelan, M., Stetson, P. B., et al., 2013, A&A, 558, 12V

[28] Zhitnitsky, A., 1980, Sov. J. Nucl. Phys., 31, 260

Axions and ALPs: a very short introduction

David J. E. Marsh[1,2]

[1]Department of Physics, King's College London, United Kingdom.
[2]Institut für Astrophysik, Georg-August Universitat, Göttingen, Germany.

DOI: http://dx.doi.org/10.3204/DESY-PROC-2017-02/marsh_david

The QCD axion was originally predicted as a dynamical solution to the strong CP problem. Axion like particles (ALPs) are also a generic prediction of many high energy physics models including string theory. Theoretical models for axions are reviewed, giving a generic multi-axion action with couplings to the standard model. The couplings and masses of these axions can span many orders of magnitude, and cosmology leads us to consider several distinct populations of axions behaving as coherent condensates, or relativistic particles. Light, stable axions are a mainstay dark matter candidate. Axion cosmology and calculation of the relic density are reviewed. A very brief survey is given of the phenomenology of axions arising from their direct couplings to the standard model, and their distinctive gravitational interactions.

1 Theory of Axions

1.1 The QCD Axion

The QCD axion was introduced by Peccei & Quinn [1], Weinberg [2], and Wilczek [3] (PQWW) in 1977-78 as a solution to the CP problem of the strong interaction. This arises from the Chern-Simons term:

$$\mathcal{L}_{\theta\mathrm{QCD}} = \frac{\theta_{\mathrm{QCD}}}{32\pi^2}\mathrm{Tr}\; G_{\mu\nu}\tilde{G}^{\mu\nu}\,, \tag{1}$$

where G is the gluon field strength tensor, $\tilde{G}^{\mu\nu} = \epsilon^{\alpha\beta\mu\nu}G_{\alpha\beta}$ is the dual, and the trace runs over the colour $SU(3)$ indices. This term is called topological since it is a total derivative and does not affect the classical equations of motion. However, it has important effects on the quantum theory. This term is odd under CP, and so produces CP-violating interactions, such as a neutron electric dipole moment (EDM), d_n. The value of d_n produced by this term was computed in Ref. [4] to be

$$d_n \approx 3.6\times10^{-16}\theta_{\mathrm{QCD}}\, e\ \mathrm{cm}\,, \tag{2}$$

where e is the charge on the electron. The (permanent, static) dipole moment is constrained to $|d_n| < 3.0\times10^{-26}\, e\,\mathrm{cm}$ (90% C.L.) [5], implying $\theta_{\mathrm{QCD}} \lesssim 10^{-10}$.

If there were only the CP-conserving strong interactions, then θ_{QCD} could simply be set to zero by symmetry. In the real world, and very importantly, the weak interactions violate CP [6]. By chiral rotations of the quark fields, we see that the physically measurable parameter is

$$\theta_{\mathrm{QCD}} = \tilde{\theta}_{\mathrm{QCD}} + \arg\,\det M_u M_d\,, \tag{3}$$

where $\tilde{\theta}$ is the "bare" (i.e. pure QCD) quantity and M_u, M_d are the quark mass matrices. Thus the smallness of $\theta_{\rm QCD}$ implied by the EDM constraint is a fine tuning problem since it involves a precise cancellation between two dimensionless terms generated by different physics.

The famous PQ solution to this relies on two ingredients: the Goldstone theorem, and the presence of *instantons* in the QCD vacuum. A global chiral $U(1)_{\rm PQ}$ symmetry, is introduced, under which some quarks are charged, inducing a chiral anomaly for $U(1)_{\rm PQ}$, the colour anomaly $\mathcal{C}$. The PQ symmetry is spontaneously broken by a complex, scalar field. The Goldstone boson is ϕ. The vacuum expectation value (VEV) of the field to be $f_a/\sqrt{2}$ to give canonical kinetic terms. f_a is known as the axion "decay constant".

An anomalous chiral rotation by ϕ/f_a of the quarks changes the fermion measure in the path integral, and leads to a change in the action:

$$S \to S + \int d^4x \frac{\mathcal{C}}{32\pi^2}\frac{\phi}{f_a}\mathrm{Tr}\, G_{\mu\nu}\tilde{G}^{\mu\nu}\,. \tag{4}$$

Due to the shift symmetry of the axion (Goldstone of $U(1)_{\rm PQ}$) the action only contains terms $\partial\phi$ and we are free to shift the axion field by an arbitrary constant and absorb the value of $\theta_{\rm QCD}$ by a field redefinition. The physical observable related to CP violation in the strong interactions is given by ϕ/f_a, which is *dynamical*.

As promised, the final ingredient of the PQ theory comes from instantons. In the dilute instanton gas (DIG, e.g. Ref. [7]) approximation the vacuum energy is $E_{\rm vac} \propto (1-\cos\mathcal{C}\theta)$. There are $\mathcal{C}$ distinct vacua, which lead to $\mathcal{C} = N_{\rm DW}$ distinct types of domain wall solution [8]. The vacuum energy dependence means that we can write a quantum effective action that includes a potential for the axion. The axion mass is [2, 3]:

$$m_{a,\rm QCD} \approx 6\times 10^{-6}\ \mathrm{eV}\frac{10^{12}\ \mathrm{GeV}}{f_a/\mathcal{C}}\,, \tag{5}$$

The axion potential is $V(\phi) = m_a^2(T)f_a^2U(\theta)$ where T is temperature and $U(\theta)$ is a dimensionless periodic function. It is common to parameterise the dependence by a power law:

$$m_a(T) = m_{a,0}\left(\frac{T}{\Lambda_{\rm QCD}}\right)^{-n}\quad;\quad (T \gg \Lambda_{\rm QCD})\,, \tag{6}$$

with the mass approaching the zero temperature value for $T < \Lambda_{\rm QCD}$. At lowest order the DIG gives $n = 4$ for QCD in the standard model [9]. Lattice QCD calculations [10, 11] are consistent with the DIG at high temperature, while the low temperature behaviour is better fit by $n = 3.55 \pm 0.3$.

The axion couples to electromagnetism:

$$\mathcal{L}_{\rm int} \supset -\frac{g_{\phi\gamma}}{4}\phi F_{\mu\nu}\tilde{F}^{\mu\nu}\,,\quad g_{\phi\gamma} = \frac{\alpha_{\rm EM}}{2\pi f_a}\left(\mathcal{E} - \mathcal{C}\frac{2}{3}\cdot\frac{4+m_u/m_d}{1+m_u/m_d}\right)\,. \tag{7}$$

The first half of the interaction is allowed for any ALP with $U(1)_{\rm EM}$ anomaly $\mathcal{E}$, with the $\mathcal{C}$ part generic for the QCD axion. The EM interaction mediates axion decay to two photons with lifetime:

$$\tau_{\phi\gamma} = \frac{64\pi}{m_a^3 g_{\phi\gamma}^2} \approx 130\ \mathrm{s}\left(\frac{\mathrm{GeV}}{m_a}\right)^3\left(\frac{10^{-12}\ \mathrm{GeV}^{-1}}{g_{\phi\gamma}}\right)^2\,. \tag{8}$$

The PQWW axion is excluded (see e.g. Ref. [12]). Viable QCD axion models are split into two canonical types: "KSVZ" [13, 14], which mediate the anomaly through additional heavy quarks, and "DFSZ" [15, 16] which mediate the anomaly through the standard model quarks. There are, however, a large number of possible variations on these themes, which allow a wide range of possible couplings between the axion and the standard model [17], even in the restricted class of a single axion with mass arising from QCD instantons alone. Theories of multiple ALPs, to which we now turn in a string theory context, allow for even more variation.

1.2 Axions in Supergravity and String Theory

Consider the ten dimensional effective supergravity action for a p-form field A_p with field strength $F_{p+1} = \mathrm{d}A_p$:[1]

$$S_{10\mathrm{D}} = -\frac{1}{2}\int F_{p+1} \wedge \star F_{p+1}\,. \tag{9}$$

We dimensionally reduce this action on a 6-manifold X by writing the field A_p as a sum of *harmonic* p-forms on X, which form a complete basis:

$$A_p = \sum_i^{b_p} a_i(x)\omega_{p,i}(y)\,. \tag{10}$$

The co-orindates x are in the large $3+1$ dimensions, while y are in the compact dimensions of X. The fields a_i are the axion fields, which appear as pseudo-scalars in the dimensionally reduced action, with a shift symmetry descending from the gauge invariance of F_{p+1}.

The sum in Eq. (10) extends over the number of harmonic p-forms on X, the pth Betti number, b_p. For standard string theory compactifications [25], the Betti numbers are given by the Hodge numbers $h_{1,1}$ and $h_{1,2}$ (see e.g. Ref. [22]). The properties of such manifolds have been studied in great detail [26, 27]. For example, in the database of Ref. [28, 29] there is a peak in the distribution near $h_{1,1} = h_{1,2} \approx 30$, implying that *a random Calabi-Yau manifold constructed in this way is overwhelmingly likely to contain of order 30 axions.* This is the origin of the common lore that "string theory predicts a large number of ALPs".

Consider Type-IIB theory compactified on orientifolds [30]. The axion kinetic term is:

$$S_{4\mathrm{D}} = -\frac{1}{8}\int \mathrm{d}a_i \mathcal{K}_{ij} \wedge \star \mathrm{d}a_j\,; \quad \mathcal{K}_{ij} = \frac{\partial^2 K}{\partial\sigma_i \partial\sigma_j}\,, \tag{11}$$

where σ_i are the moduli, and K is the Kähler potential. By canonically normalising the a fields as $f_a^2(\partial a)^2$ we see that the decay constants are the eigenvalues of the Kähler metric and they scale like $f_a \sim M_{pl}/\sigma$.

Axion masses arising from a non-Abelian gauge group (just like in QCD) contribute to the potential [20] $V(\phi) = -m_{\mathrm{SUSY}}^2 M_{pl}^2 e^{-S_{\mathrm{inst}}}\cos(\phi/f_a)$. The axion mass is exponentially sensitive to the instanton action, and scales as $m_a \sim m_{\mathrm{SUSY}}\frac{M_{pl}}{f_a}e^{-S_{\mathrm{inst}}/2}$, with m_{SUSY} the scale of supersymmetry breaking. "Typical" instanton actions $S_{\mathrm{inst.}} \sim \mathcal{O}(100)$ [20] lead to *parametrically light axions.* The instanton action itself scales with the gauge coupling of the group, which is determined by the moduli and scales as $S_{\mathrm{inst}} \sim \frac{1}{g^2} \sim \sigma^2$. Thus, as the different moduli take different values, so *the axion masses can span many orders of magnitude.*

[1] Differential form notation for the uninitiated physicist is introduced in Refs. [18, 19]. For more details on axions in stirng theory, see Refs. [20, 21, 22, 23, 24].

1.3 The Multi Axion Effective Action

The paramteric scalings above are a useful guide to think about axions in string theory, and are the essential basis for the popular phenomenology of the "string axiverse" [31]. However, a theory of multiple ALPs, whether it be inspired by string theory or not, must account for the fact that both the kinetic matrix (which may or may not be the Kähler metric) and the mass matrix are indeed matrices. Thus, the distributions of axion masses and decay constants are determined not by simple scalings for a single particle, but by the properties of the eigenvalues of (possibly large, possibly random) matrices [32, 33].

The general action after chiral symmetry breaking, and below all PQ scales, moduli masses, and the compactification scale is:

$$\begin{aligned}\mathcal{L} = &- K_{ij}\partial_\mu\theta_i\partial^\mu\theta_j - \sum_{n=1}^{N_{\rm inst.}} \Lambda_n U_n(\mathcal{Q}_{i,n}\theta_i + \delta_n) \\ &- \frac{1}{4}c_i^{\rm EM}\theta_i F_{\mu\nu}\tilde{F}^{\mu\nu} - \frac{i}{2}c_i^d\theta_i\bar{N}\sigma_{\mu\nu}\gamma_5 N F^{\mu\nu} \\ &+ c_i^N\partial_\mu\theta_i(\bar{N}\gamma^\mu\gamma_5 N) + c_i^e\partial_\mu\theta_i(\bar{e}\gamma^\mu\gamma_5 e) \end{aligned} \tag{12}$$

The first term is the general kinetic term which includes mixing of different axions. I have considered only the coupling of axions to the light degrees of freedom of the standard model excluding neutrinos, since these are the ones relevant for experiment.

The second term is the most general instanton potential, with U_n an arbitrary periodic function. The sum extends over the number of instantons. The matrix $\mathcal{Q}$ is the instanton charge matrix (see e.g. Ref. [34]). For *any* theory of quantum gravity, there always exists the so-called "axion wormhole" instanton [35, 36] and thus $N_{\rm inst} \geq N_{\rm ax}$. We allow arbitrary phases for each instanton, some of which can be absorbed by shifts in the axions, leaving $N_{\rm inst} - N_{\rm ax} \geq 0$ physical phases.

Diagonalising the kinetic term first by the rotation matrix U, we see that the decay constants are given by the eigenvalues: $\vec{f_a} = \sqrt{2{\rm eig}(K)}$. The masses are found by diagonalising the matrix $\tilde{M} = 2{\rm diag}(1/f_a)UMU^T{\rm diag}(1/f_a)$ with a rotation V, where M is the mass matrix of Eq. (12). To assess whether this theory still solves the strong CP problem, we must consider the linear combination of axions that couples to the neutron EDM, its effective potential, and its VEV. Additional instantons, and other contributions to the potential, can spoil the solution by shifting the minimum. In the cosmological evolution of the axion field the temperature dependence of each term must also be considered.

Often such a spoiling of the axion symmetry is thought of in terms of the contribution of Planck suppressed operators to the action, under the common lore that "quantum gravity violates all continuous global symmetries" [37]. Understanding the axion wormhole instanton leads to a more subtle view of this point, since the symmetry breaking is in fact non-perurbative [38, 36].

2 Axion Cosmology

2.1 Axion Populations

There are four sources of cosmic axion energy density:

- Coherent displacement of the axion field. This accounts for the so-called misalignment populations of dark matter axions, and also for axion quintessence and axion inflation.
- Axions produced via the decay of a topological defect. The topological defect is a configuration of the PQ field. When the defect decays, it produces axions.
- Decay of a parent particle. Heavy particles such as moduli can decay directly into axions. If the mass of the parent is much larger than the axion, then the produced particles are relativistic.
- Thermal production. Axions are coupled to the standard model. If the couplings are large enough, a sizeable population of thermal axions is produced.

While the first two populations are traditionally thought of as distinct, in fact they are not. In a complete classical simulation of the defects directly from the PQ field, axion production is captured by the coherent field oscillations set up when the defect becomes unstable. The reason for the separation is that defects such as strings are sometimes more easily simulated using an effective description such as the Nambu-Goto action, in which case string decay and axion production must me added in as an additional effect.

These different axion populations manifest different phenomenology in cosmology:

- Coherent effects. The axion field only behaves as cold, collisionless particles on scales larger than the coherence length. This leads to wavelike effects on scales of order the de Broglie wavelength, and "axion star" formation that both distinguish axions from weakly interacting massive particles. These effects are particularly pronounced when the axion mass is very small, $m_a \sim 10^{-22}$ eV [39, 40, 41, 42].
- Theoretical uncertainty in the relic density. If the topological defects play a significant role in axion production (i.e. if the PQ symmetry is broken after inflation), then the complex numerical calculations involved in simulating their decay lead to uncertainty in the relic density from different methods.
- The cosmic axion background. Relativistic axions produced by the decay of a parent will contribute to the "effective number of neutrinos", $N_{\rm eff}$, for e.g. cosmic microwave background and BBN constraints. Magnetic fields can also convert these axions into photons, with observable signatures [43, 44, 45].
- Thermal axions. If the axion is relativistic when it decouples then it can contribute as hot dark matter. Constraints on hot dark matter are similar to bounds on massive neutrinos, and limit $m_a < 0.53 \to 0.62$ eV (depending on the analysis) for this population [46, 47, 48, 49, 50, 51, 52]. For the QCD axion this is not a competitive constraint on f_a compared to bounds from the couplings (see Section 3.1).

2.2 Cosmic Epochs

Two important epochs define the cosmological evolution of the axion field: PQ symmetry breaking, and the onset of axion field oscillations. The first process is best thought of as thermal (during inflation the distinction is more subtle), while the second process is non-thermal. We recall that during radiation domination the temperature and Hubble rate are related by

$$H^2 M_{pl}^2 = \frac{\pi^2}{90} g_{\star,\mathrm{R}}(T) T^4 \,, \tag{13}$$

where $g_{\star,\mathrm{R}}$ is the effective number of relativistic degrees of freedom (a useful analytic fit can be found in the Appendix of Ref. [53]). Once $g_\star$ becomes fixed at late times, the temperature simply falls as $1/a$ during the later epochs of matter domination and Λ domination. The factor of M_{pl} in Eq. (13) leads to a large hierarchy between H and T, separating the scales of thermal and non-thermal phenomena.

2.2.1 PQ Symmetry Breaking

Spontaneous symmetry breaking (SSB) occurs when the temperature of the PQ sector falls below the critical temperature, $T_{\mathrm{PQ}} < T_c \approx f_a$ (for more details on the thermal field theory, see Ref. [54] and references therein). Whether SSB occurs before or after the large scale initial conditions of the Universe were established (for concreteness we will assume inflation, but the same logic applies for other theories) divides axion models into two distinct classes of initial conditions:

- **Scenario A**: SSB during the ordinary thermal evolution of the Universe.
- **Scenario B**: SSB before/during inflation (or whatever).

The temperature of the PQ sector must be determined. During inflation, the relevant temperature is the Gibbons-Hawking temperature, $T_{\mathrm{GH}} = H_I/2\pi$, where H_I is the inflationary Hubble rate.[2] The bound on the CMB tensor-to-scalar ratio limits $T_{\mathrm{GH}} < 8.2 \times 10^{12}$ GeV [55, 56]. If the maximum thermalization temperature after inflation does not exceed this (or parameteric resonance does not restore the PQ symmetry [54]), then *there is a maximum possible f_a relevant to Scenario A*, of order 8.2×10^{12} GeV.

The full inhomogeneous evolution of the PQ field in Scenario A must be followed in full detail to compute the perturbation spectrum and axion relic density. In principle this is completely determined, though the complexity of the calculation, involving string and domain wall decay, means that computational approximations and assumptions have historically lead to disagreement on this front [57, 58, 59, 60]. For some modern calculations, see e.g. Refs. [61, 62]. The small-scale perturbations from SSB have relatively large amplitude and can form gravitationally bound clumps of axions on small scales known as "miniclusters" [63] with a variety of observational consequences [64, 65, 66, 67, 68, 69, 70, 71, 72, 73, 74, 75, 76].

In Scenario B the axion field evolution is much easier to compute thanks to the simplifying power of inflation, which smooths the field, leaving only small amplitude fluctuations that can be evolved using perturbation theory. The smooth background evolution is specified by the *random* initial misalignment angle, θ_i. This means that the relic density is essentially free parameter, depending on (m_a, f_a, θ_i).

A constraint on Scenario B emerges from the perturbation spectrum: scale-invariant isocurvature. The amplitude is fixed by H_I and is directly proportional to the inflationary tensor-to-scalar ratio, r_T. CMB constraints on this type of isocuvature (e.g. Refs. [77, 78]) imply that most (but not all) axion models in Scenario B are inconsistent with an observably large value of r_T [79, 80, 81, 82].

[2] More precisely, the Hubble rate when the pivot scale of primordial initial conditions became larger than the horizon.

	Scenario A	Scenario B
Relic Density	No free parameters. Complex Calculation.	Simple calculation. Depends on $\theta_i \in [0, \pi]$.
Perturbations*	Small-scale minicluster formation.	Scale-invariant uncorrelated isocurvature.
Notes	Domain wall problem.	Must occur for large f_a.

Table 1: The main differences between the two scenarios for axion initial conditions. (* in addition to the usual scale-invariant adiabatic mode)

2.2.2 Axion Field Evolution

The second important epoch for axion evolution is the onset of oscillations. The axion equation of motion is:

$$\Box\phi - \partial_\phi V = 0\,. \tag{14}$$

Taking the homogenous part in a Friedmann-Laamitre-Robertson-Walker background, and expanding the potential to quadratic order:

$$\ddot{\phi} + 3H\dot{\phi} + m_a^2(T)\phi = 0\,. \tag{15}$$

For $m_a^2\phi^2 \gg 3H\dot{\phi}$ we have $\dot{\phi} \sim m_a\phi$ and so clearly $H \sim m_a$ separates the regimes of overdamped and underdamped motion of the axion field.

The Hubble rate, H, decreases with increasing time (decreasing temperature) while the axion mass increases for increasing time (decreasing temperature). It is customary to define the oscillation temperature implicitly $3H(T_{\rm osc}) = m_a(T_{\rm osc})$.

For $T \gg T_{\rm osc}$ the axion field is overdamped: the field hardly moves and the energy density contributes to the effective cosmological constant: $\phi \sim$ const.. For $T \ll T_{\rm osc}$ the axion mass is dominant and the field undergoes damped harmonic motion behaving as non-relativistic matter [83, 84, 85, 86, 87]: $\phi \sim a^{-3/2}\cos m_a t$.

From the Friedmann equation in radiation domination, Eq. (13), we have that $T \propto \sqrt{HM_{pl}}$. Thermally coupled particles become non-relativistic when $T < m$. Axion oscillations are a *non-thermal phenomenon*: we are equating the axion mass to the Hubble scale, and we do not actually care what the temperature of the standard model sector is. The largeness of M_{pl} mean that axions typically begin oscillating for $T \gg m_a$, becoming non-relativistic at a much higher temperature than would a thermal particle of the same mass. This hierarchy of scales explains the relationship between the phenomenology of fuzzy DM and warm DM (see Section 3.2).

2.3 The Axion Relic Density

The axion energy density is found from the energy-momentum tensor, $T_{\mu\nu}$, with $\rho = -T^0{}_0$. For the homogeneous component this gives $\bar{\rho}_a = \frac{1}{2}\dot{\phi}^2 + V(\phi)$. The relic density in axions is defined as the present day energy density relative to the critical density, $\Omega_a h^2 = \bar{\rho}(z=0)/3M_H^2M_{pl}^2$, where we have used the reference Hubble rate, M_H, defined from $H_0 = 100h$ km s^{-1} Mpc^{-1}.

The exact calculation of the relic density in Scenario B is:

- Find $T_{\rm osc}$: $AH(T_{\rm osc}) = m_a(T_{\rm osc})$.
- Compute the energy density at $T_{\rm osc}$ from the (numerical) solution of the equation of motion for θ up to this time: $\rho = f_a^2\dot{\theta}^2/2 + m_a(T_{\rm osc})^2 f_a^2 U(\theta)$.

- Redshift the *number density*, $n_a = \rho_a/m_a$, as non-relativistic matter from this point on (normalising the scale factor to $a(z=0)=1$): $n_a(z=0) = m_a(T_{\rm osc}) f_a^2 \theta_i^2 / 2a(T_{\rm osc})^3$. The scale factor can be computed using conservation of entropy (see e.g. Ref. [88]).

- Compute the energy density: $\rho(z=0) = n_a(z=0) m_a(T_0)$, where T_0 is the temperature today.

The choice of A in the first bullet point is key to the accuracy of the calculation. In a full numerical solution we should take A large enough that the field has undergone many oscillations, and that indeed we are in the harmonic regime where n_a is adiabatically conserved. As long as A is thus chosen large enough, then with the numerical solution for θ the other steps are essentially exact.

For *analytic approximations*, we typically take $A = 3$ and approximate the axion energy in the second bullet point as being exactly the initial value for a quadratic potential: $\rho_i = m_a(T_{\rm osc})^2 f_a^2 \theta_i^2/2$. Making these approximations, and using the temperature evolution of the mass consistent with the QCD axion leads to the standard formulae approximating the relic density that can be found in e.g. Refs. [89, 90]. For a constant mass ALP with a quadratic potential, see Ref. [91].

The relic density depends on the mean square axion field $\langle \phi^2 \rangle = f_a^2 \theta_i^2 + H_I^2/(2\pi)^2$, and the scale-invariant isocurvature perturbations contribute to the axion abundance. It is standard to also include an "anharmonic correction factor", $f_{\rm an}(\theta)$, due to the delayed onset of oscillations when $\theta \sim \pi$ [92]. Fits for this can be found in e.g. Ref. [93], but nothing is a substitute for direct numerical solution.

It is interesting to observe that values of the decay constant that are natural in a variety of string-inspired models, $f_a \sim 10^{16-17}$ GeV, provide the correct relic density of axions for masses of the order $m_a = 10^{-18-22}$ eV [31, 91, 90, 42]. This happens to be the mass range of fuzzy DM which is accessible to tests from galaxy formation, and displays interesting signatures that could allow it to be distinguished from standard cold DM (see Section 3.2).

The relic density computation in Scenario A is far more involved. The full calculation requires solving the inhomogeneous axion equation of motion, which accounts for string and domain wall decay. For $N_{\rm DW} = 1$, these effects can be parameterised using a single rescaling of the homogeneous solution by $(1+\alpha_{\rm dec})$, with the simulations of Ref. [94] favouring $\alpha_{\rm dec.} = 2.48$ for the QCD axion. We fix the misalignment to $\theta_i = \pi/\sqrt{3}$ and introduce another factor $c_{\rm an.} \approx 2.1$ for averaged anharmonic effects fit from numerical solutions [94, 73].

3 Axion Phenomenology

3.1 Couplings

Axion couplings to the standard model have a number of effects that allow the coupling strength to be constrained in the lab and from astrophysics. A thorough review of all experimental constraints on axions is given in Ref. [95]. Global fits are presented in Ref. [96]. A review of all constraints on the photon coupling is given in Ref. [97]. Briefly, some relevant phenomena are:

- Stellar evolution. Axions can be produced from standard model particles inside stars. The axions are very weakly interacting and thus easily escape the stars and supernovae, offering an additional cooling channel. The physics and constraints are reviewed by Raffelt

in Refs. [98, 99]. A rather robust bound comes from the ratio of horizontal branch stars to red giants found in globular clusters, which bounds the axion photon coupling $g_\gamma < 6.6 \times 10^{-11}$ GeV^{-1} [100]. There is also the "white dwarf cooling hint" for axions: excess cooling of white dwarfs might be explained by axion emission via the coupling g_e [101].

- Axion mediated forces. The pseudoscalar couplings g_N and g_e mediate a spin-dependent force between standard model particles [102]. Constraints on these forces in the laboratory are not very strong compared to the bounds from stellar astrophysics [103]. However, the proposed "ARIADNE" experiment using nuclear magnetic resonance will make substantial improvements, and could even detect the QCD axion for 10^9 GeV $\lesssim f_a \lesssim 10^{12}$ GeV [104].

- "Haloscopes" and other dark matter detection techniques. Using the axion-photon interaction, g_γ, dark matter axions can be turned into photons in the presence of magnetic fields inside resonant microwave cavities [105]. The ADMX experiment is the leader in such constraints [106], but many new proposals discussed at this conference will soon also enter the game, including the ADMX high frequency upgrade. Notable new techniques that do not rely on the microwave cavity include the use of resonating circuits [107] and the ABRACADABRA proposal [108]; nuclear magnetic resonance and the CASPEr proposal [109, 110]; and dielectric dish antenna and the MADMAX proposal [111]. Together, these proposals promise to cover almost the entire parameter space for QCD axion dark matter with $f_a \lesssim 10^{16}$ GeV. It truly is an exciting time!

- Axion decays. As noted in Eq. (8) the axion-photon interaction allows axions to decay. Heavy axions decay on cosmological time scales, and are constrained by the effects on the CMB anisotropies, BBN, and CMB spectral distortions [112, 113, 114]. The strongest constraint comes from the deuterium abundance. Axions and ALPs are generally excluded for masses and lifetimes 1 keV $\lesssim m_a \lesssim$ 1 GeV and 10^{-4} s $\lesssim \tau_{\phi\gamma} \lesssim 10^6$ s

- Axion-photon conversion in astrophysics. Magnetic fields in clusters convert photons into axions and alter the spectrum of the X-ray photons arriving at Earth. The non-observation of such modulations by the Chandra satellite places a bound on the axion-photon coupling $g_\gamma \lesssim 10^{-12}$ GeV^{-1} [115]. In cosmic magnetic fields the same phenomenon induces CMB spectral distortions, constraining a product of the photon coupling and the cosmic magnetic field strength [116, 117]. Conversion of axions to photons in the Milky Way magnetic field produces a background of GHz photons correlated with the magnetic field that is accessible to observation by SKA for a range of masses and couplings consistent with QCD axion dark matter [118], and in the same range that could be detected directly by high frequency ADMX.

- Anomalous spin precession. The axion coupling to the neutron EDM, g_d, and the nucleon coupling, g_N induce spin-precession of neutrons and nuclei in the presence of the axion DM background field. For g_d this occurs in the presence of electric and magnetic fields [119, 109]. For g_N this occurs in magnetic fields, with the axion DM "wind" playing the role of a pseudo magnetic field [119, 120]. These effects are the basis of the CASPEr proposal, and have been constrained directly using archival data from nEDM [121].

- "Light Shining Through a Wall". Axions pass virtually unimpeded through materials ("walls") that are opaque to photons. Converting a laser photon into an axion using a

magnetic field, allowing it to pass through an intermediate wall, and then converting the axion back into a photon, would allow the laser to pass through the wall and indirectly give evidence for axions. This search technique [122] is the basis for the "ALPS" experiment [123, 124], which aims at constraining $g_{\phi\gamma} \sim 2 \times 10^{-11}$ GeV^{-1} in the upgraded version currently in operation.

- "Helioscopes". Axions from the sun can be converted into visible photons inside a telescope with a magnetic field [105]. Constraints on $g_\gamma \lesssim 10^{-10}$ GeV^{-1} using this technique have been presented by the CAST experiment [125, 126, 127]. The proposed "International Axion Observatory" would improve the limits by an order of magnitude [128].

3.2 Gravitation

The classical axion field, ϕ, has novel gravitational effects caused by the Compton wavelength, and by the axion potential.

- "Fuzzy" Dark Matter. As already discussed, when the axion mass is very small, $m_a \sim 10^{-22}$ eV, the field displays coherence on astrophysical length scales [39, 40, 41, 42]. This makes ULAs distinct from cold DM, and drives the lower bound on DM particle mass from cosmological constraints such as the CMB anisotropies [129, 91, 82], the high redshift luminosity function [130, 131, 132], and the Lyman-α forest flux power spectrum [133, 134]. Superficially the model resembles warm DM [135], suppressing cosmic structure formation below a certain length scale, and with the warm DM mass, m_X, roughly related to the axion mass as $m_X \sim \sqrt{m_a M_{pl}}$. However, the small scale physics is very different and fuzzy DM requires dedicated simulations, which reveal striking unique features such as soliton formation, and quasi-particles. A number of beyond-CDM simulations and semi-analytic methods have been developed to study this novel type of DM [41, 136, 137, 138, 139].

- Black hole superradiance. This gravitational phenomenon applies to all bosonic fields, with different timescales depending on the spin (zero, one, or two). A population of bosons is built up in a "gravitational atom" around the black hole *from vacuum fluctuations*. Thus this phenomenon makes no assumptions about the cosmic density or origin of the bosonic field. Spin is extracted from the black hole via the Penrose process [140]. The boson mass provides a potential barrier (a "mirror"), and the process becomes runaway [141, 142]. The resulting spin down of black holes makes certain regions on the "Regge plane" (mass versus spin plane) effectively forbidden for astrophysical black holes. Astrophysical observations of rapidly rotating black holes thus exclude bosons of certain ranges of mass [143, 31, 144, 145, 146]. For the spin zero axion, stellar mass black holes exclude 6×10^{-13} eV $< m_a < 2 \times 10^{-11}$ eV at 2σ, which for the QCD axion excludes 3×10^{17} GeV $< f_a < 1 \times 10^{19}$ GeV. The supermassive BH measurements give only 1σ exclusions 10^{-18} eV $< m_a < 10^{-16}$ eV. The energy extracted from the BH angular momentum can be emitted by the axion cloud in the form of gravitational waves (GWs). The recent direct detection of GWs by LIGO [147] opens up an exciting new opportunity to study axions and other light bosons from the inferred mass and spin distributions of BHs, and from direct GW signals of superradiance [148, 149].

- Oscillating dark matter pressure. The axion equation of state oscillates with frequency $2m_a$, originating from an oscillating pressure. The axion is only pressureless when av-

eraged over time scales larger than $(2m_a)^{-1}$. Pressure oscillations induce oscillations in the metric potentials, which manifest as a scalar strain on pulsar timing arrays (PTAs) and in gravitational wave detectors (just as gravitational waves are a tensor strain) [150]. The NANOGrav PTA sets limits an order of magnitude higher than the expected signal at $m_a = 10^{-23}$ eV [151], though SKA is forecast to be sensitive to the signal at this mass even if such ULAs constitute just 1% of the DM [150]. In GW detectors, the axion DM wind anisotropic stress, $\sigma_{ij} \propto \nabla_i\phi\nabla_j\phi$, manifests as a "scalar GW" also [152].

- Axion stars. The gradient term in the Klein Gordon equation opposes gravitational collapse of scalar fields on small scales. This leads to the existence of a class of pseudo-solitonic boson star known as an oscilloton [153, 154] for the case of a massive real scalar. For axions, these solutions are "axion stars". These objects are formed during gravitational collapse, halted by the effective pressure of the gradients. Emission of scalar waves leads to "gravitational cooling" [155], and the stars settle into the ground state. The solitons are a condensate of coherent axions. Axions stars are observed to form in the centres of DM halos in numerical simulations [41, 156, 138]. This density core may play a role in the presence of cores in dwarf spheroidal satellites of the Milky Way [157, 158, 159]. Axion stars should also be present in the centre of miniclusters, and, if axion self-scattering is efficient, entire miniclusters might thus condense [64]. Axion stars have a maximum mass above which they become unstable [160]. For weak self-interactions, $f_a \gtrsim M_{pl}$, the instability leads to black hole formation, while for stronger self-interactions the instability results in emission of relativistic axion waves [160, 161, 162, 163, 164, 165]. Axion stars could detected as they pass through the Earth using a network of magnetometers [166]. Especially compact axion stars could lead to unique signatures in gravitational wave detectors from their binary inspirals with each other and with other astrophysical objects [167].

- Inflation and Dark Energy. The periodic nature of the axion potential implies that there are maxima where the potential is locally flat. The (tachyonic) mass at the maximum is protected from perturbative quantum corrections by the shift symmetry, leading to fairly natural models for inflation [168] and dark energy [169]. The axion potential contributes to the effective cosmological constant. If the field is placed sufficiently close to the top of the potential, then a sufficient number of e-foldings of inflation can be driven (for dark energy the requirement is instead on the equation of state). Constraints on axion dark energy can be found in Ref. [170]. The simplest model of natural inflation takes $V(\phi) \propto \cos(\phi/f_a)$. After normalising the scalar CMB amplitude, this model is a two parameter family giving predicting a strip in the plane of scalar spectral index versus tensor-to-scalar ratio, (n_s, r_T). It is consistent with the *Planck* results [171], but could could be excluded by CMB-S4 [172]. Variants on axion inflation inspired by string theory are N-flation [173] and axion monodromy [174, 175]. Both models seek to deal with issues relating to super-Planckian field excursions, the Lyth bound for r_T [176], and the "weak gravity conjecture" [177], and construct string-inspired models with observably large r_T.

Acknowledgements

These brief notes contributed to the 13th Patras Workshop on Axions, WIMPs and WISPs, Thessaloniki, May 15 to 19, 2017. They rely heavily on the review Ref. [90], which is far more

complete, (though of course these notes discuss new results of the last two years). I am grateful to Thomas Bachlechner, Laura Covi, Jihn Kim, and Andreas Ringwald for useful discussions. Work at King's College London was supported by a Royal Astronomical Society Postdoctoral Fellowship. Research at the University of Göttingen is funded by the Alexander von Humboldt Foundation and the German Federal Ministry of Education and Research.

References

[1] R. Peccei and H. R. Quinn, Phys. Rev. Lett.**38**, 1440 (1977).

[2] S. Weinberg, Phys. Rev. Lett.**40**, 223 (1978).

[3] F. Wilczek, Phys. Rev. Lett.**40**, 279 (1978).

[4] R. J. Crewther, P. di Vecchia, G. Veneziano, and E. Witten, Phys. Lett. B **88**, 123 (1979).

[5] J. M. Pendlebury *et al.*, Phys. Rev. D**92**, 092003 (2015), 1509.04411.

[6] K. A. Olive and Particle Data Group, Chinese Physics C **38**, 090001 (2014), 1412.1408.

[7] S. Coleman, *Aspects of Symmetry* (Cambridge University Press, 1988).

[8] P. Sikivie, Phys. Rev. Lett.**48**, 1156 (1982).

[9] D. J. Gross, R. D. Pisarski, and L. G. Yaffe, Reviews of Modern Physics **53**, 43 (1981).

[10] S. Borsanyi *et al.*, Physics Letters B **752**, 175 (2016), 1508.06917.

[11] S. Borsanyi *et al.*, Nature **539**, 69 (2016), 1606.07494.

[12] J. E. Kim, Phys. Rept. **150**, 1 (1987).

[13] J. E. Kim, Phys. Rev. Lett.**43**, 103 (1979).

[14] M. A. Shifman, A. I. Vainshtein, and V. I. Zakharov, Nuclear Physics B **166**, 493 (1980).

[15] M. Dine, W. Fischler, and M. Srednicki, Phys. Lett. B **104**, 199 (1981).

[16] A. Zhitnitsky, Sov.J . Nucl. Phys. **31**, 260 (1980).

[17] L. Di Luzio, F. Mescia, and E. Nardi, Physical Review Letters **118**, 031801 (2017), 1610.07593.

[18] S. M. Carroll, *Spacetime and geometry. An introduction to general relativity* (Addison Wesley, 2004).

[19] M. B. Green, J. H. Schwarz, and E. Witten, *Superstring theory. Volume 2 - Loop amplitudes, anomalies and phenomenology* (Cambridge University Press, 1987).

[20] P. Svrcek and E. Witten, JHEP**6**, 51 (2006), hep-th/0605206.

[21] J. P. Conlon, Journal of High Energy Physics **5**, 078 (2006), hep-th/0602233.

[22] K. Becker, M. Becker, and J. H. Schwarz, *String Theory and M-Theory* (Cambridge University Press, 2007).

[23] A. Ringwald, ArXiv e-prints (2012), 1209.2299.

[24] M. Cicoli, M. D. Goodsell, and A. Ringwald, JHEP**10**, 146 (2012), 1206.0819.

[25] P. Candelas, G. T. Horowitz, A. Strominger, and E. Witten, Nuclear Physics B **258**, 46 (1985).

[26] R. Altman, J. Gray, Y.-H. He, V. Jejjala, and B. D. Nelson, JHEP **02**, 158 (2015), 1411.1418.

[27] Y.-H. He, (2017), 1706.02714.

[28] M. Kreuzer and H. Skarke, Adv. Theor. Math. Phys. **4**, 1209 (2002), hep-th/0002240.

[29] M. Kreuzer and H. Skarke, ArXiv Mathematics e-prints (2000), math/0001106.

[30] T. W. Grimm and J. Louis, Nucl. Phys. **B699**, 387 (2004), hep-th/0403067.

[31] A. Arvanitaki, S. Dimopoulos, S. Dubovsky, N. Kaloper, and J. March-Russell, Phys. Rev. D**81**, 123530 (2010), 0905.4720.

[32] R. Easther and L. McAllister, JCAP**5**, 018 (2006), hep-th/0512102.

[33] M. J. Stott, D. J. E. Marsh, C. Pongkitivanichkul, L. C. Price, and B. S. Acharya, Phys. Rev. D**96**, 083510 (2017), 1706.03236.

[34] T. C. Bachlechner, K. Eckerle, O. Janssen, and M. Kleban, (2017), 1703.00453.

[35] S. B. Giddings and A. Strominger, Nuclear Physics B **306**, 890 (1988).

[36] R. Alonso and A. Urbano, ArXiv e-prints (2017), 1706.07415.

[37] M. Kamionkowski and J. March-Russell, Physics Letters B **282**, 137 (1992), hep-th/9202003.

[38] R. Kallosh, A. Linde, D. Linde, and L. Susskind, Phys. Rev. D**52**, 912 (1995), hep-th/9502069.

[39] W. Hu, R. Barkana, and A. Gruzinov, Physical Review Letters **85**, 1158 (2000), astro-ph/0003365.

[40] D. J. E. Marsh and J. Silk, MNRAS**437**, 2652 (2014), 1307.1705.

[41] H.-Y. Schive, T. Chiueh, and T. Broadhurst, Nature Physics **10**, 496 (2014), 1406.6586.

[42] L. Hui, J. P. Ostriker, S. Tremaine, and E. Witten, Phys. Rev. D**95**, 043541 (2017), 1610.08297.

[43] J. P. Conlon and M. C. D. Marsh, Phys. Rev. Lett.**111**, 151301 (2013), 1305.3603.

[44] J. P. Conlon and M. C. D. Marsh, JHEP**10**, 214 (2013), 1304.1804.

[45] L. Iliesiu, D. J. E. Marsh, K. Moodley, and S. Watson, Phys. Rev. D**89**, 103513 (2014), 1312.3636.

[46] M. Archidiacono, S. Hannestad, A. Mirizzi, G. Raffelt, and Y. Y. Y. Wong, JCAP**10**, 020 (2013), 1307.0615.

[47] E. Di Valentino, S. Gariazzo, E. Giusarma, and O. Mena, Phys. Rev. D**91**, 123505 (2015), 1503.00911.

[48] E. Di Valentino *et al.*, Physics Letters B **752**, 182 (2016), 1507.08665.

[49] S. Hannestad, A. Mirizzi, and G. Raffelt, JCAP**7**, 002 (2005), hep-ph/0504059.

[50] S. Hannestad, A. Mirizzi, G. G. Raffelt, and Y. Y. Y. Wong, JCAP**8**, 015 (2007), 0706.4198.

[51] S. Hannestad, A. Mirizzi, G. G. Raffelt, and Y. Y. Y. Wong, JCAP**4**, 019 (2008), 0803.1585.

[52] S. Hannestad, A. Mirizzi, G. G. Raffelt, and Y. Y. Y. Wong, JCAP**8**, 001 (2010), 1004.0695.

[53] O. Wantz and E. Shellard, Phys. Rev. D**82**, 123508 (2010), 0910.1066.

[54] G. Ballesteros, J. Redondo, A. Ringwald, and C. Tamarit, JCAP**8**, 001 (2017), 1610.01639.

[55] Planck Collaboration *et al.*, A&A**594**, A13 (2016), 1502.01589.

[56] BICEP2 Collaboration *et al.*, Phys. Rev. Lett.**116**, 031302 (2016), 1510.09217.

[57] R. L. Davis, Phys. Rev. D**32**, 3172 (1985).

[58] D. Harari and P. Sikivie, Phys. Lett. B **195**, 361 (1987).

[59] R. A. Battye and E. P. S. Shellard, Phys. Rev. Lett.**73**, 2954 (1994), astro-ph/9403018.

[60] R. A. Battye and E. P. S. Shellard, Phys. Rev. Lett.**76**, 2203 (1996).

[61] T. Hiramatsu, M. Kawasaki, K. Saikawa, and T. Sekiguchi, Phys. Rev. D**85**, 105020 (2012), 1202.5851.

[62] V. B. Klaer and G. D. Moore, ArXiv e-prints (2017), 1708.07521.

[63] C. J. Hogan and M. J. Rees, Phys. Lett. B **205**, 228 (1988).

[64] E. W. Kolb and I. I. Tkachev, Phys. Rev. Lett.**71**, 3051 (1993), hep-ph/9303313.

[65] E. W. Kolb and I. I. Tkachev, Phys. Rev. D**49**, 5040 (1994), astro-ph/9311037.

[66] E. W. Kolb and I. I. Tkachev, Phys. Rev. D**50**, 769 (1994), astro-ph/9403011.

[67] E. W. Kolb and I. I. Tkachev, ApJLett**460**, L25 (1996), astro-ph/9510043.

[68] K. M. Zurek, C. J. Hogan, and T. R. Quinn, Phys. Rev. D**75**, 043511 (2007), astro-ph/0607341.

[69] E. Hardy, Journal of High Energy Physics **2**, 46 (2017), 1609.00208.

[70] M. Fairbairn, D. J. E. Marsh, and J. Quevillon, Phys. Rev. Lett. **119**, 021101 (2017), 1701.04787.

[71] C. A. J. O'Hare and A. M. Green, Phys. Rev. D**95**, 063017 (2017), 1701.03118.

[72] P. Tinyakov, I. Tkachev, and K. Zioutas, JCAP**1**, 035 (2016), 1512.02884.

[73] M. Fairbairn, D. J. E. Marsh, J. Quevillon, and S. Rozier, (2017), 1707.03310.

[74] I. I. Tkachev, JETP Lett. **101**, 1 (2015), 1411.3900, [Pisma Zh. Eksp. Teor. Fiz.101,no.1,3(2015)].

[75] A. Iwazaki, (2017), 1707.04827.

[76] A. Iwazaki, (2014), 1412.7825.

[77] E. Komatsu *et al.*, ApJS**180**, 330 (2009), 0803.0547.

[78] Planck Collaboration *et al.*, A&A**594**, A20 (2016), 1502.02114.

[79] M. P. Hertzberg, M. Tegmark, and F. Wilczek, Phys. Rev. D**78**, 083507 (2008), 0807.1726.

[80] D. J. E. Marsh, D. Grin, R. Hlozek, and P. G. Ferreira, Physical Review Letters **113**, 011801 (2014).

[81] L. Visinelli and P. Gondolo, Phys. Rev. Lett.**113**, 011802 (2014), 1403.4594.

[82] R. Hlozek, D. J. E. Marsh, and D. Grin, (2017), 1708.05681.

[83] J. Preskill, M. B. Wise, and F. Wilczek, Phys. Lett. B **120**, 127 (1983).

[84] M. Dine and W. Fischler, Phys. Lett. B **120**, 137 (1983).

[85] L. F. Abbott and P. Sikivie, Phys. Lett. B **120**, 133 (1983).

[86] P. J. Steinhardt and M. S. Turner, Phys. Lett. B **129**, 51 (1983).

[87] M. S. Turner, Phys. Rev. D**28**, 1243 (1983).

[88] E. W. Kolb and M. S. Turner, *The early universe.* (Addison-Wesley, 1990).

[89] P. Fox, A. Pierce, and S. Thomas, ArXiv High Energy Physics - Theory e-prints (2004), hep-th/0409059.

[90] D. J. E. Marsh, Phys. Rep.**643**, 1 (2016), 1510.07633.

[91] R. Hložek, D. Grin, D. J. E. Marsh, and P. G. Ferreira, Phys. Rev. D**91**, 103512 (2015), 1410.2896.

[92] D. H. Lyth, Phys. Rev. D**45**, 3394 (1992).

[93] A. Diez-Tejedor and D. J. E. Marsh, (2017), 1702.02116.

[94] M. Kawasaki, K. Saikawa, and T. Sekiguchi, Phys. Rev. D**91**, 065014 (2015), 1412.0789.

[95] P. W. Graham, I. G. Irastorza, S. K. Lamoreaux, A. Lindner, and K. A. van Bibber, Annual Review of Nuclear and Particle Science **65**, 485 (2015), 1602.00039.

[96] GAMBIT, S. Hoof, A Preview of Global Fits of Axion Models in GAMBIT, in *13th Patras Workshop on Axions, WIMPs and WISPs (AXION-WIMP 2017) CHALKIDIKI TBC, GREECE, May 15-19, 2017*, 2017, 1710.11138.

[97] G. Carosi *et al.*, ArXiv e-prints (2013), 1309.7035.

[98] G. G. Raffelt, Phys. Rept. **198**, 1 (1990).

[99] G. G. Raffelt, Astrophysical Axion Bounds, in *Axions*, edited by M. Kuster, G. Raffelt, and B. Beltrán, , Lecture Notes in Physics, Berlin Springer Verlag Vol. 741, p. 51, 2008, hep-ph/0611350.

[100] A. Ayala, I. Domínguez, M. Giannotti, A. Mirizzi, and O. Straniero, Phys. Rev. Lett.**113**, 191302 (2014), 1406.6053.

[101] J. Isern, White dwarfs as physics laboratories: the case of axions, in *7th Patras Workshop on Axions, WIMPs and WISPs (PATRAS 2011)*, edited by K. Zioutas and M. Schumann, p. 158, 2012, 1204.3565.

[102] J. Moody and F. Wilczek, Phys. Rev. D**30**, 130 (1984).

[103] G. Raffelt, Phys. Rev. D**86**, 015001 (2012), 1205.1776.

[104] A. Arvanitaki and A. A. Geraci, Phys. Rev. Lett.**113**, 161801 (2014), 1403.1290.

[105] P. Sikivie, Phys. Rev. Lett.**51**, 1415 (1983).

[106] S. J. Asztalos *et al.*, Phys. Rev. Lett.**104**, 041301 (2010), 0910.5914.

[107] P. Sikivie, N. Sullivan, and D. B. Tanner, Phys. Rev. Lett.**112**, 131301 (2014), 1310.8545.

[108] Y. Kahn, B. R. Safdi, and J. Thaler, Physical Review Letters **117**, 141801 (2016), 1602.01086.

[109] D. Budker, P. W. Graham, M. Ledbetter, S. Rajendran, and A. O. Sushkov, Phys. Rev. X **4**, 021030 (2014), 1306.6089.

[110] A. Garcon *et al.*, ArXiv e-prints (2017), 1707.05312.

[111] MADMAX Working Group, A. Caldwell *et al.*, Phys. Rev. Lett.**118**, 091801 (2017), 1611.05865.

[112] J. Ellis, G. B. Gelmini, J. L. Lopez, D. V. Nanopoulos, and S. Sarkar, Nuclear Physics B **373**, 399 (1992).

[113] E. Massó and R. Toldrà, Phys. Rev. D**55**, 7967 (1997), hep-ph/9702275.

[114] M. Millea, L. Knox, and B. D. Fields, Phys. Rev. D**92**, 023010 (2015), 1501.04097.

[115] J. P. Conlon, F. Day, N. Jennings, S. Krippendorf, and M. Rummel, JCAP**7**, 005 (2017), 1704.05256.

[116] A. Mirizzi, J. Redondo, and G. Sigl, JCAP**8**, 1 (2009), 0905.4865.

[117] H. Tashiro, J. Silk, and D. J. E. Marsh, Phys. Rev. D**88**, 125024 (2013), 1308.0314.

[118] K. Kelley and P. J. Quinn, ApJLett**845**, L4 (2017), 1708.01399.

[119] P. W. Graham and S. Rajendran, Phys. Rev. D**88**, 035023 (2013), 1306.6088.

[120] V. Flambaum, 9th Patras Workshop (2013).

[121] C. Abel *et al.*, Phys. Rev. **X7**, 041034 (2017), 1708.06367.

[122] J. Redondo and A. Ringwald, Contemporary Physics **52**, 211 (2011), 1011.3741.

[123] K. Ehret *et al.*, Physics Letters B **689**, 149 (2010), 1004.1313.

[124] R. Bähre *et al.*, Journal of Instrumentation **8**, 9001 (2013), 1302.5647.

[125] K. Zioutas *et al.*, Phys. Rev. Lett.**94**, 121301 (2005), hep-ex/0411033.

[126] S. Andriamonje *et al.*, JCAP**4**, 10 (2007), hep-ex/0702006.

[127] M. Arik *et al.*, Phys. Rev. Lett.**112**, 091302 (2014), 1307.1985.

[128] J. K. Vogel *et al.*, IAXO - The International Axion Observatory, in *8th Patras Workshop on Axions, WIMPs and WISPs (AXION-WIMP 2012) Chicago, Illinois, July 18-22, 2012*, 2013, 1302.3273.

[129] L. Amendola and R. Barbieri, Physics Letters B **642**, 192 (2006), hep-ph/0509257.

[130] B. Bozek, D. J. E. Marsh, J. Silk, and R. F. G. Wyse, MNRAS**450**, 209 (2015), 1409.3544.

[131] H.-Y. Schive, T. Chiueh, T. Broadhurst, and K.-W. Huang, ApJ**818**, 89 (2016), 1508.04621.

[132] P. S. Corasaniti, S. Agarwal, D. J. E. Marsh, and S. Das, Phys. Rev. D**95**, 083512 (2017), 1611.05892.

[133] V. Iršič, M. Viel, M. G. Haehnelt, J. S. Bolton, and G. D. Becker, Physical Review Letters **119**, 031302 (2017), 1703.04683.

[134] E. Armengaud, N. Palanque-Delabrouille, C. Yèche, D. J. E. Marsh, and J. Baur, MNRAS**471**, 4606 (2017), 1703.09126.

[135] P. Bode, J. P. Ostriker, and N. Turok, ApJ**556**, 93 (2001), astro-ph/0010389.

[136] J. Veltmaat and J. C. Niemeyer, Phys. Rev. D**94**, 123523 (2016), 1608.00802.

[137] X. Du, C. Behrens, and J. C. Niemeyer, MNRAS**465**, 941 (2017), 1608.02575.

[138] B. Schwabe, J. C. Niemeyer, and J. F. Engels, Phys. Rev. D**94**, 043513 (2016), 1606.05151.

[139] P. Mocz *et al.*, MNRAS**471**, 4559 (2017), 1705.05845.

[140] R. Penrose, Nuovo Cimento Rivista Serie **1**, 252 (1969).

[141] W. H. Press and S. A. Teukolsky, Nature**238**, 211 (1972).

[142] W. H. Press and S. A. Teukolsky, ApJ**185**, 649 (1973).

[143] A. Arvanitaki, M. Baryakhtar, and X. Huang, Phys. Rev. D**91**, 084011 (2015), 1411.2263.

[144] A. Arvanitaki and S. Dubovsky, Phys. Rev. D**83**, 044026 (2011), 1004.3558.

[145] P. Pani, V. Cardoso, L. Gualtieri, E. Berti, and A. Ishibashi, Phys. Rev. Lett.**109**, 131102 (2012), 1209.0465.

[146] R. Brito, V. Cardoso, and P. Pani, Classical and Quantum Gravity **32**, 134001 (2015), 1411.0686.

[147] B. P. Abbott *et al.*, Physical Review Letters **116**, 061102 (2016), 1602.03837.

[148] A. Arvanitaki, M. Baryakhtar, S. Dimopoulos, S. Dubovsky, and R. Lasenby, Phys. Rev. D**95**, 043001 (2017), 1604.03958.

[149] R. Brito *et al.*, Phys. Rev. D**96**, 064050 (2017), 1706.06311.

[150] A. Khmelnitsky and V. Rubakov, JCAP**2**, 019 (2014), 1309.5888.

[151] N. K. Porayko and K. A. Postnov, Phys. Rev. D**90**, 062008 (2014), 1408.4670.

[152] A. Aoki and J. Soda, International Journal of Modern Physics D **26**, 1750063 (2017), 1608.05933.

[153] R. Ruffini and S. Bonazzola, Physical Review **187**, 1767 (1969).

[154] E. Seidel and W.-M. Suen, Phys. Rev. Lett.**66**, 1659 (1991).

[155] E. Seidel and W.-M. Suen, Phys. Rev. Lett.**72**, 2516 (1994), gr-qc/9309015.

[156] H.-Y. Schive *et al.*, Phys. Rev. Lett.**113**, 261302 (2014), 1407.7762.

[157] D. J. E. Marsh and A.-R. Pop, MNRAS**451**, 2479 (2015), 1502.03456.

[158] A. X. González-Morales, D. J. E. Marsh, J. Peñarrubia, and L. A. Ureña-López, MNRAS**472**, 1346 (2017), 1609.05856.

[159] S.-R. Chen, H.-Y. Schive, and T. Chiueh, MNRAS**468**, 1338 (2017), 1606.09030.

[160] T. Helfer *et al.*, JCAP**3**, 055 (2017), 1609.04724.

[161] D. G. Levkov, A. G. Panin, and I. I. Tkachev, Physical Review Letters **118**, 011301 (2017), 1609.03611.

[162] P.-H. Chavanis, Phys. Rev. D**94**, 083007 (2016), 1604.05904.

[163] J. Eby, P. Suranyi, and L. C. R. Wijewardhana, Modern Physics Letters A **31**, 1650090 (2016), 1512.01709.

[164] P.-H. Chavanis, ArXiv e-prints (2017), 1710.06268.

[165] J. Eby, M. Leembruggen, P. Suranyi, and L. C. R. Wijewardhana, Journal of High Energy Physics **12**, 66 (2016), 1608.06911.

[166] D. F. J. Kimball *et al.*, ArXiv e-prints (2017), 1710.04323.

[167] G. F. Giudice, M. McCullough, and A. Urbano, JCAP**10**, 001 (2016), 1605.01209.

[168] K. Freese, J. A. Frieman, and A. V. Olinto, Phys. Rev. Lett.**65**, 3233 (1990).

[169] J. A. Frieman, C. T. Hill, A. Stebbins, and I. Waga, Phys. Rev. Lett.**75**, 2077 (1995), astro-ph/9505060.

[170] V. Smer-Barreto and A. R. Liddle, JCAP**1**, 023 (2017), 1503.06100.

[171] Planck Collaboration *et al.*, AAP **594**, A20 (2016), 1502.02114.

[172] K. N. Abazajian *et al.*, ArXiv e-prints (2016), 1610.02743.

[173] S. Dimopoulos, S. Kachru, J. McGreevy, and J. G. Wacker, JCAP**8**, 3 (2008), hep-th/0507205.

[174] E. Silverstein and A. Westphal, Phys. Rev. D**78**, 106003 (2008), 0803.3085.

[175] L. McAllister, E. Silverstein, and A. Westphal, Phys. Rev. D**82**, 046003 (2010), 0808.0706.

[176] D. H. Lyth, Phys. Rev. Lett.**78**, 1861 (1997), hep-ph/9606387.

[177] N. Arkani-Hamed, L. Motl, A. Nicolis, and C. Vafa, JHEP**6**, 60 (2007), hep-th/0601001.

The ORGAN Experiment: First Results and Future Plans

Ben T. McAllister[1], *Graeme R. Flower*[1], *Maxim Goryachev*[1], *Jeremy Bourhill*[1], *Eugene N. Ivanov*[1] *and Michael E. Tobar*[1]

[1]ARC Centre of Excellence for Engineered Quantum Systems, School of Physics, University of Western Australia, 35 Stirling Highway, Crawley, WA 6009, Australia.

DOI: http://dx.doi.org/10.3204/DESY-PROC-2017-02/mcallister_ben

We discuss the Oscillating Resonant Group AxioN (ORGAN) experiment, a high mass axion haloscope hosted at the University of Western Australia (UWA). The path-finding experiment placed limits in a narrow frequency range around 26 GHz, and the future searches, which will be enabled by novel resonator designs based on dielectric structures, will focus on wider mass ranges with increased sensitivity. The next stage of the experiment will scan from 26-27 GHz, whilst the subsequent searches will focus on the 15-50 GHz range.

1 Introduction

Several haloscope searches for dark matter axions are already underway [1, 2, 3], and all focus on axion mass ranges up to a few GHz (corresponding to masses up to a few 10s of μeV). Despite this, there is mounting motivation for higher mass axion searches. Claimed results from Josephson junctions [5], and the exciting SMASH result [4] both point to axions in the mass range 50 - 200 μeV, which corresponds to 12.5-50 GHz in photon frequency for a haloscope.
In order to test these results a collaboration of research groups from the ARC Centre of Excellence for Engineered Quantum System (EQuS), hosted at UWA is building a multi-stage haloscope designed to operate over the next seven years. The path-finding run of the experiment is complete, and limits axions in a very narrow range.
The second phase of the experiment, scheduled to commence in 2018 will search the entire mass range of the claimed Josephson junction results, corresponding to 26-27 GHz. After this is complete, the experiment will focus on 5 GHz windows beginning at 15 GHz and finishing at 50 GHz, in order to cover the range suggested by the SMASH result that will not be accessed by other haloscopes.
In order to achieve sensitive searches in these high mass ranges novel resonator design is critical. We have developed and prototyped dielectric loaded resonant cavities optimised for axion detection, based on both the well known Bragg effect and a new effect designed to maximize the axion haloscope form factor by suppressing out of phase field components.

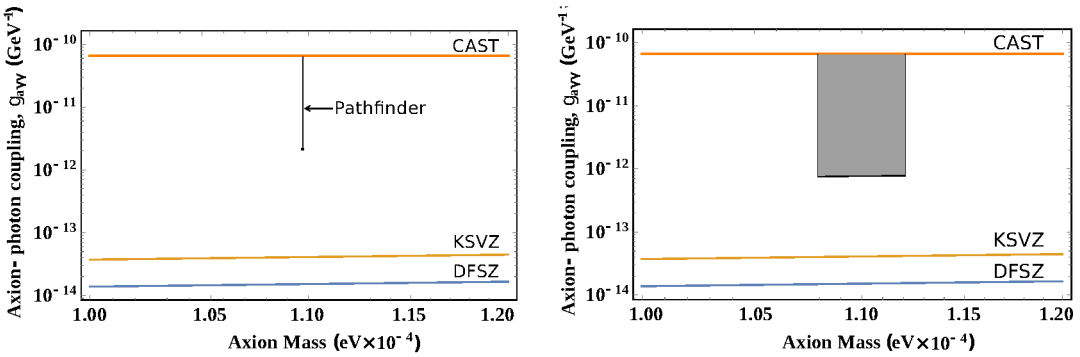

Figure 1: Left: the 90% confidence exclusion limits from the pathfinder experiment as discussed in the text. Right: the projected limits for Stage-I of ORGAN, the targeted search of the Beck Result. On both plots CAST limits are shown in orange, whilst KSVZ and DFSZ model bands are in yellow and blue respectively.

2 Path-finding Result

The path-finding experiment was conducted in December 2016. A stationary frequency (untuned) copper resonant cavity was embedded in a 7 T static magnetic at 4 K for 4 days of continuous measurement. The cavity employed a TM_{020} mode with a central frequency of 26.531 GHz, and a cryogenic loaded quality factor of ∼13,000. The cavity was critically coupled to a cryogenic HEMT-based amplifier provided by Low Noise Factory. The primary purpose of this experiment was to familiarize ourselves with the necessary components of a haloscope, to verify that our cryogenic system was capable of sustained high field, 4 K operation, and to gain experience with the data acquisition and processing required. As a consequence of running the entire experiment simultaneously we are able to place narrow exclusion limits on axions as presented in fig 1.

3 Future Searches

The future searches of the ORGAN Experiment are broken down into two broad phases, Stage-I and Stage-II. Stage-I, currently planned for 2018, will see a magnetic field upgrade from 7 to 14 T, with two small cavities at 30 mK amplified via traditional HEMT amplification at 4 K. The resonant structures to be employed are discussed briefly below. The search will focus on the 26-27 GHz range, in order to provide a direct test of the claimed Beck result [5]. Stage-II of the experiment is current scheduled to commence in 2019 and run for 6 years. This search will be broken down into a number of 5 GHz search regions, beginning at 15 GHz and concluding at 50 GHz. The multi-staged nature of this search will allow for continued research and development of new resonators and amplifiers. It is the goal of the collaboration to install quantum-limited amplification at the beginning of Stage-II in the 15-20 GHz search range, and develop new amplifiers as the search continues, with the ultimate goal of synchronizing more cavities, further upgrading the magnetic field, and achieving sub-quantum limited amplification via squeezed states or some other technology. The projected limits for the future of ORGAN are shown in fig 2. For more detail see [6].

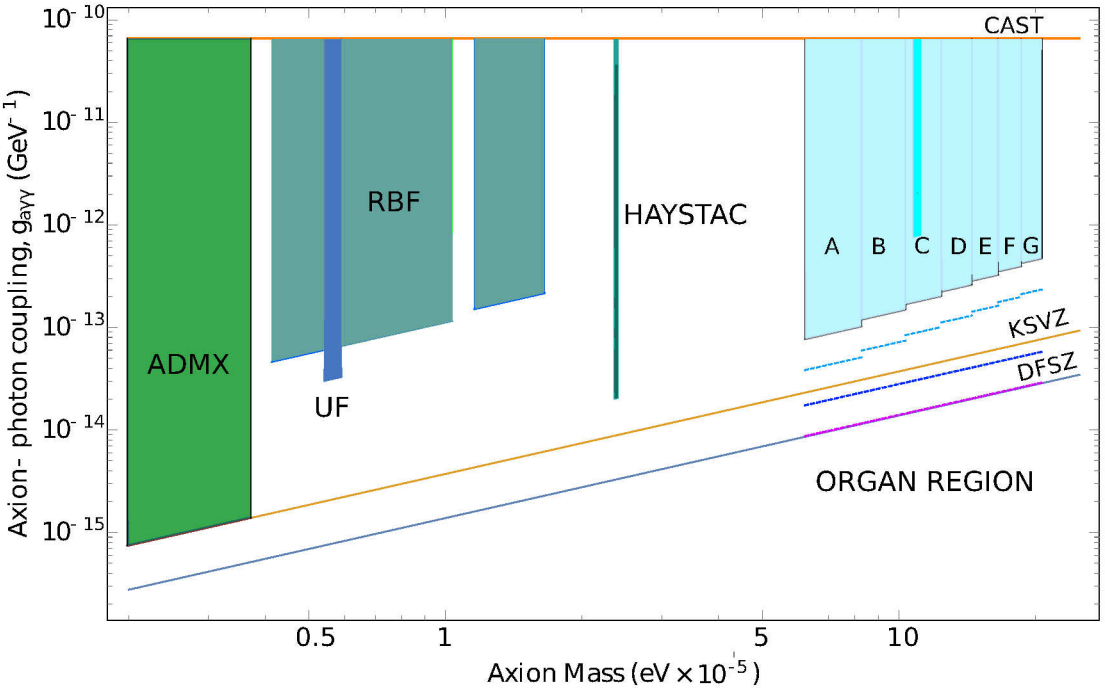

Figure 2: The projected limits of the ORGAN Experiment. Stage-II limits (in 5 GHz sections labelled A-G) are plotted, whilst the Stage-I limits are inset in darker blue inside bar C. Details of the experimental parameters predicted for these limits, and for the dashed line limits below can be found in [6].

4 Dielectric Resonators

The resonators to be employed in Stage-I and II of the ORGAN Experiment are based on a dielectric structure. The design involves careful placement of one or several dielectric rings in a location to capture and suppress the out of phase field contributions of a TM_{0n0} mode electromagnetic field to the axion haloscope form factor, thus maximizing sensitivity. Such a resonator can be tuned very rapidly with minimal position displacement via the usage of a supermode tuning mechanism. These types of resonators are most applicable to TM_{0n0} modes where n is an odd number greater than 1. The resonators for the ORGAN experiment will be based on TM_{030} and TM_{050} modes with carefully placed rings and supermode tuning. Further details of these resonators can be found in [7], and an electric field diagram of a TM_{030} mode with such a carefully placed dielectric ring is shown in fig 3. In this set-up, the ring is split and separated, enabling the supermode tuning as discussed. In this way, tuning of a few GHz is possible with small (order of mm) position displacements.

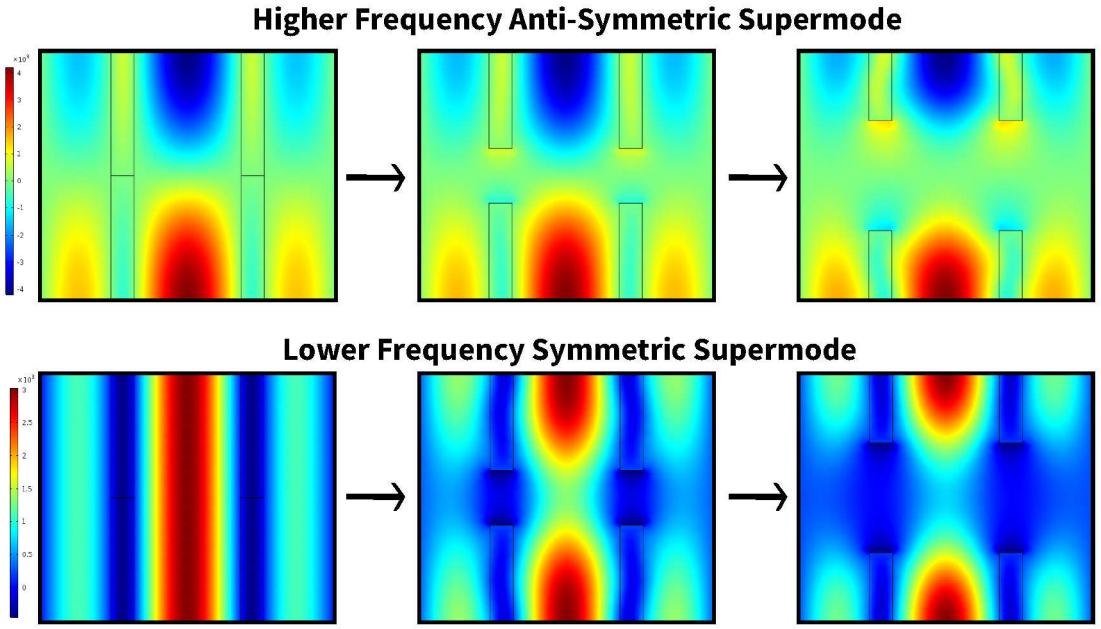

Figure 3: E_z field for a TM_{031}-like mode (top) and a TM_{030}-like mode (bottom). A dielectric ring is placed to suppress the out of phase field, and as the ring is split the frequency of the TM_{030}-like mode tunes upwards towards the TM_{031}-like mode.

5 Acknowledgements

This work was funded by Australian Research Council (ARC) grant no.CE110001013, as well as the Australian Governments Research Training Program and the Bruce and Betty Green foundation. The authors thank Stephen Parker and Justin Kruger for their contributions in the early stages of the project.

References

[1] S. J. Asztalos *et al.* [ADMX Collaboration], Phys. Rev. Lett. **104** (2010) 041301 doi:10.1103/PhysRevLett.104.041301 [arXiv:0910.5914 [astro-ph.CO]].

[2] W. Chung and S. W. Youn, New Phys. Sae Mulli **66** (2016) no.8, 1017. doi:10.3938/NPSM.66.1017

[3] B. M. Brubaker *et al.*, Phys. Rev. Lett. **118** (2017) no.6, 061302 doi:10.1103/PhysRevLett.118.061302 [arXiv:1610.02580 [astro-ph.CO]].

[4] G. Ballesteros, J. Redondo, A. Ringwald and C. Tamarit, JCAP **1708** (2017) no.08, 001 doi:10.1088/1475-7516/2017/08/001 [arXiv:1610.01639 [hep-ph]].

[5] C. Beck, Phys. Dark Univ. **7-8** (2015) 6 doi:10.1016/j.dark.2015.03.002 [arXiv:1403.5676 [hep-ph]].

[6] B. T. McAllister, G. Flower, J. Kruger, E. N. Ivanov, M. Goryachev, J. Bourhill and M. E. Tobar, Phys. Dark Univ. **18** (2017) 67 doi:10.1016/j.dark.2017.09.010 [arXiv:1706.00209 [physics.ins-det]].

[7] B. T. McAllister, G. Flower, L. E. Tobar and M. E. Tobar, arXiv:1705.06028 [physics.ins-det].

Recent results of search for solar axions using resonant absorption by ^{83}Kr nuclei

A.V. Derbin[2], *I.S. Drachnev*[2], *A.M. Gangapshev*[1], *Yu.M. Gavrilyuk*[1], *V.V. Kazalov*[1], *V.V. Kobychev*[4], *V.V. Kuzminov*[1], *V.N. Muratova*[2], *S.I. Panasenko*[3], *S.S. Ratkevich*[3], *D.A. Tekueva*[1], *E.V. Unzhakov*[2], *S.P. Yakimenko*[1]

[1]Institute for Nuclear Research, RAS, Moscow, Russia
[2]NRC "Kurchatov Institute" Petersburg Nuclear Physics Institute, St. Petersburg, Russia
[3]Kharkov National University, Kharkov, Ukraine
[4]Institute for Nuclear Research of NAS Ukraine, Kiev, Ukraine

DOI: http://dx.doi.org/10.3204/DESY-PROC-2017-02/muratova_valentina

A search for resonant absorption of the solar axion by ^{83}Kr nuclei was performed using the proportional counter installed inside the low-background setup at the Baksan Neutrino Observatory. The obtained model independent upper limit on the combination of isoscalar and isovector axion-nucleon couplings $|g_3 - g_0| \leq 8.4 \times 10^{-7}$ allowed us to set the new upper limit on the hadronic axion mass of $m_A \leq 65$ eV (95% C.L.) with the generally accepted values S=0.5 and z=0.56.

1 Introduction

If the axion exists, the Sun should be one of the most intense sources of these particles. The aim of this work is to search for monochromatic axions with an energy of 9.4 keV emitted in the M1 transition in the ^{83}Kr nuclei in the Sun [1]. Axions on the Earth can be detected in the inverse reaction of resonance absorption by detecting particles (γ- and X-ray photons, as well as conversion and Auger electrons) appearing at the decay of an excited nuclear level. The probability of the emission and subsequent absorption of axions depends only on the coupling constant with nucleons, which is minimally model dependent and is proportional to axion-nucleon coupling constant $(g_{AN})^4$.

The axion flux was calculated in [1] for the standard solar model BS05 [2] characterized by a highmetallicity [3]. The differential flux at the maximum of the distribution is [1]:

$$\Phi_A(E_{M1}) = 5.97 \times 10^{23} \left(\frac{\omega_A}{\omega_\gamma}\right) \mathrm{cm}^{-2}\mathrm{s}^{-1}\mathrm{keV}^{-1}. \quad (1)$$

where ω_A/ω_γ is the branching ratio of axions to photons emission. The cross section for resonance axion absorption is given by an expression similar to the expression for the photon-absorption cross section, the correction for the ratio ω_A/ω_γ being taken into account.

$$\sigma(E_A) = 2\sqrt{\pi}\sigma_{0\gamma} \exp\left[-\frac{4(E_A - E_M)^2}{\Gamma^2}\right] \left(\frac{\omega_A}{\omega_\gamma}\right), \quad (2)$$

where $\sigma_{0\gamma}$ is the maximum cross section of the γ -ray resonant absorption and $\Gamma = 1/\tau$. The total cross section for axion absorption can be obtained by integrating $\sigma(E_A)$ over the axion spectrum. The expected rate of resonance axion absorption by the ^{83}Kr nucleus as a function of the ratio ω_A/ω_γ, the combination of isoscalar and isovector coupling constants $|g_3 - g_0|$ and axion mass m_A can be represented in the form ($S = 0.5$, $z = 0.56$)[1]:

$$R_A[\mathrm{g}^{-1}\mathrm{day}^{-1}] = 4.23 \times 10^{21}(\omega_\mathrm{A}/\omega_\gamma)^2 \quad (3)$$

$$= 8.53 \times 10^{21}(g_3 - g_0)^4(p_A/p_\gamma)^6 \quad (4)$$

$$= 2.41 \times 10^{-10}(m_A/1\ \mathrm{eV})^4(\mathrm{p_A/p_\gamma})^6. \quad (5)$$

Figure 1: A large proportional counter (LPC) with a casing of copper inside passive shilding.

2 Experimental setup

A large proportional counter filled with of ^{83}Kr (99.9 %) was used to detect X-rays and gammas, as well as conversion and Auger electrons, appearing in the decay of the excited level with an energy of 9.4 keV. The LPC is a cylinder with inner diameters of 137 mm. A gold-plated tungsten wire of 10 μm in diameter is stretched along the LPC axis and is used as an anode. In order to reduce the influence of edge effects on the collection of the charge, the ends of the anode wire were surrounded by copper tubes (3 mm in diameter and 38 mm in length), which were at the anode potential and excluded gas amplification in this region. With the inclusion of Teflon insulators, the distance from the working area to the flanges of the chamber was 70 mm. The length of the working area of the chamber was 595 mm, which corresponded to a volume of 8.77 L. The chamber operated at a pressure of 1.8 bar. The mass of ^{83}Kr isotope in the working volume was 58 g.

The LPC is surrounded by passive shield made of copper (∼20 cm), lead (∼20 cm) and polyethylene (8 cm). The setup is located in the Deep Underground Low-Background Laboratory of Institute for Nuclear Research of Russian Academy of Sciences (BNO INR RAS)[4], at

the depth of 4900 m w.e., where the cosmic muon flux is reduced by $\sim 10^7$ times in comparison to that above ground, and evaluated as $(2.6 \pm 0.09) \times 10^{-9}$ cm^{-2}s^{-1}.

A signal from the anode was supplied to a charge-sensitive preamplifier. The shape of the pulse was digitized in a time interval of 164 μs with a frequency of 12.5 MHz and was transmitted to a computer through a USB port. The rise time of the leading edge of the pulse and the ratio of amplitudes of secondary and primary pulses were determined for each event, because these parameter makes it possible to select events near the cathode and nonpoint events such as multiple Compton scattering. The procedure of the analysis of the shape of pulses was described in more detail in [5].

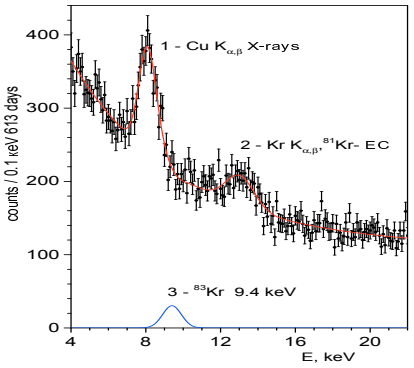

Figure 2: Energy spectra of the Kr LPC measured for 613 days, fitting results (red line) and expected axion peak for $3S_{lim}$ (blue line).

3 Results

The background spectra collected during 613.25 days and fit result curve are presented in Fig.2. Two peaks are clear visible in the energy range (4-26) keV. The peak with energy 8.05 keV associates with the detection of K$_{\alpha 1,2}$ X-rays of copper. The structure of the second peak is more complicated, it is mixture of Kr and Br K$_{\alpha 1,2}$ X-rays and 13.5 keV from K-capture of cosmogenic ^{81}Kr. It is seen that the 9.4 keV peak is not manifested. The maximum likelihood method was used to determine the intensity of the peak. The fit of spectrum corresponding to the minimum χ^2 is shown by red solid line in Fig. 2. The minimum of χ^2 corresponds to the nonphysical value of the area of the 9.4 keV peak $S_A = -(102 \pm 92)$ events. The standard χ^2-profile method was used to determine the upper bound on the number of events in the peak. The upper bound thus determined for the number of events in the peak is $S_{lim} = 127$ for 95 % C.L.

The expected number of registered axions is

$$S_A = RMT\epsilon \leq S_{lim}, \tag{6}$$

where $M = 58$ g is mass of ^{83}Kr isotope, $T = 613.25$ days is time of data taking, and $\epsilon = 0.825$ is the detection efficiency.

The upper limit on the excitation rate of ^{83}Kr by solar hadronic axions is defined as $R_{exp} = 4.29 \times 10^{-3}$ g^{-1}day^{-1}. The relation $R_A \leq R_{exp}$ limits the region of possible values of the coupling constants g_0, g_3 and axion mass m_A. In accordance with Eqs. (3-5), and on condition that $(p_A/p_\gamma) \cong 1$ provided for $m_A < 3$ keV one can obtain:

$$(\omega_A/\omega_\gamma) \leq 1.0 \times 10^{-12}, \tag{7}$$

$$|g_3 - g_0| \leq 8.4 \times 10^{-7}, \text{ and} \tag{8}$$

$$m_A \leq 65 \text{ eV} \quad \text{at } 95\% \text{ C.L.} \tag{9}$$

The limit (9) is stronger than the constrain obtained with 14.4 keV ^{57}Fe solar axions [6]) and is stronger than our previous result obtained in ^{83}Kr experiment [1]. As in the case of ^{57}Fe nucleus the obtained limit on axion mass strongly depends on the exact values of the parameters S and z.

4 Acknowledgments

This work was supported by the Russian Foundation of Basic Research (grants 17-02-00305A, 16-29-13014ofi-m, 16-29-13011ofi-m, 15-02-02117A, 14-02-00258A) and in part by the Russian Science Foundation (grant 17-12-01009).

References

[1] Yu.M. Gavrilyuk, A.M. Gangapshev, A.V. Derbin et al., JETP Letters, 101, 664 (2015)

[2] J.H. Bahcall, A.M. Serenelli, S. Basu, Astrophys. J. 621, L85 (2005)

[3] N. Grevesse, A.J. Sauval Space Sci. Rev. 85, 161 (1998)

[4] Ju.M. Gavriljuk et al., NIM A729, 576 (2013)

[5] Ju.M. Gavrilyuk et al., Instr. Exper. Techn. 53, 57 (2010), Phys. Rev. C87, 035501 (2013)

[6] A.V. Derbin, V.N. Muratova, D.A. Semenov, E.V. Unzhakov, Phys. At. Nucl. 74, 596 (2011)

Searching for galactic axions through magnetized media: QUAX status report

G. Ruoso[1], *D. Alesini*[2], *C. Braggio*[3,4], *G. Carugno*[3,4], *N. Crescini*[1,4], *D. Di Gioacchino*[2], *P. Falferi*[5,6], *S. Gallo*[3,4], *U. Gambardella*[8], *C. Gatti*[2], *G. Iannone*[8], *G. Lamanna*[9], *C. Ligi*[2], *A. Lombardi*[1], *R. Mezzena*[6,7], *A. Ortolan*[1], *R. Pengo*[1], *C. C. Speake*[10]

[1]INFN, Laboratori Nazionali di Legnaro, Legnaro (PD), Italy
[2]INFN, Laboratori Nazionali di Frascati, Frascati (Roma), Italy
[3]INFN, Sezione di Padova, Padova, Italy
[4]Dip. di Fisica e Astronomia, Padova, Italy
[5]Istituto di Fotonica e Nanotecnologie, CNR, Povo (TN), Italy
[6]INFN, TIFPA, Povo (TN), Italy
[7]Dip. di Fisica, Povo (TN), Italy
[8]Dip. di Fisica E.R. Caianiello, Fisciano (SA), Italy and INFN, Sez. di Napoli, Napoli, Italy
[9]Dip. di Fisica and INFN, Sez. di Pisa, Pisa, Italy
[10]School of Physics and Astronomy, Univ. of Birmingham, Birmingham, United Kingdom

DOI: http://dx.doi.org/10.3204/DESY-PROC-2017-02/ruoso_giuseppe

The current status of the QUAX R&D program is presented. QUAX is a feasibility study for a detection of axion as dark matter based on the coupling to the electrons. The relevant signal is a magnetization change of a magnetic material placed inside a resonant microwave cavity and polarized with a static magnetic field.

1 Introduction

The QUAX (QUaerere AXion) program explores the feasibility of an apparatus to detect axions as a dark matter component by exploiting its interaction with the spin of electrons (See [1] and references therein). Due to the motion of the Solar System through the galactic halo, the Earth is effectively moving through the cold dark matter cloud surrounding the Galaxy and an observer on Earth could detect such axion wind. In particular, its effect on a magnetized material can be described as an effective oscillating rf field with frequency determined by m_a and amplitude related to f_a. Thus, a possible detector for the axion wind can be a magnetized sample with Larmor resonance frequency tuned to the axion mass by means of an external polarizing static magnetic field: e.g. 1.7 T for 48 GHz, corresponding to a 200 μeV axion mass, in the case of the interaction with the electron spin that is considered hereafter. The interaction with the axion effective field drives the total magnetization of the sample, and so produce oscillations in the magnetization that, in principle, can be detected. To optimize the detection scheme, the sample is placed inside a microwave cavity. The cavity and the magnetized sample have to be cooled down at ultra-cryogenic temperature to reduce the noise due to thermal photons.

By using the Lagrangian that describes the interaction between axion and electron, it is

possible to derive the amplitude of the effective magnetic field $B_a \equiv \frac{g_p}{2e}\nabla a$. Here, g_p is the dimensionless pseudo-scalar coupling, a is the axion field, and e is the electron charge. Axions represent the best example of non-thermal dark matter candidate. In the following we will suppose that axions are the dominant component. The axion velocities are distributed according to a Maxwellian, with a velocity dispersion $\sigma_v \approx 270$ km/sec. We can treat the axion as a classical field, and the the effective magnetic rf field associated with the mean axion field has the amplitude and frequency given by

$$B_a = 2.0 \cdot 10^{-22} \left(\frac{m_a}{200\,\mu\text{eV}}\right) \text{ T}, \quad \frac{\omega_a}{2\pi} = 48 \left(\frac{m_a}{200\,\mu\text{eV}}\right) \text{ GHz}, \tag{1}$$

respectively, with a relative linewidth $\Delta\omega_a/\omega_a \simeq 5.2 \times 10^{-7}$. Among various axion models, this detection scheme is sensitive to axions described by the DFSZ model [2].

2 The experiment

To detect the extremely small rf field B_a we exploit the Electron Spin Resonance (ESR) in a magnetic sample. In particular, we want to collect the power deposited in the sample by the axion wind due to its interaction with the electron spin. To enhance the interaction we will tune the ferromagnetic resonance of the sample, i.e. the Larmor frequency of the electron, to the mass value of the searched for axion. The sample is placed inside a microwave resonant cavity which is used to reduce the effect of radiation damping and to optimize power collection. The axion wind will effectively drive the magnetization of the magnetic sample, and this will result in the emission of rf radiation that can be collected by using an antenna critically coupled to the cavity mode. It is useful to write the expected output power by referring to relevant experimental design parameters. For a magnetic sample of volume V_s and spin density n_S we have

$$P_{\text{out}} = \frac{P_{\text{in}}}{2} = 3.8 \times 10^{-26} \left(\frac{m_a}{200\,\mu\text{eV}}\right)^3 \left(\frac{V_s}{100\text{ cm}^3}\right) \left(\frac{n_S}{2 \cdot 10^{28}/\text{m}^3}\right) \left(\frac{\tau_{\text{m}}}{2\,\mu\text{s}}\right) \text{ W}, \tag{2}$$

where the chosen axion mass m_a is determined by a magnetizing field $B_0 = 1.7$ T. τ_{m} is the characteristic time of the detector system, connected to the microwave cavity and magnetic resonance linewidths.

At the moment we are performing an R&D to study the feasibility of this proposal. Among the relevant issues that we are working at we can mention: 1) **magnetic material**: it should have a spin density of about $2\times10^{28}/\text{m}^3$ with a ferromagnetic linewidth of about 150 kHz, over a total volume of 100 cm^3; 2) **microwave cavity**: a Q factor of the order of 10^6, operated in a static magnetic field and housing the magnetic material; 3) **magnetizing field**: provide a source up to a 2 T field with high uniformity and stability, both at the ppm level; 4) **microwave receiver**: linear amplifier are limited to quantum noise, so we foresee the use of a microwave single photon counter; 5) **complete apparatus**: the system has to work around 100 mK, with the noise budget limited only by the thermal photons. Some detail for a few of this topics are given below.

2.1 The magnetic material

We are currently working with Yttrium Iron Garnet (YIG), which has a spin density of about $2\times10^{28}/\mathrm{m}^3$ at room temperature, and slightly higher at cryogenic temperature. Highly polished spheres have a linewidth at room temperature of about 2 MHz.

We studied the temperature dependance of the linewidth, and we confirmed what was suggested in the literature: standard YIG samples are contaminated by rare earth (at the ppm level) and wider linewidths is observed at low temperature. High purity YIG spheres instead shows no temperature dependance of the linewidth, down to $\sim$ 10 K. We are now investigating other materials like paramagnets (BDPA, K_3CrO_4) or ferrimagnets (GaYIG, Lithium ferrite).

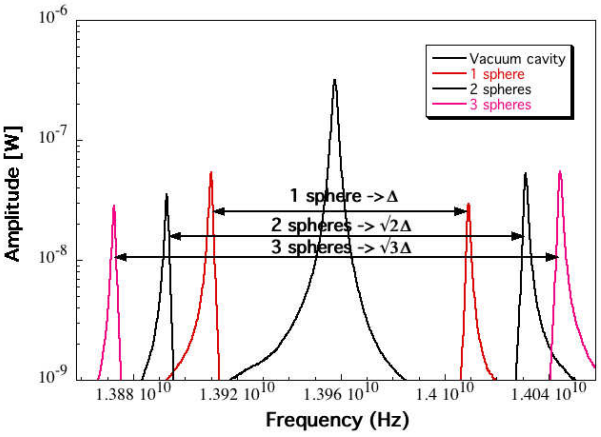

Figure 1: Hybridization measurements with 1, 2 and 3 magnetized YIG spheres coupled to the microwave cavity mode.

Single spheres of YIG are of limited size (a few mm diameter): in order to reach reasonable volumes one has to use many spheres that must be properly aligned to the external polarizing field. The proper alignment can be checked by measuring the coupling between the ferromagnetic resonance of the material and the microwave cavity resonance. In case of strong coupling, hybridization occurs and the single mode splits in two, with a mode separation proportional to the square root of the total number of active spins. Figure 1 shows that the mode separation scales with the square root of the number of spheres as expected. Moreover, no effect on the sample linewidth is evident.

2.2 The resonant cavity

The resonant cavity of the QUAX experiment must provide a high quality factor (from few hundred thousands to 1 million) for the TM110 mode at a resonant frequency of about 48 GHz when immersed in a magnetic field of 1.7 T. Moreover, the cavity must allow the penetration of the external magnetic field without deforming it and its resonant frequency must be tunable in a range of about a hundred MHz. For the R&D phase, the resonant frequency has been reduced to 14 GHz corresponding to $m_a = 60\,\mu$eV and to a lower external field of intensity 0.5 T. We aim at reaching these goals through an optimal mechanical design and the proper choice of inner surface materials. The cavity design foresees conical-shaped end-caps to reduce the current dissipation at interfaces, an asymmetric cross-section of the inner cylinder to remove the mode degeneracy and a frequency tuning obtained through the lateral insertion of longitudinal tuning bars able to shift the frequency of 100 MHz for 2 mm insertion with small deterioration of the quality factor. With a 14 GHz copper-cavity, 2 cm inner diameter and 5 cm length, cooled down to 4 K we reached a quality factor about 50,000. To

improve quality we are investigating hybrid cavities, with copper end-caps and lateral surfaces made of bulk or sputtered type II superconductor: Nb (Figure 2), NbTi film and MgB_2.

A longitudinal cut on the lateral surface allows the magnetic field to penetrate the inner region of the superconducting cylinder. We performed a complete characterization of the Nb cavity with magnetic and RF measurements at 4 K in an external magnetic field up to the critical field, about 0.5 T. The program will continue with tests of NbTi and MgB_2 [3] RF cavities at the nominal critical fields of 0.5 T and 1.7 T.

Figure 2: Nb cavity instrumented before the insertion in the LHe criostat.

2.3 The complete apparatus

We have set-up a reduced scale apparatus to start the evaluation of noise performances of the QUAX detector. A copper cylindrical microwave cavity (resonant frequency 14 GHz) is equipped with a YIG sphere and immersed into a superconducting solenoid. By using a home made ultra stable current generator (at about 30 amps) a 0.5 T field sets the ferromagnetic resonance of the YIG at the cavity resonance frequency. The hybrid modes are then sensed with a critically coupled wire antenna; the antenna output is amplified by an HFET low noise cryogenic pre-amplifier, followed by a room temperature amplifier. The signal is then down converted with a mixer and sampled with a 2 MHz fast ADC. We effectively measure a 1 MHz window centered at one of the two resonant hybrid modes of the system cavity plus YIG. The cavity, the magnet and the pre-amplifier are housed inside a liquid helium cryostat and the working temperature is about 5 K. We have seen that the rms noise coincides with the expected value due to the thermal background, indicating that no extra noise is added by the material. After integration for about an hour, the analysis of the power fluctuations gave us the limit sensitivity of about 10^{-22} W. For the current configuration this correspond to a limit in the axion effective magnetic field of about 10^{-16} T.

Acknowledgments

We would like to thank E. Berto, F. Calaon, M. Iannarelli, G. Pileggi and M. Tessaro for technical help.

References

[1] R. Barbieri *et al.*, Phys. Dark Univ. **15**, 135 (2017).

[2] M. Dine, W. Fischler, and M. Srednicki, Phys. Lett. B **104**, 199 (1981); M. Dine, W. Fischler, and M. Srednicki, Nucl. Phys. B **189**, 575 (1989); A.R. Zhitnitsky, Soviet J. Nucl. Phys. **31**, 260 (1980).

[3] G. Giunchi *et al.*, Supercond. Sci. Technol. **20**, L16-L19 (2007).

Status of the HAYSTAC Experiment

Maria Simanovskaia[1], *Karl van Bibber*[1],
[1]University of California, Berkeley, USA

DOI: http://dx.doi.org/10.3204/DESY-PROC-2017-02/simanovskaia_maria

Dark matter axions may be detected by their resonant conversion to photons in a tunable microwave cavity permeated by a strong magnetic field. HAYSTAC (Haloscope At Yale Sensitive To Axion Cold dark matter) incorporates a dilution refrigerator and Josephson parametric amplifier and has thus achieved a system equivalent noise temperature of twice the Standard Quantum Limit. First data run results exclude axion models a factor of ~ 2.3 above the benchmark KSVZ model over the mass range $23.55 - 24.0$ μeV. These are the first limits within the axion model band in the $10-100$ μeV mass decade. Ongoing R&D is oriented to significantly increase the detector sensitivity through application of a squeezed vacuum state receiver, distributed Bragg reflectors, and photonic band-gap resonators.

1 Introduction

The axion is a compelling dark matter candidate in the 1-100 μeV range that arises from the Peccei-Quinn mechanism to solve the strong charge-parity problem in the Standard Model of Particle Physics [1]. Axions constituting the dark matter of our Milky Way halo may be resonantly converted to a weak RF signal in a tunable high-Q microwave cavity permeated by a strong magnetic field, under the condition that the cavity frequency equal the mass of the axion, i.e. $h\nu = mc^2$ [2]. The conversion power is given by

$$P \sim g_{a\gamma\gamma}^2 \, (\rho_a/m_a) \, B^2 \, Q_C \, V C_{nml} \tag{1}$$

where $g_{a\gamma\gamma}^2$ is the axion-photon coupling, m_a and ρ_a the mass of the axion and its local halo density, B the magnetic field strength, and V, Q_C and C_{nml} the volume, quality factor and form factor of the microwave cavity. While the expected signal power is exceedingly small for all experiments to date ($\sim 10^{-24}$ W), the critical factor for detection is the signal-to-noise ratio,

$$SNR = \frac{P}{k\,T_S}\sqrt{\frac{t}{\Delta\nu_a}} \tag{2}$$

which depends not only upon the signal power, but also the bandwidth of the signal line ($\Delta\nu_a/\nu_a \sim 10^{-6}$ for virialized axions), the integration time t, and most importantly the system noise temperature T_S. The system noise temperature is the sum of the thermal contribution and the noise equivalent temperature contribution from the amplifier,

$$k\,T_S = h\nu\left(\frac{1}{e^{h\nu/kT}-1}+\frac{1}{2}\right) + k\,T_A \tag{3}$$

which for $kT \gg h\nu$, reduces to $T_S \approx T + T_A$. Linear amplifiers are subject to an irreducible noise temperature, called the Standard Quantum Limit (SQL), $kT_{SQL} = h\nu$, but there are strategies to evade this limit, which are explored in HAYSTAC.

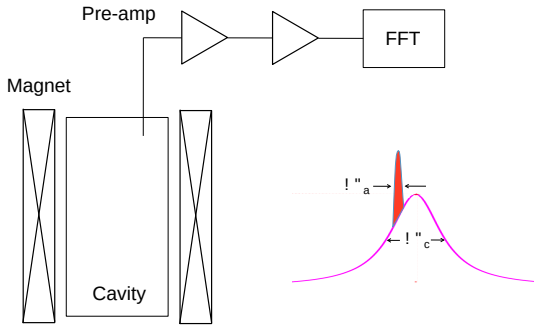

Figure 1: Schematic of the microwave cavity search for dark matter axions. The axion signal is designated by the narrow peak (red) within the bandpass of the cavity (pink).

2 Experiment Description

Our collaboration is composed of groups at Yale University (where the detector is sited), University of California at Berkeley, University of Colorado at Boulder, and Lawrence Livermore National Laboratory. A visual presentation of our axion detector is shown in Figure 2 and a full description of the design and operational experience can be found in Reference [3]. The microwave cavity and Josephson parametric amplifier (JPA) are cooled by a dilution refrigerator to an operating temperature of 100 mK. A magnetic field is applied to the cavity by a superconducting magnet with a maximum field of 9.4 T made by Cryomagnetics, Inc. The JPA requires a magnetic field-free environment to operate, thus a sophisticated magnetic shielding system was designed to cancel out the fringe field from the main magnet less than 75 cm away.

2.1 Cavity

The cavity is a copper-coated, stainless-steel cylinder (25.4 cm long, 10.2 cm diameter) with an off-center tuning rod (5.1 cm diameter). By moving the tuning rod with stepping motors and Kevlar lines, the TM_{010}-like mode frequency is scanned over its dynamic range of $3.6 - 5.8$ GHz. The quality factor of the TM_{010}-like mode of interest is $Q_C \sim 20,000$ when critically coupled.

2.2 Josephson Parametric Amplifier

The receiver is a JPA that is tunable over $4.4 - 6.5$ GHz with 20 dB of gain. The magnetic field-free environment required by the JPA is achieved by an actively excited bucking coil, four persistent 100-turn coils of superconductor, two layers of Amumetal, a thin lead sheet, and a thin niobium sheet in the JPA canister (both lead and niobium sheets are superconducting at the experiment's operating temperature). These multiple layers of field cancellation provide an

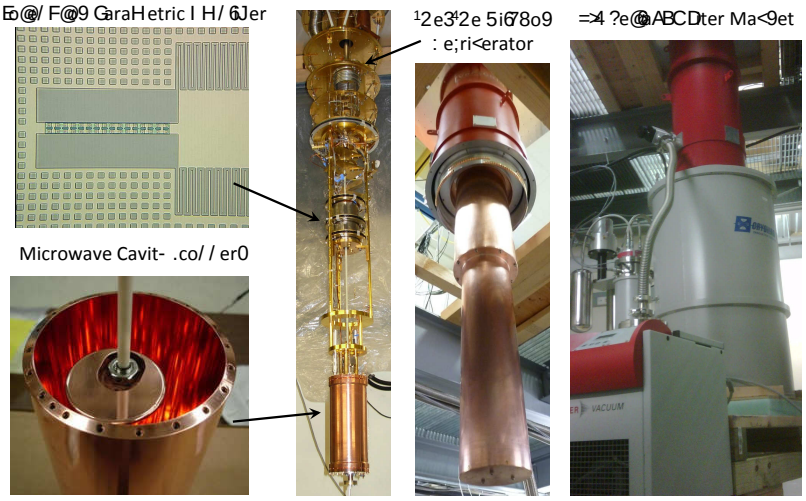

Figure 2: Top left is a microphotograph of the JPA. Bottom left is a photo of the copper-coated, stainless steel resonant microwave cavity with tuning rod inside. To the right of these is a photo of the integrated experiment with the JPA in its magnetic shielding and the cavity on the bottom of the gantry. Next on the right is the same integrated setup covered by thermal shields. Finally, rightmost photo is of the magnet.

operable environment for the JPA where the field changes by less than 0.01 of a flux quantum as the magnetic field is ramped to 9 T.

2.3 Operations

First results from HAYSTAC excluded axions with coupling $g_{a\gamma\gamma} \gtrsim 2 \times 10^{-14}$ GeV^{-1} over the mass range $23.55 < m_a < 24.0\,\mu$eV [4]. The system noise temperature $T_S \sim 1100$ mK was higher than expected due to poor thermal contact between the rod and the cavity. Since the first data run, we have improved the thermal link to the rod and commissioned an AttoCube piezoelectric rotator to smooth tuning. At the time of writing, we have completed our second run with a total noise temperature of approximately 600 mK to extend our exclusion region to $5.6 - 5.8$ GHz; the second run analysis is being finalized.

In the near future, we plan to switch to a more stable dilution refrigerator (Blue Fors), and deploy a squeezed-vacuum state receiver that pushes the limits of sensitivity even further.

2.4 Research and Development

Aside from operating the detector, we are also developing new technologies for improving searches at higher frequencies. As seen in Equations 1 and 2, improving the Q_C and C_{nml} will increase our power and signal-to-noise ratio. Also, while scanning, we encounter frequency ranges in which our TM_{010}-like mode of interest crosses and interacts with other resonant cavity modes. At these mode crossings, we cannot have a good understanding of the conversion power of the axion and therefore of our sensitivity. These mode crossings prevent smooth scanning

and leave gaps in possible exclusion areas. We are working to improve Q_C, C_{nml} and spectral cleanliness of the cavity.

One way to improve spectral cleanliness is to apply photonic band gap (PBG) concepts to the cavity design. A PBG structure is an open lattice with a defect that traps, for example, the TM_{010}-like mode of interest while allowing TE modes to radiate out [5]. Without a forest of TE modes to scan through, we can accelerate the scan rate of the experiment dramatically and take data without missing frequency ranges. Another concept we are working on to suppress unwanted TE modes is cutting slits of sufficient size in the walls of the cavity to prevent azimuthal currents from flowing on the inner surface.

Another R&D effort is to improve the form factor C_{nml} by considering distributed Bragg resonator (DBR) concepts. Strategically-placed sapphire inserts have been used to achieve room temperature $Q \sim 650,000$ of a TE mode at 9.0 GHz [6]. We are looking into applying these concepts by exploring the effect of inserting dielectric shells at natural nodes of a TM_{0m0} mode to confine the mode away from the lossy metal wall. The TM_{030} mode of a 10-cm-diameter cavity with a 2.5-cm-diameter rod with and without a shell is at 12 GHz with form factor $C_{030} \approx 0.1$ and 9 GHz with form factor $C_{030} \approx 0.6$, respectively. Unfortunately, the form factor decreases significantly once the rod is moved off-center and the symmetry is broken, so we are looking into ways to tune while preserving symmetry.

Finally, our collaborators at the University of Colorado / JILA are developing and testing a squeezed-vacuum state receiver that we hope to deploy within the next year. This squeezed-state receiver uses a JPA to initialize the cavity in a squeezed state and reads it out with another JPA [7]. To our knowledge, this would be the first data production experiment of any kind to employ squeezed states of the vacuum.

Acknowledgments

This work was supported by NSF Grants PHY-1306729 and PHY-1362305, Heising-Simons Foundation Grant 2014-182, and U.S. DOE Contract DE-AC52-07NA27344. M. Simanovskaia is supported by NSF Graduate Research Fellowship Grant DGE-1106400 and Berkeley Fellowship.

3 Bibliography

References

[1] R. D. Peccei, and H. R. Quinn, "CP Conservation in the Presence of Pseudoparticles" Phys. Rev. Lett. **38**, 1440 (1977).

[2] P. Sikivie, "Experimental tests of the 'invisible' axion," Phys. Rev. Lett. **51**, 1415 (1983); "Detection rates for 'invisible' axion searches," Phys. Rev. D **32**, 2988 (1985).

[3] S. Al Kenany *et al.*, "Design and operational experience of a microwave cavity axion detector for the $20-100\,\mu$eV range," Nucl. Instrum. Methods Phys. Res. Sect. A **854**, 11 (2017).

[4] B. M. Brubaker *et al.*, "First Results from a Microwave Cavity Axion Search at $24\,\mu$eV," Phys. Rev. Lett. **118**, 061302 (2017).

[5] E. Yablonovich, "Photonic band-gap structures," J. Opt. Soc. Am. B **10**, No. 2 (1993).

[6] C. A. Flory, and R. C Taber, "High performance distributed Bragg reflector microwave resonator," IEEE transactions on ultrasonics, ferroelectrics, and frequency control **44**, No. 2 (1997).

[7] H. Zheng, M. Silveri, R. T. Brierley, S. M. Girvin, and K. W. Lehnert, "Accelerating dark-matter axion searches with quantum measurement technology," arXiv preprint arXiv:1607.02529 (2016).

Towards a medium-scale axion helioscope: the physics case and a proposal in Troitsk

*Sergey Troitsky**

Institute for Nuclear Research of the Russian Academy of Sciences,
60th October Anniversary Prospect 7a, 117312, Moscow, Russia

DOI: http://dx.doi.org/10.3204/DESY-PROC-2017-02/troitsky_sergey

I discuss the physics case for a medium-scale axion helioscope with sensitivities in the axion-photon coupling a few times better than CAST. Search for an axion-like particle with these couplings is motivated by several persistent astrophysical anomalies. Then I report on the project of such a helioscope, TASTE, to be constructed in INR, Troitsk, Russia. On behalf of pre-collaboration, I discuss early conceptual design, existing infrastructure, projected sensitivity and timeline of this experiment.

1 Submission

Recent progress in astrophysics makes it possible to use observational data to search for axions and axion-like particles (ALPs), or to constrain their parameters. Detailed studies of stellar energy losses constrain $g_{a\gamma\gamma} \lesssim 6.6 \times 10^{-11}$ GeV^{-1} at the 68% confidence level, at the same time giving a weak indication in favour of the presence of an axion or ALP with $g_{a\gamma\gamma} \sim (2.9 \pm 1.8) \times 10^{-11}$ GeV^{-1} at the 68% confidence level, see Ref. [2] for references and a wider discussion. However, a much stronger evidence for the existence of an ALP with the photon coupling in this domain comes from the gamma-ray astronomy (for a brief review and more references, see Ref. [3]).

Indeed, the Universe is filled with background radiation, on which energetic gamma rays produce electron-positron pairs [4]. This process limits the mean free path of energetic photons to a small fraction of the Universe, strongly dependent on the photon energy. Analyses of ensembles of gamma-ray sources at distances corresponding to large optical depths indicate [5, 6] that the suppression is much weaker than expected. The statistical significance of this anomaly, 12.4 standard deviations [6], makes it a strong argument in favour of existence of unaccounted processes related to the gamma-ray propagation. Interestingly, all the studies which indicate the anomaly have been based on minimal models of the extragalactic background light (EBL), on the level of the sum of the light from observed galaxies [7], while the very recent dedicated observations making use of two different approaches [8, 9], indicate the EBL intensity twice higher. Proved to be true, these EBL values would make the gamma-ray propagation anomaly even more dramatic.

Potential astrophysical explanations in terms of secondary particles [10, 11] have troubles explaining the effect for most distant sources and, more importantly, are at odds with the ob-

*On behalf of the TASTE group of interest. Based on Ref. [1]

servations of strong variability of gamma-ray sources at large optical depths, e.g. [12]. One is forced to invoke new physics for the solution to the anomaly. The pair-production probability might be modified in the presence of a weak Lorentz-invariance violation; however, this violation would also result in non-observation of any TeV photons by Cerenkov atmospheric telescopes because the development of photon-induced air showers would also be suppressed, and is therefore excluded [13, 14].

The remaining viable explanation points to ALPs. Thanks to the interaction (**??**), photon and ALP mix in external magnetic fields [15, 16], while the ALP does not produce e^+e^- pairs. Depending on the parameters, this may result either in axion-photon oscillations in intergalactic magnetic fields, which would enlarge the mean free path of photons from distant sources [17, 18], or in a conversion of a part of emitted photons to ALPs in the magnetic field in the source or in its close environment, subsequent propagation of these ALPs through the Universe and reconversion back to photons in the Milky Way or its surroundings [19, 20]. Present upper limits on extragalactic magnetic fields together with constraints on ALP parameters from non-observation of gamma radiation from supernova SN1987A, persistence of the gamma-ray propagation anomaly up to high redshifts and some hints on the Galactic anisotropy in the anomaly manifestation make the second scenario more favourable [21], though the first one is not yet excluded. The second, Galactic-conversion, scenario may be realized for $g_{a\gamma\gamma} \sim \left(10^{-11} - 10^{-10}\right)$ GeV^{-1} and $m_a \sim \left(10^{-9} - 10^{-7}\right)$ eV. Experimental searches for a particle with parameters in this range is therefore strongly motivated.

Like other stars, our Sun contains a huge thermonuclear reactor in its center, and axions or ALPs, if exist, should be produced there. They can be detected on the Earth with an axion helioscope [15], a tube pointing to the Sun and filled with magnetic field allowing for ALP-photon conversion and subsequent photon detection. The CERN Axion Solar Telescope (CAST) is, up to day, the most powerful helioscope which has recently delivered the world-best upper limit on $g_{a\gamma\gamma}$ [22]. Amusingly, a weak excess of events was found in some runs, but it is not statistically significant. CAST has now finished its solar axion runs. An ambitious new project, the International Axion Observatory (IAXO), has been proposed a few years ago [23, 24] and is now at the research and design stage.

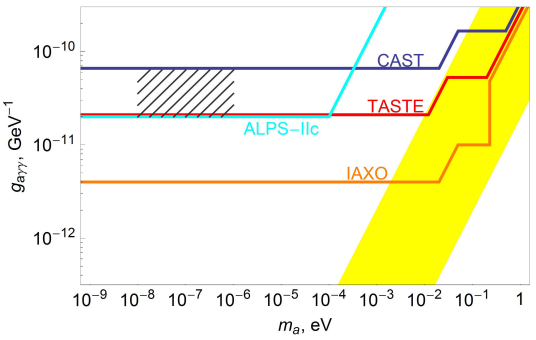

Figure 1: A sketch of comparison of sensitivities of proposed experiments to ALP parameters with the CAST limits. The yellow band is favoured by QCD axion models, the hatched area is favoured by the Galactic ALP conversion scenario explaining the anomalous transparency of the Universe.

In Fig. 1, we compare the projected sensitivity of our helioscope (Troitsk Axion Solar Telescope Experiment, TASTE) with those of two other projects aimed to explore the axion-photon coupling beyond the CAST limits, IAXO and ALPS-IIc.

Both projected experiments plan to cover the range of the parameter space motivated by the gamma-ray transparency of the Universe. However, there are significant differences with our proposal, which make all three projects complementary.

Indeed, ALPS-IIc, a light-shining-through-wall experiment, will be based on the resonant-

regeneration technique, which has not been demonstrated at work yet. If it works as planned, the first scientific runs are expected in 2020. Compared to helioscopes, this experiment will not cover the region of higher-mass ALPs and therefore will not explore the standard QCD axion scenario.

IAXO is a huge next-generation axion helioscopes with expected sensitivity superceding other projects. Given its scale and cost, the start of the full-scale experiment is planned beyond 2022. TASTE may be considered as a pathfinder for IAXO, aimed to scan physically interesting ALP and axion parameter space at much shorter timescale and at much lower cost.

Since the incoming solar-ALP flux is the same for all devices, it is customary to determine the sensitivity of a new helioscope to $g_{a\gamma\gamma}$ through the CAST sensitivity. Our goal is to have the sensitivity to $g_{a\gamma\gamma}$ three times better than CAST, and this determines technical requirements for the experiment.

The principal benefit of the new device with respect to CAST will be in the cross section of the conversion zone. Indeed, CAST used a decommissioned magnet from the Large Hadron Collider (LHC). For TASTE, we will construct a dedicated magnet so we are free to enlarge the cross-section area. However, the limitation comes from the X-ray telescope: the largest available ones have the diameter of ~ 60 cm. We therefore keep this diameter fixed in our proposal. On the other hand, we plan to use available superconducting cable, whose parameters and amount determine the working magnetic field value $B \sim 3.5$ T and the magnet length $L \sim 12$ m. Our goal is to have the tracking time fraction $\epsilon_t \sim 0.5$. For the X-ray optics, we use parameters of the SODART telescope. The area of the image in the focal plane $a = 0.5$ cm^2 is determined from Eq. (3.8) of Ref. [24]. For the detector efficiency and background, we take the best available presently values. These parameters result in the rough estimate of sensitivity 3 times better than CAST, that is down to $g_{a\gamma\gamma} \sim 2 \times 10^{-11}$ GeV^{-1}.

Two principal complications drive our preliminary magnet design. Firstly, the magnetic field should be perpendicular to the tube axis. Secondly, the entire system should be installed on a moving mount and hence its weight should be minimized. We therefore select a dipole-like magnet with active (iron-free) shielding, inspired in particular by some of proposals for the detector magnets of the Future Circular Collider (FCC), see Ref. [1] for details and references. Active shielding implies the use of additional external coils to close magnetic flux lines and to suppress stray fields. The magnet, in our preliminary conceptual design, consists of three identical sections, each of ~ 4 m length. The bore diameter is 60 cm, as dictated by the X-ray telescope part. The bore will be kept cold in order to possibly host equipment for dark-matter axion searches at certain stages of the project. The coil configuration and the magnetic-field map for one section are presented in Ref. [1].

Our plan is to construct one section first and to test it without the moving mount and the X-ray telescope; we call this stage of the experiment "LabTASTE" because the 4-meter magnet with a cold bore may be used as a laboratory to test various approaches to axion searches. It will be sufficient to perform dark-matter experiments. In parallel, depending on the availability of funds, two other magnet sections will be manufactured and RnD works for the X-ray part, as well as to the technical design of the moving platform, will be finalized.

To make the magnet, we plan to use ~ 35 km of superconducting cable available at INR. It has been manufactured in 1990s for the MELC experiment [25] proposed to search for $\mu - e$ conversion in INR, Troitsk. This experiment has never been launched but the conductor is still kept in INR. Studies suggest that the conductor can be safely used in magnetic fields of ~ 5 T at the current of ~ 3.5 kA, which is implied by our design. We note that the magnet design presented here is very preliminary; parameters of the magnet should be optimized at the

technical-design stage.

In our proposal, we aim at the maximal usage of available resources and plan to benefit from the cryogenic equipment of the Troitsk-nu-mass experiment [26] in INR. At the first stage of the project, LabTASTE, the system will be used in turns with Troitsk-nu-mass.

Though focusing of energetic X-ray photons is not an easy task, numerous X-ray telescopes have been developed for space-based astronomical instruments (a brief overview of their relevant parameters is given e.g. in Ref. [23]). In 1990s, the Soviet–Danish Roentgen Telescope (SODART) [27] has been developed and manufactured for the Spectrum-Roentgen-Gamma (SRG) space observatory which, however, has never been launched. The modern version of the SRG satellite, being considered for launch in 2018, will carry other scientific instruments. We propose to use one of two SODART X-ray mirrors in the TASTE project.

For the TASTE experiment, we plan to select the appropriate X-ray detector through additional RnD studies. Options to be considered include several solid-state detectors under development for astrophysics, high-energy physics and axion searches. The approaches followed by various groups participating in TASTE are described e.g. in Refs. [28, 29, 30]. One of the most challenging parameters of the detector is its low background. While present-day background rate values for astrophysical detectors are too high for our purposes, they are dominated by cosmic-ray contamination, which will be reduced by a combination of the passive shielding and a dedicated veto system. The detectors themselves will be tested and the shielding will be designed in the Low-background Measurement Laboratory in Baksan Neutrino Observatory of INR. Details of the detector design will be discussed elsewhere.

As discussed above, we preview two stages of the experiment, LabTASTE and the full TASTE. Subject to available funds, these projects may be realized in parallel, and this is the scenario we imply in the timeline presented in Fig. 2. A rough estimate of the budget, not including materials and equipment already available (the superconducting cable, the helium plant, the vacuum vessels and the X-ray telescope, as well as available infrastructure at the INR campus in Troitsk), gives ~ 5.5 MEuro, of which ~ 1.4 MEuro for LabTASTE.

To summarize, we propose a multi-purpose discovery experiment to search for axions and other hypothetical light particles, predicted by extensions of the Standard Model of particle physics and motivated by recent astrophysical observations. Our projected device, with its total cost on the scale of ~ 5 MEuro, would test, on the timescale of less than 5 years, several models of the anomalous transparency of the Universe, dark matter and even dark energy, as well as a particular part of the parameter space relevant for the axion solution of the strong CP problem.

Acknowledgments

The author thanks the organizers for their kind invitation to the 13th Patras workshop in Thessaloniki and for the exciting scientific atmosphere there. This was the first public announcement of the TASTE project, and I appreciate very much hot and productive discussions during the workshop, notably with Maurizio Giannotti, Igor Irastorza, Axel Lindner, Javier Redondo, Andreas Ringwald, Yannis Semertzidis, Claude Vallee and many others, not counting our discussions within the TASTE team just starting its life.

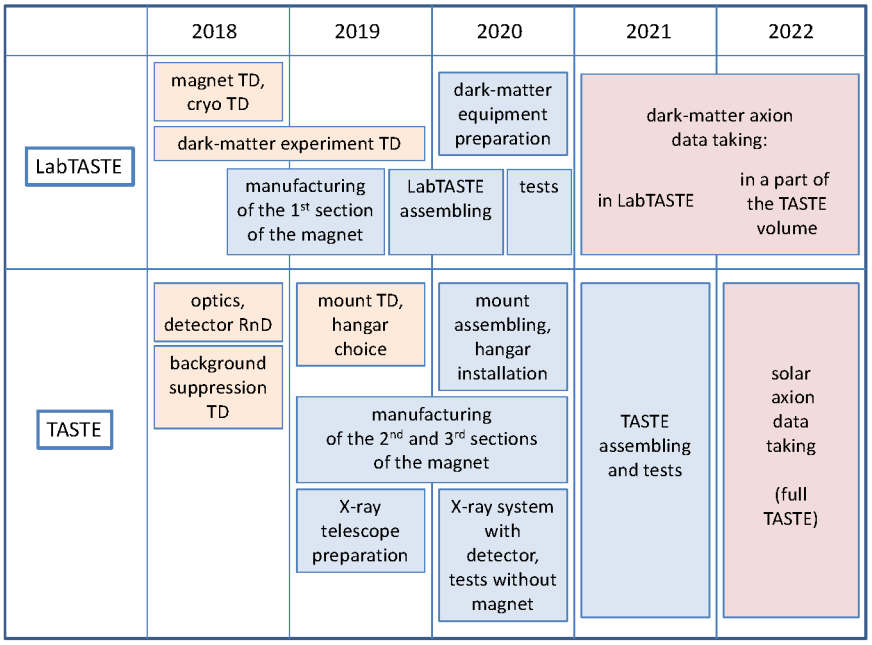

Figure 2: TASTE estimated timeline.

References

[1] V. Anastassopoulos *et al.* [TASTE Collaboration], arXiv:1706.09378 [hep-ph] (*JINST*, in press).

[2] M. Giannotti, I. Irastorza, J. Redondo and A. Ringwald, *JCAP* **1605** (2016) no.05, 057 doi:10.1088/1475-7516/2016/05/057

[3] S. V. Troitsky, *JETP Lett.* **105** (2017) 55 doi:10.1134/S0021364017010052

[4] A.I. Nikishov, *Sov. Phys. JETP* **14** (1962) 393 [*ZhETF* **41** (1962) 549].

[5] D. Horns and M. Meyer, *JCAP* **1202** (2012) 033 [arXiv:1201.4711 [astro-ph.CO]].

[6] G. I. Rubtsov and S. V. Troitsky, *JETP Lett.* **100** (2014) 355 [*Pis'ma ZhETF* **100** (2014) 397] [arXiv:1406.0239 [astro-ph.HE]].

[7] R.C. Keenan, A.J. Barger, L.L. Cowie and W.-H. Wang, *Astrophys. J.* **723** (2010) 40 [arXiv:1102.2428].

[8] S. Matsuura *et al.*, *Astrophys. J.* **839** (2017) 7 doi:10.3847/1538-4357/aa6843

[9] K. Mattila, P. Vaisanen, K. Lehtinen, G. von Appen-Schnur, Ch. Leinert, *Mon. Not. Roy. Astron. Soc.* (2017) accepted [arXiv:1705.10790 [astro-ph.GA]].

[10] W. Essey and A. Kusenko, *Astropart. Phys.* **33** (2010) 81 doi:10.1016/j.astropartphys.2009.11.007

[11] T. A. Dzhatdoev, E. V. Khalikov, A. P. Kircheva and A. A. Lyukshin, *Astron. Astrophys.* (2017) accepted doi:10.1051/0004-6361/201629660

[12] A. Abramowski *et al.* [H.E.S.S. Collaboration], *Astrophys. J.* **802** (2015) no.1, 65 doi:10.1088/0004-637X/802/1/65

[13] G. Rubtsov, P. Satunin and S. Sibiryakov, *Phys. Rev.* D **89** (2014) 123011 doi:10.1103/PhysRevD.89.123011

[14] G. Rubtsov, P. Satunin and S. Sibiryakov, *JCAP* **1705** (2017) 049 doi:10.1088/1475-7516/2017/05/049

[15] P. Sikivie, *Phys. Rev. Lett.* **51**, 1415 (1983) [Erratum-ibid. **52**, 695 (1984)].

[16] G. Raffelt and L. Stodolsky, *Phys. Rev.* D **37**, 1237 (1988).

[17] C. Csaki, N. Kaloper, M. Peloso and J. Terning, *JCAP* **0305** (2003) 005 [hep-ph/0302030].

[18] A. De Angelis, M. Roncadelli and O. Mansutti, *Phys. Rev.* D **76** (2007) 121301 [arXiv:0707.4312 [astro-ph]].

[19] M. Simet, D. Hooper and P. D. Serpico, *Phys. Rev.* D **77** (2008) 063001 [arXiv:0712.2825 [astro-ph]].

[20] M. Fairbairn, T. Rashba and S. V. Troitsky, *Phys. Rev.* D **84** (2011) 125019 [arXiv:0901.4085 [astro-ph.HE]].

[21] S. Troitsky, *Phys. Rev.* D **93** (2016) 045014 doi:10.1103/PhysRevD.93.045014

[22] V. Anastassopoulos *et al.* [CAST Collaboration], *Nature Phys.* **13** (2017) 584 doi:10.1038/nphys4109

[23] I. G. Irastorza *et al.*, *Towards a new generation axion helioscope*, *JCAP* **1106** (2011) 013 doi:10.1088/1475-7516/2011/06/013

[24] E. Armengaud *et al.*, *JINST* **9** (2014) T05002 doi:10.1088/1748-0221/9/05/T05002

[25] R. M. Dzhilkibaev and V. M. Lobashev, *Sov. J. Nucl. Phys.* **49** (1989) 384 [*Yad. Fiz.* **49** (1989) 622].

[26] V. N. Aseev *et al.* [Troitsk Collaboration], *Phys. Rev.* D **84** (2011) 112003 doi:10.1103/PhysRevD.84.112003

[27] J. Polny, N.J. Westergaard, F.E. Christensen, H.U. Noergaard-Nielsen and H.W. Schnopper, *Proc. SPIE* **3113** (1997) 349. doi:10.1117/12.278864;

[28] A. V. Derbin, I. S. Drachnev, A. S. Kayunov and V. N. Muratova, *JETP Lett.* **95** (2012) 339 [*Pisma Zh. Eksp. Teor. Fiz.* **95** (2012) 379] doi:10.1134/S002136401207003X

[29] E. Verbitskaya *et al.*, *JINST* **12** (2017) C03036. doi:10.1088/1748-0221/12/03/C03036

[30] V. Levin *et al.*, *Proc. SPIE* **9905** (2016) 990551.

CULTASK, Axion Experiment at CAPP in Korea

Woohyun Chung[1],

[1]Center for Axion and Precision Physics Research, IBS, Korea

DOI: http://dx.doi.org/10.3204/DESY-PROC-2017-02/woohyun_chung

CAPP's flagship axion experiment, CULTASK has been built on a low vibration facility at Munji campus of KAIST in Korea. We have so far installed 4 dilution refrigerators with two 8T superconducting magnets, which allow us to explore axion mass range of 2∼ 2.5 GHz and 1.35∼1.6 GHz, respectively. A resonant cavity (10 cm OD) with a sapphire tuning rod driven by piezoelectric actuator system was successfully cooled down below 30 mK and showed very high unloaded Q-factor (∼120,000) even under 8T magnetic field. RF receiver employs 1K HEMT amplifier out of the cavity, but the design is flexible enough to replace it with SQUID amplifier when R&D is completed soon. I will present the status and possibly the very first data of CULTASK and our future plans. I will also discuss about the progress of our R&D projects, development of superconducting cavities and SQUID amplifiers.

1 Introduction

The design of the axion experiment at the Center for Axion and Precision Physics Research (CAPP) of the Institute for Basic Science (IBS) of Korea is based on P. Sikivie's haloscope technique[1] which has been refined by the Axion Mark Matter eXperiment (ADMX)[2] since 1996. In this scheme, axions resonantly convert to microwave photons by a reverse Primakoff interaction inside a tunable cavity permeated by a strong magnetic field. The feeble signal from the cavity is amplified through a SQUID amplifier and transmitted to a room temperature RF receiver unit to be processed further. HAYSTAC[3] recently reported results from a new microwave cavity detector designed to search axions in a mass band above 10 μeV, employing advanced quantum electronics.

CAPP's first small scale axion detector is ready to make an engineering run and we are in parallel driving a research and development plan to achieve the sensitivity required for the wider range of axion models. The R&D plan includes high field superconducting magnets with various bore sizes (18T with 7 cm, 25T with10 cm and 12T 32 cm bore), high Q-factor superconducting cavities, high-gain gigahertz superconducting quantum interference device (SQUID) amplifiers and multi-cavity phase locking scheme for higher axion mass.

2 R&D Projects for Axion Research at CAPP

A powerful 25 T superconducting magnet is being developed and will be delivered by BNL (Brookhaven National Laboratory) in early 2019. This ultra high field magnet being developed by BNL has exceptionally big 10 cm bore and is based on a next generation technology called HTS (High Temperature Superconductor). Meanwhile, 18T superconductor magnet with 7 cm bore has been fabricated by Korean company, SuNAM with the same HTS technology will be delivered on September this year. Another superconducting magnet in the pipeline is a big bore (32 cm) LTS magnet with 12T. The compact (outer diameter of only 30 cm) design of the 25 T HTS magnet is intended to produce even higher field above 35T by adding a layer of 12T LTS magnet outside in the future. If successful, this magnet will be the highest-field superconducting magnet in the world with HTS technology.

The effort of developing high-Q factor cavity is lead by Prof. Jhinhwan Lee of KAIST (Korea Advanced Institute of Science and Technology). There are two routes we are trying to make the cavity's inner surface superconducting to increase the Q-factor for the frequency range of interest, 1 to 5 GHz. One is to coat superconductors directly (for example, by sputtering) to the inner surface of resonant cavities and the other is to apply HTS tapes to the inner wall. Various configurations and different coating materials are being experimented now to overcome the effect of high magnetic field (>8T) that goes through the cavity and to achieve the high Q-factor ($> 10^6$) for the resonant mode of choice (TM_{010}). This is a rather long term project to pursue in parallel with others. Meanwhile we have prepared and tested variety of sample cavities (OFHC Cu, 5N Al and 6N Al) for enhancing Q-factors in a cryogenic temperature. The technique of annealing is crucial for improving a Q-factor and we are at the stage of calibrating annealing furnace. The other important factor that has an impact on Q-factor is surface roughness. The high precision diamond-cutting technology is employed and the surface tolerance is less than 50 nm.

Even though increasing the magnetic field inside and the Q-factor of the resonant cavity would raise the conversion power of axions to photons, the biggest effect could be the temperature of the whole detector system which is usually the sum of the physical temperature of the resonant cavity including a tuning rod and the noise temperature of RF components. The RF noise temperature is dominated by that of the first amplifier, 1K HEMT or SQUID amplifier in our case. In order to search the wide range of axion mass in a reasonable time period, lowering the system temperature is essential to increase the scanning speed of the detector. Our axion detector already exhibits the coldest physical temperature (<30 mK), however 1K HEMT shows around 1 K of noise temperature yet. It is therefore crucial for CAPP to utilize recent progress in quantum electronics technology of SQUID or JPA (Josephson Parametric Amplifier), to reduce the noise and push it close to quantum limit ($\sim$ 50 mK per GHz) in order to improve the signal-to-noise ratio and speed up the experiment.

The first sample of dc SQUID amplifiers (center frequency of 2.5 GHz) developed by Dr. Yong-Ho Lee of KRISS (Korea Research Institute of Standards and Science) and commercially available ez-SQUID (by Michael Mueck) have been delivered and being tested now. We are also considering the collaboration with IPHT(Leibniz Institute of Photonic Technology) for developing SQUIDs working for different ranges of frequencies. JPA is another excellent candidate for extremely low noise amplifier that becomes very popular these days because of quantum computing (Qubits). We are currently testing one JPA from Konrad Lehnert of JILA (Joint Institute for Laboratory Astrophysics), but the JPC(Josephson Parametric Converter) from Yale's spin-off company, QCI is also on our list of future purchase.

3 CAPP Ultra Low Temperature Axion Search in Korea (CULTASK)

Refrigerators					Magnets			
Manufacturer	Model	Install ation	Usage	Location	Strength & Bore size	Material	Manufacturer	Delivery
BlueFors (BF3)	LD400	2016	RF and Cavity test	RF room				
BlueFors (BF4)	LD400	2016	JPA & RF chain test	RF room				
Janis	HE3	2017	Magnet test	LVP 4	9T 12 cm	NbTi	Cryo-Magnetics	2017
BlueFors (BF5)	LD400	2017	Axion Exp DAQ & RF	LVP 6	8T 16.5 cm	NbTi	AMI	2016
BlueFors (BF6)	LD400	2017	Axion Exp Large bore	LVP 7	8T 12 cm	NbTi	AMI	2017
Leiden	DRS1000	2017	Axion Exp	LVP 3	25T 10 cm	HTS	BNL/CAPP	2019
Oxford	Kelvinox	2017	Axion Exp	LVP2	12T 32 cm	NbSn	Oxford	2019

Figure 1: Refrigerators and Magnets at CAPP (KAIST Munji campus)

CAPP's experimental hall is finally ready in a building located at KAIST Munji campus with completed low vibration facility for 7 stations, each with a 20 ton concreate block sitting on air springs. Adding two more dilution refrigerators (BlueFors LD400) installed and tested in March 2017, we are now operating 4 dry-type dilution refrigerators and three wet-type refrigerators will be added to the low vibration pads (LVP) later this year.

Currently, two refrigerators are designed for testing RF components (directional couplers, cryogenic circulators, resonant cavities and HEMT or SQUID amplifiers) and the other two refrigerators equipped with 8T superconducting magnet (12 cm and 16.5 cm inner bores) are for setting up small scale axion engineering runs. These refrigerators are designed to cool down and warm up relatively quick ($20 \sim 24$ hours or $40 \sim 48$ hours when there is a 50 kg magnet attached) and fully automatic with a script so that it could cool down all the way with a touch of a button. Figure 1 lists refrigerators and superconducting magnets installed and to be installed in 2017.

3.1 Engineering Run in 2016

We have set up a small scale but rather complete, mid-to-low sensitivity axion experiment with one of the BlueFors dilution refrigerators as a starter. This detector includes 8T NbTi superconducting magnet, 9 cm inner diameter OFHC Cu cavity (split type), cryogenic RF chain (antenna probe, directional coupler, cryogenic circulators and 1K HEMT amplifiers), and a system of room temperature RF receiver for readout. In addition, there is a DAQ system (CULDAQ) that controls, monitors the whole detector, and collects and stores data for analysis.

The split-type microwave resonant cavity of 9 cm inner diameter (2.5 GHz for TM_{010} mode) was fabricated and a support structure with frequency tuning system. The frequency tuning system with a sapphire tuning rod controlled by piezoelectric actuator has gone through a

precision test recently, with a rotator resolution of 1/1000 degree, which corresponds to 2.5 $\sim$ 5 kHz per step. The linear piezoelectric actuator controls the antenna to extract the signal from the cavity. After the annealing and surface treatment, cavity's Q-factor at low temperature reached around 120,000 when sapphire tuning rod was at the center. The physical temperature of the cavity and the support structure reaches 28 mK with complete setup including antenna probe and frequency tuning rod that are connected to piezoelectric actuators. Sapphire tuning rod is designed to be thermally linked to the cavity.

The cryo-RF receiver chain has been set up with 1K HEMT amplifier (right out of the cavity) that dominates noise temperature budget and the total system temperature ranges from 1.4 to 2 K, as expected. Without quantum-limited SQUID amplifiers, we won't be able to reach KSVZ[4][5] sensitivity, however, this engineering run could provide us a great opportunity to prepare ourselves for evaluating and maximizing performance of other RF electronics components. SQUID amplifier test is well on the way and it is possible to incorporate one in our chain before this year ends.

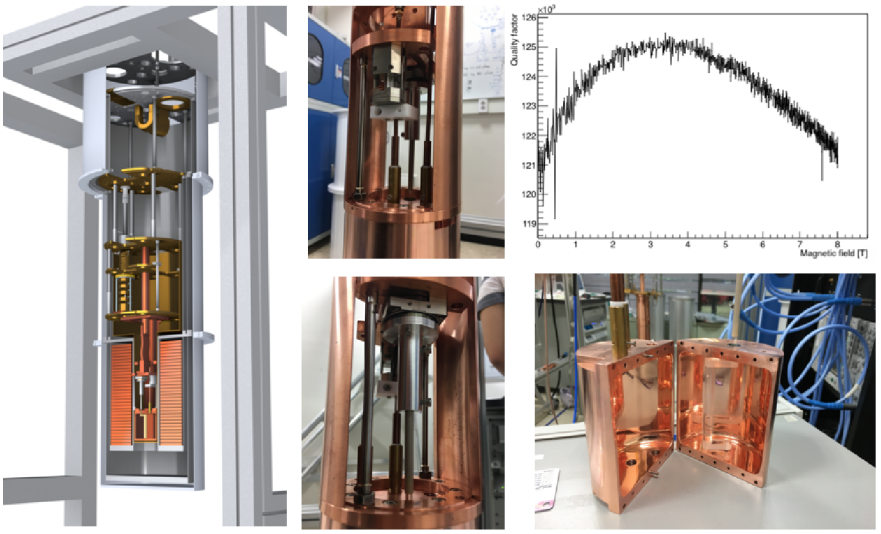

Figure 2: CULTASK Resonant cavity and Frequency Tuning System in Dilution Refrigerator

Figure 2 shows a complete axion detector set-up with frequency tuning system. The split cavity with sapphire rod is also shown and the plot exhibits how the cavity Q-factors changes when magnetic field ranging 0 to 8 teslar.

4 Plans beyond 2017

Four dilution refrigerators are operational now with two 8T NbTi superconducting magnets (12 cm and 16.5 cm inner bore) for CULTASK engineering runs. Three more wet-type refrigerators will be added and the more powerful 18T 7cm bore HTS magnet is scheduled to be delivered at the end of this year. More superconducting magnets with much higher field (25 T) and bigger bore size (35 cm) are also planned in the pipeline. Powerful magnets with different bore

sizes along with efforts on multi-cavity phase locking study would help us to search axions throughout the whole possible mass range. Employing quantum-limited SQUID amplifier or JPA will provide huge improvements on booting axion conversion power and scanning speed, and eventually pave a way to search axions KSVZ QCD axion sensitivity region and beyond.

5 Conclusion

Our quest to establish a state-of-the-art axion experiments in Korea is well on the way. The low vibration experimental space is complete, 7 dilution refrigerators are going to be running next year, powerful and bigger bore superconducting magnets are going to be delivered, and the engineering run of CULTASK is ready to go forward at this stage. We should be able to start collecting physics quality data this year, at least for a single frequency. The addition of SQUID amplifiers, ultra high field magnets and high Q-factor cavities with superconducting coating will improve the sensitivity and make a major contribution to axion research in coming years.

6 Acknowledgments

This work was supported by IBS-R018-D1-2017-a00/ IBS-R018-Y1-2017-a00 in the Republic of Korea.

References

[1] P. Sikivie, Phys. Rev. Lett. 41 (1983) 1415

[2] S. J. Asztalos *et al.*, Phys. Rev. Lett. 104, 041301 (2010)

[3] B. M. Brubacker *et al.*, Phys. Rev. Lett. 118, 061302 (2017)

[4] J. E. Kim, Phys. Rev. Lett. 43, 103 (1979).

[5] M. A. Shifman, A. I. Vainshtein and V. I. Zakharov, Nucl. Phys. B 166, 493 (1980).

Searching for Axion Like Particles using Spin Polarized Noble Gases and Other Methods

H. Yan, H. Zheng, M. Peng, X.Q. Tu

Key Laboratory of Neutron Physics, Institute of Nuclear Physics and Chemistry, CAEP, Mianyang, Sichuan, 621900,China

DOI: http://dx.doi.org/10.3204/DESY-PROC-2017-02/yan_hai

Exotic spin dependent interactions can be meditated by ALPs(Axion Like Particle). Not only ALPs are possible candidates for dark matter, but also they might provide the most promising solution to the strong CP problem. Furthermore, recently, various models of new physics beyond the standard model have been studies in which new massive particles such as axion, familon, and majoron, etc. were theoretically introduced. Many of these exotic new interactions are spin dependent. For these interactions to be detected, the source or the probe particles have to be spin polarized. Spin polarized neutron beam, atom beam or noble gases are good probes to detect these new interactions. We proposed to use ^{3}He atom beams to search for three types of new interactions[1]. Using the atom beam method, sensitivities on three different types of spin dependent interactions could be improved by as much as 10^2 to 10^8 over the current experiments at the millimeter range. We Searched for New Spin- and Velocity-Dependent Interactions by spin relaxation of polarized ^{3}He Gas. Using the best available measured T_2 of polarized ^{3}He gas atoms as the polarized source and the Earth as an unpolarized source, we obtain constraints on two new interactions. We present a new experimental upper bound on possible vectoraxial-vector (VVA) type interactions for ranges between 1 and 10^8 m[2].

1 Introduction

New physics beyond the Standard Model is possible. New interactions meditated by new particles were theoretically proposed in many occasions[3] . New macroscopic interactions meditated by WISPs (weakly-interacting sub-eV particles) is an example. The interaction ranges of these new forces range from nanometers to astronomical distance scales. The fact that the dark energy density is on the order of (1 meV)^4 corresponding to a length scale of 100 μm also encourages people to search for new physical phenomena around this scale [**?**]. The Axion is another example. It is not only a possible dark matter candidate but also provides probably the most promising solution to the strong CP problem. Various experiments have been performed or proposed recently to search for a subset of these new interactions which could couple to the spin of the neutron/electron[4, 5, 6, 7, 8, 9, 10, 11, 1].

2 Another Motivation to Search for New Interactions

The idea that new interactions might be spin dependent is quite fascinating. Except motivations for solving the dark matter and the strong CP problem, there could be another motivation.

Figure 1: Basic properties of two fundamental particles

As shown in Fig.1, if there are two fundamental particles, what are their most important properties? Probably, they are the mass, charge and spin of the particles.

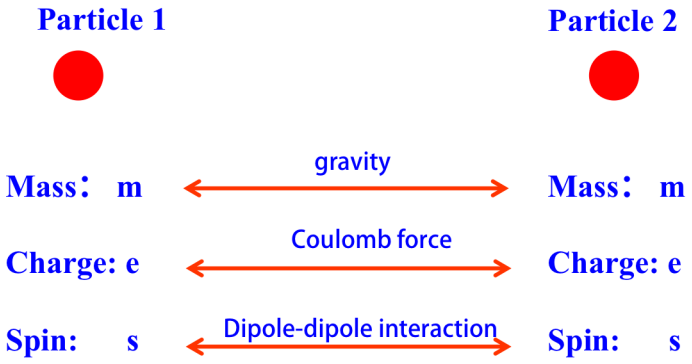

Figure 2: Conventional interactions between two fundamental particles

As shown in Fig.2, for the two fundamental particles, there are conventional interactions which couple their fundamental properties. In more detail, there is gravity which couples the two particles's mass, Coulomb force which couples the two charges and magnetic dipole-diople interaction which couples two spins.

Could it be possible that there are new interactions which can couple different types of the particle properties? As shown in Fig.3, could there be a new interaction which couples the

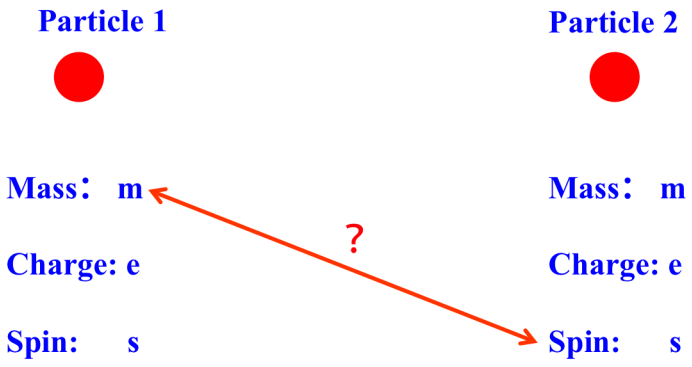

Figure 3: New interactions which can couple different types of properties

mass to the spin of the particles? Considering mixing is not uncommon in modern physics, new experiments measuring the interactions shall be performed to verify if the interactions exist.

3 Several New Spin Dependent Interactions

In Ref.[12], interactions between non-relativistic fermions assuming only rotational invariance can be classified into 16 different operator structures involving the spin and momenta of the particles. For all these sixteen interactions, only one interaction does not require either of the two particles to be spins polarized; six interactions require at least one particle to be spin polarized and the remaining nine require both particles to be spin polarized.

Experimental constraints on possible new interactions of mesoscopic range which depend on the spin of one or both of the particles are much less stringent than those for spin-independent interactions. This is not surprising since macroscopic objects with large nuclear or electron polarization are not easy to arrange outside an environment that includes large magnetic fields, which can produce large systematic effects in delicate experiments. On the other hand the addition of the spin degree of freedom opens up a large variety of possible new interactions to search for which might have escaped detection to date.

Among the six type interactions which only one particle needs to be spin polarized, the scalar-pseudoscalar interaction $V_{SP}(r)$($V_{9,10}$ in Ref.[12]'s notation) originated from the coupling $\mathcal{L}_\phi = \bar{\psi}(g_s + ig_p\gamma_5)\psi\phi$[13, 14],or the monopole dipole interaction has begun to attract more scientific attention recently. The interaction between the polarized spin 1/2 fermion of mass m and another unpolarized nucleon can be expressed as:

$$V_{SP}(r) = \frac{\hbar^2 g_S g_P}{8\pi m}\left(\frac{1}{\lambda r} + \frac{1}{r^2}\right)\exp\left(-r/\lambda\right)\vec{\sigma}\cdot\hat{r} \tag{1}$$

where $\lambda = \hbar/m_\phi c$ is the interaction range, m_ϕ is the mass of the new scalar boson,$\vec{s} = \hbar\vec{\sigma}/2$ is the spin of the polarized particle and r is the distance between the two interacting particles.

While for the vector-axial-vector interaction $V_{VA}(r)$($V_{12,13}$ in Ref.[12]'s notation) originated from the coupling $\mathcal{L}_X = \bar{\psi}(g_V\gamma^\mu + g_A\gamma^\mu\gamma_5)\psi X_\mu$, this parity violating interaction has the form:

$$V_{VA}(r) = \frac{\hbar g_V g_A}{2\pi}\frac{\exp(-r/\lambda)}{r}\vec{\sigma}\cdot\vec{v} \tag{2}$$

where $\vec{v}$ is the relative velocity between the probe particle and source particle,$\lambda = \hbar/m_X c$ is the interaction range, m_X is the mass of the new vector boson. $V_{VA}(r)$ is the Yukawa potential times the $\vec{\sigma}\cdot\vec{v}$ factor,which makes this interaction quite interesting. Another interaction requiring only one particle to be spin polarized is the axial-axial interaction $V_{AA}(r)$($V_{4,5}$ in Ref.[12]'s notation), which is also originated from the $\mathcal{L}_X$ coupling, can be written as:

$$V_{AA}(r) = \frac{\hbar^2 g_A^2}{16\pi mc}(\frac{1}{\lambda r} + \frac{1}{r^2})\exp(-r/\lambda)\vec{\sigma}\cdot(\vec{v}\times\hat{r}) \tag{3}$$

All these interactions are in the form of $\vec{s}\cdot\vec{B'}$ where $\vec{B'}$ can be viewed as a pseudo magnetic field[14]. For an unpolarized source mass as a plane plate of thickness d and surface normal vector $\hat{y}$, as in Ref.[15, 14], for a spin polarized probe particle moving with velocity $\vec{v}$, the corresponding pseudo-magnetic fields due to these three interactions can be derived as:

$$\vec{B}_{SP} = \frac{1}{\gamma}\frac{\hbar g_S g_P}{2m}\rho_N\lambda e^{-\frac{\Delta y}{\lambda}}[1-e^{-\frac{d}{\lambda}}]\hat{y} \tag{4}$$

$$\vec{B}_{VA} = \frac{2}{\gamma}g_V g_A\rho_N\lambda^2 e^{-\frac{\Delta y}{\lambda}}[1-e^{-\frac{d}{\lambda}}]\vec{v} \tag{5}$$

$$\vec{B}_{AA} = \frac{1}{\gamma}\frac{g_A^2}{4}\rho_N\frac{\hbar}{mc}\lambda e^{-\frac{\Delta y}{\lambda}}[1-e^{-\frac{d}{\lambda}}]\vec{v}\times\hat{y} \tag{6}$$

where $\Delta y > 0$ is the distance from the probe particle to the sample surface,ρ_N is the nucleon number density of the sample,γ the gyromagnetic ratio of the probing particle.

4 Searching for New Interactions Using Polarized ^3He Beams

In order to further improve the sensitivity of detecting the spin dependent short range interactions, we propose an experiment using nuclear spin polarized ^3He atom beams. Though in principle other spin-1/2 species as ^{129}Xe might also work, the polarized ^3He beam technique is more convenient since it has been well developed and applied to study the surface dynamics in condensed matter physics for many years[16, 17]. Ref.[18] is a very nice review for the recent developments of the so called polarized ^3He spin-echo technique. The schematic drawing of the proposed experiment is shown as Fig.1. The ^3He beam is firstly produced by the standard atomic beam method[**?**] of expanding compressed ^3He gas through a fine nozzle into vacuum. The speed of the beam can be controlled by adjusting the nozzle temperature. Then the beam is polarized by a beam polarizer which is made of hexapole magnets[17]. High intensity ($1.5\times10^{14} atoms/s$ reported in Ref.[19]), small size($2mm$ beam diameter at target according to Ref.[19]) and high polarization (more than 90% reported in Ref.[16]) ^3He beams can be produced. The polarized ^3He beam will then fly over the surface of the high density sample as a lead plate. The beam polarization will be rotated by the new spin dependent

interactions if exist.

To reduce the background, the sample is firstly shielded with multiple cylindrical layers of high permeability materials as the μ-metal. In this way, the background field could initially be reduced to $\sim 10^{-9}T$[20]. Then the sample is further shielded by several superconducting layers as thin lead foils. The residual field could be reduced to be less than $10^{-11}T$[21]. After passing the sample area, the beam goes through an analyzer which is another series of hexpole magnets[22]. Only the right polarization state atoms are focused and can go through the analyzer to reach the helium detector. To further reduce the background, a double beam design is applied. As shown by Fig.4, another polarized beam produced by the same way will fly over the other sample surface, then it will be analyzed and detected similarly. The new spin dependent interaction signal can be extracted from the rotation difference between the two beam spins. In Ref.[23, 5], the uniformity of the residual background field reaches 10^{-4} level for a $5cm \times 5cm$ beam size. In this work, a higher uniformity is expected since the beam size is much smaller($2mm$ beam diameter). Thus from the difference, at most, a $\sim 10^{-15}T$ background is estimated and it is considered to be the main systematic for the proposed experiment. There are no systematics from the standard model since now the probe particle does not contact with the sample directly.

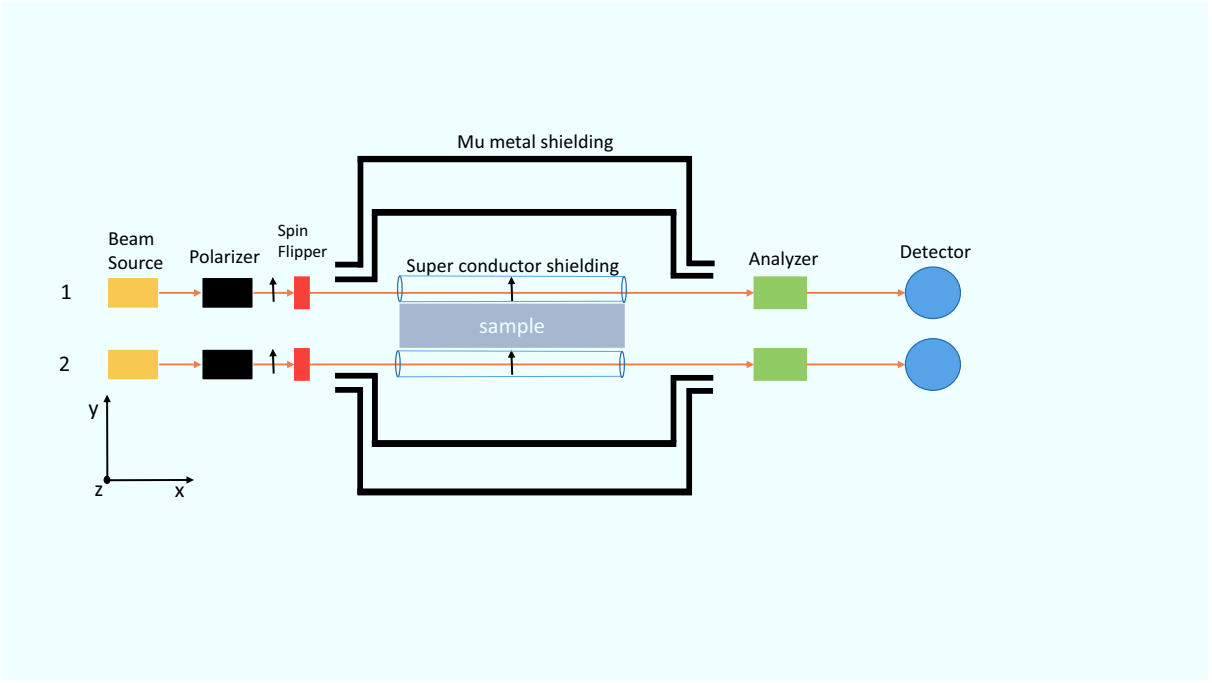

Figure 4: Color online, schematic drawing of the proposed experiment set up,top view .

For different spin dependent interactions, different polarization and beam path arrangements can be made to detect the specified interaction. In more detail, for the interaction $V_{SP}(r)$, the pseudo-magnetic field for beam 1 of Fig.4 is along $+\hat{y}$ direction while for beam 2 $-\hat{y}$ direction.

For $V_{VA}(r)$, the pseudo-magnetic field direction is along the beam moving direction either for beam 1 or beam 2. For $V_{AA}(r)$, the pseudo-magnetic field is along $+\hat{z}$ direction for beam 1 and $-\hat{z}$ for beam 2. To detect V_{SP}, both beam 1 and beam 2 can be set to be polarized along $+\hat{z}$ or $-\hat{z}$ direction. The difference of the spin rotation angles between the two beams will cancel the common background field effect and only leave the pseudo-magnetic field effect since it induces opposite rotation angle for each beam. Since the beams are polarized along $\hat{z}$, the spin rotation difference will not be sensitive to $V_{AA}(r)$ which is along the $\pm\hat{z}$ or $V_{VA}(r)$ which will rotate the two beam polarizations along $\hat{v} = +\hat{x}$ by the same amounts. Similarly, $V_{AA}(r)$ can be detected by setting the both beam polarizations along $+\hat{y}$ or $-\hat{y}$ direction. To detect $V_{VA}(r)$, one of the beam path could be flipped thus the relative velocity between the probe beam and the source sample is reversed. If the beam polarization is along $\hat{y}$ direction, the reversed beam setup will be only sensitive to $V_{VA}(r)$. This beam path reversing feature is possible for the atomic beam techniques since all the components are compact enough while it is not easy to be realized for the neutron beams without losing intensity significantly.

By incorporating background reduction designs as combination shielding by μ-metal and superconductor and double beam paths, the precision of spin rotation angle per unit length could be improved by a factor of $\sim 10^4$. By this precision, in combination with using a high density and low magnetic susceptibility sample source mass, and reversing one beam path if necessary, sensitivities on three different types of spin dependent interactions could be possibly improved by as much as $\sim 10^2$ to $\sim 10^8$ over the current experiments at the millimeter range[1].

5 Searching for New Spin-Velocity Dependent Interactions by Spin Relaxation of Polarized ^{3}He Gas

Spin polarized neutron/atom beams are convenient to probe these spin-velocity dependent interactions since a large relative velocity between the probe and the source can be easily realized. However, the number of the probe particles is limited by the phase space density of the beam. Larger phase space densities of polarized probe particles can be obtained by using ensembles of polarized gases, but the polarized noble gas ensembles which can support sensitive NMR measurements of the spin dynamics needed for this search are usually sealed in glass cells. It would be technically difficult to realize a large relative velocity between the source mass and the probe particles inside delicate glass cells.

Though $\langle\vec{v}\rangle$ is zero for atoms of the glass sealed noble gas, $\langle v^2\rangle$ is not. The nonzero $\langle v^2\rangle$ in the presence of a $\vec{\sigma}\cdot\vec{v}$ type interaction will change the spin relaxation times of polarized noble gases. Although it is a second order effect, in this case there is no need for bulk motion of either the polarized or unpolarized masses in the experiments. Thus it is possible to detect or constrain the new physics by the longitudinal spin relaxation time (T_1) or the transverse relaxation time (T_2) of polarized noble gases. Here T_1 refers to the mean time for a spin polarized ensemble to return to its thermal equilibrium state and T_2 the mean time that polarized spins to lose coherence when processing along the longitudinal main field while the polarization is tipped to the transverse direction [24]. For the best available T_1 [25] and T_2 [26, 27] data, our research indicates that the constraint on α from T_2 is tighter than that from T_1. In what follows, we will first describe how the $\alpha\vec{\sigma}\cdot\vec{v}$ interaction affects the spin relaxation times of the polarized ^{3}He gas, then we will constrain α by using the best available T_2 measured in the experiment. Furthermore, by using this constraint of α and the earth as a source, we obtain new limits

on two different types of new interactions, vector-axial-vector interaction (V_{VA}) and a linear combination of the time component of possible torsion fields from the earth.

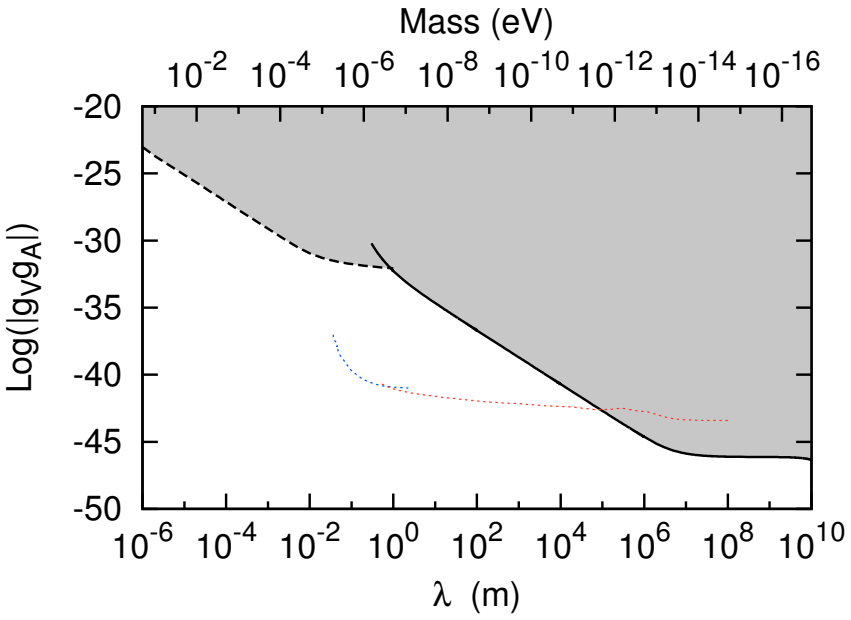

Figure 5: (Color online)Constraint to the coupling constant product $|g_V g_A|$ as a function of the interaction range λ(new vector boson mass). The bold solid line is the result of our previous work[2]; The dashed line is the result of Ref.[5]; The blue and red dotted lines are the result of Ref.[28] which were derived by combining g_V of Refs.[29, 30] with g_A of Ref.[10] from separate experiments.The dark grey area is excluded by experiments of previous work [5] and this work, both directly constrain $|g_V g_A|$ in a single experiment..

By using the spin relaxation times of polarized ^{3}He gas measured in previous experiments and the earth as a source, we have constrained two types of possible new interactions which are neutron spin-velocity dependent. We found that the best available T_2 relaxation times give slightly better constraints. We derived new experimental limits on possible Vector-Axial type interactions with ranges from $\sim$ 1m to $\sim 10^8$m. At the distance of $\sim 10^8$m, the limit is improved by $\sim$ 16 orders in magnitude in comparison with the previous result of the neutron spin rotation experiment. In combination with the previous result [5] which is more sensitive at short distances, we present the most stringent constraint derived directly from experiments on $g_V g_A$ ranging from $\sim 10^{-6}$m to $\sim 10^8$m (FIG.5). The methods presented in this work open up new possibilities to search for or constrain many possible spin-spin-velocity dependent interactions. By dedicated experiments, an improvement in sensitivity by a factor of $\sim$ 100 might be achieved using these ideas.

6 Acknowledgments

H.Y. would like to thank the organizing committee of the PATRAS meeting for help. We acknowledge support from the National Natural Science Foundation of China, under grant 91636103, 11675152. This work was also supported by National Key Program for Research and Development(Grant 2016YFA0401500 /1/2/3/4).

References

[1] H. Yan, G. A. Sun, J. Gong, B. B. Pang, Y. Wang, Y. W. Yang, J. Zhang, Y. Zhang, **European Physical Journal C**, 10/2014; 74(10).

[2] H.Yan,G.A.Sun,S.M.Peng,Y.Zhang,C.Fu, H.Guo, B.Q.Liu, **Physical Review Letters**,115,182001(2015).

[3] C.P. Patrignani *et al.* (Particle Data Group), Chinese. Phys. C,**40**,100001,(2016).

[4] F. M. Piegsa and G. Pignol, Phys. Rev. Lett. **108**, 181801 (2012).

[5] H.Yan,M.W.Snow,**Physical Review Letters**,**110**,082003(2013).

[6] W. Zheng, H. Gao, B. Lalremruata, Y. Zhang, G. Laskaris, C.B. Fu, and W.M. Snow, Phys. Rev. D **85**, 031505(R) (2012).

[7] M. Bulatowicz *et al.*, Phys. Rev. Lett. **111**, 102001(2013).

[8] K. Tullney, F. Allmendinger, M. Burghoff, W. Heil, S. Karpuk, W. Kilian, S. Knappe-Grüneberg, W. Müller, U. Schmidt, A. Schnabel, F. Seifert, Yu. Sobolev, and L. Trahms, Phys. Rev. Lett. **111**, 100801(2013).

[9] P.-H. Chu, C.H. Fu,H. Gao,R. Khaiwada,G. Laskaris,K. Li,E. Smith, W.M. Snow, H. Yan and W. Zheng, Phys. Rev. D **87**, 011105(R) (2013) .

[10] G. Vasilakis, J.M. Brown, T.W. Kornack, W. Ketter, M.V. Romalis, Phys. Rev. Lett. **104**, 261801(2009).

[11] L. Hunter, J. Gordon, S. Peck, D. Ang, J.F. Lin, SCIENCE, **339**, 928(2013).

[12] B. Dobrescu and I. Mocioiu, J. High Energy Phys. **11**, 005 (2006).

[13] J. E. Moody and F. Wilczek, Phys. Rev. D **30**, 130(1984).

[14] F.M.Piegsa and G.Pignol, Journal of Physics **340**, 012043 (2012).

[15] O.Zimmer, Physcis Letters B **685**,38(2010)

[16] M.DeKieviet, D.Dubbers, C.Schmit, D. Scholz and U.Spinola, Phys. Rev. Lett. **75**, 1919(1995).

[17] A.P.Jardine, P.Fouquet, J.Ellis and W.Allison, Rev. Sci. Instrum.**72**, 3834(2001).

[18] A.P.Jardine, H.Hedgeland, G.Alexandrowicz, W.Allison and J.Ellis, Progress in Surface Science **84**,323(2009).

[19] P.Fouquet,A.P.Jardine, S.Dworski, G.Alexandrowicz, W.Allison and J.Ellis, Rev. Sci. Instrum.**76**, 053109(2005p).

[20] T.W.Kornack, S.J.Smullin, S.-K. Lee and M.V.Romalis, Appl. Phys. Lett. **90**, 22305(2007).

[21] F.Pavese,Magnetic shielding, Handbook of Applied Superconductivity, Volume 2,Edited by Bernd Seeber Taylor and Francis (1998)

[22] S.Dworski, G.Alexandrowicz, P.Fouquet, A.P.Jardine, W.Allison and J.Ellis, Rev. Sci. Instrum.**75**, 1963(2004).

[23] W. M. Snow *et al.*, Phys. Rev. C **83**, 022501(R) (2011).

[24] C.P. Slichter, Principles of Magnetic Resonance, Springer(1989).

[25] Yu.N. Pokotilovski, Phys. Letts. B **686**, 114 (2010).

[26] A. K. Petukhov, G. Pignol, D. Jullien, and K. H. Andersen, Phys. Rev. Lett. **105**, 170401 (2010).

[27] C. Gemmel *et al.* , Eur. Phys. D **57**, 303(2010).

[28] E.G. Adelberger and T.A. Wagner, Phys. Rev. D, **88**, 031101(R)(2013)

[29] G.L. Smith, C.D. Hoyle, J.H. Gundlach, E.G. Adelberger, B.R. Heckel, and H.E. Swanson, Phys. Rev. D **61**, 022001 (1999).

[30] T.A. Wagner, S. Schlamminger, J.H. Gundlach, and E.G. Adelberger, Classical Quantum Gravity **29**, 184002 (2012).

[31] S. J. Asztalos, R. F. Bradley, L. Duffy, C. Hagmann, D. Kinion, D. M. Moltz, L. J. Rosenberg, P. Sikivie, W. Stoeffl, N. S. Sullivan, D. B. Tanner, K. van Bibber, and D. B. Yu, Phys. Rev. D. **69**, 011101(R) (2004).

Characterization of the CAPP magnetometer for GNOME

Yun Chang Shin[1], *DongOk Kim*[2], *YoungGeun Kim*[2], *Yannis K. Semertzidis*[1,2]

[1]Center for Axion and Precision Physics, IBS, Daejeon, South Korea, 34051
[2]Department of Physics, KAIST, Daejeon, South Korea, 34141

DOI: http://dx.doi.org/10.3204/DESY-PROC-2017-02/yun_chang_shin

The **G**lobal **N**etwork of **O**ptical **M**agnetometers to search for **E**xotic physics (GNOME) is an experiment to search for transient events of axion domain walls based on a novel scheme: synchronous measurements of high precision optical magnetometer signals from multiple stations around the Earth. This collaboration now consists of more than 10 magnetometer stations located geographically well apart from each other. One of them at the Center for Axion and Precision Physics (CAPP) is a newly joined station in Daejeon, South Korea and expects to start the operation of an optical magnetometer for GNOME by the end of 2017. We present initial setup and characterization of the atomic magnetometer at CAPP station.

1 Introduction

Optically pumped atomic magnetometers offer high level of performance and fundamental sensitivity in terms of delicate magnetic field measurement and they have been employed in various applications that require a high sensitive magnetic probe[1]. The inherent high sensitivity of optical magnetometers to spin dynamics may also allow other types of spin interaction from non-magnetic ones[2]. Especially optical magnetometer could be sensitive enough to detect new types of interaction between spin and hypothetical fields postulated by many theories beyond Standard Model[3],[4].

There have been a series of experiments utilizing atomic magnetometers to search for atypical spin-dependent interactions. The basic concept of such experiments is to look for anomalous shift of magnetic field caused by interaction with exotic fields rather than conventional electromagnetic fields. For example, there are experimental searches for short range spin-dependent interactions between polarized species and locally sourced mass[5]. Those experiments normally monitor the interaction between local masses.

The **G**lobal **N**etwork of **O**ptical **M**agnetometers to search for **E**xotic physics (GNOME) is an experiment to search for *transient events* of axion domain walls based on novel scheme : synchronous measurements of high precision magnetometer signals from multiple stations around the Earth. The domain walls of pseudoscalar fields are appearing in various models with spontaneously broken discrete symmetries. Such fields are predicted by many other Standard Model extensions to be made up of a significant fraction of cold dark matter. When the Earth passes through such a pseudoscalar domain wall, the gradient of the pseudoscalar field at the domain wall would exert a brief torque on atomic spins that could be detected by the highly

sensitive atomic magnetometers.

The GNOME consists of ~ 10 dedicated atomic magnetometers located at geographically separated stations on Earth. The target magnetometric sensitivity and bandwidth of each GNOME sensors are to be better than $\sim 1\text{pT}/\sqrt{\text{Hz}}$ and a bandwidth on the order of 100Hz. Each magnetometer is located within a multi-layer magnetic shield to exclude the ambient magnetic noise. The signals from the magnetometers are recorded with accurate timing provided by Global Positioning System (GPS) using a custom GPS-disciplined data acquisition system. The GNOME is designed to characterize such transient events while avoiding erroneous detections by constructing an array of magnetometers in geographically well separated locations among them. In this paper, the principal scheme of magnetometer at the Center for Axion and Precision Physics (CAPP) as a local station of GNOME is discussed.

2 Parameterization

Axion is a hypothetical particle suggested from Peccei-Quinn (PQ) mechanism as a solution of the strong CP problem in Quantum Chromodynamics (QCD). The phenomenological searches indicate that axions are invisible due to the weak coupling with matter which is suppressed by $1/f_a$. This invisibleness is realized by two different models, one is the KSVZ and the other is the DFSZ. The astonishing feature of these axion models is that they predict the formation of topological defects in the early Universe called "domain walls", a finite region in the space where the density vanishes[6],[7].

During the inflation of the early Universe, axions might acquire quantum fluctuations which extend beyond the Hubble horizon one the condition that their masses were lighter than the Hubble parameter. If the quantum fluctuations were large enough, some of the N vacua might be populated in the axion potential and it might eventually lead to the formation of domain walls after the inflation. If one assumes the axion domain walls are the predominant contribution to the cold dark matter, the domain wall may have a quasi-Maxwellian velocity distribution in the galactic reference frame with characteristic virial velocity $v \approx 10^{-3}c$ where c is the speed of light. We assume the rate of encounter with domain wall to be larger than at least once per year to make the experiment feasible. In that case, the accessible parameter space is $L \leq 10^{-3}$ly. The thickness of the such domain wall is assumed as to be on the order of Compton wavelength as

$$d \approx \frac{2\hbar}{m_a c} \approx 400\text{m} \times \frac{1\text{neV}}{m_a c^2}. \tag{1}$$

From Eq.1, one can estimate the duration of the transient signal τ as

$$\tau \approx \frac{d}{v} \approx 1\text{ms} \times \frac{1\text{neV}}{m_a c^2}. \tag{2}$$

If the bandwidth of GNOME magnetometer is set to be ~ 100Hz, it is sensitive to the axion mass $m_a \leq 0.1$neV. The coupling of the pseudoscalar field gradient to the atomic spin $\mathbf{S}$ of particle i can be expressed through the interaction Hamiltonian as

$$H_a = \frac{\hbar c}{f_i}\mathbf{S} \cdot \nabla a(\mathbf{r}); \tag{3}$$

where $\mathbf{S}$ is in the unit of $\hbar$ and the f_i is a coupling constant for the considered particle i. This leads to estimates for the energy shift or torques experienced by the spins of fermion i which is

induced from the interaction with axion domain wall as,

$$\Delta E(i) \approx \frac{\hbar c^2}{4 f_i} \sqrt{\rho_{\rm DM} m_a L}. \tag{4}$$

The more sensitive a GNOME magnetometer is to torque or energy shift, the larger the value of f_i that can be probed. From the basic concept of GNOME, one can estimate characteristics and potential sensitivity for the domain wall search with GNOME. First, the sensitivity of GNOME magnetometer, δB interpreted as energy sensitivity via

$$\delta E = g_F \mu_B \delta B, \tag{5}$$

where g_F is the Lande factor and μ_B is the Bohr magneton. With $g_F = 1/3$, energy shift becomes

$$\delta E \approx 10^{-18}\text{eV}/\sqrt{\text{Hz}} \times \frac{\delta E}{100\text{fT}/\sqrt{\text{Hz}}}. \tag{6}$$

The actual energy uncertainty scales with the square root of the duration of signal, which in turn is inversely proportional to m_a as follow:

$$\Delta E \approx 10^{-18}\text{eV} \times \frac{\delta B}{100\text{fT}/\sqrt{\text{Hz}}} \times \sqrt{\frac{m_a c^2}{10^{-12}\text{eV}}} \tag{7}$$

where the parameterization of the mass relative to 10^{-12}eV corresponding to the signal duration $\sim$ 1s.

3 Optical magnetometer at CAPP

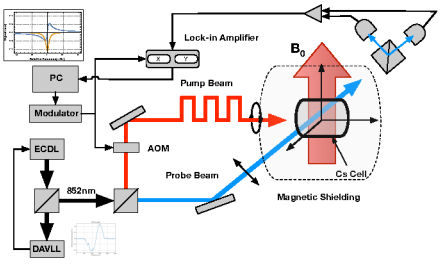

Figure 1: Schematics of CAPP magnetometer.

The magnetometer at CAPP station is a amplitude modulated nonlinear magneto-optical rotation (AM NMOR) magnetometer. The pump beam and probe beam are fed from a single external cavity diode laser (ECDL) from MOGLabs and resonant with Cs D2 transition line at 852nm. The Cs atoms are contained in a cylindrical disk cell with 6 cm in diameter and 3 cm in length. The inner surface of the cell is coated with paraffin for anti-relaxation. The cell is located within a four-layers of cylindrical magnetic shielding made by Twinleaf (MS-2). The shielding consists of three layers of Mu-metal and one inner most layer made with Ferrite. Total eight sets of integrated coil system provide uniform magnetic field along three orthogonal axes as well as first order gradient field to compensate any residual field gradient.

The laser beam from ECDL is stabilized by a laser frequency stabilization loop with Dichroic Atomic Vapor Lase Lock (DAVLL) scheme. The pump beam is amplitude modulated at $\Omega_{\rm mod} = 2\pi \times 1.5$kHz by using AOM (acousto-optics modulator) and is circularly polarized and propagating in the $\hat{\rm x}$ direction. The probe beam is linearly polarized at $\approx 45°$ to the $\hat{\rm z}$ axis and propagates in the $\hat{\rm y}$ direction. The pump beam has a diameter of $\approx$ 5mm and the probe

beam has a diameter of ≈ 2mm. The probe beam is directed into a balance photodiode after it leaves the vapor cell. The schematics of our experimental setup is shown in Fig.1.

To characterize the magnetometer from the setup, we estimated the sensitivity and the bandwidth that provide the lowest magnetic field and response time one can measure with our system. In order to measure the bandwidth, an harmonic excitation from 0.1Hz up to the frequency at which the response cannot be resolved was applied while the amplitude of the response was monitored. RF coil was added on the cell holder to provide such resonant field in addition to the main holding field. The sensitivity of the magnetometer was estimated by measuring minimum noise level which is noise equivalent magnetic field. The noise level depends on the frequency. Fig.2 shows the measured bandwidth and sensitivity of the magnetometer.

4 Summary

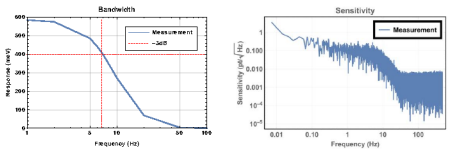

Figure 2: Bandwidth and sensitivity of the magnetometer.

The GNOME has been initiated to look for transient events of axion domain walls. One of stations at CAPP in Daejeon, South Korea is being installed and will be join the network operation of magnetometers around the world. A Cs based optical magnetometer has been adapted and characterized at CAPP to be worked as a local station for the GNOME experiment. The bandwidth and sensitivity of the magnetometer sensor have met all requirements needed as a local station. The network operation of the CAPP station along with other stations around the world will be started soon.

5 Acknowledgments

This work was supported by the Institute for Basic Science under grant no. IBS-R017-D1.

References

[1] D. Budker and M. Romalis, "Optical magnetometry", Nature Physics, **3** 227, 2007.

[2] D. J. Wineland *et al.*, "Search for anomalous spin-dependent forces using stored-ion spectroscopy", Phys. Rev. Lett. **67** 1735,1991.

[3] V. Flambaum*et al.*, "Scalar-tensor theories with pseudoscalar couplings", Phys. Rev. D **80** 105021, 2009.

[4] M. Pospelov *et al.*, "Detecting Domain Walls of Axionlike Models Using Terrestrial Experiments", Phys. Rev. Lett. **110** 021803, 2013.

[5] A. Arvanitaki and A. A. Geraci. "Resonantly Detecting Axion-Mediated Forces with Nuclear Magnetic Resonance", Phys. Rev. Lett. **113** 161801, 2014.

[6] Y. V. Stadnik and V. V. Flambaum. "New atomic probes for dark matter detection: Axions, axion-like particles and topological defects", Mod. Phys. Lett. A, **29** 40007, 2014.

[7] T. Hiramatsu *et al.*, "Axion cosmology with long-lived domain walls", Journal of Cosmology and Astroparticle Physics **1** 001, 2013.

Chapter 2

WIMP Dark Matter

Status and perspectives of DAMA/LIBRA

R. Bernabei[1,2], *P. Belli*[1,2], *R. Cerulli*[1,2], *A. Di Marco*[1,2], *V. Merlo*[1,2], *F. Montecchia*[2]*, *F. Cappella*[3,4], *A. d'Angelo*[3,4], *A. Incicchitti*[3,4], *V. Caracciolo*[5], *C.J. Dai*[6], *H.L. He*[6], *H.H. Kuang*[6], *X.H. Ma*[6], *X.D. Sheng*[6], *R.G. Wang*[6], *Z.P. Ye*[6]†

[1]Dip. di Fisica, Università di Roma "Tor Vergata", Rome, Italy
[2]INFN sez. Roma "Tor Vergata", Rome, Italy
[3]Dip. di Fisica, Università di Roma "La Sapienza", Rome, Italy
[4]INFN sez. Roma, Rome, Italy
[5]INFN, Laboratori Nazionali del Gran Sasso, Assergi (AQ), Italy
[6]Institute of High Energy Physics, Chinese Academy of Sciences, Beijing, P. R. China

DOI: http://dx.doi.org/10.3204/DESY-PROC-2017-02/cerulli_riccardo

The 250 kg highly radiopure NaI(Tl) DAMA/LIBRA experiment is in progress in the Gran Sasso Laboratory in its phase2 after an important upgrade performed in fall 2010. Considering the data collected in the first phase (DAMA/LIBRA–phase1) and with the former DAMA/NaI experiment ($\sim$ 100 kg of highly radio-pure NaI(Tl)) the DAMA Collaboration has released so far data corresponding to 14 independent annual cycles, for a total exposure of 1.33 ton $\times$ yr, exploiting the model-independent Dark Matter (DM) annual modulation signature. Cumulatively a DM annual modulation effect has been observed at 9.3 σ C.L., supporting the presence of DM particles in the galactic halo. No systematic or side reaction able to mimic the observed DM annual modulation has been found. Recent analyses considering the Mirror DM candidate will be summarized and the efforts for a possible future third phase of the DAMA/LIBRA experiment mentioned.

The DAMA project is focused on the development and use of low background scintillators for low background measurements. DAMA/LIBRA is the main experiment [1, 2, 3, 4, 5, 6, 7, 8, 9, 10, 11, 12, 13, 14, 15, 16] being the second generation highly radiopure NaI(Tl) set-up after the pioneering DAMA/NaI [17, 18]. DAMA/LIBRA is further investigating the presence of DM particles in the galactic halo by exploiting the model independent DM annual modulation signature [19, 20].

The DM annual modulation signature is due to the Earth's revolution around the Sun, which is moving in the Galaxy; as a consequence of the velocities composition, the flux of DM particles impinging a terrestrial detector is expected to follow a cosinusoidal behaviour with maximum around $\simeq$ June 2^{nd} when the projection of the Earth orbital velocity on the Sun velocity with respect to the Galactic frame is maximum, and minimum around $\simeq$ December 2^{nd} when the two velocities are opposite. It is a very effective signature because the signal induced by DM particles must simultaneously satisfy many requirements: the rate must contain a component modulated according to a cosine function (1) with one year period (2) and a phase

*also: Dip. di Ingegneria Civile e Ingegneria Informatica, Università di Roma "Tor Vergata", Rome, Italy
†also: University of Jinggangshan, Ji'an, Jiangxi, P. R. China

peaked roughly at $\simeq$ June 2^{nd} (3); the modulation must only be present in a well-defined low energy range (4); it must apply only to those events in which just one detector among many actually "fires" (*single-hit* events), since the DM particle multi-interaction probability is negligible (5); the modulation amplitude in the region of maximal sensitivity must be $\simeq$ 7% for usually adopted halo distributions (6), but it can be larger (even up to $\simeq$ 30%) in case of some possible scenarios. This signature is model independent and no systematics or side reactions able to mimic the effect and to to simultaneously satisfy all the requirements is available [1, 2, 3, 4, 7, 8, 12, 13, 17, 18, 21].

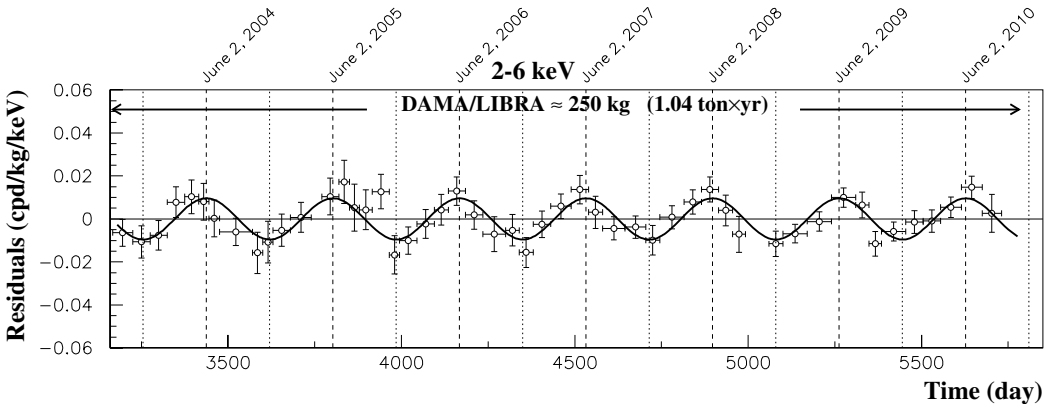

Figure 1: Experimental residual rate of the *single-hit* scintillation events measured by DAMA/LIBRA–phase1 in the (2–6) keV energy interval as a function of the time. The superimposed curve is the cosinusoidal function behaviour $A\cos\omega(t-t_0)$ with a period $T=\frac{2\pi}{\omega}=1$ yr, a phase $t_0=152.5$ day (June 2^{nd}) and modulation amplitude, A, equal to the central values obtained by best fit on the data points of the entire DAMA/LIBRA–phase1. The dashed vertical lines correspond to the maximum expected for the DM signal (June 2^{nd}), while the dotted vertical lines correspond to the minimum.

The full description of the DAMA/LIBRA set-up in all its phases is described in details in Refs. [1, 2, 3, 4, 6, 7, 8, 13].

Many independent analyses have been performed on the 14 annual cycles data; all the analyses confirm the presence of an annual modulation satisfying all the features of the signature [2, 3, 4, 8]. In Figure 1, as example, the time behaviour of the experimental residual rate of the *single-hit* scintillation events for DAMA/LIBRA–phase1 in the (2–6) keV energy interval is plotted. When fitting the *single-hit* residual rate of DAMA/LIBRA–phase1 together with the DAMA/NaI ones, with the function: $A\cos\omega(t-t_0)$, considering a period $T=\frac{2\pi}{\omega}=1$ yr and a phase $t_0=152.5$ day (June 2^{nd}) as expected by the DM annual modulation signature, the following modulation amplitude in NaI(Tl) is obtained: $A=(0.0110\pm0.0012)$ cpd/kg/keV, corresponding to 9.2 σ C.L.. When the period, and the phase are kept free in the fitting procedure the modulation amplitude is (0.0112 ± 0.0012) cpd/kg/keV (9.3 σ C.L.), the period $T=(0.998\pm0.002)$ year and the phase $t_0=(144\pm7)$ day, values well in agreement with expectations for a DM annual modulation signal. In particular, the phase is consistent with about June 2^{nd} and is fully consistent with the value independently determined by Maximum Likelihood analysis [4]. The run test and the χ^2 test on the data have shown that the modulation

amplitudes singularly calculated for each annual cycle of DAMA/NaI and DAMA/LIBRA–phase1 are normally fluctuating around their best fit values [2, 3, 4].

No modulation was found in any possible source of systematics or side reactions; thus, cautious upper limits on possible contributions to the DAMA/LIBRA–phase1 measured modulation amplitude were obtained (see Refs. [2, 3, 4]). It is worth noting that they do not quantitatively account for the measured modulation amplitudes, and are even not able to simultaneously satisfy all the many requirements of the signature. Similar analyses were also performed for the DAMA/NaI data [17, 18]. In particular, the case of neutrons, muons and solar neutrinos has been discussed in Refs. [7, 13], where it has been demonstrated that they cannot give any significant contribution to the DAMA annual modulation result. Other arguments can be found in Refs. [1, 2, 3, 4, 7, 8, 12, 13, 17, 18, 21]. In conclusion, DAMA gives model-independent evidence (at 9.3σ C.L. over 14 independent annual cycles) for the presence of DM particles in the galactic halo.

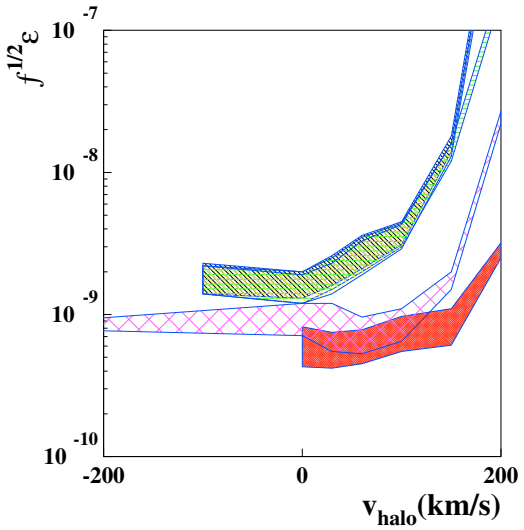

Figure 2: Example of allowed regions for the $\sqrt{f}\epsilon$ parameter as a function of v_{halo} (halo temperature $T = 5 \times 10^5$ K). The regions have been obtained by considering a composite dark halo H′(20%), He′(74%), C′(0.9%), O′(5%), Fe′(0.1%), with $v_0 = 220$ km/s and parameters in the set A. The five contours correspond to different quenching factor modeling (see [16]).

As regards comparisons, we recall that no direct model independent comparison is possible in the field when different target materials and/or approaches are used; the same is for the strongly model dependent indirect searches. In particular, the DAMA model independent evidence is compatible with a wide set of scenarios regarding the nature of the DM candidate and related astrophysical, nuclear and particle Physics scenarios; some given scenarios and parameters are discussed e.g. in Refs. [2, 5, 8, 12, 14, 15, 16, 17, 18, 22, 23, 24, 25, 26, 27, 28, 29, 30, 31, 32, 33, 34, 35, 36] and references therein. Further large literature is available on the topics.

In conclusion, both negative results and possible positive hints reported in literature can be compatible with the DAMA model-independent DM annual modulation results in various scenarios considering also the existing experimental and theoretical uncertainties. Moreover,

scenarios also exist for which the DAMA approach is favoured.

Recently it has been performed an analysis of the DAMA/LIBRA–phase1 data in the framework of a mirror dark matter candidate [15, 16]. In the mirror scenario, the DM particles originate from hidden gauge sectors. Two scenarios have been considered: the asymmetric Mirror DM in Ref. [15] and the symmetric one in Ref. [16]. In both cases, the obtained values of the $\sqrt{f}\epsilon$ (where f is the fraction of DM in the Galaxy in form of mirror atoms and ϵ is the coupling constant) parameter are well compatible with cosmological bounds [15, 16]. In the analysis several uncertainties on the astrophysical, particle physics and nuclear physics models have been taken into account in the calculation.

In the symmetric mirror DM scenario the DM particles are expected to form bubbles in the Galaxy with diameter which could be even as the size of the solar system. The dark halo is composed by different species of mirror DM particles (different mirror atoms) and, at the present epoch, is crossing a region close to the Sun with a constant velocity, v_{halo} in the Galactic frame. The velocity distribution of the particles can be considered maxwellian; it is assumed that the halo has its own local equilibrium temperature, T. In the analysis halo temperature in the range $10^4 - 10^8$ K has been considered. As an example, in Figure 2, the allowed regions for the $\sqrt{f}\epsilon$ parameter as a function of v_{halo} in different scenarios are reported; in particular, the regions have been obtained by considering a composite dark halo composed by H$'$(20%), He$'$(74%), C$'$(0.9%), O$'$(5%), Fe$'$(0.1%) with a temperature $T = 5 \times 10^5$ K. The depicted contours correspond to different quenching factor modeling (see [16]).

After the phase1, an important upgrade has been performed when all the PMTs have been replaced with new ones having higher Quantum Efficiency (QE). In this new configuration a software energy threshold at 1 keV has been reached [6]. DAMA/LIBRA is thus in its phase2, continuously running in order: 1) to increase the experimental sensitivity thanks to the lower software energy threshold of the experiment; 2) to improve the corollary investigation on the nature of the DM particle and related astrophysical, nuclear and particle physics arguments; 3) to investigate second order effects; 4) to investigate other signal features; 5) to investigate rare processes other than DM with high sensitivity.

Future improvements (possible phase3) to increase the sensitivity of the set-up can be considered by using high QE and ultra-low background PMTs directly coupled to the NaI(Tl) crystals. In this way a further large improvement in the light collection and a further lowering of the software energy threshold are expected.

References

[1] R. Bernabei et al., Nucl. Instr. and Meth. **A 592**, 297 (2008).

[2] R. Bernabei et al., Eur. Phys. J. **C 56**, 333 (2008).

[3] R. Bernabei et al., Eur. Phys. J. **C 67**, 39 (2010).

[4] R. Bernabei et al., Eur. Phys. J. **C 73**, 2648 (2013).

[5] P. Belli et al., Phys. Rev. **D 84**, 055014 (2011).

[6] R. Bernabei et al., J. of Instr. **7**, P03009 (2012).

[7] R. Bernabei et al., Eur. Phys. J. **C 72**, 2064 (2012).

[8] R. Bernabei et al., Int. J. of Mod. Phys. **A 28**, 1330022 (2013).

[9] R. Bernabei et al., Eur. Phys. J. **C 62**, 327 (2009).

[10] R. Bernabei et al., Eur. Phys. J. **C 72**, 1920 (2012).

[11] R. Bernabei et al., Eur. Phys. J. **A 49**, 64 (2013).
[12] R. Bernabei et al., Eur. Phys. J. **C 74**, 2827 (2014).
[13] R. Bernabei et al., Eur. Phys. J. **C 74**, 3196 (2014).
[14] R. Bernabei et al., Eur. Phys. J. **C 75**, 239 (2015).
[15] A. Addazi et al., Eur. Phys. J. **C 75**, 400 (2015).
[16] R. Cerulli et al., Eur. Phys. J. **C 77**, 83 (2017).
[17] R. Bernabei el al., La Rivista del Nuovo Cimento **26 n.1**, 1-73 (2003).
[18] R. Bernabei et al., Int. J. Mod. Phys. **D 13**, 2127 (2004).
[19] A.K. Drukier, K. Freese, D.N. Spergel, Phys. Rev. **D 33**, 3495 (1986).
[20] K. Freese, J.A. Frieman, A. Gould, Phys. Rev. **D 37**, 3388 (1988).
[21] R. Bernabei et al., Eur. Phys. J. **C 18**, 283 (2000).
[22] R. Bernabei et al., Int. J. of Mod. Phys. A **31**, 1642009 (2016).
[23] R. Bernabei et al., Phys. Lett. B **389**, 757 (1996).
[24] R. Bernabei et al., Phys. Lett. B **424**, 195 (1998).
[25] R. Bernabei et al., Phys. Lett. B **450**, 448 (1999).
[26] P. Belli et al., Phys. Rev. D **61**, 023512 (2000).
[27] R. Bernabei et al., Phys. Lett. B **480**, 23 (2000).
[28] R. Bernabei et al., Phys. Lett. B **509**, 197 (2001).
[29] R. Bernabei et al., Eur. Phys. J. C **23**, 61 (2002).
[30] P. Belli et al., Phys. Rev. D **66**, 043503 (2002).
[31] R. Bernabei et al., Int. J. Mod. Phys. A **21**, 1445 (2006).
[32] R. Bernabei et al., Eur. Phys. J. C **47**, 263 (2006).
[33] R. Bernabei et al., Int. J. Mod. Phys. A **22**, 3155 (2007).
[34] R. Bernabei et al., Phys. Rev. D **77**, 023506 (2008).
[35] R. Bernabei et al., Mod. Phys. Lett. A **23**, 2125 (2008).
[36] R. Bernabei et al., Eur. Phys. J. C **53**, 205 (2008).

Looking for Low-Mass WIMPs with TREX-DM

Theopisti Dafni, F. Aznar, J. F. Castel, S. Cebrián, I. Coarasa, J. Galán, J. G. Garza, F. J. Iguaz, I. G. Irastorza, G. Luzón, H. Mirallas, A. Ortiz de Solórzano, E. Ruiz-Chóliz, J. A. Villar

Grupo de Física Nuclear y Astropartículas, Universidad de Zaragoza, Zaragoza, Spain
Laboratorio Subterráneo de Canfranc, Canfranc-Estación, Spain

DOI: http://dx.doi.org/10.3204/DESY-PROC-2017-02/dafni_theopisti

TREX-DM is a low-mass WIMP detector: a gas time projection chamber (TPC) equipped with novel micromesh gas structures (Micromegas) readout planes. In the fiducial volume of ∼20 litres and a pressure of 10 bar, there will be approx. 0.160 kg of Ne, or alternatively 0.300 kg of Ar. The energy threshold foreseen is well below 0.4 keVee and the expected background level is better than 10 counts $\mathrm{keV}^{-1}\mathrm{kg}^{-1}\mathrm{d}^{-1}$, and could give competitive results in the search for low-mass WIMPs. The experiment has recently been approved by the Laboratorio Subterrneo de Canfranc and is expected to be commissioned by the end of the current year. We report on the status of the project.

1 Introduction

The Weakly Interacting Massive Particles, which appear in supersymmetric extensions of the Standard Model, are one of the strongest candidates to form the Dark Matter of the Universe. The lack of a positive signal during the last 30 years in the search of "standard WIMPs", during which the experimental efforts have reached remarkable levels of sensitivity, and the lack of proof of Supersymmetry in the data of LHC so far, have made the lower end of the WIMP mass attractive. Looking for low-mass WIMPs (<10 GeV) requires the use of light elements and a low energy threshold, aspects for which the current experiments are not optimized, but which are met by a gaseous Time Projection Chamber.

The Canfranc Underground Laboratory in the Spanish Pyrenees (Laboratorio Subterráneo de Canfranc, LSC) will host a high pressure TPC, called TREX-DM, with the primary goal of searching for low-mass WIMPs.

2 TREX-DM status and prospects

The TREX-DM detector, built and commissioned at University of Zaragoza, is described in detail in [1]. It is designed to host aprox. 20 L of pressurized gas up to 10 bar in the fiducial volume, which corresponds to 0.160 kg of Ne or 0.300 kg of Ar. The detector is equipped with novel microbulk Micromesh Gas Structures (Micromegas) (see Fig.1).

The overall concept has been developed as part of the T-REX project [2, 3], in which an intensive R&D has been done on low-background application of gaseous TPCs. Similar technology is in use to search for axions in the CAST experiment, and considered for the future IAXO experiment, in which low background at keV energies (although at surface level) is the

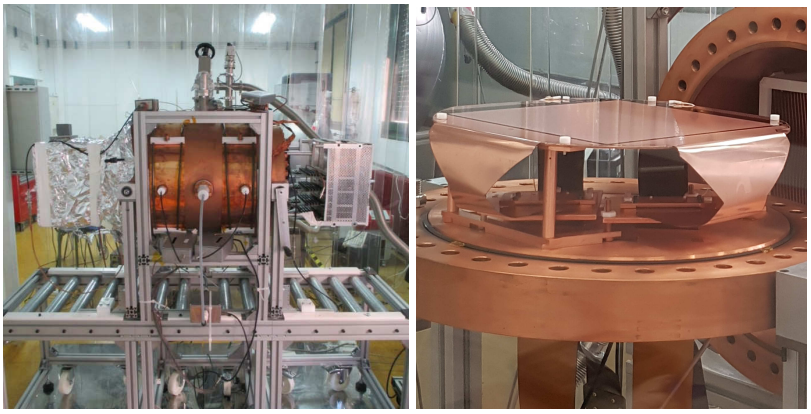

Figure 1: Left: A picture of the TREX-DM detector sitting on a platform in the laboratory in Zaragoza. Right: One of the two microbulk Micromegas recently installed.

main experimental requirement [4]. The key aspect of the detection concept is that microbulk Micromegas readouts can be built with extremely low levels of intrinsic radioactivity, that have been found to be less than 0.1μBq/cm^2 of the natural Th and U chains. Considering, in addition: the high-granularity that the Micromegas planes can have, that with the help of high-density readout electronics provide rich event information; the intrinsic amplification of gaseous ionization detection, which, combined with the high granularity, makes feasible effective thresholds of less than 1 keV; and the flexibility in the choice of target gas and pressure, that allows to tune the experiment for low-mass WIMP sensitivity and provides a unique tool for background study and identification, the choice of a gaseous TPC detector to explore the low-mass WIMP frontier is very appealing and clearly appropriate.

The microbulk Micromegas of TREX-DM are the largest area built with the microbulk technique, featuring an active area of 25×25 cm^2. They present a high granularity (256 channels in the x direction and 256 in the y) and are to be read with a self-triggered TPC data acquisition (based on the AGET electronics); the effective threshold is expected to be well below 1 keVee [1], probably down to 100 eVee.

The chamber is built with state-of-the-art radiopurity specifications, as the target background level of the experiment is of <1 counts keV^{-1}kg^{-1}day^{-1}. This number is obtained by a preliminary background model based on GEANT4 simulations and using the outcome of an exhaustive screening campaign of all the elements entering the detector construction, as well as the measured fluxes of backgrounds from environmental sources at the LSC (namely gamma-rays, neutrons and muons). Table 1 summarizes the contribution to the background budget of selected components of the experiment. This result should be validated experimentally, as simulations at very low energy (especially below 1 keV) may not be totally reliable, and the appearance of unforeseen background sources cannot be excluded. The main goal of the proposal is to confirm this prospect, and in general to get experimental insight on the origin of backgrounds at such low energies. This understanding is *per se* a very interesting quest; very few high sensitivity measurements at these energies have been done (even with other technologies) elsewhere. The precise sensitivity to the WIMP-nucleon cross-section will depend on the final

[1] Electron equivalent energy.

Component	Argon	Neon	Main contribution
Vessel (cosmogenic)	1.25	1.50	^{60}Co
Copper Boxes (cosmogenic)	0.034	0.046	^{60}Co
Field Cage (PTFE)	<0.033	<0.051	^{238}U
Field Cage (resistors)	<0.35	<0.63	^{238}U
Field Cage (kapton-Cu PCB)	<1.06	<1.81	^{238}U
Cathode (copper)	<0.0081	<0.012	^{238}U, ^{40}K
Cathode (PTFE)	<0.064	<0.085	^{238}U
Readout Planes	<1.24	<1.14	^{40}K
Connectors	<0.19	<0.24	^{238}U
Epoxy	<0.0044	<0.0056	^{232}Th
Target	0.15		^{39}Ar
Neutrons at LSC	$(2.52\pm0.22)\times10^{-2}$	$(7.06\pm0.61)\times10^{-2}$	
Muons (+ muon-induced neutrons)	0.205±0.021	0.336±0.034	
^{210}Pb in Pb shielding (*)	<0.12		
^{222}Rn in air	0.1495±0.0024	0.0841±0.0013	

Table 1: Background rates (in counts keV^{-1} kg^{-1} d^{-1}) expected in 2-7 keV$_{ee}$ from selected components inside, close to or outside the vessel and backgrounds at LSC using Ar or Ne mixtures in TREX-DM. The dominant contributions are indicated in the last column, while contributions marked with (*) are 90% C.L. limits when no event was registered in preliminary simulations. More results can be found in [1, 2, 5].

effective threshold and background achieved but, if the predictions of the model are realized experimentally, the sensitivity of TREX-DM could easily reach, and likely improve, the current bounds for WIMPs of masses of 0.1–10 GeV.

A definite, but flexible, experimental plan for TREX-DM at LSC is proposed, with a tentative temporal horizon of 3 years. After installation and commissioning during the first year, a 2-year campaign of physics runs at LSC is foreseen. The latter includes a set of runs with Ne- and (depleted) Ar-based mixtures at increasing pressures (from 1 bar to 10 bar). The number, duration and type of runs may be adapted depending on the intermediate results achieved. Figure 2 shows the projected sensitivity of TREX-DM (exclusion at 90% C.L.) in the direct detection of WIMPs, for both Ar- and Ne-based gas mixtures at 10 bar, for three different cases of background, energy threshold and exposure. If the background expectations are fulfilled, the experiment could provide a competitive result for low-mass WIMPs already in the 3-year time-span considered.

The detector is now getting adapted to the requirements for underground operation: a couple of provisional components need to be replaced by definitive radiopure versions. Its installation underground is foreseen for the end of this year.

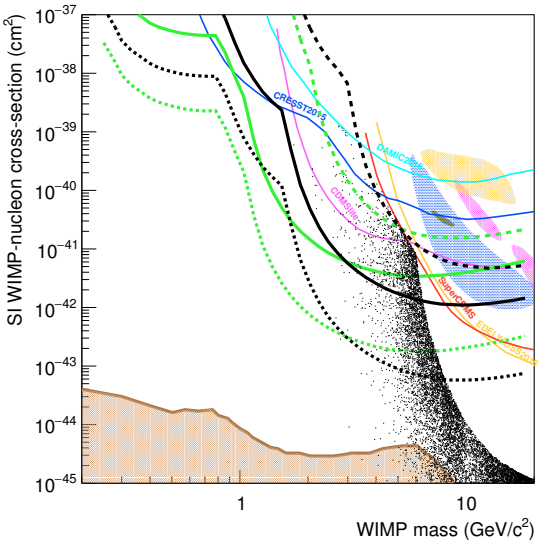

Figure 2: Projected sensitivity (90% C.L.)of TREX-DM for different assumptions (for an exposure of 0.3kg·y) for both Ar-1%C_4H_{10} (black thick lines) and Ne-2%C_4H_{10} (green thick lines): solid lines correspond to background levels of 1keV^{-1}kg^{-1}d^{-1} and a threshold of 0.4keVee (nominal scenario) while the combination of 10 keV^{-1}kg^{-1}d^{-1} and 0.4keVee (conservative scenario) is shown with dashed lines.

Acknowledgments

A few weeks before writing these proceedings, Professor J.A. Villar passed away. In deep sorrow, we all thank his dedicated work and kindness. This work has been financially supported by the European Commission under the European Research Council T-REX Starting Grant ref.ERC-2009-StG-240054 of the IDEAS program of the 7th EU Framework Program and by the Spanish Ministry of Economy and Competitiveness (MINECO) under Grants FPA2013-41085-P and FPA2016-76978-C3-1-P. We acknowledge the technical support from LSC and GIFNA staff.

References

[1] J. F. Iguaz *et al.*, "TREX-DM: a low-background Micromegas-based TPC for low-mass WIMP detection," Eur. Phys. J. **C76** 529 (2016) [arXiv:1512.01455 [physics.ins-det]].

[2] I. G. Irastorza *et al.*, "Gaseous time projection chambers for rare event detection: Results from the T-REX project. I. Double beta decay," JCAP **1603** 033 (2016) [arXiv:1512.07926 [physics.ins-det]].

[3] I. G. Irastorza *et al.*, "Gaseous time projection chambers for rare event detection: Results from the T-REX project. II. Dark Matter," JCAP **1603** 034 (2016), Err. JCAP JCAP **1605** E01 (2016) [arXiv:1512.06294 [physics.ins-det]].

[4] V. Anastassopoulos *et al.*, "New CAST Limit on the Axion-Photon Interaction," Nature Phys. **13** 584-590 (2017) [arXiv:1705.02290 [hep-ex]].

[5] F. Aznar *et al.*, "Status of the TREX-DM experiment at the Canfranc Underground Laboratory" arXiv:1709.10062 [physics.ins-det], To appear in the Proceedings of the XV International Conference on Topics in Astroparticle and Underground Physics (TAUP2017) at Journal of Physics: Conference Series.

Status of the COSINE-100 Experiment

Kyungwon Kim[1]
On behalf of the COSINE collaboration

[1]Center for Underground Physics, Institute for Basic Science (IBS), Daejeon 34047, Republic of Korea

DOI: http://dx.doi.org/10.3204/DESY-PROC-2017-02/kim_kyungwon

Presently a number of experiments are operating to search for the WIMP, a dark matter candidate. Among these experiments, DAMA/LIBRA claims to observe an annually modulated WIMP signal, while other experiments, using different technologies and target materials, exclude the DAMA/LIBRA signal region in the parameter space. The COSINE experiment aims at exploring these contradicting results by using NaI(Tl), the same target material as DAMA/LIBRA. The first phase detector with 106 kg of NaI(Tl), COSINE-100, was installed at the Yangyang underground laboratory in Korea. It consists of several shield structures, including a liquid scintillator veto system. The experiment has started physics data taking in late September 2016 and has been operating stably since then.

1 Introduction

Weakly Interacting Massive Particles(WIMPs) are well-supported dark matter candidates in the theory [1]. Numerous direct searches of WIMP have been carried out using different materials and techniques. Among these experiments, the DAMA/LIBRA experiment has reported the observation of an annual modulation signature of WIMPs [2]. However, the WIMP-nucleon cross sections inferred from this DAMA/LIBRA modulation signal are in conflict with other null observation from XENON100 [3], LUX [4] and SuperCDMS [5]. To resolve this conflict, several experiments have been performing a WIMP search using low-background NaI(Tl) crystals [6, 7, 8, 9, 10]. Using the same target material and techniques as DAMA/LIBRA, it is expected to confirm DAMA/LIBRA's observation without any ambiguity.

2 COSINE-100 experiment

COSINE-100 is a NaI(Tl) WIMP search experiment collaboration between KIMS and DM-Ice. The eight NaI(Tl) crystal array with a total mass of 106 kg was deployed at Yangyang underground laboratory in South Korea. Detectors are installed inside a substantial shield that consists, from the inside out, liquid scintillator, a copper box, lead blocks and plastic scintillator panels. Plastic scintillator panels also have a role to detect muon signals. The eight NaI(Tl) detectors are immersed into the liquid scintillator which acts as a veto system. Figure 1 shows the shield structure of COSINE-100 detector.

The room temperature and humidity are controlled by air conditioning system and the room air is circulated through a HEPA filter to maintain a clean environment. Detector room

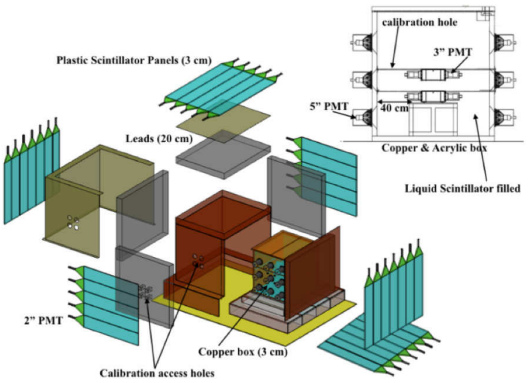

Figure 1: Shield structure of the COSINE-100 experiment. Encapsulated NaI detectors are placed inside the copper chamber which is surrounded by several shield materials for active shielding of various external backgrounds and liquid scintillator is filled in the copper chamber.

environmental parameters, the status of DAQ rate and electronics are monitored remotely online.

3 Performance of NaI detectors

Because of the low interaction rate between dark matter and ordinary matter, low background is crucial for WIMP search. We have studied backgrounds of NaI(Tl) crystals before the installation of COSINE-100 at the test setup which was in the CsI(Tl) crystals array used for KIMS-CsI experiment. Since the NaI detector is surrounded by CsI crystals, single NaI crystal hit events and multiple hit events crossing different crystal are separable using coincidence events of CsI detectors. One of the crystals installed in COSINE-100 has been studied in this setup and simulation was performed to understand backgrounds. From this study, we understand that the most stringent backgrounds in the NaI(Tl) crystal are associated to ^{40}K and ^{210}Pb [11]. The eight crystals were grown from four different types of powder, which have different levels of radioactive backgrounds.

Several criteria to reject PMT noise are required to select events. PMT noise and scintillation signal have different time characteristics of fast and relatively slow component. By using the characteristics, PMT noise is well separated from scintillation signal [10]. Noise signals produced by PMTs usually make large asymmetries in total charge between two PMTs. The charge asymmetry parameter is also used for rejection of noise events. Event selection efficiencies estimated using Compton scattering events from ^{60}Co radioactive source reach about 90% at 1 keV and 94% at 2 keV energy range in Crystal 7. It shows that event selection cuts work well for discriminating signal from noise. To reduce the events around 3 keV from ^{40}K decay, one of main backgrounds, coincidence of 1460 keV events with the liquid scintillator is required [12].

Figure 2 shows single hit events energy spectra for four crystals grown from different types of powder after all event selection criteria described above are applied. Due to high light yield around 13 p.e./keV on average, the energy threshold reaches to 2 keV. The peak near 46 keV (Figure 2, left) and slowly decreasing distribution at low energy region (Figure 2, right) reflect

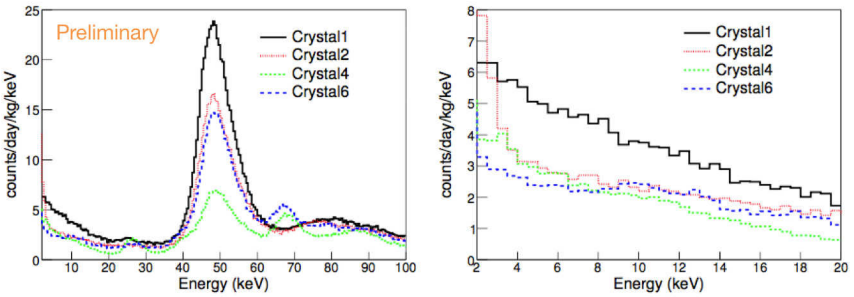

Figure 2: Energy spectrum comparisons for four crystals grown from different types of powder after event selection criteria applied. The peak near 46 keV (left) and slowly decreasing distribution (right) reflect contamination level of ^{210}Pb in a crystal.

contamination level of ^{210}Pb in a crystal. The simulation is ongoing to understand backgrounds of crystals more deeply [13]. For muon induced events rejection, data from the plastic scintillator array is under study [14].

4 Prospects of COSINE-100

We have an experience on the analysis using pulse shape discrimination (PSD) method for the NaI(Tl) crystal [15]. Based on it, it is possible to search a WIMP with a few months data using PSD analysis which allows to extract WIMP candidate events by discriminating nuclear recoil from electron recoil backgrounds. The study of WIMPs annual modulation signature is going to be performed once we have more than one year of data. Assuming 4.3 counts/day/kg/keV flat background with no modulation signal, two years of data with 1 keV threshold will give comparable sensitivity with DAMA's 90% C.L. allowed region as shown in Figure 3.

For the next phase of COSINE-100, several efforts to lower background level of the crystals are ongoing. Low energy events induced by Pb decay are measured to understand characteristics of ^{206}Pb nuclear recoil deposition on the surface of the NaI(Tl) crystals, which can mimic WIMP induced events. NaI(Tl) crystal encapsulation R&D is also ongoing by immersing the crystal in the liquid scintillator or coating plastic scintillator on the crystal to tag backgrounds more effectively.

5 Summary

The first phase of the COSINE-100 experiment deployed 106 kg of NaI(Tl) crystals at Yangyang underground laboratory. COSINE-100 has been operated stably since it started taking data at the end of September 2016. We have capability to directly test DAMA annual modulation results within two years. Through various R&D efforts, we expect to achieve a background reduction.

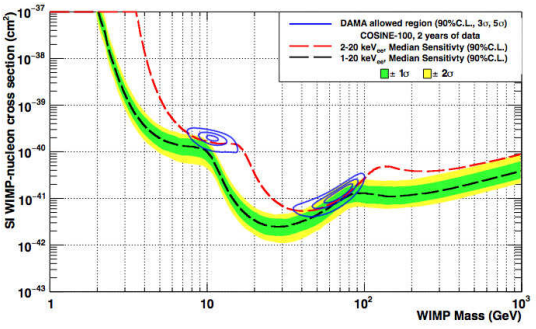

Figure 3: The median expected (black dotted line) 90% CL upper limit on the WIMP-nucleon spin-independent cross-section from the COSINE-100 experiment assuming the background only hypothesis, shown together with WIMP induced DAMA/LIBRA allowed region.

6 Acknowledgments

We thank the Korea Hydro and Nuclear Power (KHNP) Company for providing underground laboratory space at Yangyang. This work is supported by: the Institute for Basic Science (IBS) under project code IBS-R016-A1, Republic of Korea; UIUC campus research board, the Alfred P. Sloan Foundation Fellowship, NSF Grants No. PHY-1151795, PHY-1457995, DGE-1122492 and DGE-1256259, WIPAC, the Wisconsin Alumni Research Foundation, Yale University and DOE/NNSA Grant No. DE-FC52-08NA28752, United States; STFC Grant ST/N000277/1 and ST/K001337/1, United Kingdom; and CNPq, Brazil.

References

[1] G. Steigman, M. S. Turner, Nucl. Phys. B **235** (1985) 375.

[2] R. Bernabei *et al.* (DAMA/LIBRA Collaboration), Eur. Phys. J. C **67** (2010) 39.

[3] E. Aprile *et al.* (XENON100 Collaboration), Phys. Rev. Lett. **109** (2012) 181301.

[4] D. S. Akerib *et al.* (LUX Collaboration), Phys. Rev. Lett. **112** (2014) 091303.

[5] R. Agnese *et al.* (SuperCDMS Collaboration), **112** (2014) 241302.

[6] J. Amare *et al.* (ANAIS Collaboration), Nucl. Instrum. Methods, A **742** (2014) 187.

[7] J. Cherwinka *et al.* (DM-Ice Collaboration), Phys. Rev. D **90** (2014) 092005.

[8] K. Fushimi *et al.* (KamLAND-PICO Collaboration), Proceedings, 28th Workshop on Radiation Detectors and Their Uses, 26-28, 2014 (2014).

[9] J. Xu, *et al.* (SABRE Collaboration), Proceedings, 5th Topical Workshop on Low Radioactivity Techniques (LRT 2015), AIP Conf. Proc. 1 **672**, (2015) 040001.

[10] K. W. Kim *et al.* (KIMS Collaboration), Astropart. Phys. **62** (2015) 249.

[11] G. Adhikari *et al.*, Eur. Phys. J. C **77** (2017) 437.

[12] J. S. Park *et al.*, Nucl. Instrum. Methods, A, **851**, (2017) 103-107.

[13] P. Adhikari, "Background assessment of the NaI(Tl) crystals in the COSINE-100 experiment", in Proceedings, ICRC2017

[14] H. Prihtiadi, "Muon detector and muon flux measurement at Yangyang underground laboratory for the COSINE-100 experiment", in Proceedings, ICRC2017

[15] H. S. Lee *et al.*, JHEP, 08, (2015), 093

Search for low-mass Dark Matter with the CRESST Experiment

Holger Kluck[4,5], *G. Angloher*[1], *P. Bauer*[1], *A. Bento*[1,8], *C. Bucci*[2], *L. Canonica*[2,9], *X. Defay*[3], *A. Erb*[3,10], *F. v. Feilitzsch*[3], *N. Ferreiro Iachellini*[1], *P. Gorla*[2], *A. Gütlein*[4,5], *D. Hauff*[1], *J. Jochum*[6], *M. Kiefer*[1], *H. Kraus*[7], *J.-C. Lanfranchi*[3], *A. Langenkämper*[3], *J. Loebell*[6], *M. Mancuso*[1], *E. Mondragon*[3], *A. Münster*[3], *C. Pagliarone*[2], *F. Petricca*[1], *W. Potzel*[3], *F. Pröbst*[1], *R. Puig*[4,5], *F. Reindl*[4,5], *J. Rothe*[1], *K. Schäffner*[2,11], *J. Schieck*[4,5], *S. Schönert*[3], *W. Seidel*[1*], *M. Stahlberg*[4,5], *L. Stodolsky*[1], *C. Strandhagen*[6], *R. Strauss*[1], *A. Tanzke*[1], *H.H. Trinh Thi*[3], *C. Türkoğlu*[4,5], *A. Ulrich*[3], *I. Usherov*[6], *S. Wawoczny*[3], *M. Willers*[3], *M. Wüstrich*[1]

[1]Max-Planck-Institut für Physik, D-80805 München, Germany
[2]INFN, Laboratori Nazionali del Gran Sasso, I-67010 Assergi, Italy
[3]Physik-Department E15, Technische Universität München, D-85747 Garching, Germany
[4]Institut für Hochenergiephysik der ÖAW, A-1050 Wien, Austria
[5]Atominstitut, Technische Universität Wien, A-1020 Wien, Austria
[6]Eberhard-Karls-Universität Tübingen, D-72076 Tübingen, Germany
[7]Department of Physics, University of Oxford, Oxford OX1 3RH, United Kingdom
[8]Also at: LIBPhys, Departamento de Fisica, Universidade de Coimbra, P3004 516 Coimbra, Portugal
[9]Also at: Massachusetts Institute of Technology, Cambridge, MA 02139, USA
[10]Also at: Walther-Meißner-Institut für Tieftemperaturforschung, D-85748 Garching, Germany
[11]Also at: GSSI-Gran Sasso Science Institute, 67100, L'Aquila, Italy

DOI: http://dx.doi.org/10.3204/DESY-PROC-2017-02/kluck_holger

CRESST is a multi-stage experiment directly searching for dark matter (DM) using cryogenic $CaWO_4$ crystals. Previous stages established leading limits for the spin-independent DM-nucleon cross section down to DM-particle masses m_{DM} below $1\,\mathrm{GeV/c^2}$. Furthermore, CRESST performed a dedicated search for dark photons (DP) which excludes new parameter space between DP masses m_{DP} of $300\,\mathrm{eV/c^2}$ to $700\,\mathrm{eV/c^2}$.

In this contribution we will discuss the latest results based on the previous CRESST-II phase 2 and we will report on the status of the current CRESST-III phase 1: in this stage we have been operating 10 upgraded detectors with 24, g target mass each and enhanced detector performance since summer 2016. The improved detector design in terms of background suppression and reduction of the detection threshold will be discussed with respect to the previous stage. We will conclude with an outlook on the potential of the next stage, CRESST-III phase 2.

*Deceased

1 Introduction

The nature of dark matter is one of the greatest mysteries in modern physics: albeit observations ranging from galactic dynamics to the cosmic microwave background indicate evidently that most matter is dark [1], no particle constituent for dark matter was unambiguously found. Whereas few experiments claim a potential signal, e.g. DAMA/LIBRA [2], the majority observed null signals, e.g. LUX [3], SuperCDMS [4], and CRESST [5, 6]. Besides the classic WIMP, also lighter candidates were discussed during the last years, e.g. *asymmetric dark matter* [7] with masses m_{DM} in the order of $\mathcal{O}(\mathrm{GeV/c^2})$ or *dark photons* [8, 9] with masses m_{DP} on the keV-scale and below. Scattering of the former with target nuclei may cause nuclear recoils, whereas the latter may interact electromagnetically with electrons.

In this contribution we will show that CRESST is ideally suited to search for light dark matter particles. After a short introduction of the CRESST experiment in Sec. 2, we report the latest results based on CRESST-II phase 2 data, both for the search for dark photons (Sec. 3.1) and for the search of dark matter induced nuclear recoils (Sec. 3.2). Afterwards, we discuss the current status and potential of CRESST-III in Sec. 4.

2 The CRESST experiment

The multi-stage *Cryogenic Rare Event Search with Superconducting Thermometers* (CRESST), based at the *Laboratori Nazionali del Gran Sasso* (LNGS) underground laboratory in Italy, mainly looks for nuclear recoils induced by elastic scattering of dark matter particles in its target: scintillating $CaWO_4$ crystals which are operated at temperatures of the order of $\mathcal{O}(10\,\mathrm{mK})$. By simultaneously reading out two signal channels, CRESST is able to distinguish nuclear recoils from electromagnetic interactions. Interactions in the target create non-thermal phonon excitations of the crystal lattice (*phonon signal*) which are recorded by a *transition edge sensor* (TES) as well as scintillation light (*light signal*) recorded by a separate light detector. The scintillation efficiency depends on the type of interaction: for nuclear recoils it is quenched with respect to electromagnetic interactions, i.e. for a given phonon signal the light signal is reduced. A cut on the light-to-phonon signal ratio efficiently selects nuclear recoils against electromagnetic interactions, since the energies of all types of interactions are precisely measured by the phonon signal. A detailed description can be found in [5, 6] and references therein.

3 Latest results from CRESST-II phase 2

CRESST-II phase 2 operated 18 target crystals, each encapsulated together with a light detector in a detector module. Here, we focus on results obtained by two of these modules, *TUM40* [5] and *Lise* [6].

3.1 Search for dark photons

Dark photons are long-lived vector particles which may constitute dark matter as discussed in [8, 9]. Via kinetic mixing κ with standard model photons they may get absorbed with a cross-section $\sigma_{\mathrm{DP}} \approx \kappa c^2 \sigma_\gamma$ approximately proportional to the photoelectric cross-section σ_γ. Due to the negligible velocity of galactic dark matter the resulting signature would be a distinct peak at the rest mass $m_{\mathrm{DP}}c^2$ of the dark photon.

For our dark photon search [10] we used the same data set of detector module Lise which we also used for a search for dark matter-nucleon scatterings in [6]. Contrary to the search for nuclear recoils in [6], the light-to-phonon signal ratio was inefficient to reject backgrounds because both, a potential dark photon signal and radioactive decays as the main background component, result in recoiling electrons.

To search for a potential signal peak at a given rest mass $m_{\mathrm{DP}}c^2$, a Gaussian together with an empirical background model was fitted to the data using a Bayesian approach. Repeating this procedure in 50 eV steps between 0.3 keV and 2 keV resulted in an improved limit on the kinetic mixing κ [10] as shown in Fig. 1: between 300 and 700 eV/c^2 CRESST could exclude new parameter space.

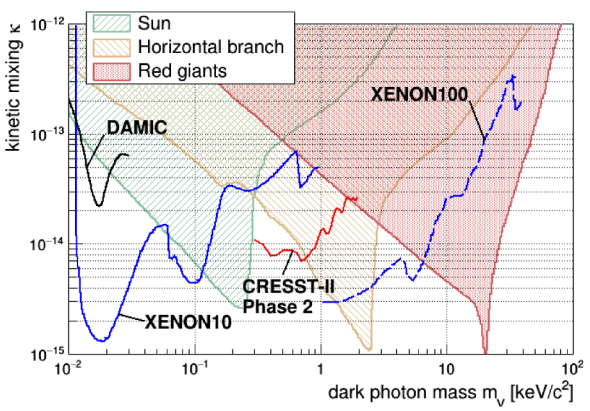

Figure 1: Parameter space for the kinetic mixing between dark photons and standard model photons. Shown in *red* are the exclusion limit for CRESST-II phase 2 obtained with the detector module Lise in comparison with results from LXe and Si based experiments together with constraints from anomalous energy loss in stars. For references see [10].

3.2 Search for dark matter-nucleon scatterings

At the respective time of publication, CRESST-II phase 2 set leading limits on the spin-independent cross section for elastic dark matter-nucleon scattering with the detector modules *TUM40* and *Lise*, the latter reaching down to $m_{\mathrm{DM}} = 500\,\mathrm{MeV}/c^2$, see Fig. 2. Both detector modules exemplify different approaches to increase the detection sensitivity for dark matter induced nuclear recoils: reduction of the background and lowering of the detection threshold.

With TUM40 we could reduce the background rate due to intrinsic contamination of the $CaWO_4$ down to $\sim$ 1-3 mBq/kg [5]. The additional background due to surface-alpha events was completely rejected by an active veto based on scintillating $CaWO_4$ sticks to hold the target [11].

Because the nuclear recoil spectrum gets steeper with decreasing dark

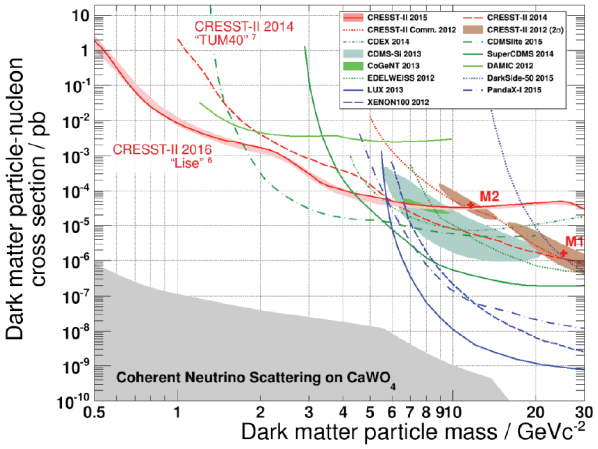

Figure 2: Parameter space for elastic spin-independent dark matter-nucleon scattering. Shown in *red* are the exclusion limits for CRESST-II phase 2 obtained with the detector modules TUM40 and Lise in comparison with results from LAr, LXe, Ge, and Si based experiments. For references see [6].

matter-particle mass, a reduced detection threshold increases especially the sensitivity for low-mass dark matter candidates. This is highlighted by the detector module Lise which featured with 307 eV the lowest detection threshold within CRESST-II phase 2 [6], cf. Fig. 2.

4 Status and potential of CRESST-III

To further increase its sensitivity for low-mass dark matter, CRESST in its third stage aims at a combination of both approaches: detector modules with high radiopurity and low detection threshold. CRESST-III phase 1 is expected to reach a detection threshold of 100 eV. In phase 2 we plan to reduce the background by a factor of 100 compared to TUM40 [12].

CRESST-III phase 1 is equipped with 10 CRESST-III detector modules, each featuring 24 g of target mass of at least TUM40 quality and each held by iSticks: an active rejection technique against holder related backgrounds e.g. relaxation events [13]. Already 2 targets are produced from $CaWO_4$ crystals which were grown from chemically purified raw materials based on the ongoing R&D for CRESST-III phase 2. As prototype measurements [13] showed, the decreased target mass will lower the detection threshold towards 100 eV via a reduced heat capacity.

Since August 2016 CRESST is cooled down to operational temperature and records data. After an extensive gamma-calibration campaign in October 2016, we take physics data since November 2016, interrupted by a neutron calibration campaign in April 2017. It is planned to continue data taking for one year with all 10 modules, aiming for an total exposure of $50\,\mathrm{kg}\cdot\mathrm{d}$. 80% of the data are dynamically blinded, allowing the preparation of selection cuts on the remaining 20% which will be excluded from the final analysis.

Keeping in mind that CRESST-III aims for unprecedented low detection thresholds and under the premise that no so far unknown background appears at these energies we expect to reach a sensitivity of $\sim 5 \cdot 10^{-5}$ pb at $1\,\mathrm{GeV/c^2}$ with CRESST-III phase 1 [12]. This would be an improvement by roughly 2 orders of magnitude compared to the Lise result of CRESST-II phase 2. In CRESST-III phase 2 we plan to operate 100 detector modules for 2 years, in order to reach an exposure of $1000\,\mathrm{kg}\cdot\mathrm{d}$. With this exposure, CRESST will be close to the *neutrino floor* of $CaWO_4$ [12] where the coherent scattering of solar neutrinos on $CaWO_4$ will become a significant background for any future search for low-mass dark matter.

References

[1] G. Bertone, ed. *Particle Dark Matter*, (Cambridge University Press, 2010).

[2] R. Bernabei *et al.*, *Eur. Phys. J.* C **73**, 2648 (2013), arXiv:1308.5109.

[3] D.S. Akerib *et al.*, *Phys. Rev. Lett.* **116**, 161301 (2016), arXiv:1512.03506.

[4] R. Agnese *et al.*, *Phys. Rev. Lett.* **116**, 071301 (2016), arXiv:1509.02448.

[5] G. Angloher *et al.*, *Eur. Phys. J.* C **74**, 3184 (2014), arXiv:1407.3146.

[6] G. Angloher *et al.*, *Eur. Phys. J.* C **76**, 25 (2016), arXiv:1509.01515.

[7] K. Petraki and R.R. Volkas, *Int. J. Mod. Phys.* A **28**, 1330028 (2013), arXiv:1305.4939.

[8] M. Pospelov *et al.*, *Phys. Rev.* D **78**, 115012 (2008), arXiv:0807.3279.

[9] H. An *et al.*, *Phys. Lett.* B **747**, 331 (2015), arXiv:1412.8378.

[10] G. Angloher *et al.*, *Eur. Phys. J.* C **77**, 299 (2017), arXiv:1612.07662.

[11] R. Strauss *et al.*, *Eur. Phys. J.* C **75**, 352 (2015), arXiv:1410.1753.

[12] G. Angloher *et al.*, arXiv:1503.08065.

[13] R. Strauss *et al.*, *Nucl. Instrum. Methods Phys. Res.* A **845**, 414 (2017).

Terrestrial WIMP/Axion astronomy

Ciaran A. J. O'Hare[1,2]

[1] *University of Nottingham, Nottingham, United Kingdom*
[2] *Universidad de Zaragoza, Zaragoza, Spain*

DOI: http://dx.doi.org/10.3204/DESY-PROC-2017-02/ohare_ciaran

Predicting signals in direct dark matter (DM) detection experiments requires an understanding of the astrophysical structure of the local halo. Any uncertainty in this understanding will feed directly into all experimental results. However our terrestrial experiments are in a position to *study* this same astrophysical dependence, and in fact represent our only probe of the local halo on sub-milliparsec scales. This is best achieved in the case of WIMP dark matter if directionally sensitive experiments are feasible, but requires novel parameterizations of the velocity distribution to make model independent claims. For axions the prospects are much greater, haloscopes would be able to make better measurements of the local DM distribution than astrometric probes.

1 Introduction

The relative motion of the Solar System with respect to the largely non-rotating DM halo of the Milky Way gives rise to an anisotropic flux of DM aligned with Galactic rotation. This peak direction is characteristic of a dark matter signal but moreover, the distribution of incoming velocities will encode the galactoarchaeological history of the halo. Measuring this and understanding it will undoubtedly give insight into the formation of the Milky Way and perhaps galaxy formation in general. For instance one may desire to accurately measure the velocity of the Solar system with respect to the halo, measure any underlying anisotropy or rotation in the DM halo, or uncover substructure components left over from the hierarchical construction of the halo by tidal accretion. Additionally in the case of axions there may be unique structures (unseen in vanilla CDM) associated with the primordial dynamics of the axion field. We discuss these prospects in the context of WIMP directional detectors (Sec. 2) and axion haloscope experiments (Sec. 3), drawn from Refs. [1, 2], in which further discussion can be found.

2 WIMP astronomy

Probing the DM velocity distribution with WIMPs is possible to some extent if a sufficiently strong signal can be detected in some existing experiment. Unfortunately since conventional detectors measure only the energy of nuclear recoils, most of the 3-d velocity structure is lost (a small amount is preserved in the annual modulation). To fully extract this information in direct detection, one requires directionality (see Ref. [3] for a review). Small-scale examples of such experiments already exist. The favored approach currently is to use low-pressure gas time projection chambers to measure mm-scale recoil tracks. Although these experiments are

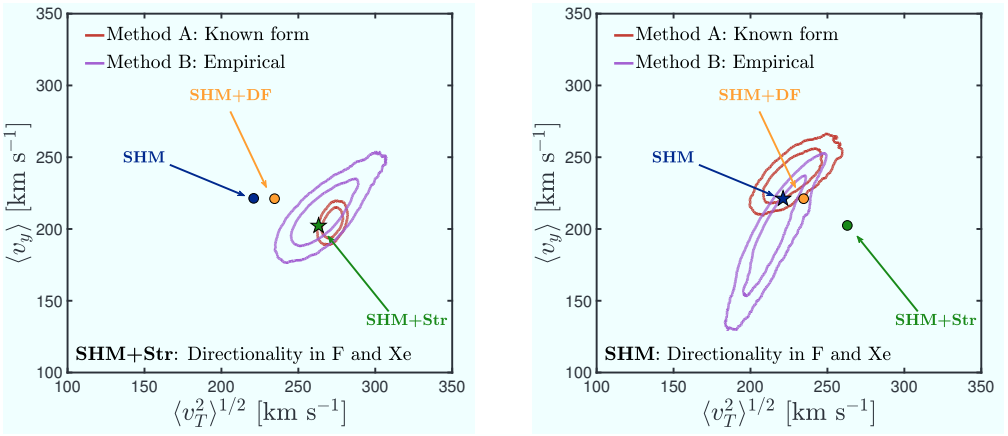

Figure 1: 68% and 95% confidence level contours for the reconstructed velocity distribution projected into the $\langle v_T^2 \rangle - \langle v_y \rangle$ plane (defined in Eq.(1)). We compare two methods of reconstruction A/B (described in the text). The markers indicate three benchmark models. The star in each panel indicates the correct underlying model.

inherently low-mass, the technology is promising. Furthermore there is a possibility that a ton-scale nuclear recoil 'observatory' will be constructed in the future.

The question is: how can we use directional information to reconstruct the velocity distribution, $f(\mathbf{v})$, in a model independent way? To describe our approach we directly compare the application of two methods on mock data:

- **Method A: Known form:** The functional form of $f(\mathbf{v})$ is known (but the parameters values are not.)

- **Method B: Empirical parameterization:** No knowledge is assumed about $f(\mathbf{v})$.

We perform the empirical parameterization with a discretized approach. We discretize initially in three angular bins, $f^k(v)$, with $k = 1, 2, 3$. Inside each bin there is a *speed* distribution which is parameterized by a Chebyshev polynomial which can suitably capture the typical shape of a speed distribution while enforcing its normalization and positivity. We align the angular bins such that the $k = 1$ bin points along the motion of the lab, $\mathbf{v}_{\rm lab}$, anticipating that the greatest anisotropy in the velocity distribution will be generated by the motion of the Earth through the halo. An advantage of this coarse-grained empirical approach is that it allows a completely model independent way of making claims about a given underlying velocity distribution. We show this by applying the method on data generated under three benchmark models that are inspired to cover the range of velocity structures possible in a real halo. These are 1) the standard halo model (SHM), 2) the SHM with the addition of a stream (SHM+Str), and 3) the SHM with the addition of a debris flow (SHM+DF).

We show in Ref. [1] that the discretized approach is successful at capturing broad features in the velocity distribution, and especially at determining whether the velocity distribution contains excesses of particles in certain bins. An intuitive way of describing the success of the parameterization is to map the reconstruction onto physical parameters. We calculate mean

values for the velocity parallel and transverse to the lab motion, respectively:

$$\begin{aligned}\langle v_y \rangle &= \int \mathrm{d}v \int_0^{2\pi} \mathrm{d}\phi \int_{-1}^{1} \mathrm{d}\cos\theta \, (v\cos\theta)\, v^2 f(\mathbf{v})\,, \\ \langle v_T^2 \rangle &= \int \mathrm{d}v \int_0^{2\pi} \mathrm{d}\phi \int_{-1}^{1} \mathrm{d}\cos\theta \, (v^2(1-\cos^2\theta))\, v^2 f(\mathbf{v})\,. \end{aligned} \tag{1}$$

In Fig. 1 we show two of the multiparameter reconstructions projected onto these parameters. The results show that the SHM and SHM+Str benchmarks can be distinguished above the 95% level in Method B, where no prior knowledge is assumed. Results for a range of distributions and experimental setups are presented in Ref. [1].

3 Axion astronomy

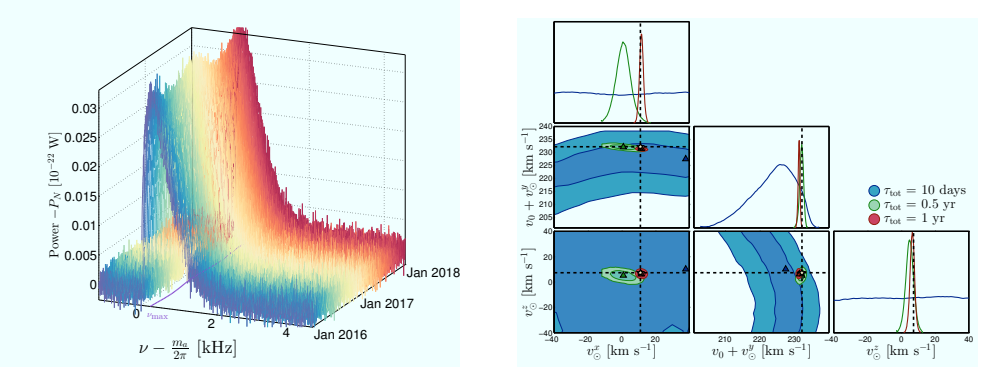

Figure 2: **Left:** simulated axion + noise power as a function of frequency (shifted by the axion mass) and time. The power displayed along the vertical axis is shifted by the mean noise P_N. **Right:** reconstructed Galactic coordinate components of $\mathbf{v}_{\rm lab}$, displayed as 68% and 95% confidence level contours in the marginalized likelihood. Dashed lines show the input values of each parameter. The colors on each set of contours indicate the amount of data taking used to achieve the reconstruction, $\tau_{\rm tot}$.

Experimental searches for DM axions are typically based on a coupling to electromagnetism that permits their conversion into photons inside a magnetic field. We follow a similar procedure to before, but inside a resonant microwave cavity experiment exploiting this process. In Fig. 2 we show a signal simulation of a hypothetical experiment based on ADMX that could be performed once the axion has been detected and a frequency range containing the axion mass has been identified. Like the nuclear recoil spectrum for WIMPs, the EM power received in a resonant cavity is dependent on the speed distribution $f(v)$. However since the axion is usually interpreted as an oscillating classical field, it is more natural to express this in terms of a power spectrum $|\mathcal{A}(\omega)|^2 \propto f(v)$. The power spectrum is introduced by writing down the modes of the axion field $a(t) = a_0 \exp(-i\omega t)$, where $\omega = m_a(1 + v^2/2)$ (ignoring any spatial dependence). The spectrum of these Fourier modes is therefore related to the distribution of values of v, i.e.

$f(v)$. Accounting for losses, the total signal power in a cylindrical cavity of volume V, quality factor Q, and magnetic field B_0, exploiting the first transverse electric field mode, is

$$P = g_{a\gamma\gamma}^2 B_0^2 V \omega_0 Q^3 \frac{4}{\chi_{0l}^2} \int_{-\infty}^{+\infty} \frac{\mathrm{d}\omega}{2\pi} \mathcal{T}(\omega) |\mathcal{A}(\omega)|^2 \,, \tag{2}$$

where χ_{0l} is the l-th zero of the 0th Bessel function of the first kind. The cavity computation introduces $\mathcal{T}(\omega)$, which is a Lorentzian centered on the resonant frequency ω_0, and describes the power loss off resonance.

As before, we reconstruct sets of input astrophysics parameters. In Fig. 2 we show mock data comprised of multiple-day long time-integrated power spectra - collected over the course of one year to exploit the annual modulation due to the lab velocity. Here we display the reconstructed values of the Galactic coordinate components of $\mathbf{v}_{\mathrm{lab}}$. We show three sets of contours which correspond to experiments of different durations. The shortest 10 day long experiment corresponds to a single time-integrated bin of the 0.5 and 1 year long experiments. The phase and amplitude of the annual modulation is essential for measuring all three components, a feat nearly impossible to this accuracy in WIMP detection. The precision achievable with 1 year of data reaches the 1 km s^{-1} level, improving upon that of current astronomical observations [4].

For axion astronomy we may also be interested in substructures that would not form from DM made of WIMPs. In particular, small bound structures of axions known as miniclusters are a consequence of the dynamics of the axion field at early cosmological times. These may be detectable on Earth today as we pass through the network of ministreams left behind as miniclusters become disrupted after passages through the stellar disk. These would show up prominently and characteristically as short lived features in the resolved power spectrum as we discuss further in Ref. [2].

4 Summary

We emphasize the differences between measuring a DM halo made of axions compared with one made of WIMPs. Even with an angular distribution of WIMP recoils, reconstructing and measuring properties of the local velocity distribution is difficult. However progress can be made with the use of empirical methods. However with axions, because we detect their conversion into photons - rather than via a stochastic scattering process - their kinematic structure is preserved and the prospects are much greater. This points towards the idea that in a post-axion discovery era haloscope experiments will be able to perform "axion astronomy". Finally, we remark that it may be possible to further push axion astronomy to directional sensitivity with the use of velocity dependent effects [5, 6].

The author aknowledges support from the STFC and the University of Zaragoza.

References

[1] B. J. Kavanagh and C. A. J. O'Hare, Phys. Rev. D **94** (2016) no.12, 123009 [arXiv:1609.08630].

[2] C. A. J. O'Hare and A. M. Green, Phys. Rev. D **95** (2017) no.6, 063017 [arXiv:1701.03118]

[3] F. Mayet *et al.*, Phys. Rept. **627** (2016) 1 [arXiv:1602.03781 [astro-ph.CO]].

[4] R. Schoenrich, J. Binney and W. Dehnen, Mon. Not. Roy. Astron. Soc. **403** (2010) 1829 [arXiv:0912.3693]

[5] I. G. Irastorza and J. A. Garcia, JCAP **1210** (2012) 022 [arXiv:1207.6129]

[6] A. J. Millar, J. Redondo and F. D. Steffen, JCAP **1710** (2017) no.10, 006 [arXiv:1707.04266]

Chapter 3

Searches in Accelerators

ALPs EFT & Collider Signatures

Rocío del Rey Bajo

Universidad Autónoma de Madrid & Instituto de Física Teórica, Madrid, Spain

DOI: http://dx.doi.org/10.3204/DESY-PROC-2017-02/delrey_rocio

We explore the leading effective interactions between the Standard Model and a generic singlet CP-odd (pseudo)Goldstone boson in two frameworks for electroweak symmetry breaking: linear and non-linear realizations, determining the basis of leading effective operators for the latter. New bounds are obtained and prospects of signals at colliders are explored. Mono-Z, mono-W, and $aW\gamma$ are signals expected in both frameworks while non-standard Higgs decays and mono-h signals may point to non-linear EWSB realizations.

1 Motivations

The Higgs discovery has set spin zero particles in the spotlight of searches for physics beyond the Standard Model. One example is the strong CP problem, whose paradigmatic solution predicts a (pseudo)Nambu-Goldstone boson (pNGB): the axion. In a QCD-like theory its mass m_a arises because of an explicit breaking of the chiral $U(1)_{PQ}$ symmetry by instantons at a scale Λ. It is related to the PQ-breaking scale f_a (in a one quark approximation, of mass m_q): [1]

$$m_a^2 f_a^2 = \Lambda^4 / \left(1 + \Lambda^4/(2m_q < \bar{\psi}\psi >)\right) . \tag{1}$$

In the SM, $\Lambda = \Lambda_{QCD} \gg m_q$, giving the relationship typical of invisible axion models: $m_a f_a \sim m_\pi f_\pi$. With an alternative confining gauge group with a scale $\Lambda' \gg \Lambda_{\rm QCD}$ this relationship may be modified, e.g. $m_a f_a \sim \Lambda'^2$. In models of this kind (eg. Ref. [2]) axions may have simultaneously a low axion scale $f_a \sim \mathcal{O}(10\,\text{TeV})$ and a high mass $m_a \sim \mathcal{O}(100\,\text{GeV})$.

The nature of the Higgs itself also raises a quandary, as the electroweak (EW) hierarchy problem remains unsolved. The lightness of the Higgs may result from its being a pNGB of a global symmetry [3], spontaneously broken by strong dynamics at a scale $\Lambda_s \gg v$, where v denotes the EW scale, as typically arises in scenarios where electroweak symmetry breaking (EWSB) is non-linearly realised. Much as the interactions of QCD pions are weighted down by the pion decay constant, those of the EW (pseudo)Goldstone Bosons – the longitudinal components of the $W^\pm$ and Z plus the h– will be weighted down by a scale f ($\Lambda_s \leq 4\pi f$)[4]. An effective field theory (EFT) approach allows to avoid the specificities of particular models.

We formulate the leading CP-invariant effective couplings of an extra CP-odd pNGB singlet scalar to SM fields, which must be purely derivative couplings when its mass is neglected. While the dominant ALP interactions in the linear –often called SMEFT– expansion have been formulated long ago [5], the analogous for the non-linear –often called Higgs EFT (HEFT)– regime is developed here.

Up to now, phenomenological analyses concentrated on ALP couplings to photons, gluons and fermions, which dominate at low energies and determine astrophysical constraints for light

ALPs. However, ALPs may show up first at colliders and the $SU(2)\times U(1)$ invariant formulation of their interactions provides new channels involving the EW gauge bosons and the Higgs.

2 Linear and Chiral Lagrangians

Focusing on interactions involving only one ALP, the effective linear ALP Lagrangian including leading (LO) and next-to-leading-order (NLO) interactions was determined long ago [5]. The complete basis for ALP interactions with the SM fields at NLO consists of four operators:

$$\mathcal{A}_{\tilde{X}} = -X^a_{\mu\nu}\tilde{X}^{a\mu\nu}\frac{a}{f_a} \quad (X = B,\, W,\, G\,), \qquad \text{and} \qquad \mathbf{O}_{a\Phi} = i(\Phi^\dagger \overleftrightarrow{D}_\mu \Phi)\frac{\partial^\mu a}{f_a}\,, \tag{2}$$

where $\mathcal{A}_{\tilde{X}}$ describe ALP couplings to gauge bosons and $\mathbf{O}_{a\Phi}$ induces a two-point function contribution that can be traded for a fermionic vertex $\sim c_{a\Phi}\,(\bar{\psi}\gamma_\mu\gamma_5\psi)\,\partial^\mu a/f_a$. In this context $\Phi = \frac{v+h}{\sqrt{2}}\mathbf{U}(x)\begin{pmatrix}0 & 1\end{pmatrix}^T$, where $\mathbf{U}(x) \equiv e^{i\sigma_a\pi^a(x)/v}$ encodes the $W^\pm$ and Z longitudinal components, denoted by $\vec{\pi}(x)$.

In non-linear setups [6, 7, 8], the physical Higgs may no longer behave as an exact EW doublet at low energies. It can be treated effectively as a generic scalar singlet with arbitrary couplings by replacing the SM $(v+h)$ dependence by $\mathcal{F}(h) = 1 + 2a\frac{h}{v} + b\left(\frac{h}{v}\right)^2 + \ldots$, whose interactions are not necessarily correlated with those of the EW-"pions" in $\mathbf{U}(x)$. [1] In non-linear EFTs $\mathcal{F}(h)$ and $\mathbf{U}(x)$ are independent building blocks. [2] We generalize the effective chiral Lagrangian to include ALP insertions,

$$\mathscr{L}^{\text{chiral}}_{\text{eff}} = \mathscr{L}^{\text{LO}}_{\text{HEFT}} + \frac{1}{2}(\partial_\mu a)(\partial^\mu a) + c_{2D}\mathcal{A}_{2D}(h) + \delta\mathscr{L}^{\text{bosonic}}_a\,. \tag{3}$$

Now, the LO Lagrangian includes the usual HEFT LO terms plus the ALP kinetic term and

$$\mathcal{A}_{2D}(h) = iv^2\,\text{Tr}[\mathbf{T}\mathbf{V}_\mu]\partial^\mu\frac{a}{f_a}\mathcal{F}_{2D}(h)\,. \tag{4}$$

If EWSB is non-linearly realised $\mathcal{A}_{2D}(h)$ may provide the dominant signals, as it appears singled out at the LO in the chiral expansion. Apart from contributing to the $Z^\mu\partial^\mu a$ two-point function, alike to $\mathbf{O}_{a\Phi}$, it additionally gives rise to $(Z_\mu\partial^\mu a)h^n$, $n \geq 1$ couplings, which are *not* redefined away as in the non-linear case. The reason is that the functional dependence on h of $\mathcal{F}_i(h)$ differs generically from that characteristic of the linear regime, in powers of $(v+h)^2$.

We find [9] that the NLO Lagrangian, $\delta\mathscr{L}^{\text{bosonic}}_a = \sum_{\tilde{X}} c_{\tilde{X}}\mathcal{A}_{\tilde{X}} + \sum_1^{17} c_i\mathcal{A}_i$, consists of 20 independent bosonic structures: three $\mathcal{A}_{\tilde{X}}$, the same as in Eq. (2) plus 17 operators $\mathcal{A}_i$ (see Ref. [9]) amongst which the ones testable with present and high luminosity LHC data are

$$\mathcal{A}_3(h) = \frac{1}{4\pi}B_{\mu\nu}\partial^\mu\frac{a}{f_a}\partial^\nu\,\mathcal{F}_3(h) \qquad \text{and} \qquad \mathcal{A}_6(h) = \frac{1}{4\pi}\,\text{Tr}[\mathbf{T}[W_{\mu\nu}, \mathbf{V}^\mu]]\partial^\nu\frac{a}{f_a}\,\mathcal{F}_6(h)\,. \tag{5}$$

3 ALP phenomenology

We showcase some salient features of the effective ALP interactions varying one $c_{\tilde{X}}$ or c_i coefficient at a time, which allows to single out the impact of each effective operator. The ALPs are considered stable on collider scales [9], so the bounds LHC presented are valid for $m_a \lesssim \mathcal{O}(\text{MeV})$.

[1] Note that the "pions" in $\mathbf{U}(x)$ are suppressed by v, where the natural GB weight is in fact the scale f; this encodes the fine-tuning affecting these models.

[2] Two $SU(2)_L$ covariant objects are used as building blocks containing $\mathbf{U}(x)$: $\mathbf{V}_\mu(x) \equiv (\mathbf{D}_\mu\mathbf{U}(x))\,\mathbf{U}(x)^\dagger$ and $\mathbf{T}(x) \equiv \mathbf{U}(x)\sigma_3\mathbf{U}(x)^\dagger$.

3.1 Signatures present in both linear and non-linear expansions

The ALP coupling to photons has been extensively tested, and is very strongly constrained: Beam Dump experiments [10] (astrophysical observations [11]) enforce $|c_\theta^2 c_{\tilde{B}} + s_\theta^2 c_{\tilde{W}}|$ to cancel to one part in 10^3 (10^8) for $m_a = 1\,\text{MeV}$ (keV). To account for these strong constraints we have performed the analyses imposing $g_{a\gamma\gamma} = 0 \longrightarrow c_{\tilde{B}} = -t_\theta^2 c_{\tilde{W}}$, effectively reducing the number of parameters by one. However, when considering the complete basis of operators from Eqs. (2) or (3), this coupling is generated simultaneously to set of couplings to the EW gauge bosons:

$$\frac{a}{f_a}\left(c_{\tilde{B}} B_{\mu\nu}\tilde{B}^{\mu\nu} + c_{\tilde{W}} W_{\mu\nu}\tilde{W}^{\mu\nu}\right) \Longrightarrow$$

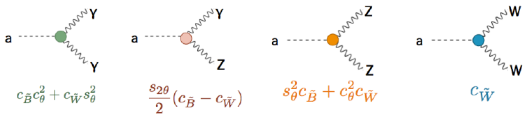

Processes where ALPs are produced through their couplings to gauge bosons allow to test directions of the $\{c_{\tilde{B}}, c_{\tilde{W}}\}$ parameter space other than the combination tested through $g_{a\gamma\gamma}$.

- **ALP coupling to Z-photon:** In the linear expansion, the coupling $-\frac{1}{4} g_{aZ\gamma}\, a\, Z_{\mu\nu}\tilde{F}^{\mu\nu}$ takes the form $g_{aZ\gamma} = 4\sin(2\theta)(c_{\tilde{W}} - c_{\tilde{B}})/f_a$ (with additional operators contributing in the non-linear case), and can be constrained through conservative bounds on $Z \to a\gamma$ from the uncertainty on the Z boson width. Combined with $g_{a\gamma\gamma}$ bounds, $c_{\tilde{B}}$ and $c_{\tilde{W}}$ take values within a limited area, see Fig. 1a. Imposing $g_{a\gamma\gamma} = 0$ leads to $|f_a/c_{\tilde{W}}| > 2.4\,\text{TeV}$.

- **Mono-Z and mono-W signatures:** The ALP can be produced in association with a W or a Z boson, and escape the LHC detectors as missing energy. Mono-Z signals can be tested reinterpreting the CMS $Z + \not{E}_T$ search [12] and, as illustrated in Fig. 1b, this allows to impose the strongest limit on $c_{\tilde{W}}$: $|f_a/c_{\tilde{W}}| > 3.8\,\text{TeV}$ with Run II data, and up to $|f_a/c_{\tilde{W}}| \gtrsim 21$ TeV if no signal is found in the high-luminosity (HL-LHC) phase, here computed as $3\,\text{ab}^{-1}$ of data from $\sqrt{s} = 13\,\text{TeV}$ collisions if nothing is found. Future mono-W searches, analysed from the ATLAS search for $W' \to \ell + \not{E}_T$ [13] may uncover $\mathcal{A}_6$, a signal of non-linearity: it will be tested up to $|f_a/c_6| < 4.5\,\text{TeV}$ at HL-LHC.

- **Associated production $pp \to W^\pm a\gamma$:** Mono-W and $aW\gamma$ both depend on similar combinations of coefficients: correlation effects are thus *a priori* expected amongst them, and their combined analysis should allow to disentangle the measurement of $c_{\tilde{W}}$ from that of c_6. Analysed independently, $aW\gamma$ will reach $|f_a/c_{\tilde{W}}| \lesssim 6.8$ TeV and $|f_a/c_6| \lesssim 0.8$ TeV at HL-LHC.

3.2 Distinctive non-linear signatures: Higgs signatures

ALP-Higgs couplings are an interesting class of new signals which may point to non-linear realizations of EWSB where aZh^n vertices are expected at LO, since they do not appear in the linear expansion below NNLO. The bounds are computed for one operator at a time (for $\mathcal{A}_{2D}$, $\mathcal{A}_3$ and $\mathcal{A}_{10}$ from Ref. [9]), but a combined analysis may allow to disentangle them.

- **Non-standard higgs decays Γ^h_{BSM}:** Current constraints from ATLAS and CMS global fits of 7 and 8 TeV data to Higgs signal strengths yield [14] $\text{Br}(h \to \text{BSM}) \leq 0.34$ (95% C.L.), with $\Gamma^h_{\text{BSM}} \simeq \Gamma_{h\to aZ}$. Interpreting this bound in terms of the LO operator $\mathcal{A}_{2D}$ gives $|f_a/\tilde{a}_{2D}| \gtrsim 2.78\,\text{TeV}$ for $m_a \lesssim 34\,\text{GeV}$, where $\tilde{a}_i \equiv c_i a_i$. These limits are expected to improve significantly at HL-LHC, which will be able to test up to $|f_a/\tilde{a}_{2D}| \lesssim 6\,\text{TeV}$.

- **Mono-h:** The $\not{E}_T$ spectrum of $pp \to ah\,(h \to 4\ell)$ is considered at 13 TeV LHC. Although this search is in principle sensitive to both $\mathcal{A}_{2D}$ and $\mathcal{A}_3$, it is not competitive with $\text{Br}(h \to \text{BSM})$ in constraining the former. On the other hand, it is more sensitive to the presence of $\tilde{a}_3$ (see Fig. 1b) and may therefore provide valuable, complementary information.

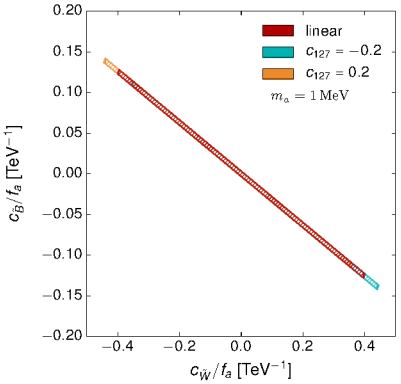

(a) *Constraints on $c_{\tilde{B}}/f_a$ and $c_{\tilde{W}}/f_a$ from the tree-level bounds on $g_{a\gamma\gamma}$ and $g_{aZ\gamma}$.*

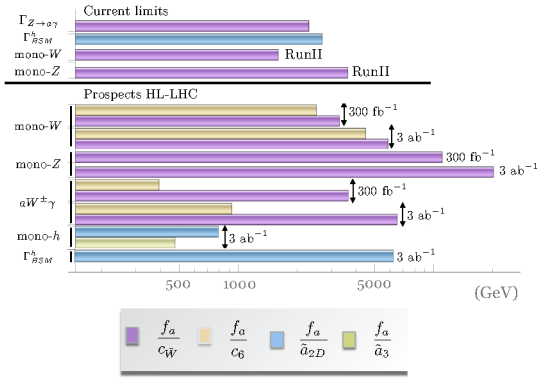

(b) *Constraints from the studies on tree-level ALP couplings in this work.*

4 Conclusions

In summary, a general approach to ALP interactions with the SM fields, considering complete effective Lagrangians that include all $SU(3) \times SU(2) \times U(1)$ invariant operators might suggest axion searches complementary to the traditional ones performed until now. Through their coupling to EW gauge bosons we show that ALPs stable at LHC, can be tested via mono-W, mono-Z, $pp \to aW\gamma$ signatures, with present data (HL-LHC) testing the operator coefficients to $f_a/c_i \sim \mathcal{O}(1\,\text{TeV})$ ($\mathcal{O}(20\,\text{TeV})$) for some operators. Furthermore, we have determined the chiral effective Lagrangian for non-linear EWSB. New additional couplings are expected, one of the most promising signals being ALP couplings to the Higgs particle. We show that LHC data for mono-h and non-standard h decays is able to test aZh and $a\gamma h$ interactions, which are not expected in linear expansions below NNLO, and are thus smoking guns for non-linearity.

References

[1] K. Choi, K. Kang, and J. E. Kim, Phys. Lett. **B181** (1986) 145–149.

[2] T. Gherghetta, N. Nagata, and M. Shifman, Phys. Rev. **D93** (2016), no. 11 115010, [arXiv:1604.01127].

[3] D. B. Kaplan and H. Georgi, Phys. Lett. **B136** (1984) 183–186.

[4] A. Manohar and H. Georgi, Nucl. Phys. **B234** (1984) 189–212.

[5] H. Georgi, D. B. Kaplan, and L. Randall, Phys. Lett. **B169** (1986) 73–78.

[6] R. Contino, *TASI Lectures in Elementary Particle Physics, 2009*, pp. 235–306, 2011. [arXiv:1005.4269].

[7] R. Alonso, M. B. Gavela, L. Merlo, S. Rigolin, and J. Yepes Phys. Lett., **B722** (2013) 330–335, [arXiv:1212.3305]. [Erratum: Phys. Lett.B726,926(2013)].

[8] I. Brivio, J. Gonzalez-Fraile, M. C. Gonzalez-Garcia, and L. Merlo, arXiv:1604.06801.

[9] I. Brivio, M. B. Gavela, L. Merlo, K. Mimasu, J. M. No, R. del Rey, and V. Sanz, arXiv:1701.05379.

[10] J. D. Bjorken, S. Ecklund, W. R. Nelson, A. Abashian, L. Mo, P. Rassmann, C. Church, and T. Nunamaker, , in *Proceedings, 4th Moriond Workshop, January 15-21, 1984*, pp. 227–242, 1984.

[11] G. G. Raffelt Lect. Notes Phys. **741** (2008) 51–71, [hep-ph/0611350].

[12] **CMS** Collaboration, Tech. Rep. CERN-PH-EP-2013-231, [arXiv:1404.0051]

[13] **ATLAS Collaboration** Collaboration, Tech. Rep. ATLAS-CONF-2015-063, CERN, Geneva, Dec, 2015.

[14] **ATLAS, CMS** Collaboration, G. Aad *et. al.*, JHEP **08** (2016) 045, [arXiv:1606.02266].

Searches for very weakly-coupled particles beyond the Standard Model with NA62

Babette Döbrich[1]*, for the NA62 collaboration* *
[1]CERN, 1211 Geneva, Switzerland

DOI: http://dx.doi.org/10.3204/DESY-PROC-2017-02/dobrich_babette

The NA62 experiment at CERN is designed to measure precisely the rare decay $K^+ \to \pi^+\nu\bar{\nu}$. The intensity and energy of the SPS proton beam used to produce the K^+, as well as the hermetic detector coverage and overall geometry, give in addition the opportunity to search for hypothesized weakly-coupled particles at the MeV-GeV mass scale. In these proceedings the focus lies on reviewing these opportunities and sketching the current status of some pertinent searches.

1 Kaon physics with NA62

The NA62 experiment aims to measure to a good accuracy the very small branching ratio (BR) of $K^+ \to \pi^+\nu\bar{\nu}$, which is $\mathcal{O}(10^{-10})$. This BR is rather precisely (<10 % level) predicted from theory and has a recognized sensitivity to new physics [1]. However, the only existing measurement of this BR is based on only seven events [2], and the experimental precision is thus not sufficient to challenge the theory prediction. NA62 aims to measure this BR at the

*The NA62 Collaboration: R. Aliberti, F. Ambrosino, R. Ammendola, B. Angelucci, A. Antonelli, G. Anzivino, R. Arcidiacono, M. Barbanera, A. Biagioni, L. Bician, C. Biino, A. Bizzeti, T. Blazek, B. Bloch-Devaux, V. Bonaiuto, M. Boretto, M. Bragadireanu, D. Britton, F. Brizioli, M.B. Brunetti, D. Bryman, F. Bucci, T. Capussela, A. Ceccucci, P. Cenci, C. Cesarotti, V. Cerny, C. Cerri, B. Checcucci, A. Conovaloff, P. Cooper, E. Cortina Gil, M. Corvino, F. Costantini, A. Cotta Ramusino, D. Coward, G. D'Agostini, J. Dainton, P. Dalpiaz, H. Danielsson, N. De Simone, D. Di Filippo, L. Di Lella, N. Doble, B. Dobrich, F. Duval, V. Duk, J. Engelfried, T. Enik, N. Estrada-Tristan, V. Falaleev, R. Fantechi, V. Fascianelli, L. Federici, S. Fedotov, A. Filippi, M. Fiorini, J. Fry, J. Fu, A. Fucci, L. Fulton, E. Gamberini, L. Gatignon, G. Georgiev, S. Ghinescu, A. Gianoli, M. Giorgi, S. Giudici, F. Gonnella, E. Goudzovski, C. Graham, R. Guida, E. Gushchin, F. Hahn, H. Heath, T. Husek, O. Hutanu, D. Hutchcroft, L. Iacobuzio, E. Iacopini, E. Imbergamo, B. Jenninger, K. Kampf, V. Kekelidze, S. Kholodenko, G. Khoriauli, A. Khotyantsev, A. Kleimenova, A. Korotkova, M. Koval, V. Kozhuharov, Z. Kucerova, Y. Kudenko, J. Kunze, V. Kurochka, V.Kurshetsov, G. Lanfranchi, G. Lamanna, G. Latino, P. Laycock, C. Lazzeroni, M. Lenti, G. Lehmann Miotto, E. Leonardi, P. Lichard, L. Litov, R. Lollini, D. Lomidze, A. Lonardo, P. Lubrano, M. Lupi, N. Lurkin, D. Madigozhin, I. Mannelli, G. Mannocchi, A. Mapelli, F. Marchetto, R. Marchevski, S. Martellotti, P. Massarotti, K. Massri, E. Maurice, M. Medvedeva, A. Mefodev, E. Menichetti, E. Migliore, E. Minucci, M. Mirra, M. Misheva, N. Molokanova, M. Moulson, S. Movchan, M. Napolitano, I. Neri, F. Newson, A. Norton, M. Noy, T. Numao, V. Obraztsov, A. Ostankov, S. Padolski, R. Page, V. Palladino, C. Parkinson, E. Pedreschi, M. Pepe, M. Perrin-Terrin, L. Peruzzo, P. Petrov, F. Petrucci, R. Piandani, M. Piccini, J. Pinzino, I. Polenkevich, L. Pontisso, Yu. Potrebenikov, D. Protopopescu, M. Raggi, A. Romano, P. Rubin, G. Ruggiero, V. Ryjov, A. Salamon, C. Santoni, G. Saracino, F. Sargeni, V. Semenov, A. Sergi, A. Shaikhiev, S. Shkarovskiy, D. Soldi, V. Sougonyaev, M. Sozzi, T. Spadaro, F. Spinella, A. Sturgess, J. Swallow, S. Trilov, P. Valente, B. Velghe, S. Venditti, P. Vicini, R. Volpe, M. Vormstein, H. Wahl, R. Wanke, B. Wrona, O. Yushchenko, M. Zamkovsky, A. Zinchenko.

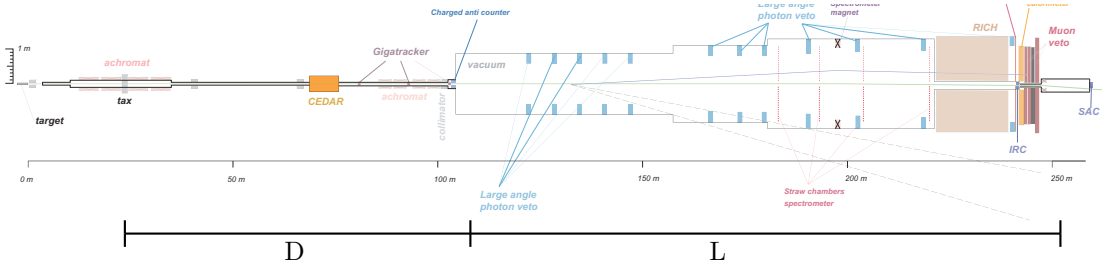

Figure 1: Layout of NA62: The SPS proton beam (from left) hits a beryllium target. A fraction of the secondary beam as well as around ∼40% of the primary protons that have not interacted in the target are guided towards an achromat, located approximately 24 m downstream of the target. This achromat, called 'TAX', is described in more detail in Figure 2. All beam components (including the remaining 400 GeV component) except for a positive component at ∼75 GeV, are stopped in the TAX. The 75 GeV component eventually is guided along a distance D to the start of a decay volume of length L downstream. Kaons from the secondary hadron beam are eventually identified (CEDAR) and measured (Gigatracker).

10% level by combining a large number of kaon decays $\mathcal{O}(10^{13})$ with a hermetic detector system, that can reject other kaon decays in the $\sim$ 60 m long fiducial volume (FV) ultimately at the $\mathcal{O}(10^{12})$ level. The detector layout is shown in Fig. 1, and a detailed description of the physics case, the experiment and its performance is provided in [3].

To date, NA62 has released a preliminary analysis of 5% of 2016 data, results are described in [4]. In 2017, $\sim 3 \times 10^{12}$ kaon decays have been collected and the experiment will continue data taking in 2018, until the long shutdown of the CERN accelerators.

Besides the main measurement, NA62 has a program to search for lepton number and lepton flavor violating decays. In addition, with existing and near-future data, NA62 has a discovery potential in the search of very weakly-coupled particles beyond the Standard Model. Such particles, if existing at the MeV-GeV scale would have comparably long lifetimes and could have escaped all past detection efforts so far. The need for an increased experimental activity in this area is widely appreciated in the HEP community, since the existence of a 'Dark Sector' can be linked to a plethora of open physics questions [5].

2 Beam-line and production modes of novel particles

The kaons of interest for NA62 are produced by interaction of the SPS 400 GeV proton beam in an upstream target, see Fig. 1. The unseparated, positively charged hadron beam is selected in momentum by an achromat, shown and described in Figure 2.

Consequently, in *standard data-taking*, besides beam halo muons, only these secondary particles (essentially π^+, p, K^+) at 75 GeV will enter the decay volume of NA62. Interestingly, even during data-taking with the upstream target in place, about 40 % of the primary protons punch through this target and eventually interact in the first collimator C1, cf. Fig 2, with their hadronic shower being absorbed. *Another possible mode for data-taking* in NA62 is to run as a 'beam-dump' such that up to 100% of the 400 GeV protons are stopped in the collimators.

Interactions of 400 GeV protons in the collimator, as well as decays of secondary mesons

before the collimator may be the source of different, so-far undiscovered, weakly-interacting particles, which travel unhindered to the NA62 decay volume and decay into visible final states. Besides the primary beam energy and protons on target (POT), the main variable for the parameter-space-coverage in these searches is geometry: Ideally, the decay volume is close enough to novel particle's production point to contain the decay products of the most short-lived particles as well as long enough to detect the most long-lived candidates. The comparably small $D \simeq 80$m, and large $L \simeq 136$ m (cf. Fig. 1) of the NA62 setup enable the experiment to extend search parameters beyond past results, e.g. from CHARM and NuCal for axion-like particle searches [6].

In both, nominal and dump data-taking modes, competitive searches for weakly interacting particles beyond the Standard Model are possible. NA62 can make a strong contribution in shedding light on the existence of 'Dark Sector particles' using:

1. **Meson decays in the FV:** The large flux of kaons and pions in NA62 suggests to search novel particles in their decays. Examples of recent preliminary results are: Firstly production searches of Heavy Neutral Leptons N in $K^+ \to l^+ N$, with $l = e, \mu$. Secondly: the search for invisibly decaying Dark Photons A' from $K^+ \to \pi^+\pi^0$, where $\pi^0 \to \gamma A'$. Preliminary results of both analyses are given in [4].

2. **Parasitic dump production:** The decay of hypothesized new particles in the NA62 decay volume produced upstream can be searched for by dedicated trigger chains (that do not require the presence of a kaon) in parallel to the main trigger. Such decays can be potentially disentangled from hadron beam decays and random track combinations. In 2017 dedicated trigger chains have been set up for multi-track events with at least one or two muons to record decays from (pseudo-)scalars (axion-like particles), Dark Photons and Heavy Neutral Leptons.

3. **Dedicated dump runs:** To achieve the best possible sensitivity in the search for weakly-coupled particles produced upstream, it is mandatory to 'close' the collimators (i.e. misalign bores for the hadron beam). In this setting, background is minimized. The current statistics collected in this mode is of the order of $\lesssim 10^{16}$ POT. Specific trigger chains for at least one track or a minimum energy in the Liquid Krypton electromagnetic calorimeter are typically required.

3 Outlook and Summary

The NA62 experiment has been designed to sustain a high beam-rate, provide full particle identification, hermetic coverage and very light-material tracking. Besides the main measurement $K^+ \to \pi^+\nu\bar{\nu}$, NA62 has the means and a program to discover weakly-coupled particles beyond the Standard Model.

Consequently, for the 2021-2023 operation of the CERN accelerators, an extended ($\sim$ one-year-long) data-taking in dump-mode is being discussed with the aim to collect around $\sim 10^{18}$ POT. Reference [7] gives physics examples, projections and results on background rejection. In the meanwhile, data collected in 2016/2017 are used to validate expectations for backgrounds and to perform first analyses possible within the statistics collected so far.

In summary, the NA62 experiment combines the opportunity for precision Standard Model measurements with the discovery potential for wide range of weakly-coupled new physics.

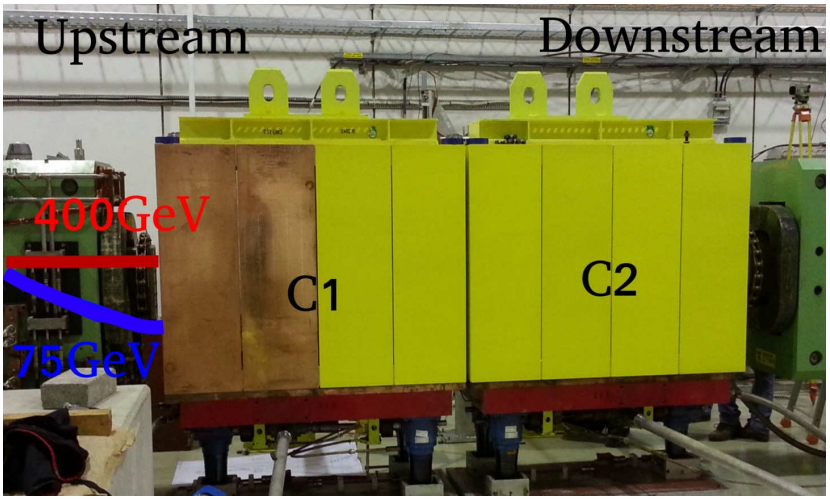

Figure 2: Picture of the 'TAX' achromat of the NA62 beamline: It is located ∼80 m upstream of the NA62 decay volume. The beam is incident from the left and is dispersed by a magnet before reaching the two collimators, labeled as C1 and C2. For simplicity, only two positive beam components are sketched, whilst in reality a wide momentum spectrum reaches the collimators. C1 (copper/iron) and C2 (full iron) are each ∼ 1.6 m long and each contain small bores (from left to right, not visible in the picture) to allow the passage of the 75 GeV component (sketched in blue) in nominal data taking. The two collimator blocks can be moved along the vertical direction, to either reduce the intensity or completely block the beam (by misaligning the bores) and act as a beam-dump. The upstream beryllium target (not visible in the picture) can be removed for special runs. In this situation the entire 400 GeV primary proton component is dumped into C1.

Acknowledgments

The author would like to thank the PATRAS 2017 organizers for their continued effort in realizing fruitful and exciting workshops in the series.

References

[1] A. J. Buras, D. Buttazzo and R. Knegjens, JHEP **1511**, 166 (2015) [arXiv:1507.08672 [hep-ph]].

[2] A. V. Artamonov *et al.* [BNL-E949 Collaboration], Phys. Rev. D **79**, 092004 (2009) [arXiv:0903.0030 [hep-ex]].

[3] E. Cortina Gil *et al.* [NA62 Collaboration], JINST **12**, no. 05, P05025 (2017) [arXiv:1703.08501 [physics.ins-det]].

[4] NA62 collaboration, 2017 Status Report to the SPSC, CERN-SPSC-2017-013, `https://cds.cern.ch/record/2256924`

[5] J. Alexander *et al.*, arXiv:1608.08632 [hep-ph]. R. Essig *et al.*, arXiv:1311.0029 [hep-ph].

[6] B. Döbrich, J. Jaeckel, F. Kahlhoefer, A. Ringwald and K. Schmidt-Hoberg, JHEP **1602**, 018 (2016) [arXiv:1512.03069 [hep-ph]].

[7] T. Spadaro for the NA62 collaboration, PBC contributions: `indico.cern.ch/event/608491/contributions/2457796/` and `indico.cern.ch/event/644287/contributions/2724460/`

Chapter 4

Astrophysical Observations

Impact of Axions on the Minimum Mass of Core Collapse Supernova Progenitors

Inma Domínguez[1], *Maurizio Giannotti*[2], *Alessandro Mirizzi*[3], *Oscar Straniero*[4]

[1]Univ. de Granada, Granada, Spain
[2]Univ. of Barry, Miami Shores, Florida, USA
[3]Univ. of Bari & INFN-Sezione di Bari, Italy
[4]INAF-Osservatorio Astronomico d'Abruzzo, Teramo, & INFN-Laboratori Nazionali del Gran Sasso, Assergi, Italy

DOI: http://dx.doi.org/10.3204/DESY-PROC-2017-02/dominguez_inma

In this study we include axions in stellar evolution models adopting the current stringest constraints for their coupling to photons and electrons. We obtain that the minimum stellar mass of Core Collapse Supernova (CCSN) progenitors is shifted up by nearly 2 $M_\odot$. This result seems to be in tension with the observationaly derived minimum mass of CCSN progenitors.

1 Introduction

Stars are known to be good laboratories for particle physics. Axions and Axions Like Particles (ALPs) may be produced in stellar interiors and freely escape, carrying energy out and thus, modifying stellar evolution.

Axions are weakly interactive particles that were introduced to explain the absence of CP violation in the strong interactions [1, 2, 3]. Later on, these particles and, in general, ALPs were proposed as dark matter candidates [4]. In well motivated axion models, like the DFSZ [5, 6], axions couple to photons and fermions. These couplings are characterized by the corresponding coupling constants, $g_{a\gamma}$ and g_{ae}, being the energy loss rates in these interactions proportional to the square of the coupling constants. In stellar interiors, ALPs that couple to photons are expected to be produced by the Primakoff process and, if they couple to electrons, mainly by the Compton and Bremsstrahlung processes (see [7]).

The ALP stellar approach consists of constraining the coupling strengths in order to avoid conflicts with astronomical observations. Moreover, there are also astronomical observations that could be better explained considering an extra-energy sink (see i.e. [8]). Among them, the observed decrease of the pulsational period of some white dwarfs [9, 10] and the shape of the observed WD luminosity function [11, 12]. In both cases the derived limits are for g_{ae}.

In this work we study the influence of axions on the value of the minimum stellar mass that experiences central carbon burning, Mup ([13]) and so, the minimum possible stellar mass that may produce a CCSN. Among CCSNe, type II-P are those expected to come from the evolution of single stars. Their bright supergiant progenitors are identified on the corresponding images taken at the SN locations before the explosion, and the progenitor masses estimated from the

luminosities of these supergiants. Masses in the range 7-10 $M_\odot$ have been estimated for the type II-P SNe 2003gd, 2005cs, 2009md, 2006my, 2012A and 2013ej (see [14]), while theoretical predictions for the minimum masses of CCSNe are above 9-10 $M_\odot$. As we will show, the presence of axions coupled to photons and electrons would increase the progenitor mass expected by these current prediction, possibly beyond observational constraints.

2 Numerical simulations & Results

We consider DFSZ axions produced through the mentioned processes (Primakoff, Compton and Bremsstrahlung), adopting for the coupling constants the most updated limits that are also provided with corresponding uncertainties:

- $g_{ae} \leq 4.3 \times 10^{-13}$ at 95% CL [15], based on the luminosity of the RGB tip derived from globular clusters (GCs).
- $g_{a\gamma} \leq 0.66 \times 10^{-10}$ GeV^{-1} at 95% CL, based on the R parameter derived for GCs [16, 17], and being also the the experimental upper limit obtained by the CAST collaboration [18].

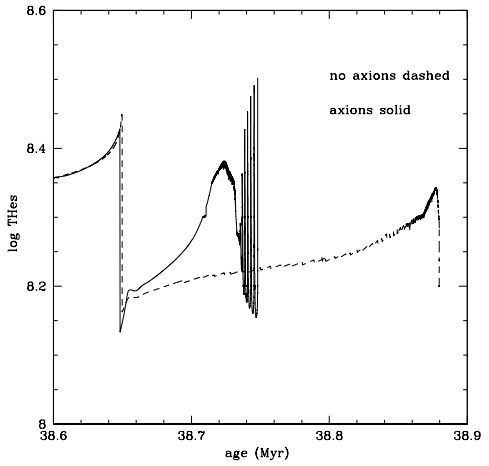

Figure 1: Evolution in time of the maximum temperature within the He-shell for the reference model of 7.5 $M_\odot$, without axions (dotted line), and for a model with the same mass, including axions (solid line).

The FUNS code [19, 20, 21], modified to include the corresponding axion processes, is used for all the numerical simulations. The axion energy loss rate for the Primakoff is taken from [7], for the Compton from [22], for the non-degenerate Bremstrahlung from [22] and for the degenerate Bremsstrahlung from [23, 24]. Rates and interpolations have been revised by the authors.

We compute models in the mass range 7 to 11 $M_\odot$, with a resolution of 0.2 $M_\odot$, and assuming solar initial chemical composition, Z= 0.013 & Y= 0.26. All models are computed from the pre-MS to central C-burning, or alternatively, to CO core cooling (along the AGB phase).

We have first identified, as a reference, the minimum initial stellar mass needed for central C-burning, Mup, without axions, and it turns out to be 7.5 $M_\odot$. Then, we compute models including the previous axion energy loss rates and we find that models in the mass range 7.5 to 9.1 $M_\odot$ do not ignite carbon, being Mup 9.2 $M_\odot$.

The main reason of this shift of Mup by 1.7 $M_\odot$ is the smaller CO core developed, for the same initial stellar mass, by models that include axions. The growth of the CO core, during the so called early-AGB phase, is halted earlier because the evolution is faster: nuclear energy has to compensate the axion energy losses within the He-shell. This effect was discussed by some of us, in another context, some years ago ([25]). The different time-scales are clearly seen in Fig. 1. The early-AGB time is reduced by the axion effect, from 2.223×10^5 yrs to 7.76×10^4 yrs wich results in final CO core masses of 1.066 $M_\odot$ for the reference model, and 0.937 $M_\odot$ for the model with axions.

We identify both, Compton and Primakoff, as being the most important processes and equaly relevant. For example, when only Primakoff is included Mup is 8.4 $M_\odot$, so Mup is shifted up, with respect to models without axions by 0.9 $M_\odot$ instead of by 1.7 $M_\odot$ when Compton is also included.

However, the change in the CO core mass for a given total stellar mass is not the only factor that influences Mup. We find that an increase of the final CO core mass by 0.113 $M_\odot$, with respect to that of the reference model, is needed for C-burning. Axions cool the degenerate inner part of the CO core and this is due the Bremmsstrahlung process. In fact, when Compton and Primakoff are included but Bremmsstrahlung is not included, Mup is 9.0 $M_\odot$ instead of 9.2 $M_\odot$.

3 Conclusions

The production of DFSZ axions in stellar interior, assuming the current stringest upper limits for the coupling constant values, represents an important energy sink. In this work we have focused on the evolution of stellar masses that are close to the observed minimum progenitor mass for CCSNe. Assumed values for g_{ae} and $g_{a\gamma}$ are 4.3×10^{-13} and 0.66×10^{-10} GeV^{-1}, respectively. Our main result is that the minimum stellar mass that experiences central carbon burning, Mup, is shifted up by 1.7 $M_\odot$, from 7.5 $M_\odot$ for the reference model to 9.2 $M_\odot$ when axions are included, implying that:

- Stars with masses smaller than 9.2 $M_\odot$, would produce CO WDs, potential progenitors of Type Ia Supernovae (SNIa). This may help to solve the problem related with the predicted low theoretical SNIa rates as compare with the rates derived from observations (see [26] for a review).
- CCSNe would only be produced by stars with masses greater than 9.2 $M_\odot$. In fact, considering that a mass interval over Mup is expected to produce ONe WDs and electron capture SNe, the minimum mass for CCSNe progenitor would be even greater. This would be in conflict with the observationaly derived minimum progenitor masses of CCSNe, 7-10 $M_\odot$ [14], .

It is remarkable that the next generation of dedicated axion experiments, like ALPSII [27] and IAXO [28], will focus on the range of parameters that is being tested by stellar models, like those considered in this work.

4 Acknowledgments

I.D ackknowledges founding from the MINECO-FEDER grant AYA2015-63588; A.M. is supported by the MIUR and INFN through the Theoretical Astroparticle Physics project; O.S. acknowledges founding from the PRIN-MIUR grant 20128PCN59.

5 Bibliography

References

[1] Peccei, R. D., & Quinn, H. R. 1977, Physical Review Letters, 38, 1440

[2] Weinberg, S. 1978, Physical Review Letters, 40, 223

[3] Wilczek, F. 1978, Physical Review Letters, 40, 279

[4] Sikivie, P. 2008, Axions, 741, 19

[5] Dine, M., Fischler, W., & Srednicki, M. 1981, Physics Letters B, 104, 199

[6] Zhimitskii, A. P., 1980, Sov. J. Phys., 31, 260

[7] Raffelt, G. G. 1990, Physical Reports, 198, 1

[8] Giannotti, M., Irastorza, I., Redondo, J., Ringwald, A. & Saikawa, K. 2017, JCAP, 10, 10

[9] Isern, J., Hernanz, M., & Garcia-Berro, E. 1992, ApJL, 392, L23

[10] Córsico, A. H., Althaus, L. G., Miller Bertolami, M. M., et al. 2012, MNRAS, 424, 2792

[11] Isern, J., García-Berro, E., Torres, S., & Catalán, S. 2008, ApJL, 682, L109

[12] Miller Bertolami, M. M., Melendez, B. E., Althaus, L. G., & Isern, J. 2014, JCAP, 10, 069

[13] Becker, S. & Iben, I. 1980, ApJ, 237, 111

[14] Smartt, S. J. 2015, Publications of the Astronomical Society of Australia, 32, 16

[15] Viaux, N., Catelan, M., Stetson, P. B., et al. 2013, Physical Review Letters, 111, 231301

[16] Ayala, A., Domínguez, I., Giannotti, M., Mirizzi, A., & Straniero, O. 2014, Physical Review Letters, 113, 191302

[17] Straniero, O., Ayala, A., Giannotti, M., Mirizzi, A., Domínguez, I. 2015, Proceedings of the 11th Patras Workshop on Axions, WIMPs and WISPs, 77

[18] CAST collaboration, Anastassopoulos, V., Aune, S., et al. 2017, arXiv:1705.02290

[19] Straniero, O., Gallino, R., & Cristallo, S. 2006, Nuclear Physics A, 777, 311

[20] Cristallo, S., Straniero, O., Gallino, R., et al. 2009, ApJ, 696, 797

[21] Cristallo, S., Piersanti, L., Straniero, O., et al. 2011, ApJSS, 197, 17

[22] Raffelt, G., & Weiss, A. 1995, PRD, 51, 1495

[23] Nakagawa, M., Kohyama, Y., & Itoh, N. 1987, ApJ, 322, 291

[24] Nakagawa, M., Adachi, T., Kohyama, Y., & Itoh, N. 1988, ApJ, 326, 241

[25] Domínguez, I., Straniero, O., & Isern, J. 1999, MNRAS, 306, L1

[26] Maoz, D., Mannucci, F., & Nelemans, G., 2014, ARAA, 52, 107

[27] Bähre, R., Döbrich, B., Dreyling-Eschweiler, J., et al. 2013, Journal of Instrumentation, 8, T09001

[28] Giannotti, M., Irastorza, I., Redondo, J. & Ringwald, A. 2016, JCAP, 5, 57

[29] Cristallo, S., Straniero, O., Piersanti, L., & Gobrecht, D. 2015, ApJSS, 219, 40

Galactic Centre and M31 EXCESS

Nils Håkansson on behalf of the FERMI-LAT Collaboration
Oscar Klein Center, Stockholm University, Stockholm, Sweden

DOI: http://dx.doi.org/10.3204/DESY-PROC-2017-02/håkansson_nils

Excesses with respect to models of the Galactic diffuse emission in gamma-ray flux have been found around a few GeV at the position of the Galactic Centre (GC) and M31. The underlying physics causing the excesses in flux could be the same but the question remains, if it is due to astrophysical processes, such as Millisecond Pulsars (MSPs), or annihilation of Dark Matter (DM). This talk was given at the *13th Patras Workshop on Axions, WIMPs and WISPs* and is an overview of two Fermi-LAT publications focused on studying and understanding the cause of the excesses, one targeting the GC and one targeting mainly M31.

1 Introduction

The region around the GC is one of the brightest in the gamma-ray sky. Gamma-ray emission in this region includes products of interactions between cosmic-rays with interstellar gas as well as many individual sources such as pulsars and supernova remnants. Many DM theories predict that DM consists of weakly interacting massive particles (WIMPs) that can self-annihilate into final state gamma-rays. A hypothesised signal from such a process is expected to be brightest towards the GC.

Various groups have, since 2009, found an *excess of GeV photons* that extends from the GC up to mid-Galactic-latitudes,see e.g. [6–8]. Some of the works advocated that the data favours an astrophysical origin of the excess rather than evidence for a DM signal, such as [9] and more recently [5], which suggests that the excess can be caused by a population of yet undetected MSPs. The difficulty in distinguishing which theory is correct comes from the fact that the gamma-ray spatial and spectral signals are almost identical at the energies of the excess found.

Recently, gamma-ray emission has been found correlated with the position of M31. Both the GC excess and the M31 emission have been studied by the Large Area Telescope on board the *Fermi* satellite (Fermi LAT). Fermi LAT detects gamma-rays between 20 MeV and above 300 GeV. More information on Fermi LAT can be found in [3].

2 Analysis Methods

The analysis of the three targets were performed using the Fermi Science tools with Pass 8 and ∼6.5 years of Fermi-LAT data. Pass 8 is a new event reconstruction that improves the effective area, energy resolution, the point spread function and event reconstruction, [4]. The excess signal from the GC is found when simultaneously fitting the different components of diffuse emission, simulated using GALPROP, and a map of point sources, from LAT 4-year

Point Source Catalog (3FGL), to the Fermi-LAT maps independently in each energy bin by maximizing the likelihood function based on Poisson statistics, [1]:

$$\log\mathcal{L} = \sum_{i,j}(d_{i,j}\log\mu_{i,j} - \mu_{i,j} - \log(d_{i,j}!)), \tag{1}$$

where $d_{i,j}$ represents the photon counts in spatial pixel i and energy bin j, and $\mu_{i,j}$ is the model counts in the same bin. The model is constructed as a linear combination of templates:

$$\mu_{i,j} = \sum_{m} f_m P^m_{i,j}, \tag{2}$$

where m labels the components of emission, $P^m_{i,j}$ is the spatial template of component m in the appropriate energy bin corrected for exposure and convolved with the Fermi-LAT PSF. The coefficients f_m are adjusted to maximize the likelihood.
Unlike the GC, M31 was also modelled as a point source.

The DM and MSPs hypotheses where tested using various models of different DM and MSPs distributions to see which was the better fit to the data. The DM annihilation hypothesis is tested by assuming a Navarro-Frenk-White (NFW) DM density profile and a generalised NFW DM density profile. To model a possible population of MSPs in the GC bulge it was assumed that their distribution is traced by the old stellar population in the bulge or alternatively distributed like the dense interstellar gas in the central molecular zone. For M31 the MSP hypothesis is tested using an average spectrum derived form observed MSPs in the Galactic plane.

3 Results

Excesses have been significantly detected around a few GeV at locations consistent with the GC and M31.

In Fig. 1 the radial flux profile as a function of distance from the GC at 2 GeV for the total gamma-ray data is compared with the MSP-like spectral component and the generalised NFW profiles in the Sample Model, i.e. one of the models from [10] which assumes that the cosmic ray source distribution traces the measured distribution of pulsars [11], as well as for a standard NFW annihilation profile. The MSP-like profile and the DM annihilation profiles are similar within $\sim 5^\circ$ of the GC, but MSP-like profile flattens at higher latitudes compared to the predictions of the generalised NFW profile.

Fig. 2 shows the best fit, a power law model, and spectral points fitted to the energy flux data for M31. However, an average MSP spectrum is almost an equally good fit to the data as the simple power law model with free parameters. It was found that a fit using an NFW profile expected for a DM signal matches the data well, due to the large uncertainty in J-factors. The J-factor determines the strength of the signal provided by annihilating or decaying DM and describes the distribution of it in an astrophysical system. In the end, neither the interpretation of the emission from M31 being due to populations of MSPs or DM can be rejected.

Based on the findings of the two papers neither of the two hypothesis, DM or MSPs, is preferred at high significance.

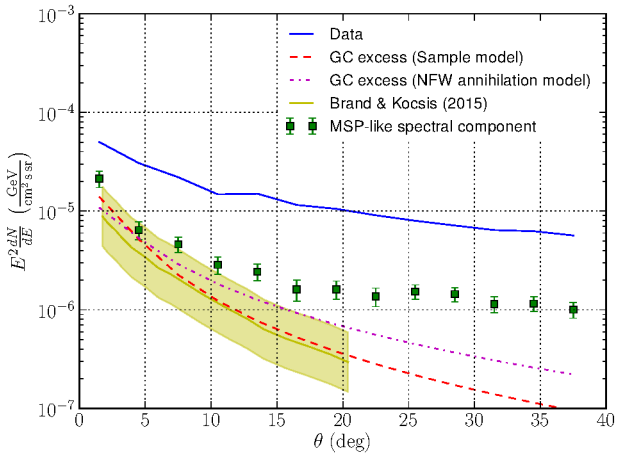

Figure 1: GC radial flux profile. Solid blue line: flux profile as a function of radial distance from the GC with bright point sources masked. Squares: radial profile of the MSP-like spectral component. Dashed red line: GC excess modeled with a general NFW (γ=1.25) profile. Dash-dotted magenta line: GC excess profile modeled an NFW profile (γ=1). Yellow band: expectation for a population of MSPs in the Galactic bulge from disrupted globular clusters. All values correspond to intensity at 2 GeV. The Fig. is from [1].

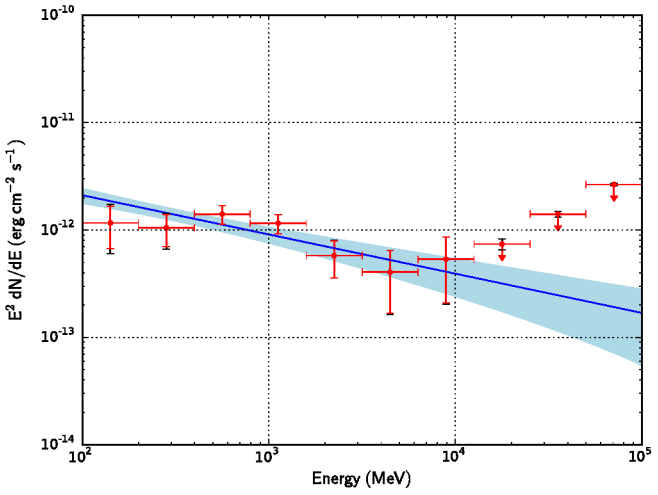

Figure 2: M31 spectrum. Solid blue line: best-fit power law model. Light-blue shaded area: 68% confidence level uncertainty domain. Red points: independent fits to data in individual energy bins. Red arrows: 95% confidence level flux upper limits. Red and black vertical error bars are the statistical and total uncertainties, respectively. The Fig. is from [2].

4 Summary

Earlier publications have found excesses of gamma-rays at a few GeV consistent with the locations of the GC and M31. The Fermi Collaboration has found that the M31 excess [2] is similar to the excess at the GC, [1]. It is still up for debate if the two similar excesses are due to DM or MSPs, or if there is another explanation altogether.

References

[1] M. Ackermann *et al.*, "The Fermi Galactic Center GeV Excess and Implications for Dark Matter", Apj. **840**, may (2017) [arXiv:1704.03910 [astro-ph.HE]].

[2] M. Ackermann *et al.*, "Observations of M31 and M33 with the Fermi Large Area Telescope: A Galactic Center Excess in Andromeda?", Apj. **836**, feb (2017) [arXiv:1702.08602 [astro-ph.HE]].

[3] W. Atwood *et al.*, "The Large Area Telescope on the Fermi Gamma-Ray Space Telescope Mission", Apj. **697**, jun (2009) [arXiv: 0902.1089 [astro-ph.IM]].

[4] W. Atwood *et al.*, "Pass 8: Toward the Full Realization of the Fermi-LAT Scientific Potential", mar (2013) [arXiv: 1303.3514 [astro-ph.IM]].

[5] Fermi-LAT Collaboration, "Characterizing the population of pulsars in the Galactic bulge with the *Fermi* Large Area Telescope", Apj. **697**, apr (2017) [arXiv: 1705.00009 [astro-ph.HE]].

[6] Goodenough, L. and Hooper, D., "Possible Evidence For Dark Matter Annihilation In The Inner Milky Way From The Fermi Gamma Ray Space Telescope", oct (2009) [arXiv: 0910.2998 [hep-ph]].

[7] Abazajian, K. N. and Kaplinghat, M., "Detection of a gamma-ray source in the Galactic Center consistent with extended emission from dark matter annihilation and concentrated astrophysical emission", PhRvD. **86**, oct (2012) [arXiv: 1207.6047 [astro-ph.HE]].

[8] B. Zhou *et al.*, "GeV excess in the Milky Way: The role of diffuse galactic gamma-ray emission templates astrophysical emission", Phys. Rev. **D91**, dec (2015) [arXiv: 1406.6948 [astro-ph.HE]].

[9] Brandt, T. D. and Kocsis, B., "Disrupted Globular Clusters Can Explain the Galactic Center Gamma-Ray Excess", ApJ. **812**, oct (2015) [arXiv: 1507.05616 [astro-ph.HE]].

[10] M. Ackermann *et al.*, "Fermi-LAT Observations of the Diffuse γ-Ray Emission: Implications for Cosmic Rays and the Interstellar Medium", ApJ. **750**, may (2012) [arXiv: 1202.4039 [astro-ph.HE]].

[11] D. Lorimer *et al.*, "The Parkes Multibeam Pulsar Survey - VI. Discovery and timing of 142 pulsars and a Galactic population analysis", MNRAS. **372**, oct (2006) [arXiv: astro-ph/0607640 [astro-ph]].

Searches for Axion-Like Particles with NGC1275: Current and Future Bounds

Nicholas Jennings

Rudolf Peierls Centre for Theoretical Physics, Oxford OX1 3NP

DOI: http://dx.doi.org/10.3204/DESY-PROC-2017-02/jennings_nicholas

Galaxy clusters contain large magnetic fields that make them excellent targets to search for ultralight Axion-Like Particles (ALPs). ALP-photon interconversion imprints quasi-sinusoidal oscillations on the X-ray spectra of point sources in or behind the cluster. The absence of substantial oscillations allows us to place bounds on $g_{a\gamma\gamma}$. Here the bounds from the *Chandra* X-ray observations of NGC1275 are presented, as well as those predicted for the *Athena* X-ray observatory, due to launch in 2028.

1 ALP-photon conversion in galaxy clusters

The probability of conversion between Axion-Like Particles (ALPs) and photons in an external magnetic field is a standard result [1, 2]. ALPs can naturally have very small masses, and for $m_a \lesssim 10^{-12}\,\mathrm{eV}$ the probability of conversion in a magnetic field takes the form:

$$P_{a\to\gamma} = \frac{1}{2}A^2\left(\frac{\omega}{\mathrm{keV}}\right)^2 \sin^2\left(C\frac{\mathrm{keV}}{\omega}\right), \tag{1}$$

where $A \propto B_\perp g_{a\gamma\gamma}/n_e$ for $B_\perp$ the magnetic field perpendicular to the ALP wave vector, $g_{a\gamma\gamma}$ the ALP-photon coupling and n_e the electron density, and $C \propto n_e L$ for domain length L. This equation holds for $A \ll 1$, which is generally true in galaxy clusters, where magnetic fields are $\mathcal{O}(\mu\mathrm{G})$ with coherence lengths $\mathcal{O}(10\,\mathrm{kpc})$, and electron densities $\mathcal{O}(10^{-3}\,\mathrm{cm}^{-3})$.

For these parameters, the ALP-photon conversion probability will imprint quasi-sinusoidal oscillations on the spectrum of a source in the energy range 1-10 keV [3, 4, 5]. Equation 1 shows that oscillations will be small and rapid at low energies, with increasing amplitude and period at higher energies. The lack of information about the 3D structure of intracluster magnetic fields precludes a precise model of these oscillations; however, their absence in the X-ray spectra of point sources in or behind clusters can constrain $g_{a\gamma\gamma}$ [6, 7].

Figure 1 illustrates the energy-dependent survival probability for a photon passing across 300 domains of a magnetic field model for the Perseus Cluster, which has an estimated central magnetic field value of $25\,\mu$G [8]. The Perseus Cluster hosts a very bright Active Galactic Nucleus (AGN) in its central galaxy NGC1275, whose intrinsic spectrum dominates the background cluster emission and is well described by an absorbed power law [9, 10], making it an ideal target for ALP searches.

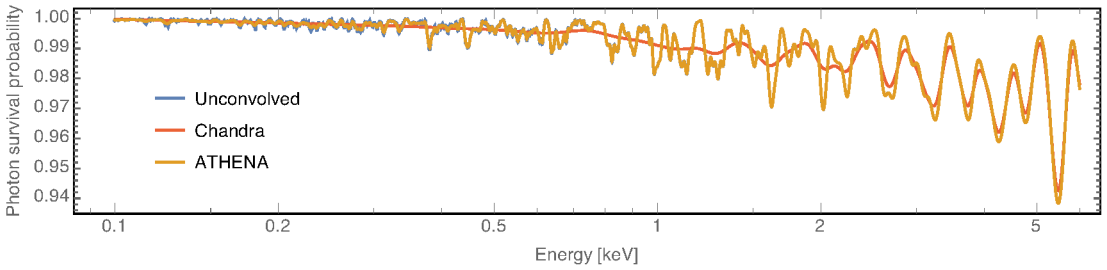

Figure 1: A randomly generated photon survival probability along the line of sight from NGC1275 to us: unconvolved (blue), convolved with a Gaussian with FWHM 150 eV (the energy resolution of *Chandra*'s ACIS-I detector (red)) and 2.5 eV for *Athena*'s X-IFU detector (orange). A central magnetic field of $B_0 = 25\,\mu$G was used, with $g_{a\gamma\gamma} = 5 \times 10^{-13}\,\mathrm{GeV}^{-1}$. At energies < 2 keV *Chandra* is unable to resolve oscillations, while *Athena's* sensitivity is almost indistinguishable from the unconvolved case.

2 Deriving bounds on $g_{a\gamma\gamma}$

We use a tangled, random domain model for the magnetic field in Perseus, with a central magnetic field value of $B_0 = 25\,\mu$G, following [8]. The electron density distribution in Perseus [11]:

$$n_e(r) = \frac{3.9 \times 10^{-2}}{[1 + (\frac{r}{80\,\mathrm{kpc}})^2]^{1.8}} + \frac{4.05 \times 10^{-3}}{[1 + (\frac{r}{280\,\mathrm{kpc}})^2]^{0.87}}\,\mathrm{cm}^{-3}, \tag{2}$$

determines the radial scaling $B(r) \propto n_e(r)^{0.7}$, based on the most conservative exponent value inferred from the cool core cluster A2199 [12]. We generate the magnetic field over 300 domains, whose lengths are drawn from a Pareto distribution between 3.5 kpc and 10 kpc with power 2.8, also motivated by A2199. In each domain the magnetic field and electron density are constant, with a random direction of $\mathbf{B}$. We generate 50 different configurations for each value of $g_{a\gamma\gamma}$, and calculate the survival probability of a photon passing through (see [4]).

We multiply this survival probability by an absorbed power law plus thermal background:

$$F_0(E) = (AE^{-\gamma} + \texttt{BAPEC}) \times e^{-n_H \sigma(E,z)}, \tag{3}$$

where A and γ are the amplitude and index of the power law, E is the energy, n_H is the equivalent hydrogen column, $\sigma(E, z)$ is the photo-electric cross-section at redshift z, and `BAPEC` is the standard plasma thermal emission model. We use parameters derived from the best fit values from the data. For each of these 50 models, we simulate 10 fake PHAs, giving a total of 500 fake data sets. We fit the fake data to the AGN spectrum model *without ALPs* and calculate the resulting reduced χ^2. If $\chi^2_{fake} < \chi^2_{data}$ (fit to the same no-ALP spectrum model) for fewer than 5% of the configurations, then that value of $g_{a\gamma\gamma}$ is excluded at 95% confidence. We repeat the process for different $g_{a\gamma\gamma}$ until this condition no longer holds, producing the bound.

3 Bounds from Chandra data of NGC1275

The *Chandra* X-ray Observatory is well suited to resolving point sources in galaxy clusters, due to its excellent angular resolution of $0.5''$. Archival data contains a set of 4 observations of NGC1275, taken with the ACIS-I instrument in 2009 (OBSID 11713, 12025, 12033 and 12036). These comprise 230 000 counts in total, and have the least pileup contamination of all the NGC1275 observations. In order to 'clean' these observations further we remove the brightest, most contaminated central pixels from the analysis. The resulting spectrum has modulations $\mathcal{O}(10\%)$. From this data we can constrain $g_{a\gamma\gamma} \lesssim 1.4 \times 10^{-12}\,\mathrm{GeV}^{-1}$ at 95% confidence, for $B_0 = 25\,\mu\mathrm{G}$ [13]. This represents a factor of 3 improvement over the bounds from SN1987A in this mass range [14]. Similar bounds have been derived from observations of M87 [15] and 2E3140 [16].

	Athena (X-IFU)	*Chandra* (ACIS-I)
Energy range	0.2–12 keV	0.3–10 keV
Energy resolution at 6 keV	2.5 eV	150 eV
Spatial resolution	5 arcsec	0.5 arcsec
Time resolution	10 μs	0.2 s (2.8 ms single row)
Effective area	2 m^2 @ 1 keV	600 cm^2 @ 1.5 keV

Table 1: Parameters taken from the *Athena* Mission Proposal and the *Chandra* Proposer's Guide.

4 Projected bounds from Athena observations of NGC1275

The *Athena* X-ray observatory, due to launch in 2028, will carry the X-ray Integral Field Unit (X-IFU), a microcalorimeter with an energy resolution of ~ 2.5 eV [17, 18]. This will allow X-IFU to resolve narrow spectral oscillations, while a readout time $\mathcal{O}(10\mu\mathrm{s})$ will ensure pileup contamination is minimised [19], despite a much larger effective area (see Table 1 for a summary of its properties).

In [20] we simulate the performance of *Athena* using the Simulation of X-ray Telescopes (`SIXTE`) code. It aims to offer an end-to-end simulation, modelling the telescope's vignetting, ARF and PSF, and X-IFU's response, event reconstruction and pileup [21]. We use `xifupipeline` to produce fake data both with and without ALPs. The procedure to determine bounds follows that of Section 2, the

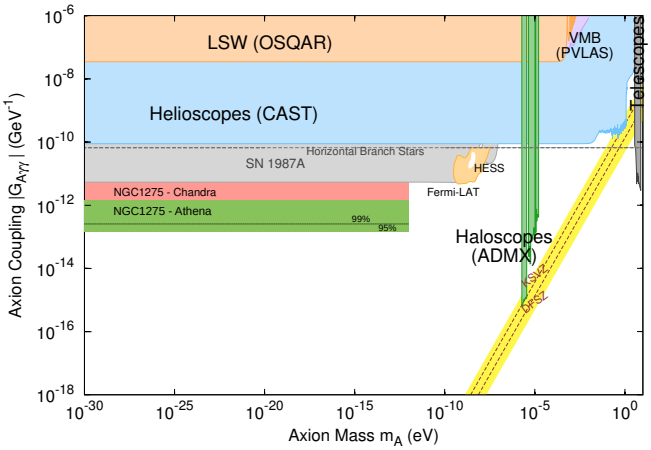

Figure 2: Overview of exclusion limits on axion couplings vs mass. Full references can be found in the Particle Data Group review on *Axions and other similar particles* [22].

only difference being that – instead of real data – we generate 100 fake data sets without ALPs and calculate the average reduced chi-squared. If this is less than the reduced chi-squareds of the data sets with ALPs for fewer than 5% of cases, then $g_{a\gamma\gamma}$ is excluded at 95% confidence.

For a simulation of 200 ks, assuming *Athena* does not see any unexpected spectral modulations, we derive a projected bound of $g_{a\gamma\gamma} \lesssim 1.5 \times 10^{-13}\,\mathrm{GeV}^{-1}$ at 95% confidence, as shown in Figure 2 alongside the *Chandra* bound and published data limits.

5 Conclusion

The absence of modulations in the X-ray spectra of point sources in galaxy clusters produce excellent constraints on $g_{a\gamma\gamma}$. The bound $g_{a\gamma\gamma} \lesssim 1.4 \times 10^{-12}\,\mathrm{GeV}^{-1}$ from *Chandra* data of NGC1275 is world-leading for $m_a \lesssim 10^{-12}\,\mathrm{eV}$. *Athena*'s groundbreaking energy resolution has the potential to push this bound down to $g_{a\gamma\gamma} \lesssim 1.5 \times 10^{-13}\,\mathrm{GeV}^{-1}$: an order of magnitude improvement, and the strongest cosmology-independent bound in this mass range of any current or currently-planned experiment.

Acknowledgments

The work presented here is funded by the European Research Council starting grant 'Supersymmetry Breaking in String Theory' (307605). N. Jennings is also funded by STFC.

References

[1] P. Sikivie, Phys. Rev. Lett. **51**, 1415-1417 (1983). doi:10.1103/PhysRevLett.51.1415
[2] G. Raffelt and L. Stodolsky, Phys. Rev. D **37**, 1237 (1988) doi:10.1103/PhysRevD.37.1237
[3] D. Wouters and P. Brun, Astrophys. J. **772**, 44 (2013) [arXiv:1304.0989 [astro-ph.HE]].
[4] S. Angus *et al.*, JCAP **1409**, 09 (2014) [arXiv:1312.3947 [astro-ph.HE]].
[5] J. P. Conlon, A. J. Powell and M. C. D. Marsh, Phys. Rev. D **93**, 12 (2016) [arXiv:1509.06748 [hep-ph]].
[6] C. Burrage *et al.*, Phys. Rev. Lett. **102**, 201101 (2009) [arXiv:0902.2320 [astro-ph.CO]].
[7] J. P. Conlon and M. C. D. Marsh, Phys. Rev. Lett. **111**, 15 (2013) [arXiv:1305.3603 [astro-ph.CO]].
[8] G. B. Taylor *et al.*, Mon. Not. Roy. Astron. Soc. **368**, 1500-1506 (2006) [arXiv:astro-ph/0602622].
[9] S. Yamazaki *et al.*, Publications of the Astronomical Society of Japan, **65**, (2013) doi:10.1093/pasj/65.2.30
[10] A. C. Fabian *et al.*, Mon. Not. Roy. Astron. Soc. **451**, 3 (2015) [arXiv:1505.03754 [astro-ph.HE]].
[11] E. Churazov *et al.*, Astrophys. J. **590**, 225-237 (2003) [arXiv:astro-ph/0301482].
[12] V. Vacca *et al.*, Astron. Astrophys. **540**, A38 (2012) [arXiv:1201.4119 [astro-ph.CO]].
[13] M. Berg *et al.*, Astrophys. J. **847**, 2 (2017) [arXiv:1605.01043 [astro-ph.HE]].
[14] A. Payez *et al.*, JCAP **1502**, 02 (2015) [arXiv:1410.3747 [astro-ph.HE]].
[15] M. C. D. Marsh *et al.*, [arXiv:1703.07354 [astro-ph.HE]].
[16] J. P. Conlon *et al.*, JCAP **1707**, 07 (2017) [arXiv:1704.05256 [astro-ph.HE]].
[17] K. Nandra *et al.*, [arXiv:1306.2307 [astro-ph.HE]].
[18] L. Gottardi *et al.*, Proc. SPIE Int. Soc. Opt. Eng. **9144**, 91442M (2014) [arXiv:1604.00553 [astro-ph.IM]].
[19] D. Barret *et al.*, Proc. SPIE Int. Soc. Opt. Eng. **9905**, 99052F (2016) [arXiv:1608.08105 [astro-ph.IM]].
[20] J. P. Conlon *et al.*, Mon. Not. Roy. Astron. Soc. doi:10.1093/mnras/stx2652 [arXiv:1707.00176 [astro-ph.HE]].
[21] J. Wilms *et al.*, Proc. SPIE Space Telescopes and Instrumentation 2014: Ultraviolet to Gamma Ray, **9144**, 91445X doi:10.1117/12.2056347
[22] C. Patrignani *et al.*, Chin. Phys. **C40**, 10 (2016) doi:10.1088/1674-1137/40/10/100001.

Evidence of vacuum birefringence from the polarisation of the optical emission from an Isolated Neutron Star

Roberto P. Mignani[1,2], *Vincenzo Testa*[3], *Denis González Caniulef*[4], *Roberto Taverna*[5], *Roberto Turolla*[5,4], *Silvia Zane*[4], *Kinwah Wu*[4], *Gaspare Lo Curto*[6]

[1]INAF - Istituto di Astrofisica Spaziale e Fisica Cosmica Milano, Milano, Italy
[2]Janusz Gil Institute of Astronomy, University of Zielona Góra, Zielona Góra, Poland
[3]INAF - Osservatorio Astronomico di Roma, Monteporzio, Italy
[4]Mullard Space Science Laboratory, University College London, Holmbury St. Mary, UK
[5]Dipartimento di Fisica e Astronomia, Universitá di Padova, Padova, Italy
[6]European Southern Observatory, Santiago de Chile, Chile

DOI: http://dx.doi.org/10.3204/DESY-PROC-2017-02/mignani_roberto

Isolated Neutron Stars are some of the most exciting stellar objects known to astronomers: they have the most extreme magnetic fields, with values up to 10^{15} G, and, with the exception of stellar-mass black holes, they are the most dense stars, with densities of $\approx 10^{14}$ g cm^{-3}. As such, they are perfect laboratories to test theories of electromagnetism and nuclear physics under conditions of magnetic field and density unattainable on Earth. In particular, the interaction of radiation with strong magnetic fields is the cause of the *vacuum birefringence*, an effect predicted by quantum electrodynamics in 1936 but that lacked an observational evidence until now. Here, we show how the study of the polarisation of the optical radiation from the surface of an isolated neutron star yielded such an observational evidence, opening exciting perspectives for similar studies at other wavelengths.

1 Introduction to isolated neutron stars

Isolated neutron stars are stellar corpses left over after supernova explosions of stars about ten times as massive as our Sun. As a consequence of the explosion, the star external layers are ejected into space to form a supernova remnant and the core of the star, ∼1.5 Sun masses, collapses into a sphere of about 10 km radius, of density $\sim 10^{14}$ g cm^{-3}, comparable to the atomic nucleus, under which free protons and electrons merge to form neutrons via inverse β decay. The core is spun up to periods of a few tens of milliseconds and the star magnetic field is amplified up to 10^{15} G, thousands billion times stronger than the Earth's. The formation of an isolated neutron star (INS) from a supernova explosion was predicted in the 1930s by astronomers Walter Baade and Fritz Zwicky, soon after the discovery of the neutron by physicist James Chadwick and, possibly, following an original intuition by physicist Lev Landau.[1]

[1]A very nice and vivid review of the true story of how the neutron star idea developed is given in Yakovlev et al. 2013, Physics Uspekhi, 56, 3, arXiv:1210.0682.

The first INS was discovered 50 years ago [11] as a source of pulsed radio emission, dubbed *pulsar*, whose period (1.33 s) could only be explained by the fast rotation of a star with a density exactly as expected for an INS. The discovery of the Crab and Vela pulsars in their associated supernova remnants closed the loop and proved that INSs indeed form after supernova explosions. The measurement of a tiny but regular decrease of the spin period for a few pulsars suggested that their rotational energy decreases with time. Pulsar properties are generally described by the *magnetic dipole model* [4, 14], where the radio emission is powered by the acceleration of particles at the expenses of the neutron star rotational energy, producing beamed radiation along its magnetic field axis which is seen as an intermittent signal as the beam crosses the line of sight (LOS) to the Earth if the neutron star rotation and magnetic axis are misaligned. From the magnetic dipole model, by equating the neutron star rotational energy loss rate to the magnetic dipole loss one can infer (under certain assumptions on the neutron star mass and radius) the value of the neutron star magnetic field $B_{\rm s} = 3.2 \times 10^{19} (P_{\rm s} \dot{P}_{\rm s})^{1/2}$ G, where $P_{\rm s}$ and $\dot{P}_{\rm s}$ are its spin period and first derivative, respectively.

Pulsars feature a very complex multi-wavelength phenomenology spanning from the radio band, where they were discovered [11] and traditionally observed, to the optical band, to the X-rays, up to the very high-energy γ-rays [1]. From one hand, this made it possible to study the emission from the neutron star magnetosphere across the entire electromagnetic spectrum, offering a broad view on the emission mechanisms therein. On the other hand, this showed the existence of pulsars that do not emit in radio, hence dubbed *radio-silent*. Multi-wavelength observations also led to the discovery of classes of INSs that are not powered by the rotational energy[6] but by, e.g. the magnetic energy, such as the *magnetars*[12], or the release of thermal radiation from the hot ($T_{\rm s} \sim 10^5$–10^6 K) and cooling neutron star surface. Seven of such *cooling* INSs are known, detected both in the soft X-rays (0.05–0.1 keV) and in the optical/ultraviolet. They have long spin periods ($P_{\rm s}$ = 3–11 s) compared to most INSs and they are endowed with magnetic fields of 10^{13}–10^{14} G [19].

2 Scientific motivation

The study of the thermal radiation from these INSs is the only way to peek directly at (or close to) the star surface. Indeed, we do not know yet whether the thermal emission is produced by the bare star surface or it is mediated by a thin atmosphere, and what the composition of such an atmosphere would be. Measurements of the polarisation degree of the thermal radiation from the star surface can help to address these issues [5], as well as to test quantum electrodynamic (QED) effects close to the neutron star surface, such as *vacuum birefringence* [7]. In brief, electromagnetic radiation in vacuum propagates along two modes, the ordinary mode (O mode), where the electric field oscillates parallel to the magnetic field plane, and the extraordinary mode (X-mode), where the electric field oscillates perpendicular to the magnetic field plane. The presence of a strong magnetic field, however, induces the formation of virtual electron/positron pairs, which change the refraction indices along the X and O modes, proportionally to the square of the magnetic field strength, and affects their propagation, changing the polarisation degree of the electromagnetic radiation. In ground-based laboratories magnetic fields B of $\sim 10^6$ G at most can be generated, and vacuum birefringence effects, when they are eventually measured, will only be tested in the weak field regime [3]. On the other hand, close to the INS surface these effects can be tested in the strong field regime. Indeed, vacuum birefringence is expected to increase dramatically the linear polarisation degree of the thermal radiation produced from

the star surface [15], from a level of a few per cent, up to 100 per cent, depending on the viewing geometry and the emission mechanisms [8, 9, 10]. The best target among the seven INSs with purely thermal emission is RX J1856.5−3754. This source has a magnetic field of $\sim 10^{13}$ G, is quite bright in the X-rays, but rather faint in the optical (magnitude 25.5, about 100 million times fainter than the naked eye limit), even if it is still the brightest of the seven. Although polarisation measurements in the X-rays should be the obvious choice for this experiment, no dedicated X-ray polarimetry satellite is currently operational, with the first one, the NASA's *Imaging X-ray Polarimetry Explorer* [21] to be launched early next decade with possibly the ESA's *X-ray Imaging Polarimeter Explorer* [16] and the chinese *enhanced X-ray Timing Polarimetry* satellite [22], due to follow. However, none of them will be sensitive in the soft X-ray band. Therefore, we opted for a measurement of the linear polarisation in the optical, exploiting a mature technique in optical astronomy.

3 Observations and Results

Owing to the target faintness, we observed it with the Very Large Telescope of the European Southern Observatory, an array of four telescopes of 8.2m in diameter located at the Cerro Paranal Observatory (Chile). We used the second Focal Reducer and low dispersion Spectrograph [2] mounted at one the VLT unit telescopes. The camera is equipped with polarisation optics to measure linear polarisation through a Wollaston prism acting as a beam splitting analyser and two super-achromatic phase retarder 3×3 plate mosaics installed on rotatable mountings to be moved in and out of the light path. We used four half-wave retarder plate angles of 0°, 22.5°, 45°, and 67.5°, which correspond to the retarder plate orientations relative to the Wollaston prism. A filter with central wavelength $\lambda = 555.0$ nm and width $\Delta\lambda = 61.6$ nm was inserted along the light path. We acquired a total exposure of 7920 s per retarder plate angle. The degree of linear polarisation of a source is calculated from the normalised Stokes parameters $P_{\rm U} \equiv U/I$ and $P_{\rm Q} \equiv Q/I$ computed from the source fluxes in the ordinary and extraordinary beams [13] as P.D. $= ({P_{\rm Q}}^2 + {P_{\rm U}}^2)^{1/2}$. In this way, we measured a P.D. $= 16.43\% \pm 5.26\%$. Owing to the target faintness, we carefully verified that our measurement is not dominated by systematic errors and/or observational biases. We tested the absolute accuracy of our polarisation measurement against polarised calibration targets and found that this is accurate to $0.13\% \pm 0.06\%$. In a similar way, we estimated the spurious polarisation of the polarisation optics to be $0.09\% \pm 0.06\%$ from the observations of un-polarised calibration targets. Since our observations were taken in New Moon, the contamination of the sky background polarisation is also close to zero. Since our target is at a distance of 400 light years, we verified that our polarisation measurement was not affected by dust grains along the line of sight by comparing the measured P.D. $= 16.43\% \pm 5.26\%$ with that of 42 stars in the field and found that for the latter it is consistent with zero.

We compared our measurement with the predictions for four different emission models: a plain back body (BB), a magnetised, completely ionised hydrogen atmosphere, and, a condensed surface model (both in the fixed and free ion limit), based on numerical simulations [17, 5]. Figure 1 shows the simulation corresponding to the BB case, where the P.D. is shown as a function of the angles χ and ξ between the LOS and the INS spin axis and between the INS magnetic and spin axis, respectively. The plot on the left accounts for QED effects. As it can be seen, the measured P.D. (black solid and dashed lines) is consistent with the model predictions and the constraints on χ and ξ imposed by the pulsed X-ray light curve profile [18].

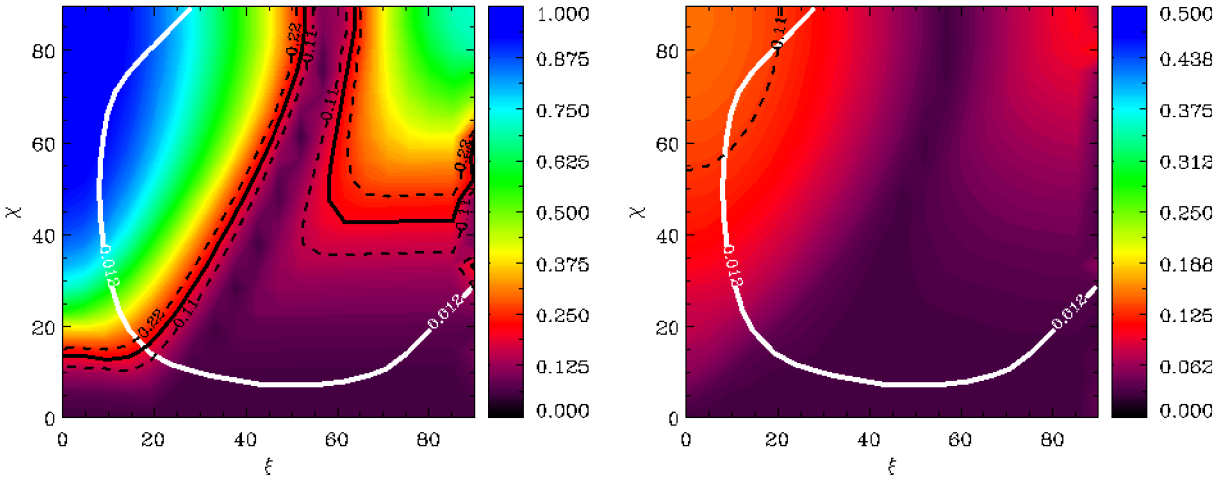

Figure 1: Simulated P.D. of RX J1856.5−3754 as a function of the angles χ and ξ, i.e. between the LOS and the INS spin axis and between the INS magnetic and spin axis, respectively. A BB emission model is assumed. The white solid line represents the constraints on χ and ξ inferred from the pulsed X-ray light curve [18], whereas the black solid line corresponds to our measurement, including 1σ errors (black dashed line). The plots on the left and on the right represent the cases when we accounted or not for QED effects, respectively.

This is also the case for the other simulations performed for the other tested emission models [13]. Therefore, we cannot discriminate, based on the current polarisation measurement, which of these models better describes the optical emission from RX J1856.5−3754. Decreasing the error on P.D. through deeper observations and deriving more constraining limits on χ and ξ is what we need to discriminate between different models. Interestingly, however, our simulations shows that when not accounting for QED effects all of the considered emission models predicts values of P.D. that are only marginally consistent with our observations, see Fig. 1 (right) for the BB case. This is a clear indication that QED effects play a crucial role in setting the actual value of the polarisation degree, see also discussion in [20]. Therefore, this is the first, indirect though, observational evidence of the phenomenon of *vacuum birefringence*, as predicted by QED over 80 years ago [7].

Follow-up polarimetry observations of RX J1856.5−3754 recently obtained at the VLT with the same instrument set-up but for a twice as long integration time will consolidate our result. Polarimetry measurements in other filters will also be important to test the dependence of the effect on the wavelength. Measuring polarisation for other INSs similar to RX J1856.5−3754 would be important to verify the effect on sources with different magnetic field values. This is observationally challenging, however, since all these other sources are fainter than RX J1856.5−3754, which requires a more massive investment of observing time. In the X-rays, polarimetry measurements with the upcoming X-ray polarimetry missions, sensitive between 2 and 8 keV, will make it possible to search vacuum birefringence effects in magnetars, which have an X-ray spectrum harder than RX J1856.5−3754 and even higher magnetic field values, and for which polarisation measurements in the optical are complicated by their larger distances, uncertain counterparts, and foreground polarisation contamination.

4 Acknowledgments

RPM thanks the organisers for the invitation to participate to the PATRAS 2017 conference and acknowledges financial support from an "Occhialini Fellowship".

References

[1] A.A. Abdo, et al., ApJS, **298**, 17 (2013)

[2] I. Appenzeller, K. Fricke, W. Fürtig, et al., The Messenger, **94**, 1 (1998)

[3] F. Della Valle, l. Ejlli, U. Gastaldi, G. Messineo, E. Milotti, R. Pengo, G. Ruoso, G. Zavattini, The European Physical Journal C, **76**, 24 (2016)

[4] T. Gold, Nature, **218**, 731 (1968)

[5] D. González Caniulef, S. Zane, R. Taverna, R. Turolla, & K. Wu, MNRAS, **459**, 3585 (2016)

[6] A. K. Harding, Frontiers of Physics, **8**, 679 (2013)

[7] W. Heisenberg & H. Euler, Z. Physik, **98**, 714 (1936)

[8] J. S. Heyl & N. J. Shaviv, MNRAS, **311**, 555 (2000)

[9] J. S. Heyl & N. J. Shaviv, Phys. Rev. D, **66**, 023002 (2002)

[10] J. S. Heyl, N. J. Shaviv, D. Lloyd, MNRAS, **342**, 134 (2003)

[11] A. Hewish, S. J. Bell, J. D. H. Pilkington, P. F. Scott, R. A. Collins, Nature, **217**, 709 (1968)

[12] S. Mereghetti, ASpR, **47**, 1317 (2011)

[13] R. P. Mignani, V. Testa, D. Gonzalez Caniulef, R. Taverna, R. Turolla, S. Zane, K. Wu, MNRAS, **465**, 492 (2017)

[14] F. Pacini, Nature, **219**, 145 (1968)

[15] A. Y. Potekhin, Physics Uspekhi, **57**, 735 (arXiv:1403.00774) (2014)

[16] P. Soffitta, et al., Proceedings of the SPIE, **9905** (2016)

[17] R. Taverna, R. Turolla, D. Gonzalez Caniulef, S. Zane, MNRAS, **454**, 3254 (2015)

[18] A. Tiengo & S. Mereghetti., ApJL, **657**, L101 (2007)

[19] R. Turolla, Astrophysics and Space Science Library, **357**, 141 (2009)

[20] R. Turolla, S. Zane, R. Taverna, D. González Caniulef, R. P., Mignani, V. Testa, K. Wu., arXiv:1706.02505 (2017)

[21] M. Weisskopf, et al., Proceedings of the SPIE, **9905** (2016)

[22] S. N. Zhang, et al., Proceedings of the SPIE, **9905** (2016)

Conversion of TeV photons in realistic extragalactic magnetic field

Daniele Montanino[1], *Franco Vazza*[2,3], *Alessandro Mirizzi*[4] *Matteo Viel*[5,6,7]

[1]Università del Salento, and INFN, sezione di Lecce, Italy
[2]INAF, Istituto di Radio Astronomia di Bologna, Italy
[3]Universität Hamburg, Germany
[4]Università di Bari and INFN, sezione di Bari, Italy
[5]International School for Advanced Studies, Trieste, Italy
[6]INAF, Osservatorio Astronomico di Trieste, Italy
[7]INFN, sezione di Trieste, Italy

DOI: http://dx.doi.org/10.3204/DESY-PROC-2017-02/montanino_daniele

Very High Energy (TeV) photons can evade absorption by conversion into axion-like (ALPs) particles in the extragalactic magnetic field (EMF). We show that using realistic simulations of the EMF we obtain an even stronger conversion than those obtained with the simplified cell model. This effect would be probed with the upcoming Cherenkov Telescope Array detector.

1 Photon-ALP conversion in Extragalactic Magnetic Field

Axion-like particles (ALPs) are ultralight pseudo-scalar bosons a with a two-photon vertex $a\gamma\gamma$, predicted by several extensions of the Standard Model. In the presence of an external magnetic field, the $a\gamma\gamma$ coupling leads to the phenomenon of photon-ALP mixing [1]. This effect allows for the possibility of direct searches of ALPs in laboratory experiments.

Due to the $a\gamma\gamma$ coupling, ultra-light ALPs can also play an important role in astrophysical observations. In particular, an intriguing hint for ALPs has been recently suggested by Very High-Energy (VHE) γ-ray experiments. In this respect, recent observations of cosmologically distant γ-ray sources by ground-based γ-ray Imaging Atmospheric Cherenkov Telescopes have revealed a surprising degree of transparency of the Universe to VHE photons [2, 3], where one would have expected a significant absorption of VHE photons by pair-production processes ($\gamma_{\rm VHE} + \gamma_{\rm EBL} \to e^+e^-$) on the extragalactic background light (EBL).

However, the range of the parameters where ALPs would impact the cosmic transparency is constrained from other observations as shown in Fig. 1. In particular, for ALPs with masses $m_a \leq 10^{-9}$ eV, the strongest bound on $g_{a\gamma}$ is derived from the absence of γ-rays from SN 1987A (see [4] for a review).

Anyway, the distribution of the extragalactic magnetic fields has been poorly characterized in previous works on ALP conversions. In particular, a cell-like structure (hereafter the *cell* model) has been adopted with many domains of equal size ($l \sim 1$ Mpc) in which the magnetic

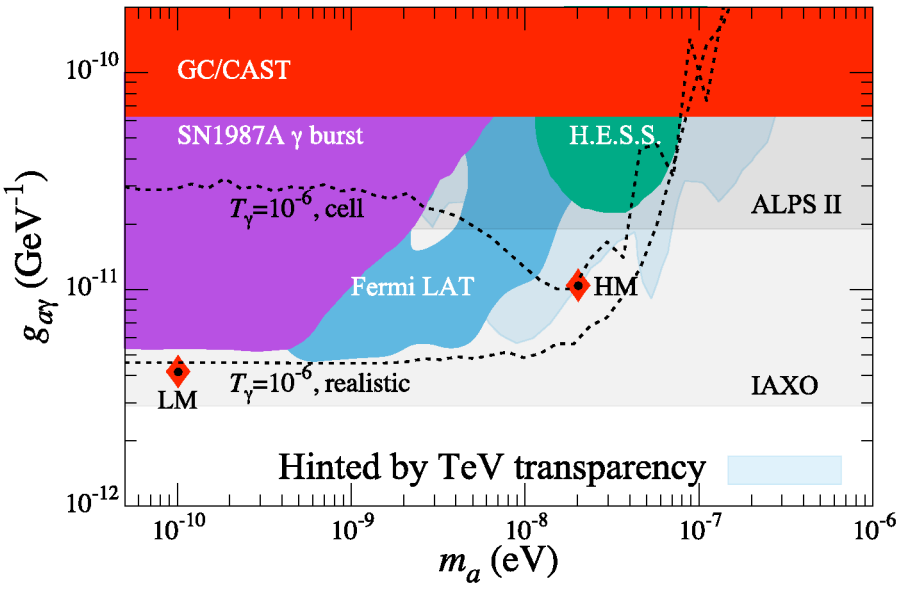

Figure 1: Limits on ALP parameter space in the plane $(m_a, g_{a\gamma})$. The parameter space where ALPs could explain the low γ-ray opacity is shown in light blue. The horizontal grey bands represent the sensitivity of future ALPS-II and IAXO experiments. The two small squares represent cases of low-mass (LM, $m_a = 10^{-10}$ eV and $g_{a\gamma} = 4 \times 10^{-12}$ GeV^{-1}) and high-mass (HM, $m_a = 2 \times 10^{-8}$ eV and $g_{a\gamma} = 10^{-11}$ GeV^{-1}) ALPs where conversions in realistic extragalactic magnetic fields would affect the TeV photon transparency. Contour lines corresponding to $T_\gamma = 10^{-6}$ for the cell and realistic models are also shown. See the text for more details.

field has (constant) random values and directions [5]. Only recently it has been pointed out that in more realistic situations, the magnetic field direction would vary continuously along the propagation path, and this would lead to sizable differences in the ALP conversions with respect to the cell model.

We have studied for the first time the photon conversions into ALPs using recent magneto-hydrodynamical cosmological simulations [6, 7]. In this more realistic case the magnetic fields can locally fluctuate in filaments of matter up to two orders of magnitude larger that what found in the cell model and photon-ALP conversions are enhanced compared to previous estimates. Indeed, significant conversions are found both in the low-mass region below the SN 1987A bound both in the high-mass region on the right of the recent Fermi-LAT bound. These two ranges are indicated with small squares in Fig. 1.

In Fig. 1 dashed lines represent the contour lines corresponding to the photon transfer function $T_\gamma = 10^{-6}$ for the cell model and simulated model of the extragalactic B-field for a source at $z = 0.3$ and at energy $E = 20$ TeV. Each contour corresponds to the 95$^{\text{th}}$ percentile of the distribution of T_γ. In other words, there is a 5% probability that T_γ is larger than the indicated value. From these curves is evident the enhancement of the area probed with the realistic model at a fixed value of T_γ as we will see in the following section.

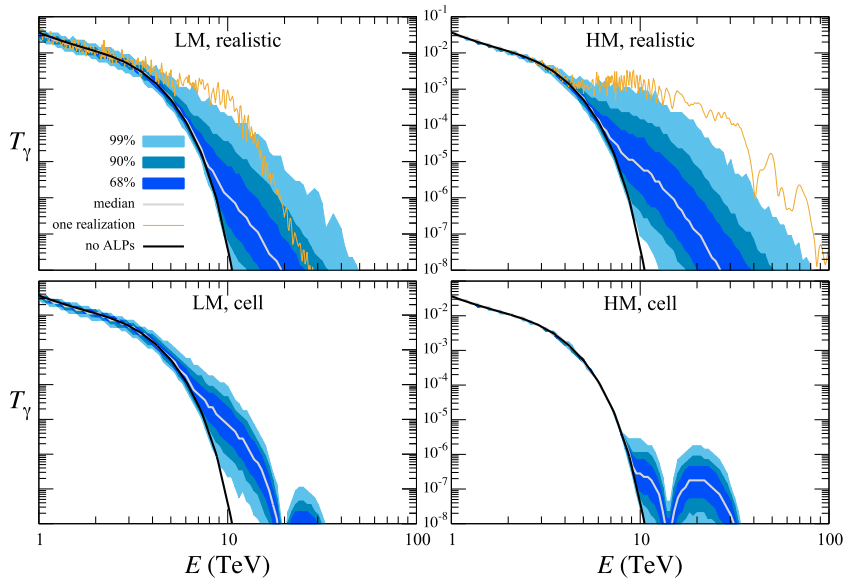

Figure 2: Photon transfer function $T_\gamma(E)$ for a source at redshift $z = 0.3$ for LM and HM cases. Upper panels refer to realistic models of extragalactic magnetic field, while lower panels are for the cell model. See the text for details.

We have solved the propagation equation for the photon-ALP ensemble, both with a random cell model and with the realistic magnetic field. In the first case denoting $\mathbf{b}_k$ a random unit vector inside each cell, during their path with a total length L along the line of sight, the beam crosses $n = L/l_c$ domains, where l_c is the size of each domain: The set $\{\mathbf{B}_k\}_{1\leq k\leq n} = \{B_0 \cdot \mathbf{b}_k\}_{1\leq k\leq n}$ represents a given random realization of the beam propagation. We have used a fixed (comoving) value of $B_0 = 1.9$ nG which corresponds to the r.m.s. of the strength of the realistic magnetic field on all configurations and a fixed size of $l = 1.4$ Mpc per cell, which is the typical coherence length of magnetic fields in the realistic model, based on spectral analysis.

2 Results

In Fig. 2 we present the photon transfer function $T_\gamma(E)$ in function of the photon energy E for a source at redshift $z = 0.3$. In the left panels we consider, the parameters corresponding to LM parameters while in the right panels we the HM parameters marked in Fig. 1. Upper panels refer to realistic simulations for magnetic field, while lower ones are for the cell model. The black solid curve represents the T_γ expected in the presence of only absorption onto EBL. The solid grey curve represents the median T_γ in the presence of ALPs conversions. The orange curve corresponds to conversions for a particular realization of the extragalactic magnetic field. The shaded band is the envelope of the results on all the possible realizations of the extragalactic magnetic field at 68 % (dark blue), 90 % (blue) and 99 % (light blue) C.L., respectively by simulating 10^3 different realizations of the extragalactic magnetic field in the cell case, or

extracting an equivalent number of 1-dimensional beams of cells randomly extracted from the outputs of the cosmological simulation at increasing redshift. According to conventional physics, it turns out that the T_γ gets dramatically suppressed at high energies ($E > 2$ TeV). As expected, including ALP conversions with cell magnetic fields, the enhancement of T_γ with respect to the standard case is modest since it is suppressed by the small coupling (left panel) or the high ALP mass (right panel). However, when we consider ALP conversions in realistic magnetic fields the enhancement of T_γ is striking.

ALP conversions in such models would produce a considerable hardening of the spectrum at high enough energies, thereby making it possible to detect VHE photons in a range where no observable signal would be expected according to conventional physics or to conversions with cell magnetic fields. An example of a particular realization is shown by the orange curve. In this specific case we see that the observable photon flux at high energies can be significantly larger than the average one. On this specific line of sight the enhancement of T_γ with respect to the standard case would reach 3 order of magnitudes.

Depending on the particular magnetic realization crossed by the photons, it is also possible to observe a suppression of the photon flux stronger than in the presence of conventional physics. Nevertheless, from Fig. 2 one infers that the cases in which T_γ is enhanced at high energies are much more probable. From these results it is evident that using realistic models of the extragalactic magnetic fields has a strong impact on the mechanism of photon-ALP conversions to reduce the cosmic opacity.

3 Conclusions

We have studied the conversions of VHE photons into ALPs proposed as a mechanism to reduce the absorption onto EBL, using for the first time realistic models of extragalatic magnetic fields, obtained from magneto-hydrodynamical cosmological simulations. We find an enhancement of the magnetic field with respect to what predicted in the naive cell model, due to the fact that simulated magnetic fields display larger fluctuations, correlated with density fluctuations of the cosmic web. This effect would give a significant boost to photon-ALP conversions. Notably, using the cell model the parameter space for photon-ALP conversions at VHE energies was strongly constrained by SN 1987A and Fermi-LAT data. However, using realistic models of the magnetic field we have found significant conversions also in regions of the parameter space consistent with previous bounds. This mechanism can produce a significant hardening of the VHE photon spectrum from faraway sources and we expect such signature to emerge at energies $E \geq 1$ TeV. Therefore, this scenario is testable with the present generation of Imaging Atmospheric Cherenkov Telescope, covering energies in the range from ~ 50 GeV to ~ 50 TeV.

References

[1] G. Raffelt and L. Stodolsky, Phys. Rev. D **37**, 1237 (1988).

[2] F. Aharonian *et al.* [H.E.S.S. Collaboration], Nature **440**, 1018 (2006).

[3] D. Horns and M. Meyer, JCAP **1202**, 033 (2012).

[4] M. Meyer, D. Horns and M. Raue, Phys. Rev. D **87**, no. 3, 035027 (2013).

[5] A. De Angelis, O. Mansutti and M. Roncadelli, Phys. Rev. D **76**, 121301 (2007).

[6] F. Vazza, M. Brggen, C. Gheller and P. Wang, Mon. Not. Roy. Astron. Soc. **445**, no.4, 3706 (2014).

[7] D. Montanino, F. Vazza, A. Mirizzi and M. Viel, Phys. Rev. Lett. **119**, no. 10, 101101 (2017).

Axion-electron coupling from the RGB tip of Globular Clusters

O. Straniero[1], *I. Dominguez*[2], *M. Giannotti*[3], *A. Mirizzi*[4]

[1]INAF-Osservatorio di Teramo, Teramo, Italy, and INFN sezione LNGS, Assergi, Italy
[2]University of Granada, Granada, Spain
[3]Barry University, Miami, USA
[4]University of Bari, Bari, Italy, and INFN sezione di Bari, Italy

DOI: http://dx.doi.org/10.3204/DESY-PROC-2017-02/straniero_oscar

We present a preliminary study of the Globular Cluster RGB devoted to improve the available constraint for the axion-electron coupling. By means of multi-band IR photometry of the cluster M3 we obtain $g_{ae}/10^{-13} < 2.57$ (95% C.L.).

1 Introduction.

Shortly after the central H exhaustion, the envelope of a Globular Cluster star rapidly expands up to a few hundred solar radii. Then the star starts to climb the Red Giant Branch (RGB) and its luminosity progressively increases. Meanwhile, the He-rich core contracts, temperature and density increase, until electron degeneracy develops. Initially, the efficient conductive heat transport ensured by degenerate electrons makes the core almost isothermal. Later on, due to the central energy loss caused by plasma neutrinos, an off-center temperature maximum settle on. When the temperature rises above the threshold for the He ignition, a thermonuclear runaway occurs (He flash). This event coincides with the tip of the RGB. As firstly noted by [1] the luminosity of a RGB star essentially depends on the core mass. Then, as a consequence of the shell-H burning, which is active at the bottom of the envelope, the core mass increases and, in turn, the luminosity should increase. Therefore, the RGB tip luminosity can be used to constrain the input physics that controls the growth of the He core mass during the RGB. In this framework a discrepancy between the observed RGB tip luminosity and its theoretical prediction may be considered a hint of missed physical processes. In the following we will discuss the potential of RGB luminosity to constrain the coupling between axions and electrons. Like plasma-neutrinos, axions possibly produced in the core of a star which is climbing the red giant branch is an effective energy sink mechanism affecting the energy balance within the core and, in turn, the luminosity at the time of the off-center He ignition. The general rule is simple, the larger the production rate of weakly interactive particles produced by some thermal process the brighter the tip of the RGB. In this case the dominant axion production process is Bremsstrahlung, while Primakoff and Compton are suppressed because of the high electron degeneracy. [2] make use of I-band photometric data of M5, a well studied cluster of the Milky Way, to derive an upper bound for the strength of the axion-electron coupling: $g_{13} < 4$ (95% C.L.), or $g_{13} = 2 \pm 2$. Here we present a project we started with the aim to improve

cluster	[M/H]	N	$< \delta m_{bol} >$	M_{obs}^{tip}	σ_{stat}	σ_{obs}
M3	-1.16	125	0.045	-3.655	0.070	0.250

Table 1: Parameters used to estimate the magnitude of the RGB tip of M3. [M/H]= $log\frac{Z}{X} - log\left(\frac{Z}{X}\right)_{\odot}$ is the cluster metallicity and N is the number of stars within 2 mag from the tip.

this constraint. Instead of a monochromatic photometry of a single cluster, we will exploit multi-color near-IR photometric studies of a sample of galactic clusters from which bolometric magnitude can be directly derived and compared to the theoretical expectations. Brightest RGB stars are rather cool objects and their spectral energy distribution is dominated by near-IR light. In addition, to increase the statistical significance of the stellar sample our strategy is to combine high angular resolution data of the crowded central regions (with HST or ground based adaptive optic telescopes), with large field photometries to cover the external regions of the cluster. The statistical significance of the stellar sample is an important issue for a correct determination of the RGB tip luminosity, a problem often ignored in previous studies. Our statistical approach to address this problem is discussed in the following section. To illustrate the potential of the method we will present the case of M3, another well studied Cluster in the northern sky.

2 The observed brightest RGB star versus the RGB tip.

The observed brightest star on the RGB does not necessarely coincide with the brightest point on the theoretical RGB evolutionary track or isochrone. In principle, the probability to observe the brightest RGB star as close as possible to the RGB tip depends on the total number of stars in the upper portion of the RGB. To estimate this probability, we make use of synthetic color-magnitude diagrams (CMDs, see [3]). In practice, we calculate a series of synthetic CMDs having the same input parameters (age, metallicity and the like) and the same number N of RGB stars with bolometric magnitude in the range m_{bol}^{tip} and m_{bol}^{tip}+2. Although all the synthetic diagrams are computed with the same set of input parameters, the m_{bol} of the brightest star varies from CMD to CMD because of statistical fluctuations. In this way, for each N we calculate the probability density function (PDF) for δm_{bol}, which is the difference between the m_{bol} of the tip and that of the brigthest star. Then, for each PDF (each N) we calculate the median and the standard deviation. As N increases, the median approaches the mode, the most probable value, which is always $\delta m_{bol} = 0$. In other words, the observed brightest star approaches the RGB tip as $N \to \infty$. Then, the absolute magnitude of the RGB is given by: $M_{bol}^{tip} = m_{bol}^{brightest\ star} - < \delta m_{bol} > -(m - M)_0 - A$, where $m_{bol}^{brightest\ star}$ is the apparent bolometric magnitude of the brightest RGB star, $< \delta m_{bol} >$ is the median of the corresponding PDF, $(m - M)_0$ is the distance modulus and A is the extinction coefficient. Then, the total error budget is: $\sigma_{obs}^2 = \sigma_{stat}^2 + \sigma_d^2 + \sigma_A^2 + \sigma_{ph}^2 + \sigma_{BC}^2$, where σ_{stat} is the standard deviation of the appropriate PDF_N, and the other 4 uncertainties, which represent the errors on distance, extinction, photometry and bolometric corrections, are obtained according to the available measuremts.

As an example, in table 2 we report the estimated value of the tip bolometric magnitude for the cluster M3. The apparent bolometric magnitude of the brightest RGB star has been derived by [4], basing on a near-IR photometric dataset obtained by combining HST and 2MASS data.

In this case the major source of uncertainty is due to the distance.

3 The theoretical RGB tip.

Models of Globular Cluster stars have been computed by means of the FUNS code (for more details, see [5] and references therein). Our theoretical predictions for the RGB tip bolometric magnitude as a function of the cluster metallicity is well represented by the following relation:

$$M^{tip}_{theory} = 0.0161[M/H]^2 - 0.1716[M/H] - 3.87 \quad (1)$$

In the case of M3 we get $M^{tip}_{theory} = -3.65$, which is very close the observed one. In general, uncertainties of the theoretical estimation of the RGB tip luminosity may be due to the main energy sources, such as the key nuclear reaction rates, or to the energy sinks, such as the plasma neutrino rates. The shell-H burning rate is controlled by the slower reaction of the CNO cycle, i.e., the ^{14}N$(p,\gamma)^{15}$O reaction, whose reaction rate has been directly measured by the LUNA collaboration down to 70 KeV [6]. This limit is very close to the Gamow's peak energy for this reaction at the temperature of the shell-H burning of a RGB star. According to the STARLIB database, we assume a $\pm$ 10% uncertainty for this reaction. The corresponding uncertainty for the theoretical tip bolometric magnitude is: $\sigma_{^{14}N(p,\gamma)^{15}O} = 0.007$ mag. On the other hand, the start of the He burning, which coincides with the RGB tip, is controlled by the the 3α reaction. For T$\geq$ 100 MK, the typical He ignition temperature, the uncertainty for the 3α reaction rate is $\sim \pm 10\%$ [7]. This uncertainty implies an error for the estimated tip bolometric magnitude of $\sigma_{3\alpha} = 0.0075$ mag. Note that the estimated error bars for the nuclear reaction rates do not include the uncertainty in the electron screening. The rate of plasma neutrinos production has been independently derived by several groups ([8], [9] and reference therein). This calculations commonly assume that the neutrino dipole moment, μ, is 0 (or negligible). A non-zero μ would enhance the neutrino production rate, causing a more efficient energy sink and, in turn, leading to larger core-He masses and brighter RGB tips [12]. Such an occurrence could explain or alleviate a discrepancy between stellar models and observed RGB tip luminosities, when the observed tip is brighter than the predicted one. On the other hand, the same discrepancy may be solved by introducing an additional energy sink, such as that induced by the production of non-standard weak interactive particles (e.g. axions). Keeping in mind this warning, in the following we will assume $\mu = 0$. Note that the upper bound for g_{ae} coupling constant we will obtain assuming $\mu = 0$ remains valid also in case of $\mu \neq 0$. This is not true for the hint we can get under the $\mu = 0$ hypothesis. Other model uncertainties are due to the adopted chemical composition, in particular, the metallicity and the initial He mass fraction. In the case of M3 we assume M/H= -1.16 ± 0.2 and Y= 0.25 ± 0.01 that corresponds to $\pm$0.035 mag and $\pm$0.015 mag on the RGB tip luminosity, respectively. Therefore, the total theoretical uncertainty is $\sigma_{theory} = 0.04$.

4 Axion-electron coupling from RGB tip

In this section we explore the hypothesis of an additional energy sink caused by the production of hypothetical bremstrahlung axions. Therefore, we have computed models for different values of the axion-electron coupling constant, namely $0 \leq g_{13} \leq 4$. The axion production rate has been computed according to the prescriptions of [11], for low density plasma, and [10], at higher

densities. Then, the inclusion of the axion cooling rate in the energy conservation equation leads to a larger core mass at the RGB tip and, in turn, to a larger luminosity. We obtain the following equation describing the relation among the RGB tip bolometric magnitude, the metallicity and the axion-electron coupling constant:

$$M_{teory}^{tip} = 0.0161[M/H]^2 - 0.1716[M/H] - 3.87 - 0.0239g_{13}^2 - 0.078g_{13} \quad (2)$$

which reduces to Eq. 1 when $g_{13} = 0$. Then, the most probable value of g_{13} is given by the maximum of the likelihood function: $L = A \exp\left[-(M_{theory}^{tip} - M_{obs}^{tip})^2/(\sigma_{theory}^2 + \sigma_{obs}^2)\right]$. In the case of M3 we obtain $g_{13} = 0.05$ with upper bound $g_{13} < 2.57$ at 95% C.L.. Because of the smaller difference between theory (no-axion) and observation, the upper bound we get for M3 is smaller than that obtained by [2] for M5. A more substantial improvement of this bound may be obtained by combining data of more clusters, to increase the statistical significance of the sample, and increasing the accuracy of the distance determination, which is the major source of error. In this context the final data release of the astrometric satellite GAIA will produce a big impact [13].

References

[1] Paczyński, B. "Evolution of Single Stars III. Stationary Shell Sources," Acta Astronomica, **20**, 287 (1970).

[2] Viaux N. *et al.*, "Neutrino and Axion Bounds from the Globular Cluster M5 (NGC 5904)," PhRvL, **111**, 231301 (2013).

[3] Straniero O.. *et al.*, "Axion-Photon Coupling: Astrophysical Constraints," in "Proceedings of the 11th Patras Workshop on Axions, WIMPs and WISPs (Patras2015)", p. 77 (2015).

[4] Valenti E. , Ferraro F. R., Origlia L., "Red giant branch in near-infrared colour-magnitude diagrams - II. The luminosity of the bump and the tip," MNRAS, **354**, 815 (2004).

[5] Straniero O., Gallino R., Cristallo S., "s process in low-mass asymptotic giant branch stars," NuPhA, **777**, 311 (2006).

[6] Formicola A. *et al.*, "Astrophysical S-factor of 14N(p,γ)15O", PhLB, **591**, 61 (2004).

[7] Fynbo H. O. U. *et al.*, "Revised rates for the stellar triple-α process from measurement of 12C nuclear resonances," Nature, **433**, 136 (2005).

[8] Haft M., Raffelt G., Weiss A., "Standard and nonstandard plasma neutrino emission revisited," The Astrophysical Journal, **425**, 222 (1994).

[9] Esposito S. *et al.*, "Radiative Corrections to Neutrino Energy Loss Rate in Stellar Interiors," MPLA, **17** , 491 (2002).

[10] Nakagawa M. , Kohyama Y., Itoh N., "Axion Bremsstrahlung in Dense Stars," The Astrophysical Journal, **322**, 291 (1987).

[11] Raffelt G., Weiss A., "Red giant bound on the axion-electron coupling reexamined," PhRvD, **51**, 1495

[12] Viaux N. *et al.*, "Particle-physics constraints from the globular cluster M5: neutrino dipole moments," Astronomy and Astrophysics, **558**, A12 (2013).

[13] Pancino E. *et al.*, "Globular clusters with Gaia," MNRAS, **467**, 412 (2017).

Chapter 5

Electric Dipole Moment

Compton Back Scattering Polarimetry for Storage Ring Electron EDM Experiment

Seongtae Park[1], *Yannis K. Semertzidis*[1,2]

[1]Center for Axion and Precision Physics Research, IBS, Daejeon 34051, Republic of Korea
[2]Department of Physics, KAIST, Daejeon 34141, Republic of Korea

DOI: http://dx.doi.org/10.3204/DESY-PROC-2017-02/park_seongtae

In this study, we present the result of feasibility study on the Compton polarimeter as a candidate for storage ring electron EDM experiment. The cross sections and analyzing powers of the scattered photons are calculated for both longitudinal and transverse electron polarizations. The optimum photon energy is calculated to be 8.9 keV for electrons with momentum of 15 MeV/c. The polarimeter figure of merit is calculated and compared with p-C interaction case.

1 Introduction

A well-known polarimeter concept for the storage ring proton EDM experiment is the nuclear elastic scattering method. This method is very effective (high analyzing power ∼0.6) especially for the proton-Carbon interaction around the proton magic momentum of 701 MeV/c [1, 2, 3, 4]. However, since this method is based on the hadronic elastic interaction between the spin polarized proton and carbon nuclei, it cannot be used for leptonic particles.

For the leptonic particles such as electron or muon, several different physics processes can be considered as polarization analyzers. First, Mott scattering is an electron scattering by the Coulomb field of a heavy nucleus. Møller polarimeter is utilizing collisions between polarized beam electrons and outer shell electrons of target material which are also polarized. In this study, we discuss the feasibility of Compton back scattering method as the electron polarimeter for storage ring electron EDM measurement. The calculation results of cross sections, analyzing powers, figure of merit and other experimental parameters are discussed and compared with other methods.

2 Interaction of circularly polarized photons with spin polarized particle beam

The interaction between polarized photon and spin polarized electron is well described in the references [5, 6]. Let's assume that a photon, whose Stokes vector is represented as $\vec{\xi} = (1, \xi_1, \xi_2, \xi_3)$, is interacting with an electron having spin vector $\vec{\zeta} = (\zeta_1, \zeta_2, \zeta_3)$. The

resulting final form of the differential cross section of the scattered photons is [7]

$$d\sigma = \frac{1}{2} r_0^2 \left(\frac{\omega'}{\omega_0{}'} \right)^2 (\Phi_0 + \Phi_1 + \Phi_2), \tag{1}$$

with

$$\begin{cases} \Phi_0 = 1 + \cos^2\theta' + \frac{1}{m_e}(\omega_0' - \omega')(1 - \cos\theta') \\ \Phi_1 = (\xi_1 \cos 2\varphi' + \xi_2 \sin 2\varphi') \sin^2\theta' \\ \Phi_2 = -\xi_3 \frac{1}{m_e}(1 - \cos\theta')\vec{\zeta} \cdot (\vec{k}_0' \cos\theta' + \vec{k}'). \end{cases}$$

Where $r_0 = e^2/mc^2$ is the classical radius of electron, $\vec{k}_0', \vec{k}'$ are initial and final photon wave vectors normalized by the electron mass energy, $\vec{\zeta}$ is the electron spin vector (vector in 3-dim space, not Stokes vector), and θ' is the scattering angle of outgoing photons. The primes indicate electron rest frame values and all units are in natural units, thus $\hbar = c = 1$. $\vec{k}_0' - \vec{k}'$ plane determines the y' axis and accordingly x' axis by the right-hand rule. Note that the spin polarization ($\vec{\zeta}$) dependent interaction term appears only in the Φ_2 and is only sensitive to circularly polarized photons (ξ_3).

Let's assume that we have photons with Stokes vector $\vec{\xi} = (1, 0, 0, P_\gamma)$ and electrons whose spin vector is described by $\vec{\zeta} = (\zeta_1, \zeta_2, \zeta_3)$. Then, we can define asymmetry in the photon scattering cross section with different photon polarizations, $P_\gamma = +1, -1$ (right and left circularly polarized, respectively).

$$A = \frac{d\sigma_+ - d\sigma_-}{d\sigma_+ + d\sigma_-} = \frac{\Phi_2}{\Phi_0} = -P_\gamma P_p F(\theta', \omega_0') \tag{2}$$

with

$$F(\theta', \omega_0') = \frac{\omega' \sin\theta' (1 - cos\theta')}{(1 + \cos^2\theta') + (\omega_0' - \omega')(1 - \cos\theta')}, \tag{3}$$

and

$$F(\theta', \omega_0') = \frac{(\omega_0' + \omega') \cos\theta' (1 - cos\theta')}{(1 + \cos^2\theta') + (\omega_0' - \omega')(1 - \cos\theta')} \tag{4}$$

where ω_0', ω' are initial and final photon energies normalized by the electron mass energy, $d\sigma_+, d\sigma_-$ are scattering cross-sections measured with right/left circularly polarized photons, respectively. Equations (3) and (4) are analyzing powers for transverse electron polarization and longitudinal electron polarization, respectively.

3 Optimal photon energy

In storage ring electron EDM experiment, we will be storing polarized electron beam at the momentum of 15 MeV/c (the magic momentum). In this case photon energy required for maximum analyzing power can be calculated using the relationship

$$\omega_0' = 2\gamma\omega_0, \tag{5}$$

where ω_0 is the initial photon energy measured in lab frame and γ is Lorentz factor of moving electron. Here, recall the prime is for electron rest frame values. The analyzing power increases

with photon energy and is maximum at $\omega_0' = 1$ for the transverse electron polarization. This can be easily shown by plotting the Eq. (3). By using the relationship between γ (=29 for electron magic momentum of 15 MeV/c) and photon wavelength λ,

$$\lambda = \frac{2.48\gamma}{m_e}[eV \cdot \mu m], \tag{6}$$

one can get the optimal wavelength of 0.14 nm which corresponds to the energy of 8.9 keV.

For the longitudinal electron polarization case, if the same energy of photon ($\omega_0' = 1$) is used, the analyzing power F is 0.8 and this is about 2.4 times bigger than the transverse electron polarization case (F=1/3). As a conclusion, the longitudinal polarization is more sensitive than the transverse polarization. Thus, we propose to use longitudinal polarization for the electron polarization analysis.

4 Figure of merit

The polarimeter figure of merit is defined by the Eq. (7).

$$FOM \equiv 2N_0\Pi^2, \ or \ \sigma\Pi^2 \tag{7}$$

where $2N_0$ is total number of particles used in the measurement and Π is analyzing power. Fig. 1 shows the resulting figure of merit as a function of scattering angle θ' along with the differential cross section and analyzing power. As can be seen in Fig. 1 (c), the best FOM can be achieved in the angle range of $\theta' = \pi/2 \sim 3\pi/2$ for the longitudinal electron polarization case. The FOM is an important parameter for assessing polarimeter efficiency. In this study, we assumed an example experimental conditions and the resulting figure of merit for this Compton polarimeter was about 4.5×10^3. The detailed calculation will be published elsewhere.

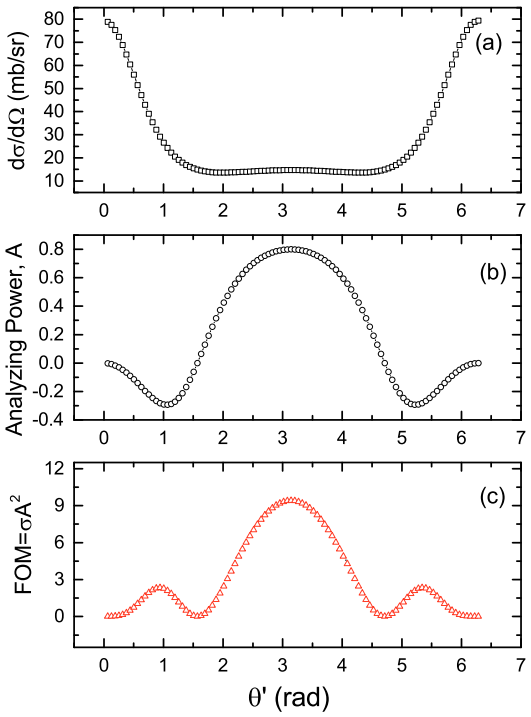

Figure 1: Cross section (a), analyzing power (b) and figure of merit (c).

One can do a similar calculation for p-C polarimeter case. Let's assume that we have 10^{11} protons/storage and extract them for 10^3 s. This gives 10^8 protons/s on target. Assuming 1 % of detector efficiency, the total number of protons arriving on the detector plane is 10^6/s. If we use average analyzing power of 0.6 for the p-C scattering for the angle range of 5∼20 deg, the approximate FOM becomes $FOM_{pC} = 10^6 \times 0.6^2 = 3.6 \times 10^5$. Comparing this result with the Compton case, p-C scattering polarimeter is more efficient by

2 orders of magnitude. This is because the p-C interaction have higher hadronic elastic cross sections compared to Compton back scattering.

As mentioned above, all these calculations are based on the assumptions with some experiment parameters. In order to get realistic numbers, all the parameters used in the calculation have to be replaced with real numbers of the experiment setup.

5 Summary and conclusion

In this study, we used circularly polarized photons as an analyzing tool for electron polarization measurement. We calculated the cross sections of back scattered photons off both transversely and longitudinally polarized electron beams and found the longitudinal beam was more sensitive for the polarization analysis. The optimal energy of the photon was calculated to be 8.9 keV. At this energy, the maximum analyzing power was about 0.8. By using some experimental parameters as an example, the figure of merit is calculated and compared with the case of p-C scattering polarimeter which is being developed for storage ring proton EDM experiment. Based on all the calculations we made in this study, we conclude that the Compton back scattering method could be a good candidate for the storage ring electron EDM measurement.

6 Acknowledgments

This work was supported by IBS-R017-D1 of the Republic of Korea..

References

[1] G. Waters *et al.*, Nucl. Instrum. Meth **A 153**, 401 (1978).

[2] R.D. Ransome, S.J. Greene, C.L. Hollas, B.E. Bonner, M.W. McNaughton, C.L. Morris and H.A. Thiessen, Nucl. Instrum. Meth. **A 201**, 315 (1982).

[3] B. Bonin *et al.*, Nucl. Instrum. Methods **A 288**, 379 (1990).

[4] M.W. McNaughton *et al.*, Nucl. Instrum. Meth. **A 241**, 435 (1985).

[5] Fano, U., J. Opt. Soc. Am. **39**, 859 (1949).

[6] H. A. Tolhoek, Rev. Mod. Phys. **28**, 277 (1956).

[7] A. Stillman, PAC 95/HEACC 95 Proceedings.

Chapter 6

Magnetic Monopoles

Hunting magnetic monopoles and more with MoEDAL at the LHC

Vasiliki A. Mitsou on behalf of the MoEDAL Collaboration

Instituto de Física Corpuscular (IFIC), CSIC – Universitat de València, Valencia, Spain

DOI: http://dx.doi.org/10.3204/DESY-PROC-2017-02/mitsou_vasiliki

The MoEDAL experiment at the LHC is optimised to detect highly-ionising particles such as magnetic monopoles, dyons and (multiply) electrically-charged stable massive particles predicted in a number of theoretical scenarios. MoEDAL, deployed in the LHCb cavern, combines passive nuclear track detectors with magnetic monopole trapping volumes, while backgrounds are being monitored with an array of MediPix detectors. The detector concept and its physics reach is presented with emphasis given to recent results on monopoles.

1 Introduction

MoEDAL (Monopole and Exotics Detector at the LHC) [1], the 7^{th} experiment to operate at the Large Hadron Collider (LHC), is designed to search for manifestations of new physics through highly-ionising (HI) particles in a manner complementary to ATLAS and CMS [2]. The main motivation for the MoEDAL experiment is to pursue the quest for magnetic monopoles at LHC energies. Nonetheless the detector is also designed to search for any massive, long-lived, slow-moving particle [3] with single or multiple electric charges arising in many scenarios of physics beyond the Standard Model [4].

2 The MoEDAL detector

The MoEDAL detector [1] is deployed around the intersection region at the LHC Point 8 in the LHCb Vertex Locator (VELO) cavern. A schematic view of the MoEDAL experiment is shown in Fig. 1. It is a unique and largely passive detector comprising different detector technologies.

2.1 Nuclear track detectors

The main sub-detector system is made of a large array of CR39®, Makrofol® and Lexan® nuclear track detector (NTD) stacks surrounding the intersection area. The passage of a HI particle through the plastic detector is marked by an invisible damage zone along the trajectory. The damage zone is revealed as a cone-shaped etch-pit when the plastic detector is chemically etched. Then the sheets of plastics are scanned looking for aligned etch pits in multiple sheets. The MoEDAL NTDs have a threshold of $Z/\beta \sim 5$, where Z is the charge and $\beta = v/c$ the velocity of the incident particle.

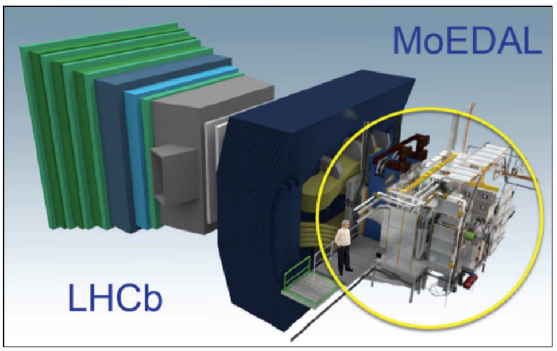

Figure 1: A three-dimensional schematic view of the MoEDAL detector (in the yellow circle) around the LHCb VELO region at Point 8 of the LHC.

Another type of NTD installed is the Very High Charge Catcher ($Z/\beta \sim 50$). It consists of two flexible low-mass stacks of Makrofol®, deployed in the LHCb acceptance between RICH1 and the Trigger Tracker. It is the only NTD (partly) covering the forward region, adding only $\sim 0.5\%$ to the LHCb material budget while enhancing considerably the overall geometrical coverage of MoEDAL.

2.2 Magnetic trappers

A unique feature of the MoEDAL detector is the use of paramagnetic magnetic monopole trappers (MMTs) to capture magnetically-charged HI particles. The aluminium absorbers of MMTs are subject to an analysis looking for magnetically-charged particles at a remote SQUID magnetometer facility [5]. For the 2015 run at 13 TeV, the MMT consisted of 672 aluminium rods for a total mass of 222 kg that were placed 1.62 m from the IP8 LHC interaction point under the beam pipe on the side opposite to the LHCb detector.

2.3 TimePix radiation monitors

The only non-passive MoEDAL sub-detector is an array of TimePix pixel devices distributed throughout the MoEDAL cavern, forming a real-time radiation monitoring system of HI beam-related backgrounds. The operation in time-over-threshold mode allows a 3D mapping of the charge spreading in the volume of the silicon sensor, thus differentiating between various particles species from mixed radiation fields and measuring their energy deposition.

3 Magnetic monopoles

The MoEDAL detector is designed to fully exploit the energy-loss mechanisms of magnetically charged particles [6–8] in order to optimise its potential to discover these messengers of new physics. There are various theoretical scenarios in which magnetic charge would be produced at the LHC [4]: (light) 't Hooft-Polyakov monopoles [8, 9], electroweak monopoles [10], global monopoles [11] and monopolium [7,12–14]. Magnetic monopoles that carry a non-zero magnetic charge and dyons possessing both magnetic and electric charge are predicted by many theories including grand-unified and superstring theories [15, 16].

A possible explanation for the non-observation of monopoles so far is Dirac's proposal [6, 7, 12] that monopoles are not seen freely because they form a bound state called *monopolium* [13, 14, 17] being confined by strong magnetic forces. Monopolium is a neutral state, difficult to detect directly at a collider detector, although its decay into two photons would give a rather clear signal for ATLAS and CMS [18], which however would not be visible in MoEDAL. Nevertheless the LHC radiation detector systems can be used to detect final-state protons $pp \to pXp$ exiting the LHC beam vacuum chamber at locations determined by their fractional momentum losses [19]. Such technique would be appealing for detecting monopolia.

4 Searches for monopoles in MoEDAL with MMTs

The high magnetic charge of a monopole —being at least one Dirac charge $g_D = 68.5e$— implies a strong magnetic dipole moment, which may result in strong binding of the monopole with the nuclei of the aluminium MMTs. In such a case, the presence of a monopole trapped in an MMT bar would de detected through a non-zero *persistent current*, defined as the difference between the SQUID currents before and after its passage through the sensing coil.

The Run-2 MMT configuration was analysed and no magnetic charge $> 0.5g_D$ was detected in any of the exposed samples when passed through the ETH Zurich SQUID. Hence cross-section limits are obtained for Drell-Yan (DY) pair production of spin-1/2 and spin-0 monopoles for $1g_D \leq |g| \leq 5g_D$ at 13 TeV [20], as shown in Fig. 2 (left), improving previous bounds set by MoEDAL at 8 TeV [21]. However, the large monopole-photon coupling invalidates any perturbative treatment of the cross-section calculation and hence any result based on the latter is only indicative. This situation may be resolved if thermal production in heavy-ion collisions —that does not rely on perturbation theory— is considered [22].

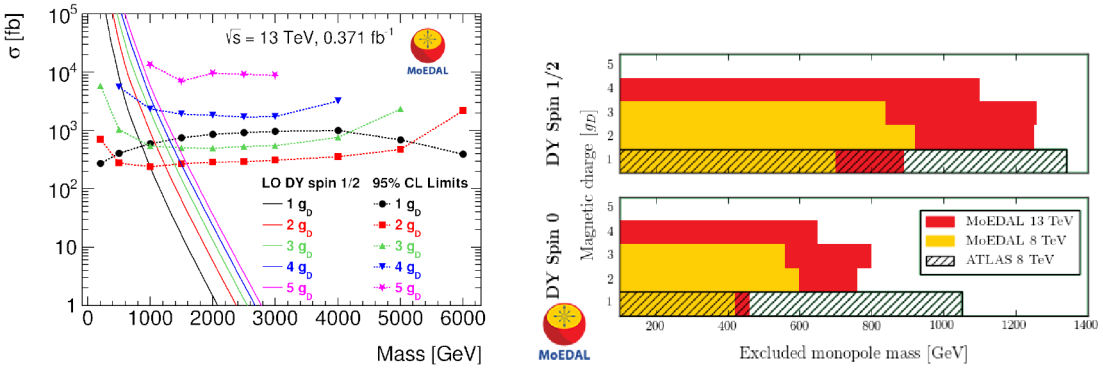

Figure 2: Left: Cross-section upper limits at 95% C.L. for DY monopole production as a function of mass for spin-1/2 monopoles [20]. Right: Excluded monopole masses for DY production for spin-1/2 (top) and spin-0 (bottom) monopoles. The MoEDAL results obtained at 8 TeV [21] and 13 TeV [20] are superimposed on the ATLAS 8-TeV limits [24].

Under the assumption of Drell-Yan cross sections, mass limits are derived for $g_D \leq |g| \leq 4g_D$ at the LHC, complementing ATLAS results [23, 24], which placed limits for monopoles with magnetic charge $|g| \leq 1.5g_D$ (c.f. Fig. 2, right). The ATLAS bounds are better that the MoEDAL ones for $|g| = 1g_D$ due to the higher luminosity delivered in ATLAS and the loss of acceptance in MoEDAL for small magnetic charges. On the other hand, higher charges are difficult to be probed in ATLAS due to the limitations of the level-1 trigger deployed for such searches. Limits on monopole production cross sections set by various colliders are presented in Ref. [15], while general limits including searches in cosmic radiation are reviewed in Ref. [25].

5 Summary and outlook

MoEDAL extends considerably the LHC reach in the search for (meta-)stable HI particles. The latter are predicted in a variety of theoretical models and include: magnetic monopoles, SUSY

long-lived spartners, quirks, strangelets, Q-balls, etc [4, 26]. The MoEDAL Collaboration is preparing new analyses with more Run 2 data, with other detectors (NTDs) and with a large variety of interpretations involving not only magnetic but also electric charges.

Acknowledgments

The author acknowledges support by the Spanish MINEICO under the project FPA2015-65652-C4-1-R, by the Generalitat Valenciana through the MoEDAL-supporting agreement CON.21.2017-09.02.03, by the CSIC CT Incorporation Program 201650I002, by the Severo Ochoa Excellence Centre Project SEV 2014-0398, and by a 2017 Leonardo Grant for Researchers and Cultural Creators, BBVA Foundation.

References

[1] J. Pinfold *et al.* [MoEDAL Collaboration], "Technical Design Report of the MoEDAL Experiment," CERN-LHCC-2009-006, MoEDAL-TDR-001; MoEDAL web page: `http://moedal.web.cern.ch/`

[2] A. De Roeck *et al.*, Eur. Phys. J. C **72**, 1985 (2012).

[3] M. Fairbairn *et al.*, Phys. Rept. **438**, 1 (2007); S. Burdin *et al.*, Phys. Rept. **582**, 1 (2015).

[4] B. Acharya *et al.* [MoEDAL Collaboration], Int. J. Mod. Phys. A **29**, 1430050 (2014).

[5] M. D. Joergensen *et al.*, arXiv:1206.6793 (2012); A. De Roeck *et al.*, Eur. Phys. J. C **72**, 2212 (2012).

[6] P. A. M. Dirac, Proc. Roy. Soc. Lond. A **133**, 60 (1931).

[7] P. A. M. Dirac, Phys. Rev. **74**, 817 (1948).

[8] G. 't Hooft, Nucl. Phys. B **79**, 276 (1974); A. M. Polyakov, JETP Lett. **20**, 194 (1974).

[9] V. Vento and V. S. Mantovani, arXiv:1306.4213 [hep-ph] (2013).

[10] Y. M. Cho and D. Maison, Phys. Lett. B **391**, 360 (1997); W. S. Bae and Y. M. Cho, J. Korean Phys. Soc. **46**, 791 (2005); Y. M. Cho, K. Kimm and J. H. Yoon, Mod. Phys. Lett. A **31**, no. 09, 1650053 (2016); Phys. Lett. B **761**, 203 (2016); J. Ellis, N. E. Mavromatos and T. You, Phys. Lett. B **756**, 29 (2016).

[11] M. Barriola and A. Vilenkin, Phys. Rev. Lett. **63**, 341 (1989); A. K. Drukier and S. Nussinov, Phys. Rev. Lett. **49**, 102 (1982); P. O. Mazur and J. Papavassiliou, Phys. Rev. D **44**, 1317 (1991); N. E. Mavromatos and S. Sarkar, Phys. Rev. D **95**, no. 10, 104025 (2017).

[12] Y. B. Zeldovich and M. Y. Khlopov, Phys. Lett. **79B**, 239 (1978).

[13] C. T. Hill, Nucl. Phys. B **224**, 469 (1983).

[14] V. K. Dubrovich, Grav. Cosmol. Suppl. **8N1**, 122 (2002).

[15] A. Rajantie, Contemp. Phys. **53**, 195 (2012); Phys. Today **69**, no. 10, 40 (2016).

[16] T. W. Kephart, G. K. Leontaris and Q. Shafi, arXiv:1707.08067 [hep-ph].

[17] L. N. Epele *et al.*, Eur. Phys. J. C **56**, 87 (2008); Eur. Phys. J. C **62**, 587 (2009).

[18] L. N. Epele *et al.*, Eur. Phys. J. Plus **127**, 60 (2012); arXiv:1607.05592 [hep-ph] (2016).

[19] M. Kalliokoski, J. W. Lämsä, M. Mieskolainen and R. Orava, arXiv:1604.05778 [hep-ex] (2016).

[20] B. Acharya *et al.* [MoEDAL Collaboration], Phys. Rev. Lett. **118**, 061801 (2017).

[21] B. Acharya *et al.* [MoEDAL Collaboration], JHEP **1608**, 067 (2016).

[22] O. Gould and A. Rajantie, arXiv:1705.07052 [hep-ph].

[23] G. Aad *et al.* [ATLAS Collaboration], Phys. Rev. Lett. **109**, 261803 (2012).

[24] G. Aad *et al.* [ATLAS Collaboration], Phys. Rev. D **93**, 052009 (2016).

[25] L. Patrizii and M. Spurio, Ann. Rev. Nucl. Part. Sci. **65**, 279 (2015).

[26] V. A. Mitsou [MoEDAL Collaboration], EPJ Web Conf. **95**, 04042 (2015); PoS **EPS-HEP2015**, 109 (2015); J. Phys. Conf. Ser. **873**, no. 1, 012010 (2017); N. E. Mavromatos and V. A. Mitsou [MoEDAL Collaboration], EPJ Web Conf. *to appear* [arXiv:1612.07012 [hep-ph]].

Chapter 7

Dark Energy, Neutrinos and other Topics

The case for preserving our knowledge and data in physics experiments

Frank Berghaus

University of Victoria, Victoria, Canada

DOI: http://dx.doi.org/10.3204/DESY-PROC-2017-02/berghaus_frank

This proceeding covers tools and technologies at our disposal for scientific data preservation and shows that this extends the scientific reach of our experiments. It is cost-efficient to warehouse data from completed experiments on the tape archives of our national and international laboratories. These subject-specific data stores also offer the technologies to capture and archive knowledge about experiments in the form of technical notes, electronic logs, websites, etc. Furthermore, it is possible to archive our source code and computing environments. The paper illustrates these challenges with experience from preserving the LEP data for the long term.

1 Introduction

Data from particle physics experiments are collected with significant financial and human effort and are mostly unique. Experiment data are maintained by personal effort of scientists until they are judged no longer worth that effort. The tools and knowledge to interpret the data are lost as the members of the experiment move on to other projects. When later discoveries or new hypotheses for beyond-the-Standard-Model Physics renew interest in this forgotten data, theorists resort to recasting previously published results. Often this requires either extrapolations and assumptions or the need to be overly conservative in the possible interpretations because the original data or input needed to understand the data have been lost. This imposes limits on the scientific reach of our data. This is particularly worrisome as new physics is suspected in an increasing number of possible directions.

The physics programs of large experiments are completed only a few years upon the shutdown of the experiment. Without additional care, the utility of data diminishes even over the period of a few years as software and computing environments evolve and expert personnel and knowledge transition to new projects.

2 Requirements For Long-Term Preservation

The DPHEP Study group was initiated in 2009[1] to "to get a common vision on these issues and create a multi-experiment dynamics for further reference". The study group identified the following tasks, in order of priority :

[1] As a subgroup of the International Committee on Future Accelerators

1. *Experiment level projects*: The curation and preparation of data to be preserved must come from experts on the individual experiments. Some effort during the data-taking leads to a significant improvement in the ability to move experiment data to long-term preservation.

2. *International organization*: The responsibility of data preservation past the lifetime of an experiment must fall on a long-lived organization trusted by the experiment. The DPHEP collaboration [1] was formed to coordinate that long-lived institutional support.

3. *Common R&D projects*: Most challenges of providing long-term data preservation are shared between experiments. Concrete inter-experiment projects are facilitated by the DPHEP organization.

2.1 Knowledge, Data, and Software

To evaluate a new physics model against existing data one needs to run the detector simulation on the predictions of the physics model. The output of the detector simulation is reconstructed by the experiment reconstruction software, which yields a data format suitable for physics analysis. The detector simulation and reconstruction software are complex and require knowledge specific to each experiment. This knowledge is captured partially in internal documents during the operation of the experiment.

The software used by physics experiments is usually developed assuming a homogeneous computing environment and are therefore not portable. The large data volumes involved necessitate custom formats and protocols to optimize the performance of data acquisition, processing and analysis. Upon completion of the experimental programme the software and the ecosystem of supporting services are no longer maintained. Additional care needs to be taken when planning to access data in the long term and using experiment software given the pace of computing and software evolution.

Bit preservation of the scientific datasets as well as the knowledge, software, and computing environments identified above must be guaranteed. It is therefore advisable to choose an institution which operates the tools and services outlined in section 3 as a trusted repository. There exist multiple international agencies that assess the trustworthiness of a repository for long-term preservation, for example the Data Seal of Approval[2], the German nestor [2], and the ISO 16363.

3 Services and Tools

This section summarizes the tools and services commonly used to solve the challenges of data preservation. When evaluating the tools to preserve data one should keep in mind the target audience[3] and timescale for preservation. These should be clearly stated in the data preservation policy and sets the effort and tools required.

[2] `https://datasealofapproval.org`

[3] Example target audience are the collaboration, fellow physicists, or the general public.

3.1 Digital Libraries

Digital libraries provide databases to warehouse the documents that provide knowledge preservation. Care should be taken in curating the documents that are submitted to the digital library and a librarian should be considered to help to categorize these documents. The knowledge necessary to understand the experiment should not only be captured on documents held in the digital library but the target audience must be able to find these documents.

There exist many digital libraries, and some care should be taken when choosing the digital library to warehouse your documents. Generally, there are institutional (e.g. the CERN Document Server), subject-specific (HEPData), and generic digital libraries (Zenodo)[4].

3.2 Virtualization and Containerization

Digital libraries are a suitable place to house the source code. Active maintenance of that source code usually ceases after the lifetime of an experiment. Software and hardware that source code relies upon continue to evolve. That means, on its own, the source code will eventually only serve as documentation. To use old binaries or compile the old source code the operating system, compiler, and necessary libraries need to be captured. Two technologies exist to facilitate this capture: virtualization and containerization. A virtual machine runs a complete operating system with drivers for hardware interfaces emulated by a host computer. A container is a user-space isolated by operating system features of the host. Virtual machines provide a mechanism of abstracting hardware architecture while containers do not. The choice should be informed by the period for which the data should be preserved.

Even virtual machines will be subject to some effects of software and hardware evolution. To ensure long-term preservation the virtual machine itself must be maintained. This maintenance is independent of the software contained in the virtual machine. Defining a test of the software environment such as a representative analysis that can be run by an automated system is advisable. An elegant solution to this problem is provided by the CernVM [3]. Note that containers may (and often are) run in virtual machines. The two technologies may readily be combined. Umbrella [4] is a tool to determine and capture the dependencies of your software in a container environment.

3.3 Tape Archives

Documents in a digital archive, virtual machines, containers and scientific data are digital objects. Their long-term preservation is ensured by storage technology. Tape libraries are the current state of the art for rarely accessed data since they provide longevity[5] at low cost. Figure 1 shows a cost model for an LHC-sized data archive including purchasing and maintenance costs for tape libraries, drives and media[6]. The cost decreases even with the increasing data volume because the high cost of the tape libraries, robots, and readers are at the beginning while the additional tapes are relatively cheap. Furthermore the data density of the tape media is projected to increase by $\sim 32\%$ per year [1].

In the software design for the experiment, it is advisable to use common standards to access the data such as a POSIX filesystem or HTTP. While experiment or subject-specific tools

[4] All of these are based on Invenio `http://invenio-software.org`

[5] Tapes usually claim to provide data integrity for a few decades. To ensure data integrity in a large archive tape media is exchanged every 3-5 years.

[6] But excludes the cost of software development, licensing and the manpower for operation.

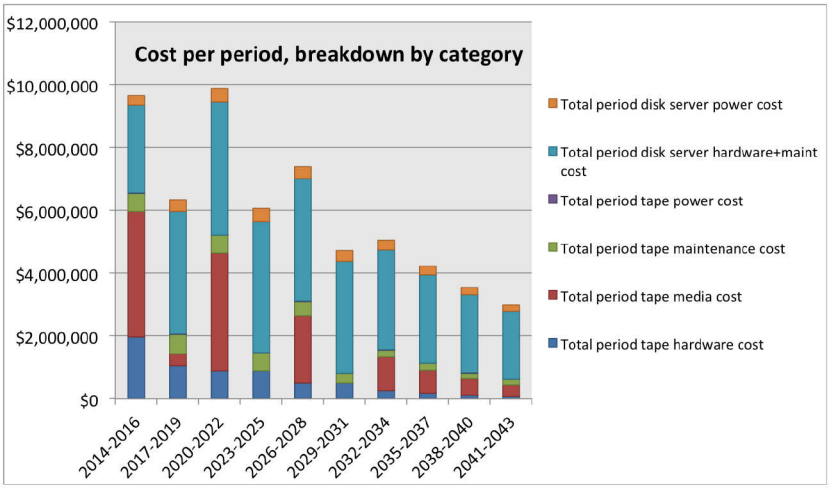

Figure 1: Cost projection for LHC Data on tape. The corresponding approximate growth in data volume is an increase from $\sim$ 160 PB in the 2014-2016 period to $\sim$ 17 EB in 2041-2043 [1].

provide high performance during active operation, support for the necessary protocols declines as the next generation of experiments adopts other tools and standards. Migration to those new standards is difficult.

4 Case Study: LEP

ALEPH, DELPHI, L3 and OPAL were the four experiments at the Large Electron-Positron Collider at CERN. Operation of the accelerator and experiments concluded in 2000. Research based on the data from these experiments is published to date, for example, search for the MSSM Higgs [5] or a di-muon signal [6]. The first shows the promise of data preservation, the second highlights the challenges of guaranteeing correctness of these analyses.

Before dissolving each LEP collaboration agreed on a data preservation and access policy. ALEPH chose to allow open access while the three others allowed analysis and publication only under the oversight of former members of the collaboration. As a result, ALEPH data may be found on open data catalogues[7], while those of the other three experiments may not. Revision of these policies proved difficult since the responsible members have moved on or think data access should remain restricted. Published and internal (technical) documents are captured by the CERN Document Server. The documentation of the experiments, including snapshots of their websites, publications and internal notes have been archived. Former collaborators from ALEPH, DELPHI, and OPAL built a running computing environment for their respective experiment [7, 8, 9]. The results are virtual machine environments which provide access to the data of the experiments. The experiment software is provided using the CERN virtual machine file system. Long-term support of this file system was pledged by the LHC community.

The LEP experiments relied on RFIO to access data directly on tape, however, they all made access to data directly on the filesystem possible. Since support for RFIO has been discontinued

[7] EUDAT at `http://b2find.eudat.eu/group/about/aleph`

access to the data is provided by a remote service[8] mounted on the virtual machine. Access is authorized through the Kerberos authentication system at CERN. The data of the ALEPH collaboration is open. To access the data of OPAL and DELPHI a collaboration representative must be contacted[9].

5 Conclusions

Criteria for planning and executing long-term data preservation strategies have been established. These strategies were tested with the LEP experiments to show that data analysis may be performed 15 years after last data taking. The software design decisions made during the development and operation of the experiment as well as the policies for data access have profound implications on the long-term usability and accessibility of scientific data. These criteria should be considered when planning new experiments.

Acknowledgements

The author would like to thank J. Shiers and the DPHEP collaboration who made this project possible. The work with the LEP experiments could only be accomplished thanks to the work of G. Ganis and M. Maggi (ALEPH), M. Schröder (OPAL), and U. Schwickerath (DELPHI). The author would also like to acknowledge the many people from the CERN IT and libraries departments who continue to contribute to this work.

References

[1] S. Amerio *et al.* [DPHEP Collaboration], "Status Report of the DPHEP Collaboration: A Global Effort for Sustainable Data Preservation in High Energy Physics," doi:10.5281/zenodo.46158 arXiv:1512.02019 [hep-ex].

[2] S. Dobratz and H. Neuroth "nestor: Network of Expertise in Long-term Storage of Digital Resources. A Digital Preservation Initiative for Germany," Microform & Imaging Review **33(2)** (2008) 52-58, doi:10.1515/MFIR.2004.52

[3] D. T. Larsen, J. Blomer, P. Buncic, I. Charalampidis and A. Haratyunyan, J. Phys. Conf. Ser. **396** (2012) 032064. doi:10.1088/1742-6596/396/3/032064

[4] H. Meng and D. Thain "Umbrella: A Portable Environment Creator for Reproducible Computing on Clusters, Clouds, and Grids" Proceedings of the 8th International Workshop on Virtualization Technologies in Distributed Computing **VTDC '15** 23-30 10.1145/2755979.2755982

[5] S. Schael *et al.* [ALEPH Collaboration], "Search for neutral Higgs bosons decaying into four taus at LEP2," JHEP **1005** (2010) 049 doi:10.1007/JHEP05(2010)049 [arXiv:1003.0705 [hep-ex]].

[6] A. Heister, "Observation of an excess at 30 GeV in the opposite sign di-muon spectra of $Z \to b\bar{b} + X$ events recorded by the ALEPH experiment at LEP," arXiv:1610.06536 [hep-ex].

[7] M. Maggi and T. Boccali, "ALEPH SCL5 Virtual Machine for Research Environment," doi:10.15161/oar.it/1411041136.04

[8] F. Berghaus and U. Schwickerath, "Computing Environment For The DELPHI Experiment At LEP," doi:10.5281/zenodo.1068952

[9] F. Berghaus and M. Schröder, "Computing Environment For The OPAL Experiment At LEP," doi:10.5281/zenodo.1068939

[8] EOS Open Storage `http://eos.web.cern.ch` mounted using the XROOT fuse module.

[9] Contact information may be found at `https://greybook.cern.ch` or `http://dphep.org`

Dark-Sector Photo-Magnetic Luminescence: The Case for a Room Temperature Chameleon Search

James R Boyce[1,2], *Andrei Afanasev*[3], *George Biallas*[2], *Geoffrey Krafft*[2,4], *Mahlon Long*[2], *John Mammosser*[5], *Dennis Manos*[1], *Robert Rimmer*[2], *Brianna Thorpe*[2,6]

[1]The College of William Mary, Williamsburg, VA, USA
[2]Thomas Jefferson National Accelerator Facility, Newport News, VA, USA
[3]George Washington University, Washington DC USA
[4]Old Dominion University, Norfolk, VA USA
[5]Oak Ridge National Laboratory, Oak Ridge, TN, USA
[6]Arizona State University, Tempe, AZ, USA

DOI: http://dx.doi.org/10.3204/DESY-PROC-2017-02/boyce_jim

We report the results of studies showing that temperature dependent photoluminescence is the likely source of unexpected large background rates in afterglow searches for dark sector phenomena, commonly called "chameleons". Using this information, we examine the possibility of a room temperature chameleon afterglow search that automatically eliminates this background. Then, without this background, we discuss a modest search effort exploring the afterglow halflife range 0.1 sec $\leq T_{1/2} \leq$ 120 sec equivalent to photon coupling constant range $8 \times 10^{12} \leq \beta_\gamma \leq 3 \times 10^{14}$.

Considered by some to be quintessential components of Dark Energy (DE), chameleon particles should be formed by a DE scalar field oscillating into photons in the presence of a magnetic field. If formed inside a vacuum chamber, their effective mass characteristics would confine them to the vacuum chamber until they reconvert back to photons (see Ref. [1,2,3]). Chameleon production and subsequent decay forms the basis of the afterglow experimental technique from Ref. [4] . Conversion probabilities between photons and chameleons can be found in Ref. [1,2,3] and the afterglow flux from decay chameleon can be found in Ref. [4].

The generic layout of afterglow experiments is shown schematically in Figure 1. Note that in this work, laser induced delayed photon emission from standard matter is considered to be "luminescence" and laser induced delayed photon emission from chameleons is "afterglow".

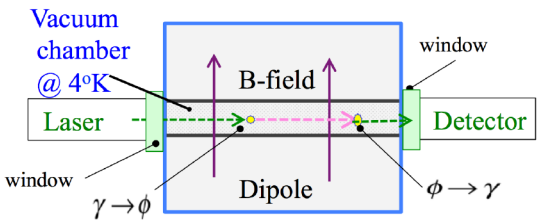

Figure 1: The generic layout of afterglow experiments.

The afterglow experiment, depicted in Figure 1, consists of a photon source laser shining through a viewport window into a vacuum chamber immersed in a dipole magnetic field where a chameleon "gas" is generated by the interaction of scalar field, photons, and magnetic field. Chameleons, by their very nature, cannot escape the vacuum chamber but can convert back to photons when they pass through the magnetic field. When the source laser is turned off the chameleon gas decays away and the resulting photons are either absorbed by the vacuum chamber walls or escape through viewports and captured by detectors.

Figure 2 shows the predicted afterglow rates. Note the build-up of chameleons while the source laser is on and the decay after the laser is turned off at t=0. All three groups, CHASE (Fermilab), GammeV-CHASE (Fermilab), and OSQAR-CHASE (CERN) reported an unexpected large backgrounds at the 4 K operating temperature of the dipole - so large, in fact, that all data within the first two minutes after laser turn-off, could not be used. The observed increase in count rates at low T could not be attributed to chameleon afterglow since the rate increase was independent of the dipole field.

The temperature dependence of the background luminescence is explained by a Jablonski diagram (see Ref. [10]) which depicts the sequence of events when a molecule absorbs a photon and then sheds the energy as it returns to the ground state. At room temperature, there are many paths back to the ground state, e.g. rotation or vibration, which do not radiate. In Figure 3, we show the proposed room temperature setup along with real luminescence images taken with the setup.

In Figure 4 we show the updated afterglow predictions for $\beta_\gamma = 20^{14}$. These plots include a background of 300 Hz that are not included in the other afterglow calculations. Even with this large background, the calculated afterglow for t=0 and 1.7 Tesla, the signal to noise ratio is significant.

And in Figure 5, we show a photograph of the current LIPSS setup to clearly show that most of the equipment needed for this experiment is on hand.

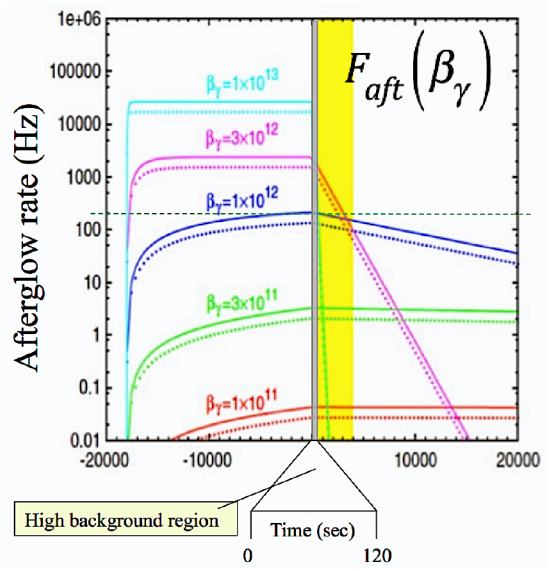

Figure 2: Predicted afterglow rates assuming several values of the coupling constant β_γ.

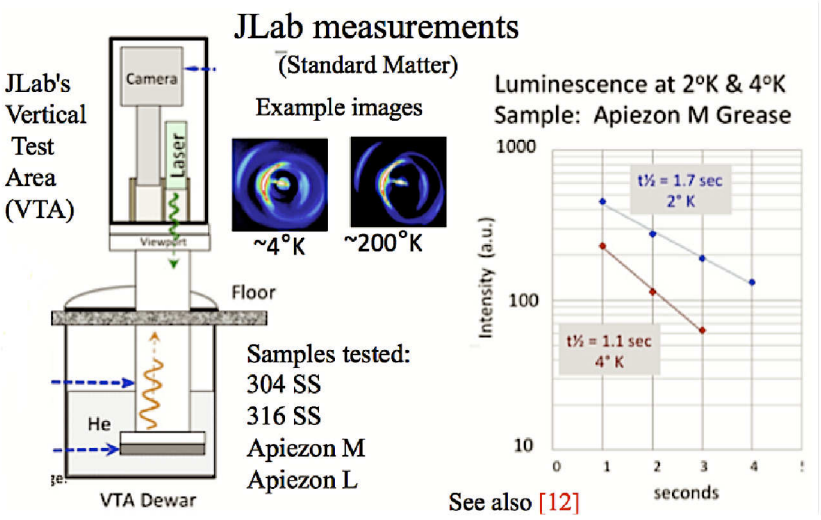

Figure 3: Temperature dependent luminescence.

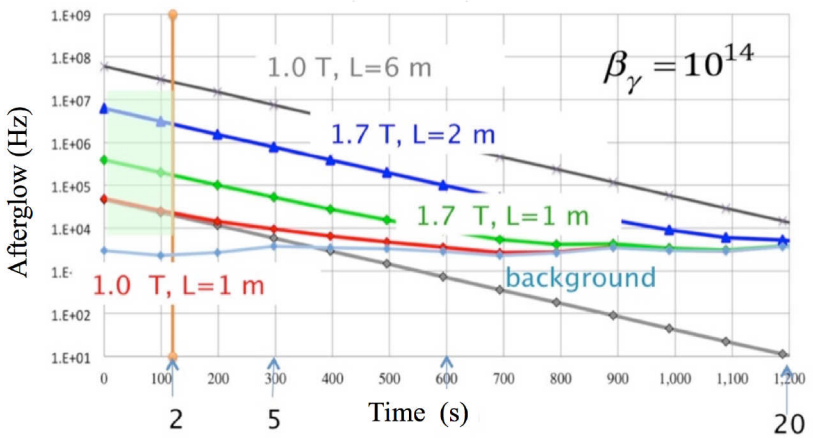

Figure 4: Afterglow in magnetic field.

In summary, we find that using 4K vacuum chambers standard matter luminescence photons contribute strongly to the background and would mask afterglow photons. Making the searches at room temperature automatically eliminates this background, permitting short decay time chameleon searches. Thus, we demonstrate how to make a room temperature chameleon search and test predictions of photon coupled chameleon scalar fields.

Acknowledgments

We are grateful for the support from the College of William & Mary, Office of Vice Provost for Research, and for the many useful discussions with Jefferson Lab staff and users. This material

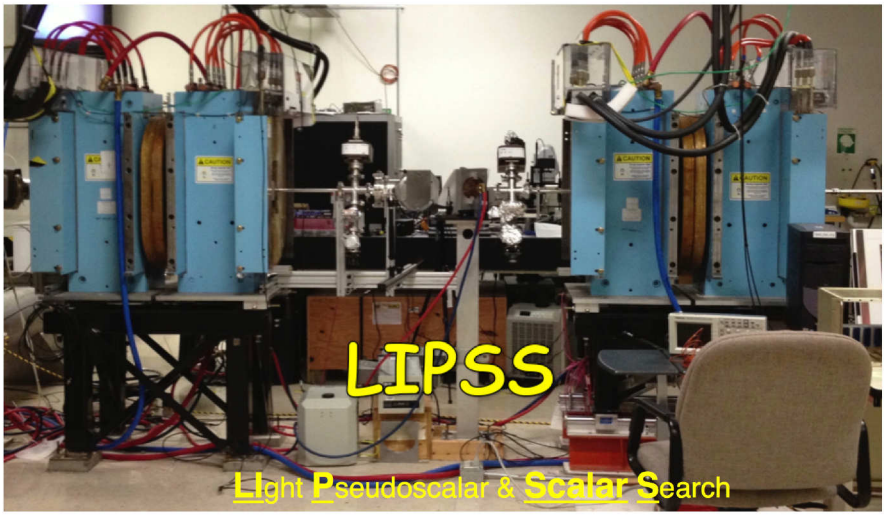

Figure 5: Image of the LIPSS experimental setup at Jefferson Lab. The dipoles are colored light blue and can be joined to form a 2 meter long, 1.7 Tesla B-Field.

is based upon work supported by the U.S. Department of Energy, Office of Science, Office of Nuclear Physics under contract DE-AC05-06OR23177.

Bibliography

[1] J.L. Hewett et al., 2012. Fundamental Physics at the Intensity Frontier.
[2] J. Khoury and A. Weltman, Phys. Rev. D 69, 044026 (2003).
[3] J. Khoury and A. Weltman, Phys. Rev. Lett. 93, 171104 (2004).
[4] A. S. Chou et al., Phys. Rev. Lett. 102, 030402 (2009).
[5] P. Sikivie, Phys. Rev. Lett. 51, 1415 (1983).
[6] P. Sikivie, Phys. Rev. D 32, 2988 (1985).
[7] P. Sikivie, Phys. Rev. D 36, 974 (1987).
[8] J. H. Steffen et al., Phys. Rev. D 86, 012003 (2012).
[9] M. Sulc, Proceedings of 12th Patras Workshop (2016).
[10] Theoretical Chemistry, Chemwiki, U.C. Davis.
[11] A. Upadhye, Phys. Rev. D 86, 035006 (2012).
[12] D. Cooke and B.L. Bennet, Journal of Luminescence 65, 83 (1996).
[13] A. Afanasev et al., (LIPSS Collaboration), Phys. Rev. Lett. 101, 120401 (2008).

*a*KWISP: investigating short-distance interactions at sub-micron scales

G. Cantatore[1], *V. Anastassopoulos*[2], *S. Cetin*[3], *H. Fischer*[4], *W. Funk*[5], *A Gardikiotis*[2], *D.H.H. Hoffmann*[6], *M. Karuza*[7,1], *Y.K. Semertzidis*[8], *D. Vitali*[9], *K. Zioutas*[2,5]

[1]University and INFN Trieste, Trieste, Italy
[2]University of Patras, Patras, Greece
[3]Bilgi University, Istanbul, Turkey
[4]University of Freiburg, Freiburg, Germany
[5]CERN, Geneva, Switzerland
[6]TU Darmstadt, Darmstadt, Germany
[7]University of Rijeka, Rijeka, Croatia
[8]CAPP, Daejeon, Korea
[9]University of Camerino, Camerino, Italy

DOI: http://dx.doi.org/10.3204/DESY-PROC-2017-02/cantatore_giovanni

The sub-micron range in the field of short distance interactions has yet to be opened to experimental investigation, and may well hold the key to understanding al least part of the dark matter puzzle. The *a*KWISP (*advanced*-KWISP) project introduces the novel Double Membrane Interaction Monitor (DMIM), a combined source-sensing device where interaction distances can be as short as 100 nm or even 10 nm, much below the $\approx 1-10$ μm distance which is the lower limit encountered by current experimental efforts. *a*KWISP builds on the technology and the results obtained with the KWISP opto-mechanical force sensor now searching at CAST for the direct coupling to matter of solar chameleons. It will reach the ultimate quantum-limited sensitivity by exploiting an array of technologies, including operation at milli-Kelvin temperatures. Recent suggestions point at short-distance interactions studies as intriguing possibilities for the detection of axions and of new physical phenomena.

1 Introduction

Sensitive measurements on interactions at short separation distances between macroscopic bodies provide a window on physics beyond the Standard Model. In this field of study, interest focuses on Casimir-type interactions, including the topological Casimir effect which might lead to the detection of axions [1], and on possible deviations from the standard gravitational interaction, modelled by a Yukawa-type potential representing the exchange of force carrier scalar particles [2, 3].These particles might be, for example, Dark Matter or Dark Energy candidates such as axions, moduli and chameleons, portals to extra-dimensions or dilatons. Each single one of these themes opens a view beyond the Standard Model.

A key parameter is the distance scale at which the interaction is probed. Current experimental efforts reach distances of the order of 1-10 μm [4] . Recently, even collider experiments

such ATLAS at LHC reported probing extra-dimensions down to a distance of 11 μm [5].

The original idea of *a*KWISP is building a novel opto-mechanical device consisting of two micro-membranes set a short distance apart, down to a few tens of nm. One of the two membranes (the "source" body) is excited in a controlled way by the radiation pressure of an amplitude-modulated laser beam. The displacements of the other membrane (the "sensing" body), possibly due to interactions with the source body, are then monitored by a Fabry-Perot interferometer at resonance with a second laser beam. Displacement sensitivities as low as 10^{-15} m/$\sqrt{\text{Hz}}$ can be reached at room temperature [6] thanks to the combination of two large quality factors, the finesse of the Fabry-Perot optical resonator ($\approx 10^5$) and the figure of merit of the membrane mechanical resonator ($\approx 10^5$).

*a*KWISP enters the short-distance interaction field with the novel Double Membrane Interaction Monitor (DMIM) concept where interaction distances can be as short as 10nmand plans to reach the ultimate quantum-limited sensitivity by achieving milli-Kelvin equivalent membrane temperatures with a combination of cryogenic and optical cooling [7].

Figure 1 shows an example of projected coverage by *a*KWISP in the parameter space of Yukawa-type corrections to the standard gravitational potential between two macroscopic bodies. α and λ represent the interaction strength and range, respectively. This coverage is obtained when operating *a*KWISP at a temperature of 3 mK with thermally limited sensitivity and 10^5 s integration time, corresponding to the detection of a force as feeble as 10^{-20} N.

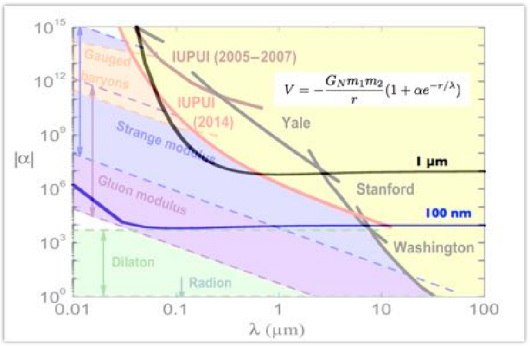

Figure 1: Projected *a*KWISP coverage in the parameter space of a Yukawa-type interaction between two macroscopic bodies. α and λ represent the interaction strength and range, respectively. The black curve refers to a 1 μm separation distance between the two DMIM membranes, while the blue curve refers to a 100 nm one (see also text). The background plot is taken from [4].

2 The *a*KWISP experimental setup

The *a*KWISP concept is based on the Double Membrane Interaction Monitor (DMIM) device. It consists of two thin (thickness $<$ 200 nm) and taut Si_3N_4 membranes set parallel to each other at a distance which can be as short as 10 nm. Typical membrane dimensions are $5 \cdot 5$ mm^2. One of the two membranes is coated with an Al layer in order to be able to excite its oscillations

in a controlled way by reflecting a laser beam off it, and in addition it has a 1 mm diameter hole at its center to allow free passage of a second laser beam which monitors the displacements of the second membrane. Both membranes have a 3 nm thick carbon conductive coating to allow setting them at a common electrical potential in order to reduce the effects of static charges. Figure 2 shows a sketch of the DMIM device we have invented for aKWISP. A prototype set of suitable membranes for a DMIM has already been produced by Norcada Inc., Canada, and will be tested in the INFN Trieste optics laboratory.

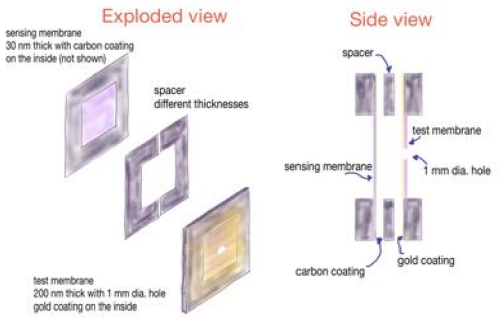

Figure 2: Sketch of the Double Membrane Interaction Monitor (DMIM) (see text).

In the aKWISP experimental apparatus, the DMIM is placed inside an optical Fabry-Perot interferometer kept at resonance, by means of an electro-optic active feedback [8], with a 1064 nm "sensing" laser beam. The Fabry-Perot is mounted inside a vacuum chamber to avoid noise due to the Brownian motion of air.

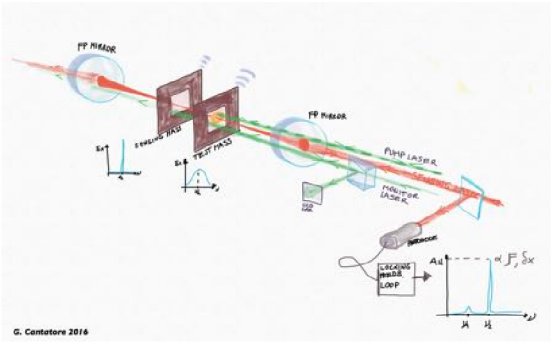

Figure 3: Conceptual schematic of a possible aKWISP experimental setup (see text).

Thanks to the hole in the source membrane, the sensing beam measures only the displacements of the sensing membrane: these modify the frequency of the standing optical wave resonating within the Fabry-Perot causing a detuning, which is then detected by the electro-optic feedback loop. This sensing scheme has already been demonstrated in [6] where a single-

membrane sensor has achieved a force sensitivity of $1.5 \cdot 10^{-14}$ N/$\sqrt{\text{Hz}}$ ($7.5 \cdot 10^{-16}$ m/$\sqrt{\text{Hz}}$ in terms of displacement) at room temperature. An opto-mechanical particle detector based on this principle, called KWISP, is now searching at CAST for the direct coupling to matter of solar chameleons [9]. A second laser beam ("pump" beam), operating at a different wavelength (532 nm in our case) where the mirrors of the Fabry-Perot resonator are practically transparent, is used to excite oscillations in the source membrane by reflecting it off the Al coating. The frequency and amplitude of these oscillations can be controlled by a suitable amplitude modulation impressed on the pump beam. Figure 3 shows a schematic sketch of a possible setup for *a*KWISP.

The ultimate sensitivity reachable with this class of opto-mechanical devices depends on temperature [10]. In order to reach equivalent temperatures in the milli-Kelvin range the DMIM could be inserted in the payload of a suitable cryostat/refrigerator and further cooled by means of optical cooling techniques [7].

3 Perspectives

Highly sensitive measurements on short-distance interactions may uncover a host of hitherto unobserved physical processes, opening a window beyond the Standard Model. Among these, axions, moduli and chameleon particles, as well as portals towards extra dimensions and perhaps dilatons, may play a role. Casimir-type forces are also an open field of study when interaction distances range below 1 μm. Recently, the "topological" Casimir effect, which has never been observed, has been proposed as a tool to search for axions [1]. The key parameter in all these investigations is the distance between the two interacting bodies, which must be less than 1 μm in order to open access to unexplored regions in parameter space (see Figure 1). The DMIM proposed here has the potential of lowering this distance to reach the 100 nm or perhaps even the 10 nm range. Using this device, the *advanced*-KWISP proposal presents a novel scheme to study sub-nuclear scale phenomena using a high sensitivity table-top opto-mechanical sensor based on precision technologies, such as micro-membranes and interferometric sensing coupled to cryogenic and optical cooling

References

[1] C.J. Cao and A. Zhitnitsky, Phys. Rev. D **96**, 015013 (2017).

[2] V.A. Kuz'min, I.I Tkachev, and M.E. Shaposhnikov, Pis'ma Zh. Eksp. Theor. Fiz. **36**, 2, 49-52 (1982).

[3] J.E. Moody and F. Wilczek, Phys. Rev. D **30**, 1 (1984).

[4] Y.-J. Chen *et al.*, Phys. Rev Lett. **116**, 221102 (2016).

[5] Private communication by C. is Clement, University of Stockholm, 2016; see also CERN PhD thesis from ATLAS group at `https://cds.cern.ch/record/2194414?ln=en`, page 192, and`arXiv:1604.07773`.

[6] M. Karuza, G. Cantatore, A. Gardikiotis, D.H.H. Hoffmann, Y.K. Semertzidis and K. Zioutas, Phys. Dark Univ. **12**, 100-104 (2016).

[7] M. Karuza *et al.*, New J. of Phys. **14**, 9, 095015 (2012).

[8] G. Cantatore *et al.*, Rev. Sc. Instr. **66**, 4, 2785-2787 (1995).

[9] S. Baum, G. Cantatore, D.H.H. Hoffmann, M. Karuza, Y.K. Semertzidis, A. Upadhye and K. Zioutas, Phys. Lett. B, **739**, 167-173 (2014); `http://cast.web.cern.ch/CAST/`; K. Zioutas, G. Cantatore and M. Karuza, "Cast: enlightening the dark", CERN Courier, Jan.-Feb. 2016, p. 29.

[10] S. Lamoreaux, `arXiv:0808.4000`.

Measurement of ^{144}Pr beta-spectrum with Si(Li) detectors for the purpose of determining the spectrum of electron antineutrinos.

A.V. Derbin[1], S. V. Bakhlanov[1], I. S. Drachnev[1], I. P. Filipov[1], E. V. Lukyanchenko[2], I. N. Machulin[2], V. N. Muratova[1], N. V. Pilipenko[1], D. A. Semenov[1], E. V. Unzhakov[1]

[1]NRC KI Petersburg Nuclear Physics Institute, 188300, Gatchina, Russia
[2]National Research Centre Kurchatov Institute, 123182 Moscow, Russia

DOI: http://dx.doi.org/10.3204/DESY-PROC-2017-02/derbin_alexander

Here we present the specifications of the newly developed beta-spectrometer based on thick full absorption Si(Li) detector. The spectrometer can be used for precision measurements of various beta-spectra, namely for the beta-spectrum shape study of ^{144}Pr, which is considered to be the most promising anti-neutrino source for sterile neutrino searches.

1 Introduction

Precision measurements of beta-spectra have always been and are still playing an important role in several fundamental physical problems, predominantly in neutrino physics. It was the continuous shape of beta-decay spectrum, that has driven W. Pauli towards the neutrino hypothesis. The initial beta-spectrum measurements for the purpose of determining the neutrino mass were carried out by G. Hanna and B. Pontecorvo [1] via gas counter that registered electrons produced by decays of tritium added into the detector volume.

Magnetic and electrostatic spectrometers possess the superior energy resolution, but at the same time such devices appear to be very complex and large-scale instalments. Since the electron free path at 3 MeV (which is, basically, the maximum beta-transition energy for long-living isotopes) does not exceed 2 g/cm^3, solid state scintillation and ionization detectors were effectively employed for detection of electrons [2, 3]. The main drawback of solid state scintillators is their relatively poor energy resolution, which stands at approximately 10% at 1 MeV. In case of semiconductor detectors there is a significant probability of back-scattering from the detector surface that depends on the detector material. The most widespread silicon-based semiconductors have the backscattering probability of the order of 10% for 100 keV electrons at normal incidence [4]. In case of electron energies above 1 MeV and high Z detector materials, it also becomes important to take the bremsstrahlung into account.

The considered Si(Li) spectrometer was developed for precision measurement of ^{144}Ce-^{144}Pr beta-spectrum in order to determine the antineutrino energy spectrum. The ^{144}Ce-^{144}Pr antineutrino source will be used for experimental sterile neutrino searches by Borexino SOX collaboration [5].

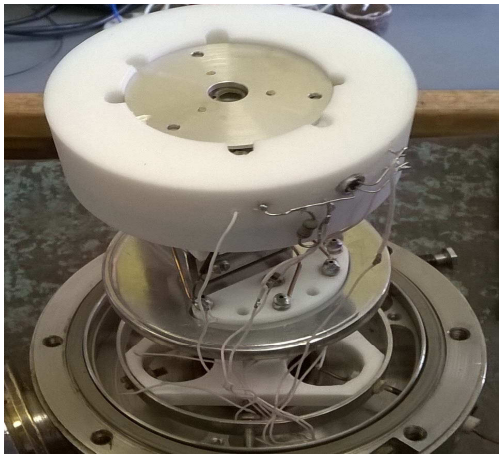

Figure 1: The photo of the beta-spectrometer with the full-absorption Si(Li) detector.

2 Experimental setup

The photo of the experimental setup based on full absorption Si(Li) detector is shown in Fig.1. The sensitive region of the Si(Li) detector fabricated at NRC KI PNPI has a diameter about 15 mm and a thickness of 6.5 mm. These dimensions ensure effective absorption of electrons with energies up to 3 MeV. The detector was equipped with an tungsten collimator with a diameter of 14 mm and a thickness of 2 mm. The negative bias voltage of 1 kV was applied directly to the gold coating of the detector. The energy resolution determined for 59.6 keV gamma-line of ^{241}Am turned out to be FWHM = 900 eV.

The entire setup was placed inside the vacuum cryostat and cooled down to the liquid nitrogen temperature. The detector was equipped with charge-sensitive preamplifier with resistive feedback and cooled field-effect transistor. As noted above, the spectrometer was designed with intent of measuring the beta-spectrum of ^{144}Pr in the energy range of $(0-3)$ MeV. In order to perform measurements in such a broad dynamic range, the Si(Li) detector was equipped with two separate spectrometric channels, each with spectrometric amplifier and 14-bit analogue-to-digital converter set up as a standalone module. Channel settings were adjusted to register events within $(0.01-0.5)$ MeV and $(0.05-6.0)$ MeV energy intervals. The choice of the upper energy limit at 6 MeV was conditioned by our intention to monitor the possible alpha-activity of the sample under investigation. A dedicated DAQ control software allows one to acquire and record two 16000-channel spectra from the Si(Li) detector.

3 Results

In order to determine the main characteristics of the spectrometer we used a ^{207}Bi source, providing gamma-rays, X-rays and conversion and Auger electrons. The ^{207}Bi spectrum, measured with the Si(Li) detector, is shown in Fig.2 for the intervals $(0.01-2.0)$ MeV and $(450-580)$ keV, respectively. The ^{207}Bi source with an activity of 10^4 Bq was placed inside the vacuum cryostat at a distance of 14 mm from the Si(Li) detector surface. Three of the most intense ^{207}Bi

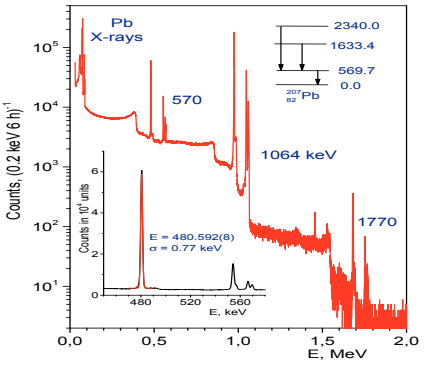

Figure 2: The spectrum of ^{207}Bi source measured with the Si(Li) detector in energy range of $(0.01-2.0)$ MeV. The inset shows the electron peaks corresponding to internal conversion from K-, L-, M-shells of the 570 keV nuclear level.

gamma-lines have energies of 569.7 keV, 1063.7 keV and 1770.2 keV and are emitted with probabilities of 0.977, 0.745 and 0.069 per single ^{207}Bi decay, respectively. The corresponding peaks of conversion electrons form K-, L- and M-shells are clearly visible in the spectrum in Fig.2. The electron energy resolution determined via 480 keV line is FWHM = 1.8 keV.

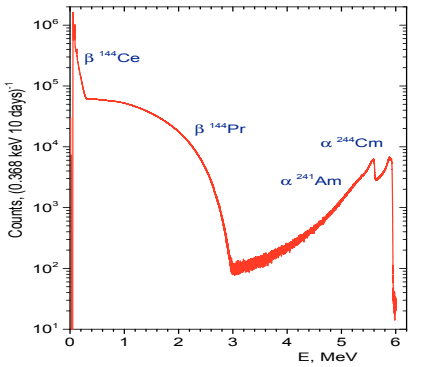

Figure 3: The spectrum of ^{144}Ce-^{144}Pr measured with the Si(Li) detector.

The low-energy part of the spectrum was used to evaluate the thickness of non-sensitive layer on the surface of Si(Li) detector. This area contains a set of peaks corresponding to Pb X-rays from K- and L-series and Auger electrons. The observed position of 56.94 keV Auger peak ($e_{KL_1L_2}$) appeared to be 56.22 keV. Inclusive of the golden coating thickness of (500 A°), the measured 59 keV electron energy loss of 720 eV corresponds to 4700 A° of non-sensitive

layer.

The energy spectrum of the ^{144}Ce-^{144}Pr source, measured with the Si(Li) detector during 10 days, is shown in Fig.3. The total spectrum contains gamma- and electron peaks. The spectrum contains characteristic X-ray lines of Np at 13.9 keV, 17.8 keV and 20.8 keV, produced by trace amounts of alpha-decaying ^{241}Am contained in the ^{144}Ce source. The peaks at 59.6 keV, 80.1 keV and 133.5 keV are related to the gamma-transitions of ^{237}Np and ^{144}Pr nuclei. The most intense peaks at 35.8 keV and 41 keV correspond to K_{α_1,α_2}- and K_β-lines of Pr X-rays. The spectrum of electrons from beta-decay of ^{144}Ce$-^{144}$Pr consists of also conversion and Auger electrons from 133.5 keV gamma-transition. After the main measurements were completed the thin silicon detector was mounted and γ- and X-rays activity was measured by Si(Li)-detector in anticoincidence with thin Si-detector. Inclusion of this spectrum into the analysis allows us to account for overall gamma- and X-ray contribution.

The differential energy spectrum of electrons in $\beta-$decay is discribed as

$$N(W)dW \sim pW(W-W_0)^2 H(W)F(Z,W)L_0(Z,W)C_{A,V}(Z,W)S(Z,W)G(Z,W)B(W), \quad (1)$$

where W and p are total energy and momentum of electron and $F(W,Z)$ is Fermi function, Additionally the following correction factors have to be taken into account: finite size of the nucleus correction for electromagnetic $L_0(Z,W)$ and weak $C_{A,V}(Z,W)$ interaction; screening corrections of the nuclear charge by electrons $S(Z,W)$; radiative corrections $G(Z,W)$ and weak magnetism correction $B(W)$. The antineutrino spectrum can be calculated after the parameters of shape factor $H(W)$ will be extracted from the analysis of experimental spectrum.

4 Conclusion

The beta-spectrometer with of 6.5 mm thick Si(Li)-detector has been developed. The spectrometer can be used for precision measurements of the beta-spectrum shapes of various radioactive nuclei, in particular to measure the beta-spectra of ^{144}Pr, which is the most promising antineutrino source for searching for neutrino oscillations to a sterile state.

5 Acknowledgments

This work was supported by the Russian Science Foundation (grant 17-12-01009) and in part by the Russian Foundation of Basic Research (grants 17-02-00305A, 16-29-13014ofi-m and 15-02-02117A)

References

[1] G. C. Hanna and B. Pontecorvo. The β-spectrum of H^3. *Phys. Rev.*, 75, 983 (1949)

[2] J. J. Simpson. Evidence of heavy-neutrino emission in beta decay. *Phys. Rev. Lett.*, 54, 1891 (1985)

[3] A. V Derbin, A. I. Egorov, V. N. Muratova, et al. Search for 17 kev neutrinos in ^{63}Ni beta-decay. *JETP Lett.*, 58, 3 (1993)

[4] A. V. Derbin, A. I. Egorov, S. V. Bakhlanov, and V. N. Muratova. Measurement of the ^{45}Ca β spectrum in search of deviations from the theoretical shape. *JETP Lett.*, 66, 81 (1997)

[5] G. Bellini et al. SOX: Short distance neutrino oscillations with Borexino. *JHEP*, 2013(8), 38 (2013)

Search for hidden-photon Dark Matter with FUNK

R. Engel[1]*, *D. Veberič*[1], *C. Schäfer*[1], *A. Andrianavalomahefa*[1], *K. Daumiller*[1], *B. Döbrich*[2], *J. Jaeckel*[3], *M. Kowalski*[4,5], *A. Lindner*[4], *H.-J. Mathes*[1], *J. Redondo*[6], *M. Roth*[1], *T. Schwetz-Mangold*[1], *and R. Ulrich*[1]

[1]Institute for Nuclear Physics, Karlsruhe Institute of Technology (KIT), Germany
[2]Physics Department, CERN, Geneva, Switzerland
[3]Institute for Theoretical Physics, Heidelberg University, Germany
[4]Deutsches Elektronen Synchrotron DESY, Hamburg, Germany
[5]Department of Physics, Humboldt University, Berlin, Germany
[6]Department of Theoretical Physics, University of Zaragoza, Spain

DOI: http://dx.doi.org/10.3204/DESY-PROC-2017-02/engel_ralph

It has been proposed that an additional U(1) sector of hidden photons could account for the Dark Matter observed in the Universe. When passing through an interface of materials with different dielectric properties, hidden photons can give rise to photons whose wavelengths are related to the mass of the hidden photons. In this contribution we report on measurements covering the visible and near-UV spectrum that were done with a large, 14 m^2 spherical metallic mirror and discuss future dark-matter searches in the eV and sub-eV range by application of different electromagnetic radiation detectors.

For the introduction to the hidden-photon physics and related extension of the Standard Model see [1, 2]. For results of a similar experiment, although with a smaller mirror see [3, 4].

1 Experimental setup

For this experiment a mirror composed of 36 segments is used. For more details on the setup see [5, 6]. The experiment is set-up in a light-tight window-less room with concrete walls of at least 2 m thickness. The inner area (see Fig. 1), encompassing the camera and the mirror, is additionally light insulated with a thick black curtain and a 120 µm layer of opaque polyethylene foil.

As the light detector a 29 mm diameter photomultiplier (PMT) ET 9107BQ with very low dark-current properties was chosen. The PMT has a blue-green sensitive bialkali photocathode with the quantum efficiency extended into the ultra-violet range with the peak quantum efficiency of around 28% and excellent single electron and pulse-height resolution, suitable for the photon counting. The PMT camera is placed on a motorized linear-stage that can drive it (perpendicularly to the mirror axis) in and out of the center of the spherical mirror. The PMT front is additionally equipped with a motorized shutter that can obscure the entrance of photons.

*ralph.engel@kit.edu

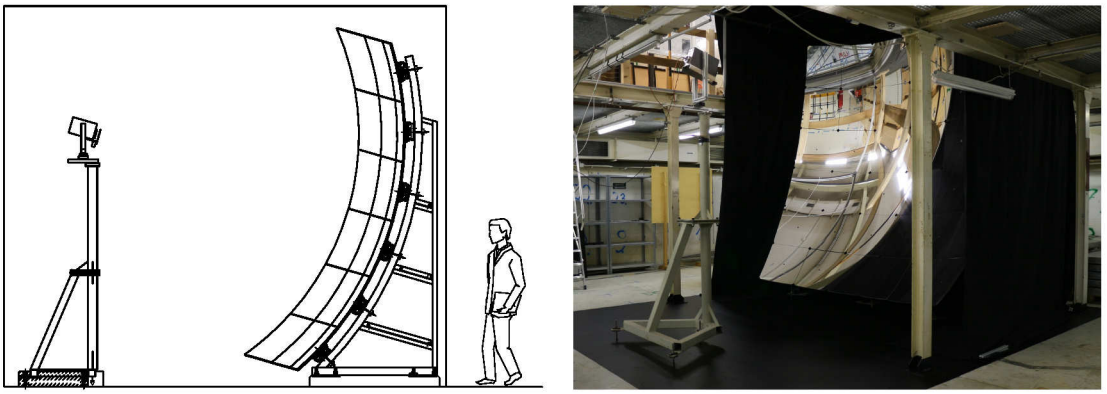

Figure 1: Schematic (left) and photo (right) of the experimental setup.

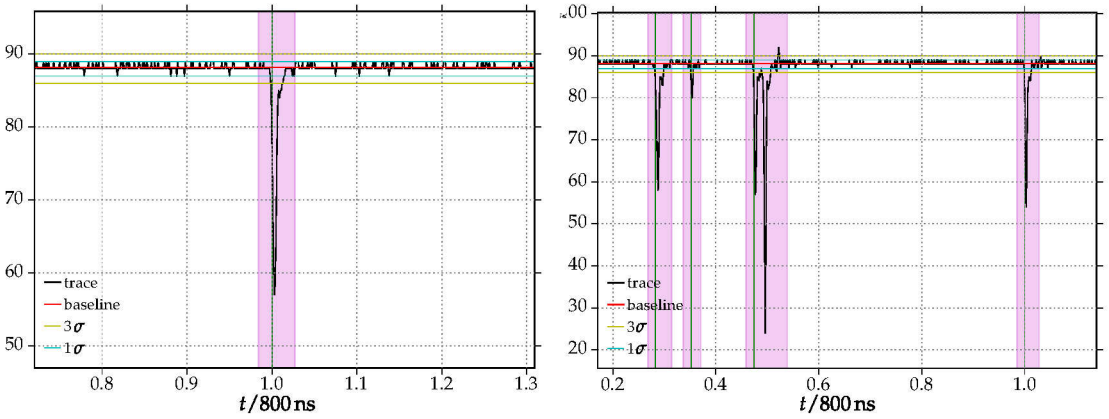

Figure 2: Typical examples of captured traces with single pulse (left) and many pulses within a short time span (right).

Signals from the PMT were digitized with the PicoScope 6404D digital oscilloscope. In Fig. 2 two examples of triggered traces are given. A single-photon (SP) pulse can be observed on the left and a trace containing several pulses in the 1.6 µs trigger window is shown on the right. Traces with multiple pulses were discarded since they can be produced only by cosmic-ray showers. Based on measurements of the SP charge spectrum with an LED flasher, Fig. 3-left, a cut on the allowed range of observed charges was also applied, as seen in Fig. 3-right. The efficiency of the latter cut on SP traces is estimated to be 75%.

2 Preliminary limit on mixing parameter

The selected photon counts for a 30-day run performed in February and March 2017 can be seen in Fig. 4-left. The data was taken in cycles of four 60 s measurements performed in all four possible combinations of the two positions of the PMT camera (*in* and 8 cm *out* of the center), and the two positions of the shutter (*open* and *close*), as schematically shown in Fig. 4-right.

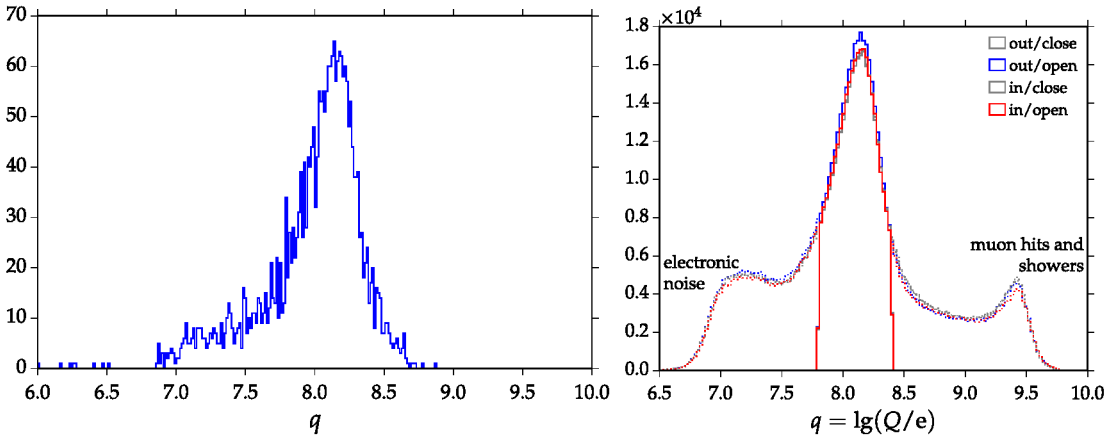

Figure 3: *Left:* Charge distribution for a flasher run with very low power setting and, therefore, composed mostly by single photo-electrons. *Right:* Charge distribution observed in one of the measurement runs. Note that in both cases $q = \lg(Q/\mathrm{e})$ where Q is the charge of a pulse.

The average rate of the whole run is $R = 0.535\,\mathrm{Hz}$ and the relative differences ΔR in the four different configurations are shown in Fig. 4-right.

The difference of the count rates between *open* and *close* for the PMT being *in* the radius point is proxy for the dark-matter signal. With the shutter *open* there are $\Delta R = 0.0032 \pm 0.0014\,\mathrm{Hz}$ more counts registered than with *closed*. Ignoring for a moment any possible systematic effects, we obtain the limit shown in Fig. 5 denoted with *FUNK sensitivity*. To determine possible systematic uncertainties that might be related to temperature changes or the limited accuracy of the measurement time, we also compare the rates with the *closed* PMT *in* and *out* of the radius point. The two count rates agree within the statistical uncertainty ($\Delta R = 0.0007 \pm 0.0014\,\mathrm{Hz}$). Nevertheless, the comparison of the count rates for the *open* PMT *in* and *out* of the radius point we found significantly larger count rate for the PMT *open* and *out* of the radius point, possibly related to the different imaging properties of the setup in the two positions. Additional measurements are in progress to better understand this systematic behavior. For now we treat this difference ($\Delta R \approx 0.025\,\mathrm{Hz}$) as an upper limit of the overall systematic uncertainty of the measurement and use it to derive a preliminary upper limit [1] on the magnitude of the mixing parameter χ in the sensitivity range of the PMT, see the line denoted *FUNK preliminary (sys)* in Fig. 5.

Summary. No significant signal was found. The detailed analysis of the data is still ongoing, thus here we are reporting only preliminary results with a maximally conservative estimate of possible systematic uncertainties.

Future plans. We are planning further searches for possible hidden-photon dark matter with measurements extended into the MHz, GHz, and THz range.

Acknowledgments. We gratefully acknowledge partial support from the Helmholtz Alliance for Astroparticle physics (HAP), funded by the Initiative and Networking Fund of the Helmholtz Association.

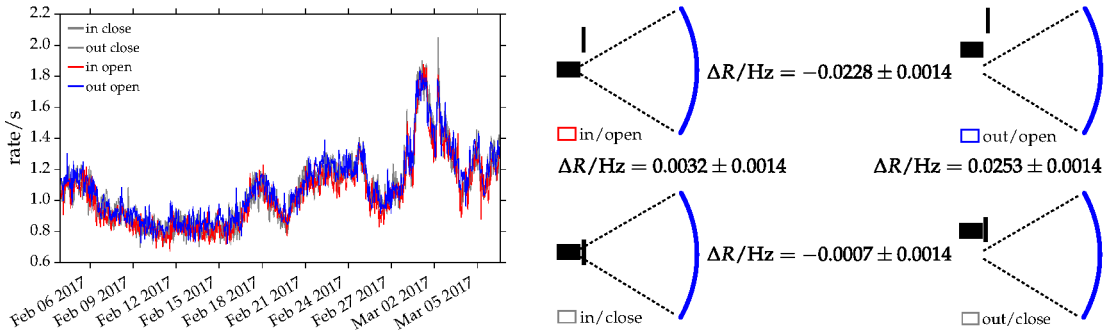

Figure 4: *Left:* observed pulse rate in one of the measurement runs. *Right:* A measurement is composed of many event cycles, where in each cycle four different 60-second measurements are performed. The schematic show these four different combinations obtained with open/closed shutter and with camera in/out.

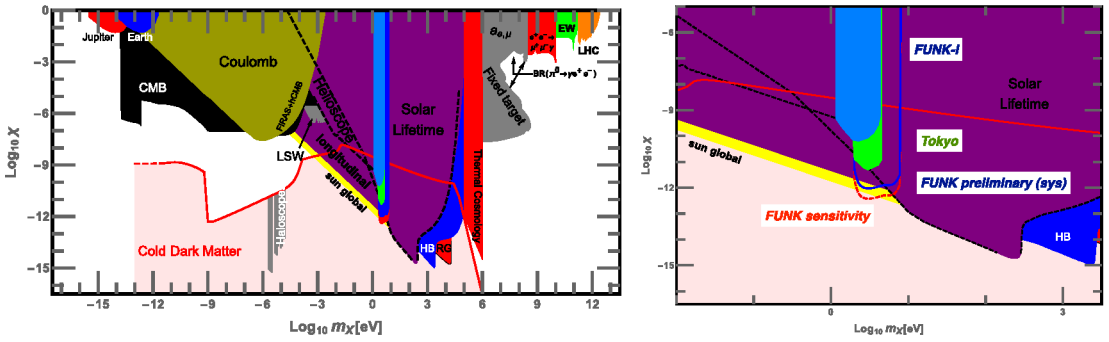

Figure 5: Preliminary limits on the mixing parameter χ derived from systematic dominated (blue) and statistics dominated (red) assumptions. The right figure is an enlargement of the right plot around the dark-matter mass window corresponding to the optical emission of the visible photons. The previous result obtained with a CCD camera [5] is also shown (light-blue).

References

[1] B. Döbrich *et al.*, "Hidden Photon Dark Matter Search with a Large Metallic Mirror," Proc. 10th Patras Workshop 2014, Geneva, Switzerland, [arXiv:1410.0200].

[2] B. Döbrich *et al.*, "The FUNK search for Hidden Photon Dark Matter in the eV range," Proc. Photon 2015 Conf., Novosibirsk, Russia, [arXiv:1510.05869].

[3] J. Suzuki, T. Horie, Y. Inoue, and M. Minowa, "Experimental Search for Hidden Photon CDM in the eV mass range with a dish antenna," JCAP **09**, 042 (2015), [arXiv:1504.00118].

[4] J. Suzuki, Y. Inoue, T. Horie, and M. Minowa, "Hidden photon CDM search at Tokyo," Proc. 11th Patras Workshop 2015, Zaragoza, Spain, [arXiv:1509.00785].

[5] D. Veberič *et al.*, "Search for dark matter in the hidden-photon sector with a large spherical mirror," Proc. 34th Int. Cosmic Ray Conf. 2015, The Hague, The Netherlands, PoS **ICRC2015**, 1191 (2016) [arXiv:1509.02386].

[6] D. Veberič *et al.*, "Search for hidden-photon dark matter with the FUNK experiment," Proc. 35th Int. Cosmic Ray Conf. 2017, Busan, Korea, PoS **ICRC2017**, 880 (2017).

Phenomenology of Majorons

Julian Heeck

Service de Physique Théorique, Université Libre de Bruxelles, CP225, 1050 Brussels, Belgium

DOI: http://dx.doi.org/10.3204/DESY-PROC-2017-02/heeck_julian

Majorons are the Goldstone bosons associated to lepton number and thus closely connected to Majorana neutrino masses. Couplings to charged fermions arise at one-loop level, including lepton-flavor-violating ones that lead to decays $\ell \to \ell' J$, whereas a coupling to photons is generated at two loops. The typically small couplings make massive majorons a prime candidate for long-lived dark matter. Its signature decay into two mono-energetic neutrinos is potentially detectable for majoron masses above MeV.

1 Majoron couplings

The difference between baryon number B and lepton number L is an anomaly-free global symmetry of the Standard Model (SM); spontaneously breaking this $U(1)_{B-L}$ symmetry results in a Goldstone boson called majoron [1, 2]. In the simplest realization, this majoron J resides in a singlet complex scalar $\sigma = (f + \sigma^0 + iJ)/\sqrt{2}$ that carries $B - L$ charge 2, f being the $B - L$ breaking scale and σ^0 the heavy CP-even majoron partner. Further introducing three right-handed neutrinos N_R, the Lagrangian reads

$$\mathcal{L} = \mathcal{L}_{\rm SM} + i\overline{N}_R\gamma^\mu\partial_\mu N_R + (\partial_\mu\sigma)^\dagger(\partial^\mu\sigma) - V(\sigma) - \left(\overline{L}yN_RH + \tfrac{1}{2}\overline{N}^c_R\lambda N_R\sigma + \text{h.c.}\right), \quad (1)$$

with the SM lepton (scalar) doublet L (H). We suppressed flavor indices and the details of the scalar potential $V(\sigma)$. $SU(2)_L \times U(1)_Y \times U(1)_{B-L}$ symmetry breaking then yields the famous seesaw neutrino mass matrix $M_\nu \simeq -m_D M_R^{-1} m_D^T$ with $m_D = yv/\sqrt{2}$ and $M_R = \lambda f/\sqrt{2} \gg m_D$.

Many of the parameters encoded in M_ν have been measured already: the mass splittings and mixing angles. However, even if we could measure all elements of M_ν, we would still not be able to reconstruct the underlying seesaw parameters m_D and M_R. As shown in Ref. [3], one can map the parameters $\{m_D, M_R\}$ bijectively onto $\{M_\nu, m_D m_D^\dagger\}$, implying that $m_D m_D^\dagger$ contains precisely those nine seesaw parameters that cannot be determined by measurements of neutrino masses and oscillations. As we will see below, this is a convenient parametrization for the phenomenology of majorons, which endow $m_D m_D^\dagger$ with physical meaning.

The tree-level couplings of the majoron J can easily be derived from Eq. (1), which in particular include the couplings $J\overline{\nu}_j i\gamma_5 \nu_j m_j/(2f)$ to the light neutrino mass eigenstates ν_j. With f at the seesaw scale and active neutrino masses m_j below eV, this coupling is incredibly tiny. At one-loop level [1, 4, 5], the majoron also obtains couplings to charged leptons ℓ and

quarks q, parametrized as $iJ\bar{f}_1(g^S_{Jf_1f_2} + g^P_{Jf_1f_2}\gamma_5)f_2$ with coefficients

$$g^P_{Jqq'} \simeq \frac{m_q}{8\pi^2 v}\delta_{qq'}T_3^q \,\mathrm{tr}K\,, \qquad g^S_{Jqq'} = 0\,, \tag{2}$$

$$g^P_{J\ell\ell'} \simeq \frac{m_\ell + m_{\ell'}}{16\pi^2 v}\left(\delta_{\ell\ell'}T_3^\ell \,\mathrm{tr}K + K_{\ell\ell'}\right), \qquad g^S_{J\ell\ell'} \simeq \frac{m_{\ell'} - m_\ell}{16\pi^2 v}K_{\ell\ell'}\,, \tag{3}$$

where $T_3^{d,\ell} = -T_3^u = -1/2$ and we introduced the dimensionless hermitian coupling matrix $K \equiv m_D m_D^\dagger/(vf)$. The majoron couplings to charged fermions are hence determined by the seesaw parameters $m_D m_D^\dagger$, which are *independent* of the neutrino masses and can in particular be much bigger than the naive one-generation expectation $M_\nu M_R$. Perturbativity sets an upper bound on K of order $4\pi v/f$, and since K is furthermore positive definite we have the inequalities $|K_{\ell\ell'}| \leq \sqrt{K_{\ell\ell}K_{\ell'\ell'}} \leq \mathrm{tr}K$. These fermion couplings are obviously crucial for majoron phenomenology and in principle even offer a new avenue to reconstruct the seesaw parameters. Note in particular the off-diagonal lepton couplings, which will lead to lepton flavor violation [4, 5] (Sec. 3).

There is one more coupling of interest, that to photons. For a massless majoron, the coupling $JF\tilde{F}$ vanishes because $B-L$ is anomaly free [4]; otherwise, it is induced at two-loop level and non-trivial to calculate. Considering only a gauge-invariant subset of diagrams, we can however obtain the simple expression [5]

$$\Gamma(J\to\gamma\gamma) \simeq \frac{\alpha^2\left(\mathrm{tr}K\right)^2}{4096\pi^7}\frac{m_J^3}{v^2}\left|\sum_f N_c^f T_3^f Q_f^2\, g\left(\frac{m_J^2}{4m_f^2}\right)\right|^2, \tag{4}$$

where the sum is over all SM fermions f with color multiplicity N_c^f, isospin T_3^f, and electric charge Q_f. The loop function is given by $g(x) \equiv -(\log[1-2x+2\sqrt{x(x-1)}])^2/(4x)$.

2 Majoron dark matter

With the relevant majoron couplings at our disposal, we can start to discuss phenomenology. First off, we are going to study the case of the majoron as a dark matter (DM) candidate. This is motivated by the fact that it generically has tiny couplings to the SM, ensuring that it is dark and stable enough to form DM [6, 7]. A prerequisite here is an explicit $U(1)_{B-L}$ breaking in the Lagrangian to generate a majoron mass m_J, making J a *pseudo*-Goldstone boson. This could simply be an explicit mass term in the scalar potential, a gravity-generated higher-dimensional operator or an axion-like anomaly-induced potential. Furthermore, a production mechanism is required to generate the observed abundance in the early Universe. With small couplings, the obvious mechanism to use here is *freeze-in*, e.g. from the coupling to the Higgs or the right-handed neutrinos [8]. For majoron masses as low as keV one has to be careful not to violate structure-formation constraints from the Lyman-α forest. In these cases, different production mechanisms are required that make J cold enough, which can naturally be found in inverse-seesaw majoron models [9, 10]. Here we will focus on DM masses above MeV for simplicity.

Assuming a massive singlet majoron to make up all of DM, the main signature then comes from its eventual decay into SM particles. As discussed above, the only decay channel at tree level is into neutrino mass eigenstates, $J \to \nu_j\nu_j$, with coupling m_j/f. These neutrinos will not oscillate, so the flavor content of the monochromatic neutrino flux follows simply from the

mass eigenstates [5]. For normal hierarchy, this implies only a small ν_e component of the flux, because the heaviest neutrino only has a tiny θ_{13}-suppressed electron component; for inverted hierarchy, the majoron decays into the two heaviest neutrinos, which results in roughly 50% electron flavor in the flux; in the quasi-degenerate regime, all flavors are equally probable.

Knowing the flavor composition of $J \to \nu\nu$ allows us to search for these neutrino lines with neutrino detectors. Borexino and KamLAND use inverse beta decay $\overline{\nu}_e p \to n e^+$ to reconstruct the neutrino energy with good accuracy. Due to the kinematic threshold of this process it is not possible to detect neutrino lines below $m_J \sim$ MeV. Above MeV, on the other hand, these experiments could indeed be sensitive to a dark-matter induced neutrino flux [5] (see Fig. 1). For higher masses, Super-K becomes most sensitive and can also utilize the ν_μ component of the flux [11]. For sub-MeV masses, limits on $J \to \nu\nu$ can still be derived from cosmology [12], but are of course less of a smoking-gun signature for majoron DM.

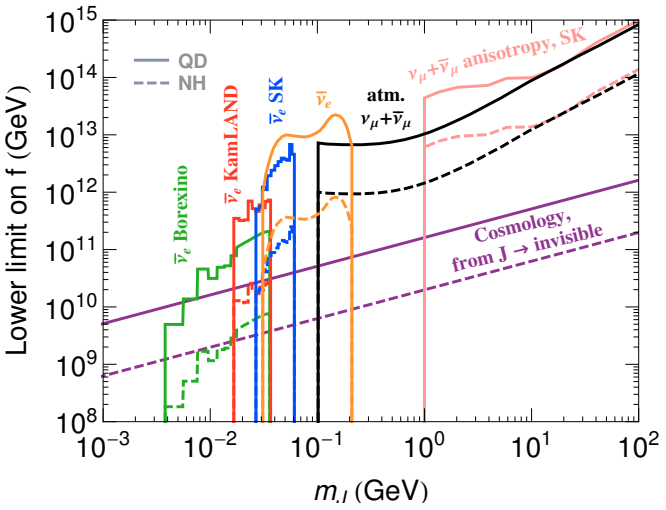

Figure 1: Lower limit on the $B - L$ breaking scale f from DM decay $J \to \nu\nu$, assuming a quasi-degenerate (solid) or normal-hierarchy neutrino spectrum (dashed) [5].

Majoron DM can thus be used to motivate neutrino line searches all the way down to MeV energies, far below what is typically considered. A natural question to ask here is whether observable neutrino fluxes are compatible with limits from visible DM decay channels, which are far more constrained. As shown above, the decays $J \to \ell\bar{\ell}', q\bar{q}, \gamma\gamma$ are indeed all unavoidably induced at loop level in the singlet majoron model. However, they all depend on parameters that are independent of the $J \to \nu\nu$ channel, making it impossible to directly compare these channels. In other words, the DM decay into visible channels probes different parameters than $J \to \nu\nu$, making them *complementary*. In the $m_J =$ MeV–100 GeV region, one can indeed obtain strong constraints on the K matrix elements from the visible channels, without invalidating our conclusion about neutrino lines [5]. For sub-MeV majoron masses, only the decay $J \to \gamma\gamma$ remains as a promising indirect detection signature [7, 13].

3 Lepton flavor violation

Going back to the majoron couplings to fermions of Eq. (3) shows that the quark couplings are diagonal at one-loop level, whereas the lepton couplings are not. Due to the rather strong lepton mass hierarchy, $m_\ell \gg m_{\ell'}$, the off-diagonal couplings can be approximately written as $-\frac{i m_\ell}{8\pi^2 v} K_{\ell\ell'} J \bar{\ell} P_L \ell' +$ h.c., which can induce the lepton-flavor-violating two-body decays $\ell \to \ell' J$ [4, 5]. If the majoron is massless or decays invisibly, the only signature of this decay is the

mono-energetic ℓ', which has to be searched for on top of the continuous energy spectrum from the SM decay channel $\ell \to \ell' \nu_\ell \overline{\nu}_{\ell'}$. Current limits translate into $|K_{\mu e}| \lesssim 10^{-5}$, $|K_{\tau \ell}| \lesssim \mathcal{O}(10^{-3})$, with good prospects for improvement at Mu3e and Belle [14, 15]. Channels with more tagging potential, such as $\ell \to \ell' J\gamma$ or $\ell \to \ell'(J \to \text{visible})$, are also promising and currently under investigation. We stress that lepton flavor violation with majorons depends on a different combination of seesaw parameters than the more commonly studied heavy-neutrino induced $\ell \to \ell'\gamma$. These channels are therefore complementary and should both be investigated.

4 Conclusion

The singlet majoron model inherits some nice properties from the seesaw Lagrangian, namely small Majorana neutrino masses and leptogenesis, while providing a new phenomenological handle. The majoron couplings to charged particles are precisely given by the seesaw parameters that are impossible to determine from the neutrino mass matrix, which could in principle allow us to reconstruct the seesaw with low-energy measurements. Since the couplings can be tiny without fine-tuning, a massive majoron makes for a promising unstable dark matter candidate, with signature decay into mono-energetic neutrinos, potentially detectable for energies above MeV. With few new parameters, which are furthermore linked to the seesaw mechanism, majoron models are simple extensions of the Standard Model that still provide rich phenomenology.

Acknowledgments

JH is a postdoctoral researcher of the F.R.S.-FNRS and thanks the PATRAS organizers for an interesting conference and Camilo Garcia-Cely for a fruitful collaboration.

References

[1] Y. Chikashige, R. N. Mohapatra and R. D. Peccei, Phys. Lett. **98B**, 265 (1981).

[2] J. Schechter and J. W. F. Valle, Phys. Rev. D **25**, 774 (1982).

[3] S. Davidson and A. Ibarra, JHEP **0109**, 013 (2001) [hep-ph/0104076].

[4] A. Pilaftsis, Phys. Rev. D **49**, 2398 (1994) [hep-ph/9308258].

[5] C. Garcia-Cely and J. Heeck, JHEP **1705**, 102 (2017) [arXiv:1701.07209 [hep-ph]].

[6] I. Z. Rothstein, K. S. Babu and D. Seckel, Nucl. Phys. B **403**, 725 (1993) [hep-ph/9301213].

[7] V. Berezinsky and J. W. F. Valle, Phys. Lett. B **318**, 360 (1993) [hep-ph/9309214].

[8] M. Frigerio, T. Hambye and E. Masso, Phys. Rev. X **1**, 021026 (2011) [arXiv:1107.4564 [hep-ph]].

[9] J. Heeck and D. Teresi, Phys. Rev. D **96**, 035018 (2017) [arXiv:1706.09909 [hep-ph]].

[10] S. Boulebnane, J. Heeck, A. Nguyen and D. Teresi, arXiv:1709.07283 [hep-ph].

[11] S. Palomares-Ruiz, Phys. Lett. B **665**, 50 (2008) [arXiv:0712.1937 [astro-ph]].

[12] V. Poulin, P. D. Serpico and J. Lesgourgues, JCAP **1608**, 036 (2016) [arXiv:1606.02073 [astro-ph.CO]].

[13] F. Bazzocchi, M. Lattanzi, S. Riemer-Sørensen and J. W. F. Valle, JCAP **0808**, 013 (2008) [arXiv:0805.2372 [astro-ph]].

[14] J. Heeck, Phys. Lett. B **758**, 101 (2016) [arXiv:1602.03810 [hep-ph]].

[15] T. Yoshinobu *et al.* [Belle Collaboration], Nucl. Part. Phys. Proc. **287-288**, 218 (2017).

't Hooft mechanism, anomalous gauge U(1), and "invisible" axion from string

Jihn E. Kim

Center for Axion and Precision Physics (IBS), 291 Daehakro, Daejeon 34141, and
Department of Physics, Kyung Hee University, 26 Gyungheedaero, Seoul 02447, Korea.

DOI: http://dx.doi.org/10.3204/DESY-PROC-2017-02/kim_jihn

Among solutions of the strong CP problem, the "invisible" axion in the narrow axion window is argued to be the remaining possibility among natural solutions on the smallness of $\bar{\theta}$. Related to the gravity spoil of global symmetries, some prospective "invisible" axions from theory point of view are discussed. In all these discussions including the observational possibility and cosmological constraints, a safe domain wall solution must be included.

1 The 't Hooft mechanism

In the bosonic collective motion in the Universe [1], so far the "invisible" QCD axion [2] seems the mostly scrutinized one because it can also provide cold dark matter (CDM) in the Universe. It is a pseudo-Goldstone boson arising from spontaneous breaking of a global symmetry [3]. In deriving a global symmetry in the process of spontaneous symmetry breaking, realizing the 't Hooft mechanism is crucial [4], which is stated as, *"If both a gauge symmetry and a global symmetry are broken by the vacuum expectation value (VEV) of a complex scalar field, then the gauge symmetry is broken and one global symmetry remains unbroken."*

Let us consider two phase field directions: one is the phase of a gauge $U(1)_1$ and the other is the phase of a global $U(1)_2$ with two corresponding symmetry generators $Q_{\rm gauge}$ and $Q_{\rm global}$. The proof of the 't Hooft mechanism is a very simple and elementary. It is obvious that the gauge symmetry is broken because the corresponding gauge boson obtains mass. Namely, only one phase or pseudoscalar is absorbed to the gauge boson, and there remains one continuous direction corresponding to the remaining continuous parameter. To see this clearly, let us introduce a field ϕ on which charges $Q_{\rm gauge}$ and $Q_{\rm global}$ act. The gauge transformation parameter is a local $\alpha(x)$ and the global transformation parameter is a constant β. Transformations are

$$\phi \to e^{i\alpha(x)Q_{\rm gauge}} e^{i\beta Q_{\rm global}} \phi, \tag{1}$$

which can be rewritten as

$$\phi \to e^{i(\alpha(x)+\beta)Q_{\rm gauge}} e^{i\beta(Q_{\rm global}-Q_{\rm gauge})} \phi. \tag{2}$$

Redefining the local direction as $\alpha'(x) = \alpha(x) + \beta$, we obtain the transformation

$$\phi \to e^{i\alpha'(x)Q_{\rm gauge}} e^{i\beta(Q_{\rm global}-Q_{\rm gauge})} \phi. \tag{3}$$

So, the $\alpha'(x)$ direction becomes the longitudinal mode of heavy gauge boson. Now, the charge $Q_{\rm global} - Q_{\rm gauge}$ is reinterpreted as the new global charge and is not broken by the VEV, $\langle\phi\rangle$, because out of two continuous directions one should remain unbroken. Basically the direction β remains as the unbroken continuous direction.

2 The domain wall problem in "invisible" axion models

It is well-known that if a discrete symmetry is spontaneously broken then there results domain walls in the course of the Universe evolution. For the "invisible" axion models, it was pointed out that the domain wall number $N_{\rm DW}$ different from 1 must have led to serious cosmological problems in the standard Big Bang cosmology [5]. Therefore, the standard DFSZ models with $N_{\rm DW} = 6$ has not worked successfully in our Universe. We consider only $N_{\rm DW} = 1$ models for "invisible" axions. The argument goes like this. In the evolving Universe, there always exists

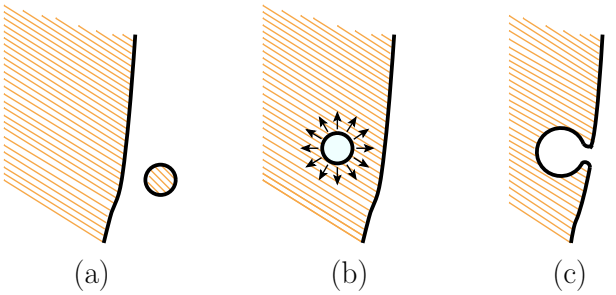

Figure 1: A horizon scale string-wall for $N_{\rm DW} = 1$ with a small membrane bounded by string.

a (or a few) horizon scale string(s) and a giant wall attached to it as shown in Fig. 1 (a). There are a huge number of small walls bounded by an axionic string which punch holes in the giant walls as shown in Fig. 1 (b). The punched holes expand with light velocity and eat up the giant string-walls as shown in Fig. 1 (c). This is the scenario that "invisible" axion models with $N_{\rm DW} = 1$ are harmless in cosmolgy. However, "invisible" axion models with $N_{\rm DW} \geq 2$ have cosmological problems. For example for $N_{\rm DW} = 2$, a horizon scale string and wall system has the configurations shown in Figs. 2 (a), (b), (c), and (d), and one can see that the horizon scale string-wall system is not erased. With inflation, the domain wall problem has to be reconsidered as discussed in [3].

Thus, it is an important theoretical question, "How can one obtain a reasonable "invisible" axion model having $N_{\rm DW} = 1$?" One obvious model is the KSVZ axion with one heavy quark. Another more sophisticated solution is the Lazarides–Shafi (LS) mechanism in which the seemingly different vacua are identified by gauge transformation [6]. The original suggestion was to use the centers of extended-GUT groups for this purpose [6], which has been used in extended GUT models. But, the LS mechanism has a limited application. More practical solutions come from using two discrete symmetry groups. This method can be extended to the Goldstone boson directions of spontaneously broken global symmetries [7]. In Fig. 3, we consider two discrete symmetries with $\mathbf{Z}_3$ and $\mathbf{Z}_2$. α_1 and α_2 are the continuous directions. In case of Goldstone directions, two pseudoscalars are $a_1 = f_1\alpha_1$ and $a_2 = f_2\alpha_2$. If the potential is nonvanishing only in one direction, then there is another orthogonal direction along which the potential is

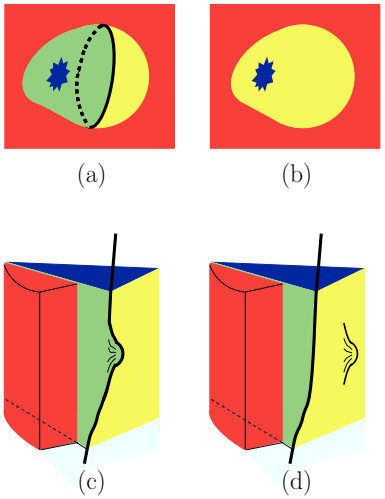

Figure 2: For $N_{\rm DW} = 2$, small DW balls (a) and (b), with punches showing the inside blue-vacuum, and the horizon scale string-wall system (c) and (d). Yellow walls are $\theta = 0$ walls, and yellow-green walls are $\theta = \pi$ walls. Yellow-green walls of type (b) are also present.

flat. This flat direction is the Goldstone boson direction. For the discrete symmetry $\mathbf{Z}_3 \times \mathbf{Z}_2$ of Fig. 3, there are six inequivalent vacua, marked as blue bullet (●), black down triangle (▼), diamond (◇), black square (■), black triangle (▲), and star (⋆). Identifying along the red dash-arrow directions encompass all six vacua, where discrete group identifications along α_1 and α_2 are shown as horizontal and vertical arcs, respectively. Notice, however, if we identify along the green dash-arrow directions, then only ■, ▲, and ⋆ are identified. Parallel to the green dash-arrow, there is another identification of ●, ▲, and ◇. Thus, there remains $\mathbf{Z}_2$. This example shows that all Goldstone boson directions are not necessarily identifying all vacua, even if N_1 and N_2 are relatively prime. The difference of red and green directions is a possibility of

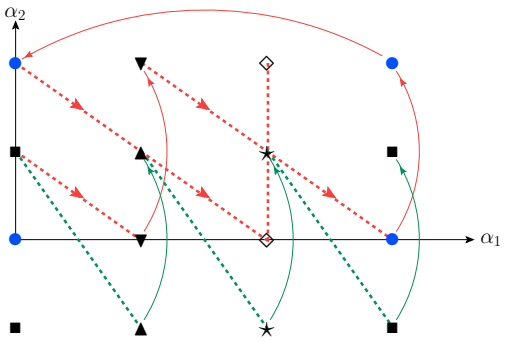

Figure 3: The Goldstone boson direction out of two pseudoscalars for $N_1 = 3$ and $N_2 = 2$ [7].

allowing a discrete group or not. In the red dash arrow case, when one unit of α_1 is increased, one unit of α_2 is increased. In this case, if N_1 and N_2 are relatively prime, then all vacua are identified as the same vacuum, forbidding any remaining discrete group. In the green dash arrow case, when one unit of α_1 is increased, two units of α_2 is increased, and $\mathbf{Z}_2$ is allowed in this direction. This fact was not noted in earlier papers [7, 8]. Since the Goldstone boson is derived from VEVs of two Higgs fields in the above example, the possibility of identifying all vacua depends on the ratio of two VEVs.

3 Global U(1) from anomalous gauge U(1)

But, the most appealing solution is the direction related to the model-independent axion (MI-axion), $B_{\mu\nu}$, arising from string compactification, which is known to have $N_{\rm DW} = 1$ [9, 8]. Even if one starts from string compactification, it is important to obtain $10^9\,{\rm GeV} \leq {\rm f_a} \leq 10^{11}\,{\rm GeV}$. For this we need the 't Hooft mechanism with an anomalous gauge symmetry $\mathrm{U}(1)_{\rm anom}$. It is explicitly discussed in Ref. [10]. It is generally known that 10 dimensional (10D) string theories do not allow global symmetries upon compactification, except the MI-axion direction, $B_{\mu\nu}$. Gauge fields arise from compactification of $\mathrm{E}_8 \times \mathrm{E}_8'$ with gauge potential A_M. In the compactification of the heterotic string, the MI-axion becomes the global shift direction [11],

$$a_{\rm MI} \to a_{\rm MI} + \text{constant}. \tag{4}$$

where $a_{\rm MI}$ is the dual of the field strength of $B_{\mu\nu}$, $H_{\mu\nu\rho} = M_{\rm MI}\epsilon_{\mu\nu\rho\sigma}\,\partial^\sigma a_{\rm MI}$. At the GUT scale, we need a global symmetry rather than the MI-axion shift symmetry of (4) such that the global symmetry is broken at the intermediate scale. Here, the 't Hooft mechanism works. $H_{\mu\nu\rho}$ couples to the non-Abelian gauge fields by the Green–Schwarz (GS) term [12]. The GS term is composed of a product with one B_{MN} and four non-Abelian gauge fields, F_{PQ}, etc., contracted with $\epsilon^{MNPQ\cdots}$. Thus, we obtain

$$\frac{1}{2}\partial^\mu a_{\rm MI}\partial_\mu a_{\rm MI} + M_{\rm MI}A_\mu\partial^\mu a_{\rm MI} + \frac{1}{2}M_{\rm MI}^2 A_\mu^2. \tag{5}$$

The GS term is generating the coupling $A_\mu\partial^\mu a_{\rm MI}$. This coupling appears when there exists an anomalous $\mathrm{U}(1)_{\rm anom}$ gauge symmetry from compactification of 10D $\mathrm{E}_8 \times \mathrm{E}_8'$ down to a 4D gauge group [13].

The anomalous gauge symmetry $\mathrm{U}(1)_{\rm anom}$ is a subgroup of $\mathrm{E}_8 \times \mathrm{E}_8'$ with gauge field A_μ. One phase, *i.e.* $\alpha = a_{\rm MI}/M_{\rm MI}$, is working for the 't Hooft mechanism, *i.e.* the coupling $M_{MI}A_\mu\partial^\mu a_{\rm MI}$ in Eq. (5), and hence one global symmetry survives below the compactification scale $M_{\rm MI}$. The compactification scale $M_{\rm MI}$ is expected to be much larger than the decay constant $f_{\rm MI}$ of the MI-axion estimated in [14]. In the orbifold compactification, there appear many gauge U(1)'s which are anomaly free except the $\mathrm{U}(1)_{\rm anom}$. After the global $\mathrm{U}(1)_{\rm anom}$ is surviving below the scale $M_{\rm MI}$, the 't Hooft mechanism can be applied repeatedly until all anomaly free gauge U(1)'s are removed around the GUT scale. After making all these anomaly-free gauge bosons massive, the VEV f_a of a SM singlet scalar ϕ breaks the global symmetry $\mathrm{U}(1)_{\rm anom}$ spontaneously and there results the needed "invisible" axion at the intermediate scale.

Because it is so important to realize the intermediate scale f_a, let us discuss this string theory mechanism first in a hierarchical scheme and then present a general case based on the generalized 't Hooft mechanism. In the literature, the Fayet–Iliopoulos terms (FI-term) for

$U(1)_{\rm anom}$ has been discussed extensively. In the hierarchical scheme, the VEVs of scalars is assumed to be much smaller than the string scale. Then, one can consider the global symmetry $U(1)_{\rm anom}$, surviving down from string compactification. Even if one adds the FI-term for $U(1)_{\rm anom}$, $|\phi^* Q_{\rm anom}\phi - \xi|^2$ with $\xi \ll M^2_{string}$, it is not much different from considering the global symmetry with the usual D-term, $|\phi^* Q_{\rm anom}\phi|^2$ (as if there is a gauge symmetry) since $\xi \ll M^2_{\rm string}$. In fact, there exists a string loop calculation obtaining ξ at string two-loop [15]. If the string two-loop calculation turns out to be hierarchically smaller (because of the two-loop) than the string scale, then the above hierarchical explanation works. Even if the FI parameter ξ is large, still there survives a global symmetry. It is based on just counting the number of continuous degrees of freedom. Let us consider two phase fields, the MI-axion and some phase of a complex scalar ϕ carrying the $U(1)_{\rm anom}$ charge. Since we consider two phases and two terms, one may guess that the gauge boson (A^μ) obtains mass and the remaining phase field also obtains mass by the FI D-term. But, it does not work that way, because there is no potential term for the phase fields to render such mass to the remaining phase field, because the charges of the gauge U(1) from $E_8 \times E_8'$ and the charge operator $Q_{\rm anom}$ in the FI D-term are identical. It is equivalent to that there is no mass term generated because the exact Goldstone boson direction (the longitudinal mode of A^μ) coincides with the phase of ϕ in the FI D-term.

To discuss it explicitly, let us consider only one anomaly free U(1) gauge boson A_μ and the FI D-term for ϕ with generator $Q_{\rm anom}$. Since ϕ carries the gauge charge $Q_{\rm anom}$, we obtain its coupling to A_μ from the covariant derivative, by writing $\phi = (\frac{v+\rho}{\sqrt{2}})e^{ia_\phi/v}$,

$$|D_\mu\phi|^2 = |(\partial_\mu - igQ_a A_\mu)\phi|^2_{\rho=0} = \frac{1}{2}(\partial_\mu a_\phi)^2 - gQ_a A_\mu \partial^\mu a_\phi + \frac{g^2}{2}Q_a^2 v^2 A_\mu^2. \tag{6}$$

The gauge boson A_μ has the coupling to $a_{\rm MI}$ by the GS term, and the sum of two terms is

$$\frac{1}{2}\left(g^2 Q_a^2 v^2\right)(A_\mu)^2 + A_\mu(M_{\rm MI}\partial^\mu a_{\rm MI} - gQ_a v\partial^\mu a_\phi) + \frac{1}{2}\left[(\partial_\mu a_{\rm MI})^2 + (\partial^\mu a_\phi)^2\right]. \tag{7}$$

Thus, we note that $\cos\theta\, a_{MI} - \sin\theta\, a_\phi$ becomes the longitudinal degree of A_μ where

$$\sin\theta = \frac{gQ_a v}{\sqrt{M^2_{\rm MI} + g^2 Q_a^2 v^2}}, \tag{8}$$

and a new global degree direction is

$$\theta_{\rm QCD} \propto \cos\theta\, a_\phi + \sin\theta\, a_{\rm MI}. \tag{9}$$

$\theta_{\rm QCD}$ is the QCD vacuum angle direction and breaking $U(1)_{\rm anom}$ at the intermediate scale produces the "invisible" axion. We obtained this important result from that only one combination of the phase fields is removed since the longitudinal degree of A_μ chooses the same generator for the shifts of $a_{\rm MI}$ and a_ϕ. Below the anomalous scale ξ, the 't Hooft mechanism is used repeatedly with anomaly free gauge U(1)'s together with the global $U(1)_{\rm anom}$ we derived above, and there survives a global symmetry $U(1)_{\rm anom}$ at the intermediate scale. Determination of the VEV f_a at the intermediate scale is such that the coefficient of $\phi^*\phi$ in the effective potential is given by $-$(intermediate scale)^2. Note that choosing $Q_{\rm anom}$ is not unique because one can add any combination of anomaly free gauge charges to $Q_{\rm anom}$, without changing physics of $U(1)_{\rm anom}$ [16].

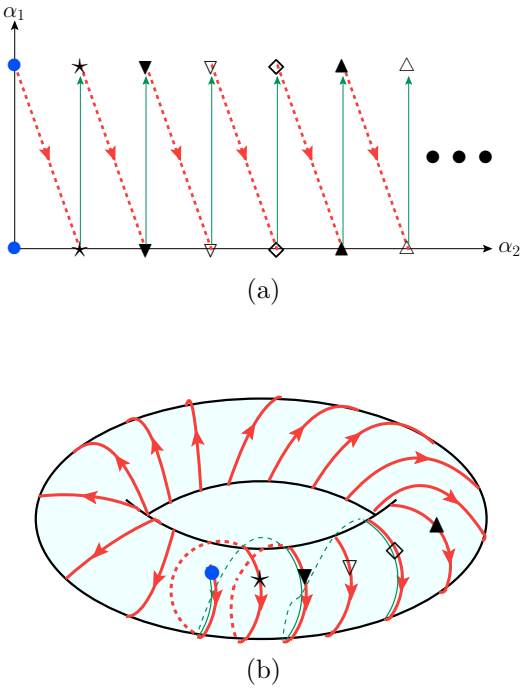

Figure 4: The MI-axion example of Fig. 3: (a) the standard torus identification, and (b) identification by the winding direction in the torus.

The global $\mathrm{U}(1)_{\mathrm{anom}}$ from string should not allow the cosmological DW problem of the "invisible" axion. The strategy with the Goldstone boson direction discussed in [7, 8] works here. For the Goldstone boson from the global $\mathrm{U}(1)_{\mathrm{anom}}$, we repeat it in Fig. 4 (a). Since $N_{\mathrm{DW}} = 1$ in the MI-axion direction (α_1 in Fig. 3), the red dash arrow direction identifies all vacua. In Fig. 4 (b), it is re-drawn on the familiar torus. The red arrows show that α_2 shifts by one unit as α_1 shifts one unit. In this case, all the vacua are identified and we obtain $N_{\mathrm{DW}} = 1$. The green lines show that α_2 shifts by two units for one unit shift of α_1. If N_2 is even, then we obtain $N_{\mathrm{DW}} = 2$ since only halves of N_2 are identified by green lines. To find out N_{DW}, it is useful to factorize N_2 in terms of prime numbers. Even though N_2 is very large, of order 10^3, there are plenty of relatively prime numbers from those factors in N_2. Figure 4 (b) is drawn with $N_2 = 17$ and the green lines also identify all vacua since 1 and 17 are relatively prime. In string compactification, it is easy to find many relatively prime numbers to all prime numbers appearing in the factors of $\mathrm{Tr}\, Q_{\mathrm{anom}}$. For example, in Refs. [16, 10], $\mathrm{Tr}\, Q_{\mathrm{anom}}$ was cited as –3492 which is expressed in terms of prime numbers as $2^2 \times 3^2 \times 97$. Not to introduce a fine-tuning on the ratio of VEVs, if we consider two VEVs are comparable, let us look for prime numbers relative to 2, 3, and 97. Near 3492, there are 3491, 3493, 3497, 3499, etc., relatively prime to 2, 3, and 97. So, a VEV of ϕ near the string scale, $\langle\phi\rangle = v_\phi/\sqrt{2}$, and the longitudinal $\mathrm{U}(1)_{\mathrm{anom}}$ degree parameter M_{MI} render a global symmetry below the compactification scale

such that the global current satisfies

$$\partial_\mu J^\mu_{\rm PQ} = \frac{1}{32\pi^2} G^a_{\mu\nu} \tilde{G}^{a\,\mu\nu}. \tag{10}$$

Namely, two comparable VEVs, $v_\phi : M_{\rm MI} = 3491 : 3493$ for example, produce an exact global symmetry $\mathrm{U}(1)_{\rm anom}$ below the compactification scale. If we neglect anomaly free gauge U(1)'s, a scalar field ϕ carrying the PQ charge houses the "invisible axion" with decay constant f_a if $\langle\phi\rangle = f_a/\sqrt{2}$. f_a is not the large ones such as v_ϕ and $M_{\rm MI}$. So, the intermediate scale f_a is not considered to be a fine tuning. f_a can come from another mechanism such as the supergravity scale [17] or by some solution of the gauge hierarchy problem.

In conclusion, forbidding the DW problem for the "invisible" axion from the global $\mathrm{U}(1)_{\rm anom}$ is not considered as a fine-tuning on the ratio of VEVs of Higgs fields. Due to the 't Hooft mechanism, the "invisible" axion scale can be lowered from the string scale down to an intermediate scale [10].

Acknowledgments

This work is supported in part by the National Research Foundation (NRF) grant funded by the Korean Government (MEST) (NRF-2015R1D1A1A01058449) and by Institute of Basic Science of Korea (IBS-R017-D1).

References

[1] J. E. Kim, Y. K. Semertzidis, and S. Tsujikawa, Front. Phys. **2** (2014) 60.

[2] J.E. Kim, Phys. Rev. Lett. **43** (1979) 103; M.A. Shifman, V.I. Vainshtein, V.I. Zakharov, Nucl. Phys. B **166** (1980) 493; M. Dine, W. Fischler and M. Srednicki, Phys. Lett. B **104** (1981) 199; A. P. Zhitnitsky,Sov. J. Nucl. Phys. **31**, 260 (1980), Yad. Fiz. **31** (1980) 497.

[3] For a recent review, see, J. E. Kim, "Fate of global symmetries in cosmology: QCD axion, quintessential axion and trans-Planckian inflaton decay-constant", 2017.

[4] G. 't Hooft, Nucl. Phys. B **35** (19871) 167.

[5] P. Sikivie, Phys. Rev. Lett. **48** (1982) 1156.

[6] G. Lazarides and Q. Shafi, Phys. Lett. B **115** (1982) 21.

[7] K. Choi and J.E. Kim, Phys. Rev. Lett. **55** (1985) 2637.

[8] J.E. Kim, Phys. Lett. B **759** (2016) 58.

[9] E. Witten, Phys. Lett. B **153** (1985) 243.

[10] J. E. Kim, B. Kyae, and S. Nam, arXiv:1703.05345 [hep-ph].

[11] E. Witten, Phys. Lett. B **149** (1984) 351.

[12] M. B. Green and J. Schwarz, Phys. Lett. B **149** (1984) 117.

[13] J. J. Atick, L. Dixon, and A. Sen, Nucl. Phys. B **292** (1987) 109; M. Dine, I. Ichinose, and N. Seiberg, Nucl. Phys. B **293** (1987) 253.

[14] K. Choi and J. E. Kim, Phys. Lett. B **154** (1985) 393.

[15] J. J. Atick and A. Sen, Nucl. Phys. B **296** (1988) 157.

[16] J. E. Kim, Phys. Rev. D **96** (2017) 055033.

[17] J. E. Kim, Phys. Lett. B **136** (1984) 378.

String Core Effect on the Axion Dark Matter Abundance

Ken'ichi Saikawa

Deutsches Elektronen-Synchrotron (DESY), Hamburg, Germany*

DOI: http://dx.doi.org/10.3204/DESY-PROC-2017-02/saikawa_kenichi

In this contribution, we highlight a problem in estimation of the mass of axion dark matter in the scenario where the Peccei-Quinn symmetry is broken after inflation. In order to obtain a definite prediction for its mass, it is necessary to evaluate its relic abundance precisely by taking account of the production from cosmic strings and domain walls. After reviewing a long-standing controversy about the axion production efficiency from decaying strings, several recent approaches aiming at resolving the uncertainty are discussed.

The axion [1, 2] is a pseudo Nambu-Goldstone boson associated with spontaneously broken global Peccei-Quinn (PQ) symmetry [3]. There is a strong motivation to search for the axion, as it provides the elegant solution to the strong CP problem in quantum chromodyamics (QCD) and can be a good candidate of dark matter in the universe [4, 5, 6]. However, there are some complications when we consider the evolution of the axion dark matter in the early universe. In particular, it is known that topological defects such as strings and domain walls are formed in the early universe if the PQ symmetry is broken after inflation, and that axions produced from these defects may have an impact on the relic dark matter abundance [7]. Therefore, it is important to know about the efficiency of axion production quantitatively in order to give an accurate estimate of its relic abundance and obtain a definite prediction for its mass m_a.

The formation and evolution of topological defects are described by a complex scalar field Φ called the PQ field. The global $U(1)$ PQ symmetry is spontaneously broken when the PQ field acquires a vacuum expectation value $|\langle\Phi\rangle|^2 = v_{\rm PQ}^2/2$ due to the potential $V(\Phi) = \lambda(|\Phi|^2 - v_{\rm PQ}^2/2)^2$, where λ is the self-coupling, and $v_{\rm PQ}$ represents the energy scale of PQ symmetry breaking, which is related to the axion decay constant, $f_a \propto v_{\rm PQ}$. At that time, vortex-like objects called strings are formed. Furthermore, these strings are attached by sheet-like objects called domain walls around the epoch of the QCD phase transition, because of the existence of the effective potential for the axion field induced by the non-perturbative effects in QCD. If the effective potential has only one non-degenerate minimum, these string-wall systems eventually collapse due to the tension of domain walls [8].

Axions are copiously produced from the collapse of such string-wall systems around the epoch of the QCD phase transition, and the axion number is expected to be frozen after they decay away. Therefore, the axion density at the present time $t_{\rm today}$ can be written as

$$\rho_a(t_{\rm today}) = m_a n_a(t_{\rm decay}) \left(\frac{R(t_{\rm decay})}{R(t_{\rm today})}\right)^3, \tag{1}$$

*Current affiliation: Max-Planck-Institut für Physik (Werner-Heisenberg-Institut), München, Germany

where $R(t)$ represents the scale factor of the universe, and $t_{\rm decay}$ represents the time at which the string-wall systems decay away. Assuming that the decay proceeds sufficiently faster than the cosmological timescale, we can roughly estimate the number density of axions at $t_{\rm decay}$ as

$$n_a(t_{\rm decay}) \sim \frac{\rho_{\rm defects}(t_{\rm decay})}{\langle E_a(t_{\rm decay})\rangle}, \tag{2}$$

where $\rho_{\rm defects}$ represents the energy density of the defects and $\langle E_a\rangle$ is the mean energy of axions radiated from them. Therefore, it is helpful to know about two factors in order to understand the axion production efficiency: One is the energy density of defects, which is believed to follow the scaling solution, $\rho_{\rm defects}(t) \approx \rho_{\rm strings}(t) = \xi\mu/t^2$, where μ is the energy of strings per unit length and ξ is a dimensionless factor. The other is the mean energy $\langle E_a(t_{\rm decay})\rangle$, which depends on the energy spectrum of radiated axions.

In the literature, there has been a long-standing controversy about the estimation of axion production efficiency from topological defects [9, 10, 11, 12, 13, 14, 15]. The authors of Refs. [9, 11, 15] claimed that the spectrum of radiated axions is hard (*i.e.* the mean energy $\langle E_a(t_{\rm decay})\rangle$ is enhanced), and that it suppresses the relic axion abundance according to Eq. (2). However, other authors [10, 12, 13, 14] did not confirm this feature, arguing that most of radiated axions have a lower frequency corresponding to the horizon size, $\langle E_a\rangle \sim 2\pi/t$. If this is the case, the axion abundance becomes larger than that estimated based on the vacuum re-alignment mechanism [4, 5, 6].

The most straightforward way to address this controversy is to perform large scale field theoretic lattice simulations [14, 16, 17, 18]. In this approach, the classical equation of motion for the complex scalar field Φ in the expanding universe is solved numerically on discretized coordinates. Based on this approach, the whole process of the evolution of defects, including the formation of strings, that of domain walls, and the collapse of the string-wall systems, was investigated in Ref. [17], and the spectrum of axions radiated from them was estimated by applying the masking analysis method introduced in Ref. [16]. The results indicated that there are $\mathcal{O}(1)$ strings per horizon volume [*i.e.* $\xi \sim \mathcal{O}(1)$], and that radiated axions are mildly relativistic. In particular, the spectrum of radiated axions peaks at lower frequencies, which supports the conclusion of Refs. [10, 12, 13, 14]. These results were refined in Ref. [18], and the prediction for the axion mass $m_a = (0.8\text{–}1.3) \times 10^{-4}\,{\rm eV}$[1] was obtained by imposing the assumption that the axion becomes the main constituent of dark matter.

In contrast to the preceding argument, there still remains an unresolved issue associated with the technical limitations of lattice simulations. In the field theoretic lattice simulations, we must consider two extremely different length scales: One is the width of the string core δ_s, which is inversely proportional to the PQ scale, $\delta_s \sim (\sqrt{\lambda} v_{\rm PQ})^{-1}$, and the other is the Hubble radius $H^{-1} \sim t$, which corresponds to the typical distance between two neighboring strings. In reality, there is a huge hierarchy between these two scales: $H^{-1}/\delta_s \sim 10^{30}$ at $t \sim t_{\rm decay}$. However, it is impossible to realize such a huge hierarchy in the lattice simulations, due to the limitation of dynamical ranges. For simulations with 512^3 grid points, we only realize $H^{-1}/\delta_s \lesssim 300$, which is far smaller than realistic values. There is a possibility that this difference gives rise to a nontrivial consequence [19], which originates from the fact that the energy of string cores acquires a large logarithmic correction due to the gradient energy of surrounding axion fields, $\mu \approx \pi v_{\rm PQ}^2 \ln(H^{-1}/\delta_s)$. When $H^{-1} \gg \delta_s$, This core energy becomes

[1] If we just use maximum and minimum values for numerical factors such as ξ and $\langle E_a(t_{\rm decay})\rangle/(2\pi/t_{\rm decay})$ without using the propagation of uncertainty law, we obtain $m_a = (0.6\text{–}1.5) \times 10^{-4}\,{\rm eV}$.

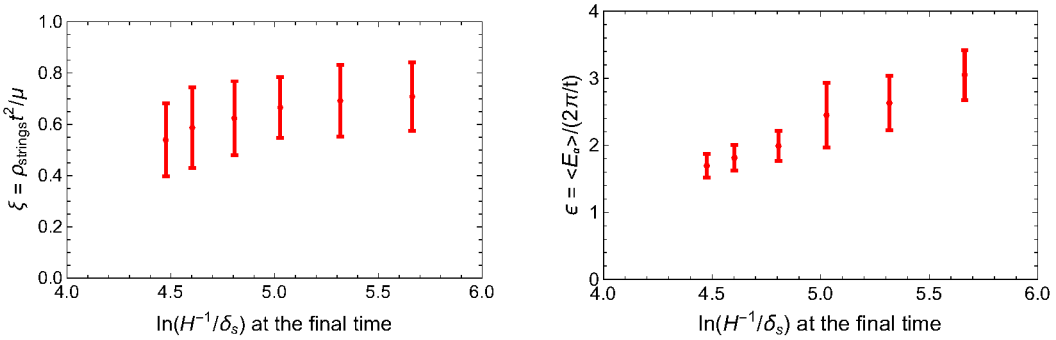

Figure 1: The renormalized string density (left) and mean energy of radiated axions (right) for various values of $\ln(H^{-1}/\delta_s)$ at the final time of the simulations.

larger than the string radiation power $P \sim v_{\rm PQ}^2$ [20], and we expect that the radiation damping becomes less efficient [21]. Therefore, it is still unclear whether strings evolve similarly to what we observe in the conventional field theoretic simulations if we take $H^{-1} \gg \delta_s$.

In order to check the dependence on the ratio H^{-1}/δ_s, we performed followup studies based on the field theoretic simulations. The setup of the simulations was the same with Ref. [17] except for that we set $m_a = 0$.[2] We varied the ratio between the string core width $\delta_s \sim (\sqrt{\lambda} v_{\rm PQ})^{-1}$ and the Hubble radius H^{-1} at the final time of the simulations by varying the self coupling of the PQ field within the range $0.093 \leq \lambda \leq 1$. From these simulations, we evaluated the density parameter of strings $\xi = \rho_{\rm strings} t^2/\mu$ and the ratio between the mean energy of radiated axions and the horizon scale $\epsilon \equiv \langle E_a \rangle/(2\pi/t)$ at the final time of the simulations. The results are shown in Fig. 1. We observed that both the string density and mean energy slightly increase with $\ln(H^{-1}/\delta_s)$, which agrees with the features pointed out in Ref. [19]. However, it is still dangerous to extrapolate these results to the realistic value, $H^{-1}/\delta_s \sim 10^{30}$. In order to investigate what happens in such cases, it is necessary to develop some alternative methods.

Recently, a couple of new approaches are proposed to investigate the dynamics of axionic strings with a large core energy. One possible way is to implement string cores as *smeared* external objects instead of directly solving the equation of motion for the complex scalar field Φ. This was performed in 2+1 D in Ref. [22], whose results showed that strings exhibit significantly different behavior at large values of $\ln(H^{-1}/\delta_s)$. However, there remains the question whether such results are peculiar to the simulations in 2+1 D spacetime. The other method was proposed in Ref. [23], which still relies on the field theoretic simulations but realizes a large string core energy by introducing additional field degrees of freedom. The axion production was investigated in Ref. [24] based on this simulation method, and the prediction for the axion mass $m_a = (2.62 \pm 0.34) \times 10^{-5}\,{\rm eV}$ was obtained based on the assumption that the axion becomes the main constituent of dark matter. It should be noted that both of these modified simulation methods are designed such that they realize the large-scale behavior of axionic strings without evaluating the dynamics of the PQ field Φ around the string core via first principles. Therefore, they are regarded as effective theories in the sense that they can correctly describe the dynamics

[2] If we take $m_a \neq 0$, strings start to collapse due to the tension of domain walls. For simplicity, here we do not consider this collapsing process, and focus only on the evolution of strings in the scaling regime.

of strings on large scales but break down at some smaller distance scales.

Let us try to figure out the implications of these new simulation results by going back to the initial argument based on energy conservation [Eqs. (1) and (2)]. In both types of modified simulation methods [22, 24], the results showed that, while strings become denser, the axion production becomes less efficient for realistic values of the string core energy, leading to a lower value of the axion mass. These facts imply that a large factor of $\rho_{\rm defects}$ in Eq. (2) should be compensated by producing more energetic axions. Therefore, it is possible that the results are sensitive to physics at smaller scales. Given the fact that these modified simulation methods can describe the infrared behavior of axionic strings but fail to describe ultraviolet modes, it is important to investigate the axion production from the decay of small scale strings in more detail. Understanding such dynamics of axionic strings is crucial to obtain a robust prediction for the mass of axion dark matter and interpret the results of forthcoming experiments.

Acknowledgments

The author would like to thank the organizers of *the 13th Patras Workshop on Axions, WIMPs and WISPs (Axion-Wimp 2017)* for a very motivating conference.

References

[1] S. Weinberg, Phys. Rev. Lett. **40**, 223 (1978).
[2] F. Wilczek, Phys. Rev. Lett. **40**, 279 (1978).
[3] R. D. Peccei and H. R. Quinn, Phys. Rev. Lett. **38**, 1440 (1977).
[4] J. Preskill, M. B. Wise and F. Wilczek, Phys. Lett. B **120**, 127 (1983).
[5] L. F. Abbott and P. Sikivie, Phys. Lett. B **120**, 133 (1983).
[6] M. Dine and W. Fischler, Phys. Lett. B **120**, 137 (1983).
[7] R. L. Davis, Phys. Lett. B **180**, 225 (1986).
[8] A. Vilenkin and A. E. Everett, Phys. Rev. Lett. **48**, 1867 (1982).
[9] D. Harari and P. Sikivie, Phys. Lett. B **195**, 361 (1987).
[10] R. L. Davis and E. P. S. Shellard, Nucl. Phys. B **324**, 167 (1989).
[11] C. Hagmann and P. Sikivie, Nucl. Phys. B **363**, 247 (1991).
[12] R. A. Battye and E. P. S. Shellard, Nucl. Phys. B **423**, 260 (1994) [astro-ph/9311017].
[13] R. A. Battye and E. P. S. Shellard, Phys. Rev. Lett. **73**, 2954 (1994) Erratum: [Phys. Rev. Lett. **76**, 2203 (1996)] [astro-ph/9403018].
[14] M. Yamaguchi, M. Kawasaki and J. Yokoyama, Phys. Rev. Lett. **82**, 4578 (1999) [hep-ph/9811311].
[15] C. Hagmann, S. Chang and P. Sikivie, Phys. Rev. D **63**, 125018 (2001) [hep-ph/0012361].
[16] T. Hiramatsu, M. Kawasaki, T. Sekiguchi, M. Yamaguchi and J. Yokoyama, Phys. Rev. D **83**, 123531 (2011) [arXiv:1012.5502 [hep-ph]].
[17] T. Hiramatsu, M. Kawasaki, K. Saikawa and T. Sekiguchi, Phys. Rev. D **85**, 105020 (2012) Erratum: [Phys. Rev. D **86**, 089902 (2012)] [arXiv:1202.5851 [hep-ph]].
[18] M. Kawasaki, K. Saikawa and T. Sekiguchi, Phys. Rev. D **91**, no. 6, 065014 (2015) [arXiv:1412.0789 [hep-ph]].
[19] L. Fleury and G. D. Moore, JCAP **1601**, 004 (2016) [arXiv:1509.00026 [hep-ph]].
[20] A. Vilenkin and T. Vachaspati, Phys. Rev. D **35**, 1138 (1987).
[21] A. Dabholkar and J. M. Quashnock, Nucl. Phys. B **333**, 815 (1990).
[22] L. M. Fleury and G. D. Moore, JCAP **1605**, no. 05, 005 (2016) [arXiv:1602.04818 [hep-ph]].
[23] V. B. Klaer and G. D. Moore, arXiv:1707.05566 [hep-ph].
[24] V. B. Klaer and G. D. Moore, arXiv:1708.07521 [hep-ph].

Search for the Dark Photon with the PADME Experiment at LNF

Viviana Scherini[1] *on behalf of the PADME Collaboration*[*]

[1]Istituto Nazionale di Fisica Nucleare, Sezione di Lecce, via per Arnesano I-73100 Lecce, Italy

DOI: http://dx.doi.org/10.3204/DESY-PROC-2017-02/scherini_viviana

Massive photon-like particles are predicted in many extensions of the Standard Model with a hidden sector where dark matter is secluded. They are vector bosons mediating the interaction between dark matter particles and can be produced in scattering of ordinary particles through a faint mixing to the photon. Most of the present experimental constraints on this "dark photon" (A') rely on the hypothesis of dominant decays to lepton pairs. The PADME experiment will search for the $e^+e^- \to \gamma A'$ process in a positron-on-target experiment, assuming a decay of the A' into invisible particles of the hidden sector. The positron beam of the DAΦNE Beam-Test Facility, at Laboratori Nazionali di Frascati of INFN, will be used. A fine-grained, high-resolution calorimeter will measure the momentum of the photon in events with no other activity in the detector, thus allowing to measure the A' mass as the missing mass in the final state. In about one year of data taking, a sensitivity on the interaction strength (ε^2 parameter) down to 10^{-6} is achievable in the mass region $M_{A'} < 23.7$ MeV. The experiment is currently under construction and it is planned to take data in 2018. The status of PADME and its physics potential will be reviewed.

1 Introduction

The PADME experiment [1], hosted in the DAΦNE [2] Beam-Test Facility (BTF) [3] at Laboratori Nazionali di Frascati (LNF) of INFN, is designed to search for the dark photon by using an intense positron beam hitting a light target. The A' can be observed by searching for an anomalous peak in the spectrum of the missing mass measured in events with a single photon in the final state. The measurement requires the precise determination of the 4-momentum of the recoil photon, performed by an homogeneous electromagnetic calorimeter.

The collaboration aims to complete the design and construction of the experiment by the end of 2017 and to collect $\sim 10^{13}$ positrons on target by the end of 2018.

[*]The PADME Collaboration is: P. Creti, G. Chiodini, F. Oliva, V. Scherini (INFN Lecce); A.P. Caricato, M. Martino, G. Maruccio, A. Monteduro, S.Spagnolo (INFN Lecce e Dip. di Matematica e Fisica, Università del Salento); P. Albicocco, R. Bedogni, B. Buonomo, F. Bossi, R. De Sangro, G. Finocchiaro, L.G. Foggetta, A. Ghigo, P. Gianotti, M. Palutan, G. Piperno, I. Sarra, B. Sciascia, T. Spadaro, E. Spiriti (INFN Laboratori Nazionali di Frascati); C. Taruggi (INFN Laboratori Nazionali di Frascati and Università degli Studi di Roma "Tor Vergata"); L. Tsankov, (University of Sofia "St. Kl. Ohridski); G. Georgiev, V. Kozhuharov (University of Sofia "St. Kl. Ohridski" and INFN Laboratori Nazionali di Frascati); F. Ameli, F. Ferrarotto, E. Leonardi, P. Valente (INFN Roma1); S. Fiore (INFN Roma1 e ENEA) G.C.Organtini, M.Raggi (INFN Roma1 e Dip. di Fisica, "Sapienza" Università di Roma)

A comprehensive review of the dark sector, along with a summary of the ongoing experimental programs addressing the theoretical hypotheses motivating the search for the dark photon, can be found in Ref. [4].

2 The PADME Detector

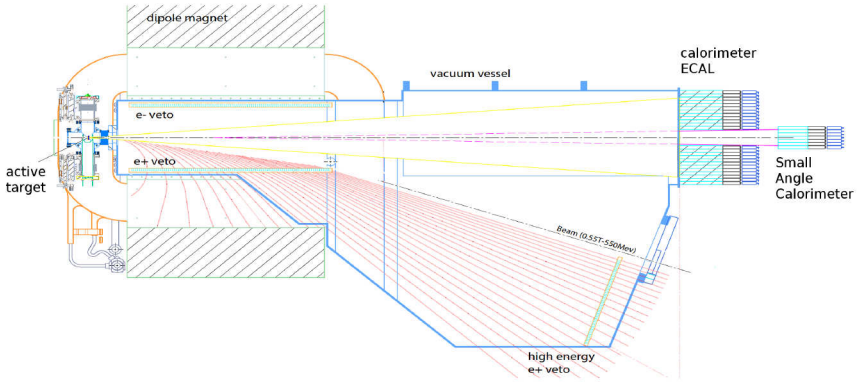

Figure 1: Layout of the PADME detector: the active target, the veto detectors inside the dipole magnet, the HEPVeto near to the non-interacting beam exit, the ECAL and the SAC.

In its baseline configuration, PADME will use the positron beam of 550 MeV energy delivered by the LINAC of the DAΦNE. The time structure of the pulsed beam is a sequence of bunches with a controllable positron population (from single particle to about 10^4) of constant intensity in a time span of 40 ns and a maximum repetition rate of 50 Hz. The experimental apparatus, whose layout is shown in Fig. 1, consists of:

- a 2×2 cm^2 polycrystalline CVD diamond active target [5, 6], aimed at measuring the beam intensity and position (with a precision of a few mm) by means of perpendicular conductive strips. The low Z helps to reduce the occurrence of Bremsstrahlung processes. The small thickness (100 μm) reduces the probability of e^+ multiple interactions.
- a dipole magnet, located 20 cm down-stream of the target, designed to deflect non-interacting beam particles out of the detector and to direct the positrons that lost part of their energy towards veto detectors. The field is 0.5 Tesla over a gap of 23 cm for 1 m length.
- a system of $1 \times 1 \times 18$ cm^3 bars of plastic scintillators used as veto detector for charged particles divided in 3 parts: two arrays of scintillator fingers on the left and right internal walls of the dipole act as positron and electron veto, and another one near the beam dump detects high energy positrons having lost a small part of their energy (mainly through Bremsstrahlung processes).
- a highly segmented electromagnetic calorimeter of cylindrical shape (ECAL) [7] with axis on the beam line located at about 3 m from the target. Its final design implements an active volume of 616 $2 \times 2 \times 23$ cm^3 BGO crystals covering the angular region $20 \div 83$ mrad. The expected energy resolution is $\sim \frac{(1 \div 2)\%}{\sqrt{E}}$ for < 1 GeV electrons and photons.

- a Small Angle fast Calorimeter (SAC) made of $492 \times 2 \times 20\text{cm}^3$ lead glass (SF57) bars with angular coverage $0 \div 20$ mrad, placed behind the central hole of the main calorimeter, thus instrumenting the region of maximum flux of Bremsstrahlung photons produced in the target, mainly aimed at suppressing background from $3\,\gamma$ events.

The target and all veto detectors will be hosted in a vacuum chamber to minimize the interactions of the beam with the atmosphere.

3 Signal and Background

The detector will identify events with a single photon generated in the e^+e^- annihilation taking place in the interaction of the positron beam with the target. The dominant Standard Model processes expected to occur are Bremsstrahlung and $e^+\ e^- \to \gamma\gamma(\gamma)$. The probability that their kinematics will mimic a dark photon production event in the PADME detector can be reduced through an optimization of the ECAL geometry and granularity and of the veto system. The thin target and the adjustable beam intensity play a crucial role in reducing events pile-up.

A signal event is satisfying the following requirements: one cluster in the ECAL fiducial volume (with energy in a range optimized depending on $M_{A'}$), no hits in the vetoes, and no photons with energy larger than 50 MeV in the SAC.

The sensitivity estimation is based on GEANT4 simulations extrapolated to 10^{13} e^+ positrons on target. This number of particles can be obtained by running PADME for 2 years at 50% efficiency with 5000 e^+ per 40 ns bunch at a repetition rate of 49 Hz. The obtained result for A' decaying into invisible particles is shown in Fig. 2. Smaller values of the coupling constant ϵ can be explored by increasing the bunch length. The favored $(g\text{-}2)_\mu$ region can be explored in a model independent way (the only hypothesis on the A' is the coupling to leptons) up to masses of 23.7 MeV [7].

4 Status and Perspectives

The PADME experiment is pioneering for the first time the missing mass technique to constrain directly the A' invisible decay in the parameter region preferred by the $(g\text{-}2)_\mu$ and also to investigate other phenomena, not mentioned here, such as Axion Like Particles (ALPs) [9], Dark Higgs [10] and the fifth force [11]. Early Monte Carlo studies applied to dark photon invisible decay modes demonstrated that PADME can reach a sensitivity down to the level of $\epsilon^2 \sim 1 \cdot 10^{-6}$ in the mass range $M_{A'} < 23.7$ MeV.

The PADME experiment is expected to run in early 2018 and the preparation of the several detector components proceeds according to the schedule. In particular, the dipole magnet is ready and only the mechanical support for final integration must be prepared. In addition, the prototypes of calorimeters and charged veto detector systems have been finalized and tested. All the crystals and scintillator bars are ready for final assembly. A prototype diamond detector has been successfully tested and the final active diamond target is under construction. The readout and digitizing system ($1 \div 5$ Gs/s and 12bit ADC for about 1000 channels) is also available.

An upgraded pulsing system has been recently commissioned, allowing to deliver beam pulses of increasing length, up to $5\,\mu$s, so that, after having optimized the RF power and phases and the magnetic focusing in the LINAC, electron or positron beams could get accelerated close

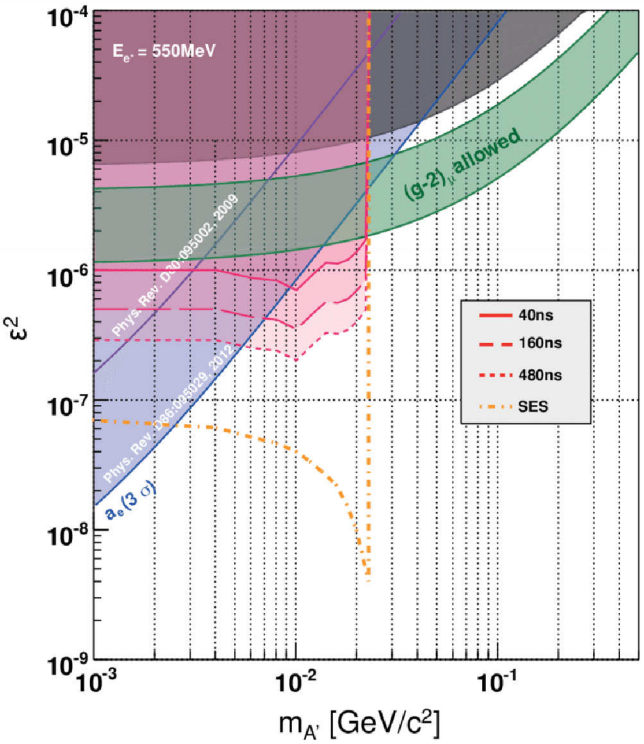

Figure 2: PADME estimated sensitivity for A' decaying into invisible particles for different values of the bunch length. The SES curve refers to single event sensitivity (no background).

to the maximum energy, with a width of several hundreds of ns. An upgrade of the DAΦNE LINAC energy up to 1 GeV has been also proposed [3]. This will extend the parameter space to lower values of ϵ and increase the A' mass range to $M_{A'} < 32$ MeV.

References

[1] M. Raggi and V. Kozhuharov, Adv. High Energy Phys. 2014, 959802 (2014).

[2] A. Ghigo et al., Nucl. Inst. Meth. Phys. Res. A**515**, 524 (2003).

[3] P. Valente et al., *Linear Accelerator Test Facility at LNF Conceptual Design Report*, (2016) [arXiv:1603.05651 [physics.acc-ph]].

[4] J. Alexander et al., *Dark Sectors 2016 Workshop: Community Report*, (2016) [arXiv:1608.08632 [hep-ph]].

[5] M. De Feudis et al., Diam. Relat. Mater. **75**, 25 (2017)

[6] G. Chiodini et al., JINST **12**, C02036 (2017).

[7] M. Raggi et al., Nucl. Instr. Meth. Phys. Res. A**862**, 31 (2017) [arXiv:1611.05649 [physics.ins-det]].

[8] P. Fayet, Phys. Lett. B**675**, 267 (2009) [arXiv:1408.4256 [hep-ph]].

[9] W. J. Marciano et al., Phys. Rev. D**94**, 115033 (2016) [arXiv:1607.01022 [hep-ph]].

[10] A. Anastasi et al., KLOE-2 Collaboration, Phys. Lett. B**747**, 365 (2015).

[11] J. L. Feng et al. Phys. Rev. Lett. **117**, 071803 (2016) [arXiv:1604.07411 [hep-ph]].

Duration of Classicality of Homogeneous Condensates with Attractive Interactions

Sankha Chakrabarty, Seishi Enomoto, Yaqi Han, Pierre Sikivie, Elisa Todarello

Department of Physics, University of Florida, Gainesville, FL 32611, USA

DOI: http://dx.doi.org/10.3204/DESY-PROC-2017-02/sikivie_pierre

Dark matter axions and other highly degenerate bosonic fluids are commonly described by classical field equations. In a recent paper [1] we calculated the duration of classicality of homogeneous condensates with attractive contact interactions and of self-gravitating homogeneous condensates in critical expansion. According to their classical equations of motion, such condensates persist forever. In their quantum evolution parametric resonance causes quanta to jump in pairs out of the condensate into all modes with wavevector less than some critical value. We estimated in each case the time scale over which the condensate is depleted and after which a classical description is invalid.

This contribution to the Proceedings of the 13th Patras Workshop on Axions, WIMPs and WISPs (Thessaloniki, May 15 to 19, 2017) is a summary of our recent paper "Gravitational interactions of a degenerate quantum scalar field" [1]. We quote extensively from the Introduction to that paper, and then state the paper's main results on the duration of classicality of homogeneous condensates with attractive interactions.

One of the leading candidates for the dark matter of the universe is the QCD axion. It has the double virtue of solving the strong CP problem of the standard model of elementary particles [2, 3] and of being naturally produced with very low velocity dispersion during the QCD phase transition [4], so that it behaves as cold dark matter from the point of view of structure formation [5]. Several other candidates, called axion-like particles (ALPs) or weakly interacting slim particles (WISPs), have properties similar to axions as far as the dark matter problem is concerned [6]. ALPs with mass of order 10^{-21} eV, called ultra-light ALPs (ULALPs), have been proposed as a solution to the problems that ordinary cold dark matter is thought to have on small scales [7]. Axion dark matter has enormous quantum degeneracy, of order 10^{61} [8] or more. The degeneracy of ULALP dark matter is even higher [9]. In most discussions of axion or ALP dark matter, the particles are described by classical field equations. The underlying assumption appears to be that huge degeneracy ensures the correctness of a classical field description.

However it was found in refs. [8, 10, 11, 12] that cold dark matter axions thermalize, as a result of their gravitational self-interactions, on time scales shorter than the age of the universe after the photon temperature has dropped to approximately one keV. When they thermalize, all the conditions for their Bose-Einstein condensation are satisfied and it is natural to assume that this is indeed what happens. Axion thermalization implies that the axion fluid does not obey classical field equations since the outcome of thermalization in classical field theory is a UV catastrophe, wherein each mode has average energy k_BT no matter how high the mode's oscillation frequency, whereas the outcome of thermalization of a Bosonic quantum field is to produce a Bose-Einstein distribution. On sufficiently short time scales, the axion fluid does

obey classical fields equations. It behaves then like ordinary cold dark matter on all length scales longer than a certain Jeans length [13, 14]. However, on longer time scales, the axion fluid thermalizes. When thermalizing, the axion fluid behaves differently from ordinary cold dark matter since it forms a Bose-Einstein condensate, i.e. almost all axions go to the lowest energy state available to them. Ordinary cold dark matter particles, weakly interacting massive particles (WIMPs) and sterile neutrinos do not have that property.

Axion thermalization has implications for observation. It was found [10] that the axions which are about to fall into a galactic potential well thermalize sufficiently fast that they almost all go to their lowest energy state consistent with the total angular momentum they acquired from tidal torquing. That state is one of rigid rotation in the angular variables (different from rigid body rotation but similar to the rotation of water going down a drain), implying that the velocity field has vorticity ($\vec{\nabla} \times \vec{v} \neq 0$). In contrast, ordinary cold dark matter falls into gravitational potential wells with an irrotational velocity field [15]. The inner caustics of galactic halos are different in the two cases. If the particles fall in with net overall rotation the inner caustics are rings whose cross-section is a section of the elliptic umbilic catastrophe, called caustic rings for short [16, 17]. If the particles fall in with an irrotational velocity field, the inner caustics have a tent-like structure [15] quite distinct from caustic rings. Observational evidence had been found for caustic rings. The evidence is summarized in ref. [18]. It was shown [19, 20] that axion thermalization and Bose-Einstein condensation explains the evidence for caustic rings of dark matter in disk galaxies in detail and in all its aspects, i.e. it explains not only why the inner caustics are rings and why they are in the galactic plane but it also correctly accounts for the overall size of the rings and the relative sizes of the several rings in a single halo. Finally it was shown that axion dark matter thermalization and Bose-Einstein condensation provide a solution [20] to the galactic angular momentum problem [21], the tendency of galactic halos built of ordinary cold dark matter (CDM) and baryons to be too concentrated at their centers. An argument exists therefore that the dark matter is axions, at least in part. Ref. [20] estimates that the axion fraction of dark matter is 35% or more.

The above claimed successes notwithstanding, axion thermalization and Bose-Einstein condensation is a difficult topic from a theoretical point of view. Thermalization by gravity is unusual because gravity is long-range and, more disturbingly, because it causes instability. Bose-Einstein condensation means that a macroscopically large number of particles go to their lowest energy state. But if the system is unstable it is not clear in general what is the lowest energy state. The idea that dark matter axions form a Bose-Einstein condensate was critiqued in refs. [22, 23, 24]. It was concluded in ref. [24] that "while a Bose-Einstein condensate is formed, the claim of long-range correlation is unjustified."

The aim of our recent paper [1] was to clarify aspects of Bose-Einstein condensation that appear to cause confusion, at least as far as dark matter axions are concerned. One issue is whether a Bose-Einstein condensate needs to be homogeneous (i.e. translationally invariant as is a condensate of zero momentum particles). We answer this question negatively. A Bose-Einstein condensate can be, and generally is, inhomogeneous. Nonetheless, merely by virtue of being a Bose-Einstein condensate, it is correlated over its whole extent, and its extent can be arbitrarily large compared to its scale of inhomogeneity.

A second question is whether Bose-Einstein condensation can be described by classical field equations. We state the following to be true. The behavior of the condensate is described by classical field equations on time scales short compared to its rethermalization time scale. However when the condensate rethermalizes, as it must if situated in a time-dependent background or if it is unstable, it does not obey classical field equations. A phenomenon akin to

Bose-Einstein condensation does exist in classical field theory when a UV cutoff is imposed on the wave-vectors, i.e. all modes with wavevector $k > k_{\rm max}$ are removed from the theory. $k_{\rm max}$ is related to the critical temperature $T_{\rm crit}$ for Bose-Einstein condensation in the quantum field theory. We emphasize however that the relationship $k_{\rm max}$ and $T_{\rm crit}$ necessarily involves a constant, such as $\hbar$, with dimension of action. Furthermore, if we replace the quantum axion field by a cutoff classical field, even if a phenomenon similar to Bose-Einstein condensation does occur, there is no proof or expectation that the cutoff classical theory reproduces the other predictions of the quantum theory. In particular, the phenomenology of caustic rings cannot be reproduced in the classical field theory, with or without cutoff, because vorticity (the circulation of the velocity field along a closed curve) is conserved in classical field theory. In contrast, the production of vorticity and the appearance of caustic rings is the expected behavior of the quantum axion fluid.

A broadly relevant question is the following: over what time scale is a classical description of a highly degenerate but self-interacting Bosonic system valid? We call that time scale the duration of classicality of the system. In ref. [1] we calculated the duration of classicality of a homogeneous condensate, initially at rest but with attractive $\lambda\phi^4$ interactions ($\lambda < 0$). According to its classical equations of motion, such a condensate persists indefinitely. According to its quantum evolution, quanta jump in pairs out of the condensate into all modes with wavevector less than

$$k_J = \sqrt{\frac{|\lambda| n_0}{2m}} \tag{1}$$

where m is the particle mass and n_0 is the condensate density. We find that the condensate is depleted over the time scale

$$t_{c,\lambda} \sim \frac{2m}{k_J^2} \ln\left(\frac{32\pi^{\frac{3}{2}} n_0}{k_J^3}\right) \quad , \tag{2}$$

which is its duration of classicality. We also calculated the duration of classicality of a homogeneous self-gravitating condensate in critical expansion, i.e. forming a matter dominated universe which is at the boundary of being open or closed. The condensate is initially described by the wavefunction [9]

$$\Psi_0(\vec{r}, t) = \sqrt{n_0(t)} e^{i\frac{1}{2} m H(t) r^2} \tag{3}$$

where $H(t)$ is the Lemaître-Hubble expansion rate and

$$n_0(t) = \frac{1}{6\pi G m t^2} \tag{4}$$

is the density. Again, according to its classical equation of motion, the condensate lasts forever. According to its quantum evolution, quanta jump in pairs out of the condensate into all modes with wavevector less than

$$\ell_J(t)^{-1} = (16\pi G n(t) m^3)^{\frac{1}{4}} \quad . \tag{5}$$

The condensate is depleted after a time of order

$$t_c \sim \frac{t_*}{(G m^2 \sqrt{m t_*})^{\frac{1}{2}}} \tag{6}$$

where t_* is the initial time when all particles were assumed to be in the condensate. A classical description is invalid after time t_c.

Although we only analyze the behavior of homogeneous condensates in [1], we expect our conclusions to apply to inhomogeneous condensates as well. Indeed, a homogeneous condensate can be seen as a limiting case of inhomogeneous condensates. Since homogeneous condensates are depleted by parametric resonance, the same must be true for inhomogeneous condensates, at least in the limit of small deviations away from homogeneity. In fact in simulations of a five oscillator toy model [10, 25] we find that the condensates which persist forever according to their classical evolution are the condensates with the longest duration of classicality in their quantum evolution. We explained this result on the basis of analytical arguments [1]. By analogy with the behavior of the five oscillator toy model, we expect inhomogeneous condensates in quantum field theory to have shorter durations of classicality than homogeneous ones.

Related topics were discussed in two recent papers [26, 27]. Inter alia, ref. [26] solves the classical equations of motion for an initially almost homogeneous condensate with attractive contact interactions numerically on a lattice. If it were strictly homogeneous, the condensate would persist forever. Perturbations are introduced to mimic quantum fluctuations. As the perturbations grow, the condensate is depleted in a manner which appears qualitatively consistent with our quantum field theory treatment. Ref. [27] discusses, as we do, the duration of classicality of the cosmic axion fluid. The conclusions of ref. [27] differ from ours.

1 Acknowledgments

PS gratefully acknowledges the hospitality of the Theoretical Physics Group at the University of Oxford, the Center for Axion and Precision Physics in Daejeon, Korea, and the Institute for the Physics and Mathematics of the Universe in Tokyo. This work was supported in part by the U.S. Department of Energy under grant DE-FG02-97ER41209 and by the Heising-Simons Foundation under grant No. 2015-109.

References

[1] S. Chakrabarty, S. Enomoto, Y. Han, P. Sikivie and E. Todarello, arXiv:1710.02195.

[2] R. D. Peccei and H. Quinn, Phys. Rev. Lett. **38** (1977) 1440 and Phys. Rev. **D16** (1977) 1791; S. Weinberg, Phys. Rev. Lett. **40** (1978) 223; F. Wilczek, Phys. Rev. Lett. **40** (1978) 279.

[3] J. Kim, Phys. Rev. Lett. **43** (1979) 103; M. A. Shifman, A. I. Vainshtein and V. I. Zakharov, Nucl. Phys. **B166** (1980) 493; A. P. Zhitnitskii, Sov. J. Nucl. **31** (1980) 260; M. Dine, W. Fischler and M. Srednicki, Phys. Lett. **B104** (1981) 199.

[4] J. Preskill, M. Wise and F. Wilczek, Phys. Lett. **B120** (1983) 127; L. Abbott and P. Sikivie, Phys. Lett. **B120** (1983) 133; M. Dine and W. Fischler, Phys. Lett. **B120** (1983) 137.

[5] J. Ipser and P. Sikivie, Phys. Rev. Lett. 50 (1983) 925.

[6] P. Arias et al., JCAP 1206 (2012) 013.

[7] S.-J. Sin, Phys. Rev. D50 (1994) 3650; J. Goodman, New Astronomy Reviews 5 (2000) 103; W. Hu, R. Barkana and A. Gruzinov, Phys. Rev. Lett. 85 (2000) 1158; E.W. Mielke and J.A. Vélez Pérez, Phys. Lett. B671 (2009) 174; V. Lora Jet al.,JCAP 2 (2012) 011; D.J.E. Marsh and J. Silk, MNRAS 437 (2014) 2652; H.Y. Schive, T. Chiueh and T. Broadhurst, Nature Phys. 10 (2014) 496; B. Li, T. Rindler-Daller and P. Shapiro, Phys. Rev. D89 (2014) 083536; L. Hui, J.P. Ostriker, S. Tremaine and E. Witten, Phys. Rev. D95 (2017) 043541, and references therein.

[8] P. Sikivie and Q. Yang, Phys. Rev. Lett. 103 (2009) 111301.

[9] N. Banik, A.J. Christopherson, P. Sikivie and E.M. Todarello, Phys. Rev. D95 (2017) 043542

[10] O. Erken, P. Sikivie, H. Tam and Q. Yang, Phys. Rev. D85 (2012) 063520.

[11] K. Saikawa and M. Yamaguchi, Phys. Rev. D87 (2013) 085010.

[12] J. Berges and J. Jaeckel, Phys. Rev. D91 (2015) 025020.

[13] M.Y. Khlopov, B.A. Malomed and Y.B. Zeldovich, MNRAS 215 (1985) 575.

[14] M. Bianchi, D. Grasso and R. Ruffini, Astron. Astrophys. 231 (1990) 301.

[15] A. Natarajan and P. Sikivie, Phys. Rev. D73 (2006) 023510.

[16] P. Sikivie, Phys. Lett. B432 (1998) 139.

[17] P. Sikivie, Phys. Rev. D60 (1999) 063501.

[18] L. Duffy and P. Sikivie, Phys. Rev. D78 (2008) 063508.

[19] P. Sikivie, Phys. Lett. B695 (2011) 22.

[20] N. Banik and P. Sikivie, Phys. Rev. D88 (2013) 123517.

[21] A.M. Burkert and E. D'Onghia, Astrophys. and Space Science Library 319 (2004) 341, and references therein.

[22] S. Davidson and M. Elmer, JCAP 1312 (2013) 034.

[23] S. Davidson, Astropart. Phys. 65 (2015) 101.

[24] A.H. Guth, M.P. Hertzberg and C. Prescod-Weinstein, Phys. Rev. D92 (2015) 103513.

[25] P. Sikivie and E.M. Todarello, Phys. Lett. B770 (2017) 331.

[26] J. Berges, K. Boguslavski, A. Chatrchyan and J. Jaeckel, arXiv:1707.07696.

[27] G. Dvali and S. Zell, arXiv: 1710.00835.

The SHiP (Search for Hidden Particles) proposal

Eric van Herwijnen[1]

[1]CERN, Geneva, Switzerland

DOI: http://dx.doi.org/10.3204/DESY-PROC-2017-02/van_herwijnen_eric

SHiP is a new general purpose fixed target facility [1] at the CERN SPS. The 400 GeV proton beam from the SPS will be dumped on a heavy target, integrating 2×10^{20} POT (Protons On Target) in 5 years. The detector will probe models with light long-lived exotic particles and masses below $\mathcal{O}(10)$ GeV/c^2. The sensitivity to Heavy Neutrinos will allow probing the mass range between the kaon and the charm meson mass. Another, emulsion based, detector will measure the ν_τ deep inelastic scattering cross sections. Recoiling electrons will allow the direct detection of light dark matter.

1 The objective of SHiP

Despite intensive searches at the LHC and elsewhere, no significant deviations from the Standard Model of particle physics have been found. However, a number of experimental facts cannot be explained by the Standard Model, such as: neutrino masses and oscillations, dark matter, inflation and the baryonic asymmetry of the universe (BAU). Many theoretical models explain these facts by introducing very weakly interacting new particles with masses up to a few GeV/c^2. SHiP will try to find experimental support for some of these models.

2 Extensions of the Standard Model

It is possible that the particles responsible for the BSM problems have not been observed due to their extremely feeble interactions, rather than their heavy masses. Even in the scenarios in which BSM physics is related to high-mass scales, many models contain degrees of freedom with suppressed couplings that stay relevant at much lower energies.

2.1 Portals

It could be that some of the new particles do not interact directly with the SM sector. These "hidden sectors" may nevertheless be accessible thourgh sufficiently light particles ("mediators"), which are coupled to SM particles via renormalizable interactions with small dimensionless coupling constants ("portals"). There are 3 types of portal, depending on the mass dimension of the SM singlet operator: vector (dark photons), scalar (hidden scalars) and neutrino (HNLs). The production branching ratios of hidden sector particles are $\mathcal{O}(10^{-10})$, with $c\tau \sim \mathcal{O}$(km) and they would travel unperturbed through matter.

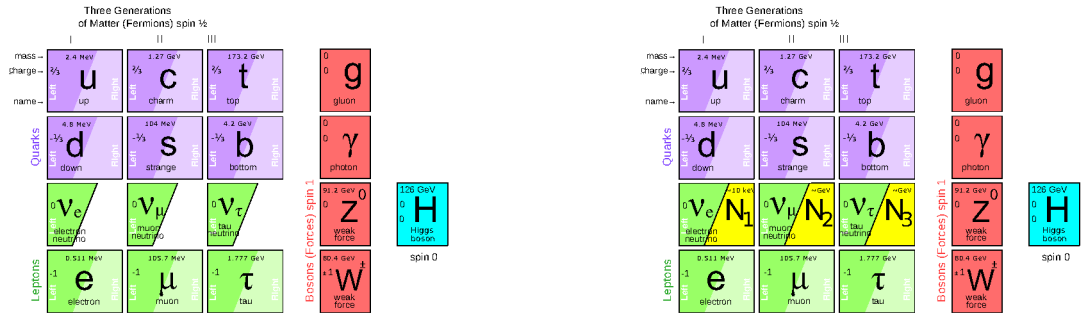

(a) The Standard Model (b) νMSM

Figure 1: Adding three right handed Majorana HNLs to the Standard Model

2.2 The ν Minimal Standard Model (νMSM)

Many current observations can be explained by a minimal extension of the Standard Model: the addition of three right-handed heavy neutral leptons (HNLs) (see Figure 2.2, [2]). A light $\mathcal{O}(1\ keV)$ N_1 serves as dark matter candidate, mass-degenerate $\mathcal{O}(100\ \mathrm{MeV/c^2}$ – few $\mathrm{GeV/c^2})$ $N_{2,3}$ give mass to the active neutrinos via the see-saw mechanism, and $N_{2,3}$ account for leptogenesis and hence explain baryogenesis by increased CP violation. In the νMSM, HNL production takes place in semi-leptonic decays from charm ($M_{HNL} < 2$ GeV/c^2) and beauty ($M_{HNL} < 5$ GeV/c^2), see Figure 2(a). Some examples of HNL decays into SM particles are shown in Figure 2(c) and branching ratios in Figure 2(b)(see [3]).

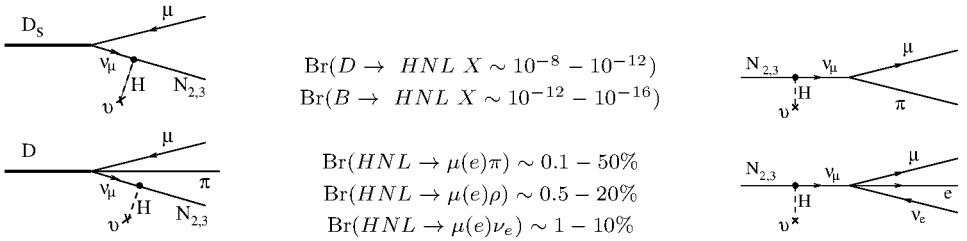

(a) HNL production

$\mathrm{Br}(D \to\ HNL\ X \sim 10^{-8} - 10^{-12})$
$\mathrm{Br}(B \to\ HNL\ X \sim 10^{-12} - 10^{-16})$

$\mathrm{Br}(HNL \to \mu(e)\pi) \sim 0.1 - 50\%$
$\mathrm{Br}(HNL \to \mu(e)\rho) \sim 0.5 - 20\%$
$\mathrm{Br}(HNL \to \mu(e)\nu_e) \sim 1 - 10\%$

(b) HNL production/decay BRs

(c) HNL decays

Figure 2: HNL production from charm/beauty (a) and HNL decays (c)

3 Experimental requirements and detector design

Because the hidden particles are expected to be predominantly accessible through the decays of heavy hadrons, the facility is designed to maximise their production and detector acceptance. With 2×10^{20} POT, the charm production at the SPS exceeds any existing facility. The hidden particles having a significant p_T, the detector should be placed close to the target (see Figure 3). A critical component of SHiP is the muon shield, which deflects the high flux of muon background away from the detector. The detector is designed to reject the background

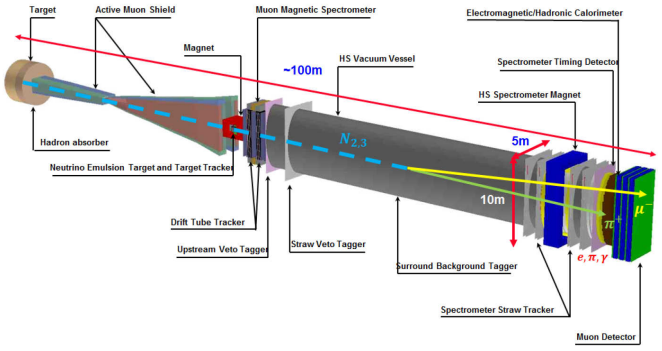

Figure 3: The SHiP detector

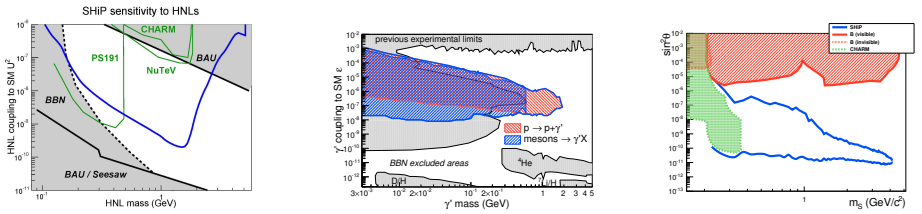

(a) HNL (b) Dark photon (c) Hidden scalars

Figure 4: SHiP sensitivities (blue) compared to theoretical and experimental limits

down to below 0.1 events in the sample of 2×10^{20} POT.

A large magnetic spectrometer is located downstream of a 50 m-long and 5×10 m-wide decay volume. To suppress the background from neutrino interactions, the decay volume is maintained under vacuum. The spectrometer is designed to accurately reconstruct the decay vertex, mass and impact parameter of the decaying particle at the target. Calorimeters followed by muon chambers identify electrons, photons, muons and charged hadrons. A high-resolution timing detector measures the coincidence of the decay products to reject combinatorial backgrounds.

The decay volume is surrounded by background taggers to detect neutrino and muon inelastic scattering in the surrounding structures, which may produce long-lived SM V^0 particles such as K_L, etc. The experimental facility also hosts a compact emulsion spectrometer based on the Opera [4] concept, upstream of the hidden-particle decay volume.

4 Sensitivities

The sensitivities of SHiP to HNL, dark photon and hidden scalars are shown in Figure 4. From these figures it can be seen that SHiP probes a unique range of couplings and masses.

5 Neutrino physics and light dark matter detection

Over 5 years of running $5.7 \times 10^{15} \nu_\tau$ and $\bar{\nu_\tau}$ candidates via $pN \to XD_s(\to \tau\nu_\tau)$ are expected. With these fluxes we expect $\sim 10^4(10^3)\nu_\tau(\bar{\nu_\tau})$, $\sim 10^5 \nu_e(\bar{\nu_e})$ and $\sim 10^6 \nu_\mu(\bar{\nu_\mu})$ interactions. This will enable the first direct observation of $\bar{\nu_\tau}$, the first independent measurement of σ_{ν_τ} and $\sigma_{\bar{\nu_\tau}}$ cross-sections.

The emulsion spectrometer can be transformed into a light dark matter emulsion calorimeter to detect electron recoils. For this, the emulsion is interleaved with heavy absorber strips. By reconstructing the electron direction and energy one can distinguish LDM- from ν-scattering.

6 Status of the project

The SPSC has positively reviewed the Technical Proposal [1] and the CERN Research Board has recommended SHiP to proceed with a Comprehensive Design Study. A report will be given to the Physics Beyond Colliders working group so that it can provide input to the next European Strategy Group.

During the Comprehensive Design phase the layout of the experimental facility and the geometry of the detectors will be further optimized. This involves a detailed study of the muon-shield magnets and the decay volume. A measurement of the μ-flux coming from a replica SHiP target is planned at the SPS in 2018 [5]. It also comprises revisiting the neutrino background in the fiducial volume, together with the background detectors, to decide on the required type of technology for evacuating the decay volume.

The SHiP collaboration currently consists of over 250 members from 49 institutes in 17 countries. The SHiP physics case was demonstrated to be very strong by a collaboration of more than 80 theorists in the SHiP Physics Proposal [6].

7 Conclusions

The intensity frontier greatly complements the search for new physics at the LHC. Major improvements and new results are expected during the next decade in neutrino and flavour physics, proton-decay experiments and measurements of the electric dipole moments. CERN will be well-positioned to make a unique contribution to exploration of the hidden-particle sector with the SHiP experiment at the SPS.

References

[1] The SHiP Collaboration, *Technical Proposal. An Experiment to Search for Hidden Particles (SHiP) at the SPS*, April 2015, CERN-SPSC-2015-016.

[2] T. Asaka and M. Shaposhnikov, *The νMSM, dark matter and baryon asymmetry of the universe*, *Phys.Lett.*,**B620**, 17-26, (2005). doi: 10.106/j.physletb.2005.06.020.

[3] D. Gorbunov and M. Shaposhnikov, *How to find neutral leptons of the νMSM?*, 2007, arXiv:0705.1729

[4] R. Acquafredda et al., *The OPERA experiment in the CERN to Gran Sasso neutrino beam*, *JINST*, **4**, P04018, (2009). doi: 10.1088/1748-0221/4/04/P04018.

[5] E. van Herwijnen et al., Muon-flux measurements for SHiP at H4, CERN-SPSC-2017-020 (June 2017), https://cds.cern.ch/record/2267770.

[6] S. Alekhin et al., *A facility to Search for Hidden Particles at the CERN SPS: the SHiP physics case*, *Rep. Prog. Phys.* **79**, 124201, (2016). doi:10.1088/0034-4885/79/12/124201.

List of Authors

List of Participants

Ahn Moo Hyun – CAPP / IBS / KOREA
Ahn Sae Byuk – Kobe University
Aprile Elena – Columbia University
Anastassopoulos Vassilis – University of Patras
Arias Paola – USACH (CHILE)
Avignone Frank – University of South Carolina
Baier Justin – ALU Freiburg
Baker Oliver – Yale University
Baudis Laura – University of Zurich
Bayirli Arif – Bogazici University
Berghaus Frank – University of Victoria
Bertram Iain – University of Lancaster
Blanchard John – Helmholz Institut Mainz
Boyce James – Jefferson Lab
Cantatore Giovanni – CERN & INFN Trieste
Carosi Gianpaolo – Lawrence Livermore Nat. Lab.
Carugno Giovanni – Padova Univ. & INFN
Cerulli Riccardo – INFN - LNGS (ITALY)
Cetin Serkant – ilgi University
Chung Woo Hyun – IBS/CAPP
Creswick Richard – University of South Carolina
Crivelli Paolo – ETH ZURICH
Dafni Theopisti – Universidad de Saragoza
Davenport Martyn – CERN
Del Ray Bayo Rocio – IFT-Universidad Aut. de Madrid
Derbin Aleksandr – St. Petersburg Nuclear Ph. Inst.
Dias Alex – Universidade Federal do ABC
Dbrich Babette – CERN
Dominguez Inma – Universidad de Granada
Du Xiaolong – University of Göttingen
Engel Ralph – Karlsruhe Inst. of Technology
Fairbairn Malcolm – Physics, King's College London
Fischer Horst – ALU Freiburg
Fowlie Andrew – Monash University
Funk, Wolfgang – CERN
Gardikiotis Antonios – University of Patras
Gianniotti Maurizio – Barry University
Gondolo Paolo – University of Utah
Goryachev Maxim – Univ. of Western Australia
Hakansson Nils – OKC
Heeck Julian – Universit libre de Bruxelles
Henning Reyco – Univ. of North Carolina
Hoffmann Dieter – TU - Darmastadt
Hoof Sebastian – Imperial College London

Irastorza Igor – Universidad de Saragoza
Jaeckel Jrg – ITP Heidelberg
Jennings Nicholas – University of Oxford
Karuza Marin – University of Rijeka
Kelley Katharine – Univ. of Western Australia
Kim Jihn – Kyung Hee University
Kim Kyungwon – Inst. for Basic Science
Kluck Holger – Inst. of High Energy Physics
Knirck Stefan – Max-Planck Institut
Ko Byeong Rok – IBS/CAPP
Kouvaris Christoforos – CP3-Origins
Kunc Stepan – Techn. Univ. of Liberec
Kyratzis Dimitrios – Aristotele University of Thessaloniki
Lee Do Yu – IBS/CAPP
Lentz Erik – University of Washington
Lindner Axel – DESY
Lindote Alexandre – LIP - Coimbra
Lucio Miriam – Univ. de Santiago de Compost.
Mcallister Benjamin – ARC, Univ. of Western Australia
Mcelroy Thomas – University of Alberta
Maroudas Marios – University of Patras
Marsh David – King's College London
Martinez Santos Diego – GAIN & Univ. de Santiago de Compost.
Matlashov Andrei – IBS/CAPP
Micelli Lino – IBS/CAPP
Mignani Roberto – INAF/IASF-Milan
Mitsou Vassiliki – IFIC - SCIC Univ.Valencia
Montanino Daniele – INFN LECCE
Mueller Guido – University of Florida
Muratova Valentina – St. Petersburg Nuclear Ph. Inst.
Niemeyer Jens – University of Göttingen
Nikolaidis, Argyris – Aristotele University of Thessaloniki
Obata Ippei – Kyoto University
Ore Ciaran – University of Nottingham
Ortolan Antonello – INFN - Legnaro
Papadopoulos Sotirios – Aristotele University of Thessaloniki
Pargner Andreas – Karlsruhe Inst. of Technology
Park Seong Tae – IBS/CAPP
Quinn Peter – ICRAR / Australia
Ranitzsch Philipp Chung-On – University of Münster
Rawlik Michal – ETH ZURICH
Redondo Javier – Zaragoza Univ. - MPP Munich
Ringwald Andreas – DESY
Ruoso Giuseppe – INFN Laboratory Legnaro
Rybka Gray – University of Washington
Sadoulet Bernard – University of California
Saikawa Ken'Ichi – DESY
Savidis Georgios – Aristotele University of Thessaloniki
Scherini Viviana – INFN / LECCE

Schumann Marc – University of Freiburg
Semertzidis Yannis – IBS/CAPP
Shin Yun Chang – IBS/CAPP
Sikivie Pierre – University of Florida
Simanovskaia Maria – UC Berkeley
Spray Andrew – IBS/CAPP
Stern Ian – University of Florida
Straniero Oscar – INAF - Osservatorio Astronomico di Teramo
Szabo Kalman – Forschungszentrum Jülich
Tan Andy – University of Maryland
Tkachev Igor – Institute for Nuclear Research
Troitsky Sergey – Institute for Nuclear Research
Tzaprazi Eleni – Aristotele University of Thessaloniki
Vafeiadis Theodoros – CERN
Vallee Claude – CPPM / DESY
Van Herwijnen Eric – CERN
Vergados Ioannis – University of Ioannina
Vogl Stefan – MAX PLANCK INSTITUT
Wittman David – UC Davis
Yan Haiyang – China Academy of Engineering Physics
Yoo Jong Hee – IBS/CAPP
Youn Sung Woo – IBS/CAPP
Yu Tien-Tien – CERN
Zhitnitsky Ariel – University of British Columbia
Zioutas Konstantin – University of Patras & CERN
Zioutas Hero

119 participants

Exploring axions and WIMPs in Greece

On 15–19 May, the historic Greek city of Thessaloniki hosted the 13th annual edition of the Patras Workshop on Axions, WIMPs and WISPs. Since the first meeting in 2005, the event has evolved into an important annual conference of the astroparticle community, addressing questions related to dark matter and dark energy both from the experiment and theory sides. Related topics from neutrino or astrophysics complement the agenda. An all-time high of more than 120 scientists attended the workshop this year, indicating the ever-growing interest in the quest for dark matter and especially for axions.

As well-established dark-matter candidates, along with weakly interacting massive particles (WIMPs), axions and axion-like particles (ALPs) are a central topic of the workshop. A large number of ongoing, planned and proposed experiments cover the full axion mass range with a good chance of detection. The most stringent experimental bounds on axion-to-photon couplings still come from "helioscopes" such as the CAST experiment at CERN, which use large magnets to convert axions produced in the Sun to detectable X-ray photons. New proposals discussed at the workshop aim at improving the sensitivity of experiments but also at extending their reach to dark-matter axions and dark-energy candidates such as chameleons (scalar particles that change their coupling strength in response to the local matter density). Dedicated chameleon searches were presented, exploiting both their coupling to photons and to matter, the latter using a novel opto-mechanical detector.

Dark-matter axions are the target of "haloscopes", which search for relic axions in the galactic halo using ultra-cold resonant microwave cavities immersed in a magnetic field. Various techniques to reach higher frequencies and to move the axion-mass coverage to the meV region are under study, and first results on axion masses up to around 24 μeV were reported by the HAYSTAC collaboration. Other projects aim at reaching even higher masses: multi-vane cavities, distributed Bragg reflectors, photonic band-gap resonators and multi-layered dielectric discs. These experiments employ cutting-edge superconducting technology and use amplifiers developed for quantum-computing research. Superconducting cavities that can achieve quality factors as high as 10^6 and ultra-high field magnets (up to 25 T) are also being developed at IBS/CAPP in Korea.

Vertot

Participants of PATRAS2017, which focuses on the low-energy, high-intensity frontier.

On the theory side, talks ranged from axions in string theory to estimates of the axion mass using the tools of lattice QCD. Several contributions focused on the observed anomalous transparency of the universe for high-energy photons, which might be explained by processes involving ultra-light ALPs with masses in the neV region or below. Others discussed whether the current density of dark-matter axions might differ from the homogeneous canonical picture due to the presence of axion condensates, caustics and mini-clusters.

A plethora of experiments aim at the direct detection of feeble WIMP-induced nuclear recoils. WIMPs are one of the prime candidates for cold dark matter because they arise naturally in various theories beyond the Standard Model of particle physics. The search strategy differs slightly for low- and high-mass WIMPs, with the transition taking place at around 5 GeV/c^2, but all efforts rely on ultra-low backgrounds and low thresholds. The Patras event saw detailed reports from almost a dozen running and upcoming projects – a highlight being the first public presentation of new results from the XENON1T dark-matter experiment, which has set the most stringent limits on WIMP-nucleon scattering above WIMP masses of around 10 GeV/c^2 (see p10). WIMP physics can also be probed indirectly, for instance by the Fermi telescope, and by colliders such as the LHC. It is now clear that, while the simplest WIMP models are under some pressure given the non-detection so far, plenty of well-motivated parameter space remains.

There are also a number of promising fixed-target experiments looking for portals from the dark sector to the Standard Model, such as dark photons, and other subtle experiments to study the low-energy, high-intensity frontier. In this frame, the community can look forward to developments with CERN's "Physics Beyond Colliders" initiative (*CERN Courier* November 2016 p28) and the US "Cosmic Vision" initiative.